UNIVERSITÀ DEGLI STUDI DELL'INSUBRIA

Facoltà di Scienze Matematiche, Fisiche e Naturali

Dottorato in Fisica XXIV ciclo

Anno Accademico 2011 - 2012

SILICON PHOTOMULTIPLIERS IN HIGH ENERGY AND SPACE APPLICATIONS

CERN-THESIS-2012-081
22/06/2012

Autore: Alessandro Berra
Matricola 610382

Tutor: Dr.ssa Michela Prest
Università degli Studi dell'Insubria
Cotutor: Dr. Erik Vallazza
INFN - Sezione di Trieste

If we knew what it was we were doing,
it would not be called research, would it?
A. Einstein

Contents

Introduction **1**

1 New Frontiers in Calorimetry **5**
1.1 Calorimetry in High Energy Physics 5
1.1.1 The Compensation Technique 9
1.1.2 The Particle Flow Approach 12
1.1.2.1 The Scintillator-Tungsten ECAL 15
1.1.2.2 The Scintillator-Steel HCAL 17
1.1.3 The Dual Readout Technique 21
1.2 Calorimetry in Space Physics 28
1.2.1 Cosmic Ray Satellites 29
1.2.2 Gamma Ray Satellites 35
1.2.2.1 The Gamma-400 Experiment 37

2 Silicon PhotoMultipliers **39**
2.1 The Basic Principles of Silicon Photodetectors 39
2.1.1 Ionization Processes 42
2.1.2 Optical Excitations 44
2.1.3 Junction Breakdown 46
2.2 Silicon Photodetectors 47
2.2.1 PIN Diodes 49
2.2.2 Hybrid PhotoDetectors 50
2.2.3 Avalanche PhotoDiodes 52
2.3 Silicon PhotoMultipliers 55
2.3.1 Gain and Linearity 56
2.3.2 Dark Counts 58
2.3.3 PhotoDetection Efficiency 60
2.3.4 Optical Crosstalk 61
2.3.5 Temperature Stability 63
2.3.6 Timing Performances 64
2.3.7 Radiation Damage 65

2.3.7.1 Gamma Irradiation 66
2.3.7.2 Neutron Irradiation 66
2.3.7.3 Proton Irradiation 69
2.4 The FBK-irst Silicon PhotoMultipliers 71

3 Performance of SiPMs with scintillating bars 75
3.1 The 2008 CERN Test 76
3.1.1 The T9 Beamline 76
3.1.2 Experimental Setup 77
3.1.2.1 The Silicon Beam Chambers 77
3.1.2.2 The EMR Prototype 79
3.1.2.3 The DAQ System 81
3.1.3 SiPM Characterization 83
3.1.3.1 FBK-irst SiPM Results 84
3.1.3.2 Hamamatsu SiPMs Results 88
3.2 The 2011 Cosmic Ray Test 92
3.2.1 Experimental Setup and DAQ 92
3.2.1.1 The MAROC3 Board 94
3.2.2 Results 95
3.2.2.1 Signal to Noise Ratio 96
3.2.2.2 Detection Efficiency 97
3.2.2.3 Optical Crosstalk 98
3.2.2.4 Spatial Resolution 99
3.2.2.5 Timing Resolution 99

4 Shashlik Calorimeters and SiPMs - Prototype 0 103
4.1 The 2009 CERN Beamtests 104
4.1.1 The Prototype 0 Shashlik Calorimeter 104
4.1.2 Experimental setups and DAQ 107
4.1.2.1 Low Energy Setup 107
4.1.2.2 High Energy Setup - The H4 Beamline 108
4.1.3 Calorimeter Performance Simulation with GEANT4 . . . 111
4.1.4 Low Energy Results 117
4.1.4.1 Linearity and energy resolution 117
4.1.5 Spatial resolution 124
4.1.6 High Energy Results 126
4.2 The 2010 CERN Beamtest 131
4.2.1 Experimental Setup 131
4.2.2 Results 133

5 Shashlik Calorimeters and SiPMs - Prototype 1 137
5.1 The 2009-2010 Beamtests . . . 137
5.1.1 The Prototype 1 Shashlik Calorimeter . . . 138
5.1.2 Experimental Setups . . . 139
5.1.3 Calorimeter Performance Simulation with GEANT4 . . . 141
5.1.4 Low Energy Results . . . 144
5.1.4.1 Linearity and energy resolution . . . 144
5.1.4.2 Spatial resolution . . . 148
5.1.5 High Energy Results . . . 149
5.2 The Optical GEANT4 Simulation . . . 152
5.2.1 Energy Resolution and Linearity . . . 156
5.2.2 Spatial Resolution . . . 161
5.3 The 2011 Beamtests . . . 162
5.3.1 Calorimeter Modifications . . . 163
5.3.2 Experimental Setups . . . 167
5.3.3 Low energy Results - May 2011 . . . 170
5.3.4 Low energy Results - August 2011 . . . 174
5.3.5 High Energy Results - September 2011 . . . 177

6 From Sampling to Homogeneous Calorimeters: the Lead Tungstate Crystals 183
6.1 The $PbWO_4$ Crystals . . . 183
6.2 Experimental Setup . . . 184
6.3 Results . . . 187

Conclusions and Outlooks 191

A Electromagnetic Calorimeters 197
A.1 Homogeneous or Sampling . . . 197
A.2 Electron/Positron Energy Loss . . . 198
A.3 Photon Energy Loss . . . 200
A.3.1 Photoelectric Effect . . . 202
A.3.2 Compton Effect . . . 202
A.3.3 Pair Production . . . 203
A.4 Electromagnetic Showers . . . 204
A.4.1 Longitudinal Profile . . . 206
A.4.2 Lateral Profile . . . 209
A.5 Energy Resolution . . . 210
A.5.1 Stochastic Term . . . 212
A.5.2 Noise Term . . . 213
A.5.3 Constant Term . . . 214

A.6 Shashlik Calorimeters 215

B Noise Characterization of the MAROC Readout System 221
B.1 Alternative Readout Circuit 221
B.2 Low Frequency Jitters and Dual-Hold Readout 223
B.3 New Bias Cable 226
B.4 Slow Shaper Parameters 228

List of acronyms 233

List of figures 243

List of tables 245

Bibliography 247

Introduction

Experiments in very different physics fields, from nuclear to particle and space physics, have a common key requirement: the measurement of the energy. Particle physicists use the word *calorimetry* to refer to a number of techniques developed to measure the energy of a particle by absorbing it in a block of matter, the so-called *calorimeter*. Calorimeters exploit the fact that the primary impinging particles interact with matter creating cascades of secondary particles, which are degraded and absorbed in order to measure the total energy of the shower. As a result of these interactions, the primary particle is completely absorbed inside the calorimeter and is not available for further measurements.

Even if the energy of a charged particle can be inferred measuring its bending inside a magnetic field, calorimeters have many advantages which make them an attractive alternative with respect to *magnetic spectrometers*:

- they are sensitive to all particle types, even the neutral ones, while magnetic spectrometers are sensitive only to charged particles. Moreover, calorimeters can provide an indirect identification of neutrinos measuring the missing energy;

- the energy resolution of a calorimeter usually improves with the particle energy E as $1/\sqrt{E}$, while the energy resolution of magnetic spectrometers deteriorates linearly with energy;

- calorimeters are versatile detectors: they can provide position, direction and angular information; they can be used in the particle identification (PID) to discriminate between electrons, photons, pions and muons according to the shape of their signals; they can be used to generate the trigger of the experiment.

Thanks to the requirements of the next generation high energy physics experiments, great efforts have been made in these last years to improve the performance of hadronic calorimeters, detectors specifically designed to measure the energy of high energy hadrons. The most promising techniques are the following:

- the particle flow method, which is based on the combined use of a high resolution tracker and a very finely segmented calorimeter (usually composed of silicon pads or small scintillator tiles) inside a magnetic field to independently measure the energy of the charged (using the tracker) and neutral (using the calorimeter) particles;

- the dual readout method, which is based on the time discrimination between the scintillation and Cherenkov signals produced in dedicated materials (plastic or quartz fibers) to evaluate the different components (purely hadronic or electromagnetic) of a hadronic shower.

In both these techniques, an efficient detection of light represents the key parameter to achieve the desired detector performance. Taking into account the stringent requirements of magnetic field insensitivity, timing resolution and cost per channel, solid state photodetectors can be considered as a valuable alternative to replace the standard photomultiplier tubes for the readout of the scintillator and Cherenkov light. The theoretical development of silicon photodetectors started in the early '40s, but technical problems due to the silicon technology limits at the time made them suitable for particle physics purposes only in 1980, with the introduction of the PIN diode. Since then, different types of silicon detectors have been developed: among them, the recently introduced *silicon photomultipliers* represent a major breakthrough in the light detection field.

Silicon PhotoMultipliers (SiPMs) consist of a matrix of small passively quenched silicon avalanche photodiodes operated in limited Geiger-mode (GM-APDs) and read out in parallel from a common output node. Each pixel (with a typical size in the 20–100 μm range) gives the same current response when hit by a photon; hence the total output signal is proportional (for moderate fluxes) to the number of hit pixels. The main advantages of the SiPMs with respect to the photomultiplier tubes (PMTs) are the low bias voltage ($\sim$50 V), the small dimensions, the simple readout and the insensitivity to magnetic fields, thus making them a suitable detector for next generation high energy and space physics experiments. On the other hand, SiPMs can be affected by radiation, suffer a high temperature dependent dark noise and their dynamic range is limited by the number of pixels. For all these reasons, the SiPM technology needs to be further developed.

The goal of this thesis work is to describe the use of SiPMs as a readout system for plastic scintillators, both for tracking and calorimetry purposes. All the tests have been performed in the framework of the FACTOR (Fiber Apparatus for Calorimetry and Tracking with Optoelectronic Read-out) collaboration, a three year R&D project started in 2007 and funded by the Italian Institute of Nuclear Physics (INFN). This collaboration has a twofold purpose:

- the development and optimization of the SiPM technology;

- the test of the performance of these devices as a readout system for fiber calorimeters and scintillators in high energy and space physics experiments.

The FACTOR project actively collaborates with FBK-irst, which has in the past years designed and produced SiPMs with different size and layout, featuring excellent overall performances.

The devices used for the majority of the tests are two prototypes of shashlik calorimeters, a particular type of electromagnetic calorimeter consisting of layers of lead (the absorber) and plastic scintillator (the active material). The scintillation light is readout by wavelength shifter fibers which cross the calorimeter for its whole length. Even if shashlik calorimeters are electromagnetic devices, the sampling technique and the fibers readout make this type of calorimeter conceptually similar to the ones recently proposed to test the particle flow and the dual readout techniques. Shashlik calorimeters are characterized by a low cost, lateral segmentation and good overall performances: among the examples, the STIC calorimeter of the DELPHI experiment at LEP and, more recently, the electromagnetic section of the LHCb detector at LHC have to be cited.

The first chapter of this thesis work presents the current state of the research in new calorimetric systems, focusing in particular on hadronic calorimetry for the next generation high energy physics colliders and on space physics applications, highlighting the improvements introduced in these fields by silicon based photodetectors. The second chapter is devoted to a general overview of the silicon photodetectors and to a detailed description of silicon photomultipliers, underlining their pros and cons.

The third chapter describes the first tests performed using the SiPMs for the readout of a scintillator bar tracker, a small prototype of the Electron Muon Ranger detector for the MICE experiment. This detector has been used to study the performances of the SiPMs compared to the ones of standard photomultipliers and to test two different readout systems based on a standard charge integrating ADC and on the MAROC3 frontend ASIC.

The fourth chapter summarizes the results obtained using the SiPMs for the readout of a prototype of a shashlik calorimeter, tested at CERN using low and high energy particles to compute its linearity, energy and spatial resolution. The results led to the assembly of a second prototype, described in the fifth chapter, readout with large area SiPMs using an integrated frontend board based on the MAROC ASIC. This chapter presents also a complete simulation of the calorimeter, including scintillation and light collection optical processes, performed using the GEANT4 package.

The sixth and last chapter presents the preliminary results obtained using the SiPMs coupled to a $PbWO_4$ crystal developed for the electromagnetic calorimeter of the CMS experiment. The SiPM used for this test is a new device produced

by FBK-irst, consisting in a matrix of four different SiPMs embedded in the same silicon substrate, called *quad*, characterized by a large area and dynamic range. This test is the first application of the new quad SiPM in a real high energy physics context and can be considered an important step towards their use on a large scale.

Chapter 1

New Frontiers in Calorimetry

Calorimeters (from the latin *calor*, that means energy) are a particular type of detectors designed to measure the energy of an incoming particle. Firstly developed for cosmic rays measurements, calorimeters have become some of the most important (and, often, the most expensive) detectors in the modern high energy physics experiments, holding roles that go beyond the mere energy measurement, including also particle identification and triggering tasks.

According to the type of particles they are designed to detect, calorimeters can be divided in electromagnetic and hadronic ones. Electromagnetic calorimeters are well understood objects, whose performances are driven by QED phenomena that can be calculated or simulated with high accuracy. More details on this type of calorimeters are given in appendix A. On the contrary, hadronic calorimeters are still under study and can be considered without any doubt the calorimetry hot topic of the last 20 years.

This chapter is devoted to a brief description of the recent developments in calorimetry, with particular attention to the hadronic one both in high energy and space physics applications. Considering the vastness and the complexity of this topic, many aspects are not presented in detail: a more comprehensive description can be found in [1]. As will be shown, some of the challenges in the development of new calorimeters rely on the use of new types of photodetectors, like the silicon photomultipliers, the main subject of this thesis work, which will be described in detail in the next chapter.

1.1 Calorimetry in High Energy Physics

The calorimetric system in high energy physics (HEP) experiments is usually divided in electromagnetic and hadronic sections, which are respectively devoted to the detection of high energy leptons and hadrons. However, this distinction is not

present in other physics fields (as, for instance, in cosmic ray experiments) where the general term "calorimeter" is typically used. Moreover, hadronic particles deposit a large fraction of their energy in the electromagnetic section, thus affecting the properties of the hadronic one and making the sections distinction somehow "artificial" [2].

In the majority of recent high energy experiments, from LEP and the flavor factories to LHC, the main priority has been given to the electromagnetic part of the calorimetric system. This choice is due to the fact that a large fraction of the physics phenomena were analyzed mainly using their leptonic decays, characterized by very good purity and signal cleanliness. This feature is largely exploited by hadronic machines, like the Tevatron and the LHC, to reject also the large and overwhelming QCD background.

Focusing only on LHC, the key requirement of the two general purpose experiments (ATLAS and CMS) calorimetric system was to reconstruct with the best possible resolution the Higgs boson in the $H \to \gamma\gamma$ decay channel, which is the most sensitive one to the low mass region investigated by LHC. This led to the development of electromagnetic calorimeters characterized by a very good energy resolution [3, 4] and representing the technology state of the art in this field.

On the other hand, the goal of the next generation colliders consists in the precision measurements of the TeV-scale physics as [5]:

- the Higgs boson decay channels and quantum numbers;
- the threshold scans for the discovery of new particles;
- the research of new physics beyond the Standard Model.

For all these tasks a key role is played by the intermediate $W^{\pm}$ and Z^0 vector bosons, which should be the final state of many new (and rare) physics processes and thus need to be efficiently identified on an event by event basis. This requirement is easily fulfilled in the case of the bosons leptonic decays, but represents an important challenge in the case of the hadronic ones, which are the 67.7% and 69.9% [6] of the total branching fraction for $W^{\pm}$ and Z^0 decays and are thus needed to improve the rate of signal events. Considering the mass difference between the two vector bosons ($\Delta m = 9.76$ GeV), a jet energy resolution of the order of $30\%/\sqrt{E}$ is required (Fig. 1.1) to separate the decays of the two bosons [7]. At the moment, this energy resolution is at least a factor two better than the one achieved by the existing detectors. As an example, the energy resolution of the complete calorimetric system for hadrons is $\sim 53\%/\sqrt{E}$ for the ATLAS experiment and $\sim 85\%/\sqrt{E}$ for the CMS one [2].

The poor energy resolution of the calorimetric systems for hadrons is essentially due to the fact that the development of hadronic showers is deeply different

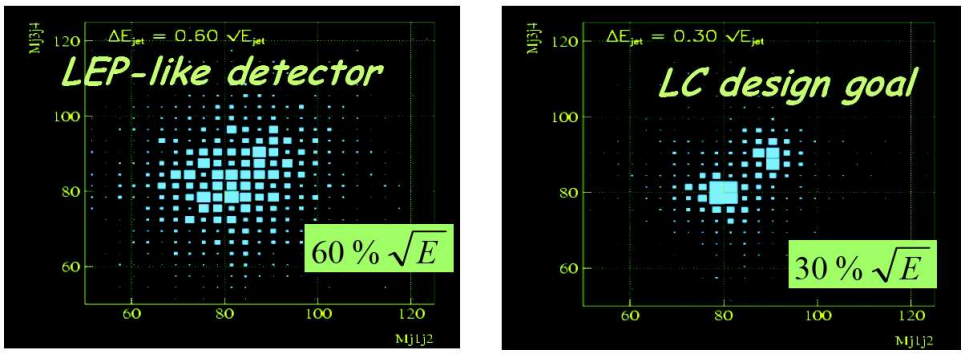

Figure 1.1: Jet energy resolution of present and ILC-like detectors and its effect on the $W^{\pm}$ and Z^0 bosons reconstruction.

from the one of electromagnetic cascades. In fact, the hadronic shower consists of two different components:

- an electromagnetic component, generated essentially by π^0s that decay into $\gamma\gamma$ pairs, which start an electromagnetic shower;
- a non-electromagnetic component, which combines essentially all the remaining processes in the shower.

From the calorimetry point of view, three main differences between these two components can be highlighted [2]:

- some fraction of the energy contained in the non-EM component is lost. This invisible energy is mainly represented by the binding energy of the nucleons released in the nuclear reactions, and may amount up to 40% of the total non-EM shower energy, with large event by event fluctuations. The invisible energy fluctuations represent the ultimate limiting factor on the precision of the energy measurement;
- the relative importance of the two components varies with the energy (Fig. 1.2): in particular the electromagnetic component increases with the energy of the primary particle since the π^0 production may also occur in secondary showers;
- the non-EM part of the hadronic shower is characterized by a large development both in the lateral and longitudinal dimensions, thus making it difficult to completely contain the cascade in the detector and introducing further sources of fluctuations due to the longitudinal and lateral leakage.

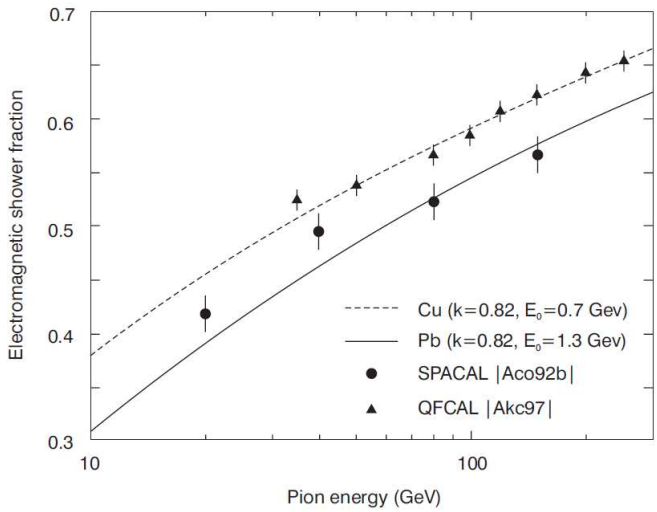

Figure 1.2: Fraction of the EM component in a hadronic shower as a function of the pion energy in copper and lead [1].

As a result of the invisible energy phenomenon, the calorimeter signals for hadrons are in general smaller than for electrons of the same energy: this effect is called *non-compensation*. Moreover, considering the fact that the fraction of the EM component increases with the energy, the energy response to hadrons is generally *non-linear*. The scale factor describing the non-EM shower profile is called *nuclear interaction length*, λ_{int}; it is defined as the average distance that a hadron travels before inducing a nuclear interaction and scales as $\sqrt[3]{A}$, with A the atomic mass number. However, compared with the radiation length X_0[1], the nuclear interaction length is much larger (as an example, in copper X_0 is equal to 1.4 cm, while λ_{int} is equal to 15 cm), thus explaining the large development of the hadronic showers. Fig. 1.3 presents the energy fraction contained in a block of material as a function of the number of nuclear interaction lengths.

As can be seen, the number of interaction lengths needed to contain 99% of the shower increases with the energy of the incident particles, arriving at 10 λ_{int}s for 138 GeV pions. Considering the large value of the λ_{int} parameter, very large detectors are needed to completely contain the hadronic showers. Many techniques have been proposed to build calorimetric systems capable to achieve the required performances for the next generation colliders: among them, the most promising are the ones based on the compensation technique, on the particle flow approach and on the dual readout concept.

[1] X_0 is the scale factor of the EM showers, see appendix A for details.

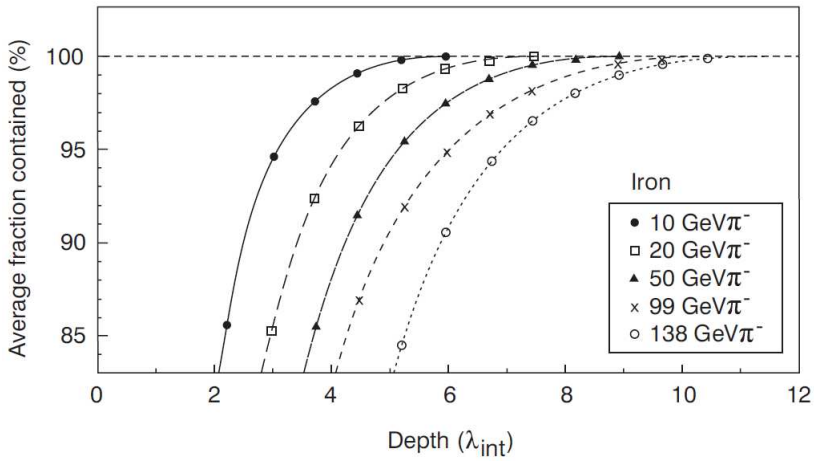

Figure 1.3: Average energy fraction contained in a block of material as a function of the number λ_{int}s and the pion energy in iron [1].

1.1.1 The Compensation Technique

Compensated calorimeters are defined as detectors that respond in the same way to the EM and non-EM component of a hadronic shower. The compensation condition is usually indicated as the e/h ratio, which is equal to 1 in the case of compensated calorimeters. Calorimeters characterized by a e/h ratio larger than 1 are defined as *under-compensated*, while calorimeters with the e/h ratio smaller than 1 are *over-compensated*. If the response to the EM and non-EM components is different, the large (and non Gaussian) fluctuations in the EM shower fraction degrade the energy resolution, dominating it especially at high energy [2].

The compensation can be achieved using sampling calorimeters with a very precise fraction of the high-Z absorber material and the hydrogenous [2] active material. In particular, using lead as the absorber material and plastic scintillator as the active one, the sampling fraction needed to achieve compensation is 4:1, as proven in [8], where 10 mm thick slabs of lead have been used with 2.5 mm thick tiles of plastic scintillator, obtaining a very good energy resolution for hadrons of $\sim$45%/$\sqrt{E}$. However, considering the small sampling fraction of such a calorimeter, the electromagnetic energy resolution was only $\sim$24%/$\sqrt{E}$.

Since the small sampling fraction is a must in the compensation technique, the only way to reduce the sampling fluctuations (thus improving both the EM and hadronic energy resolution) is to increase the sampling *frequency* of the calorimeter. This approach was followed by the LAA collaboration at CERN at the end

[2]The hydrogenous material is needed to boost the neutron response of the active material, thus equalizing *e* and *h*.

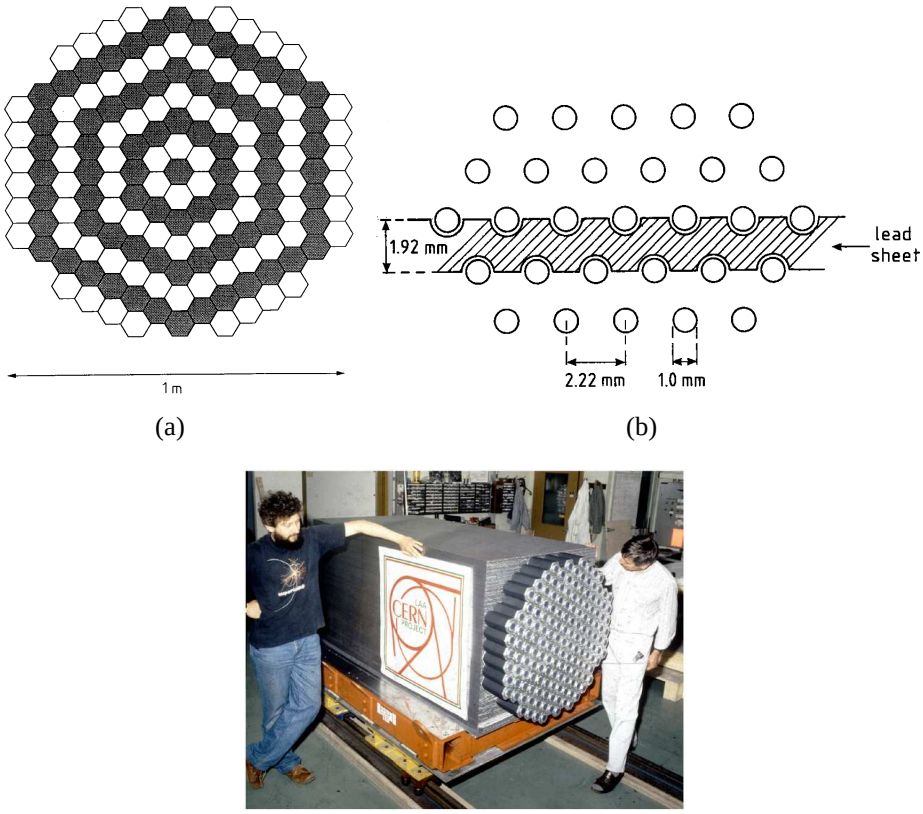

(a) (b)

(c)

Figure 1.4: The 155 towers of the SPACAL calorimeter (a), zoom on the fibers spacing inside the lead matrix (b) [9] and the final calorimeter (c).

of the ’80s, developing a calorimeter prototype with scintillating fibers as the active material and lead as the absorber, also known as Spaghetti Calorimeter (or SPACAL) [9].

The calorimeter consisted of 155 2 m deep hexagonal towers (Fig. 1.4(a)) made of extruded lead, for a total of 9.5 λ_{int} and 28 X_0. Each tower contained 1141 plastic scintillating fibers with a diameter of 1 mm and a length of 2.2 m. The fibers were embedded in the lead matrix with a spacing of 2.22 mm in order to maintain the 4:1 compensation ratio between lead and scintillator (Fig. 1.4(b)). The light readout was performed by means of photomultipliers coupled to the bundle of fibers of each tower using hexagonal light guides.

The calorimeter was tested at CERN on the H2 beamline using electrons, pions and hadronic jets (generated by the interaction of primary hadrons with a paraffin target) up to 150 GeV. In order to avoid the tunneling of the incoming particles in the fiber holes, the calorimeter was tilted of an angle $\theta_z = 3°$ with respect to the

beam axis.

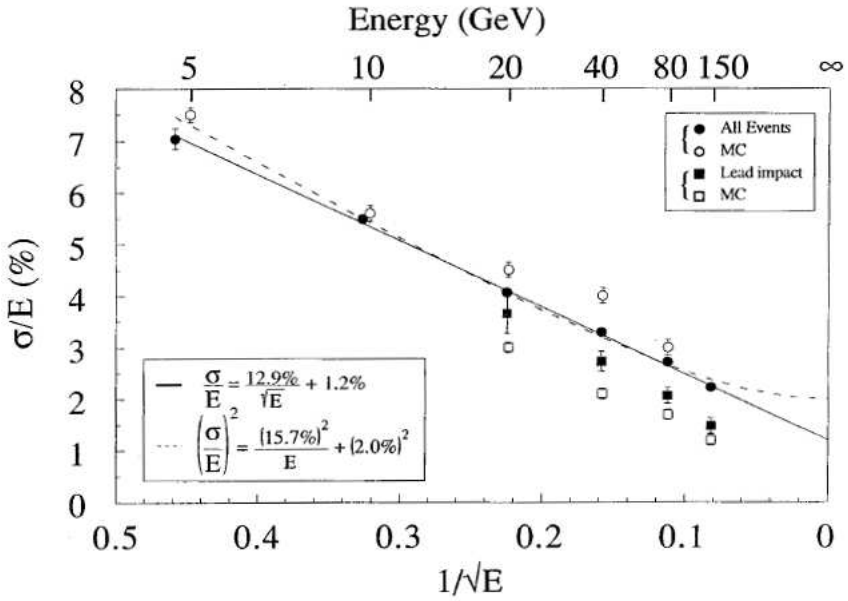

Figure 1.5: Energy resolution of the SPACAL calorimeter for electrons, compared with the Monte-Carlo simulation. The squared points are obtained selecting only the particles impinging on the lead surface.

As far as the electron events were concerned, a resolution $\sigma_E/E = 15.7\%/\sqrt{E} \oplus 1.99\%$ was obtained (Fig. 1.5). Considering the small dimension of the EM shower, the energy resolution measurement was affected by the fluctuations induced by the different impact point of the electrons on the calorimeter surface. In particular, it has been found that the electrons entering in the detector in a fiber (despite the 3° tilting) produced a larger signal, as shown in Fig. 1.6(a). The energy resolution can be improved (squared points in Fig. 1.5) selecting only the electrons impinging on the lead part of the calorimeter face. The impact-point dependence can be further reduced increasing the calorimeter tilt angle (Fig. 1.6(b)). As can be seen, the constant term is strongly dependent on the tilt angle, and it completely vanishes in the "asymptotic" position of 90°.

In the pion events analysis the main error source in the energy resolution measurement was due to the light attenuation inside the fibers. In fact, differently from the electromagnetic showers, the hadronic ones are characterized by a larger extension: because of the light attenuation the measured signal depends on how deep into the detector the light is produced. The attenuation coefficient of the fibers was determined performing a position scan, using electrons impinging on different positions of the calorimeter tilted with an angle of 90°. The results are

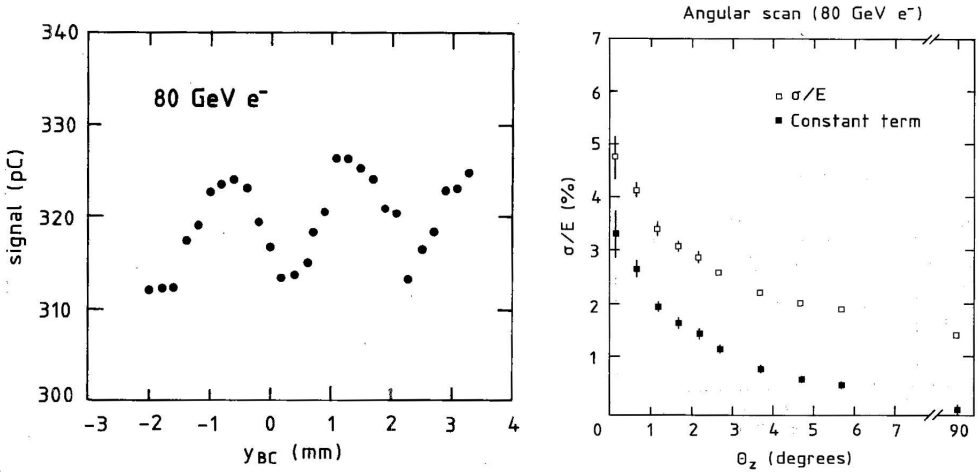

(a) (b)

Figure 1.6: Calorimeter signal as a function of the impact point parameter (a); constant term of the energy resolution as a function of the tilt angle (b) [9].

presented in Fig. 1.7(a). After the correction for the light attenuation, the energy resolution was $33.3\%/\sqrt{E} \oplus 2.2\%$, as presented in Fig. 1.7(b). This result is, at the moment, the best ever obtained in terms of energy resolution for a hadronic calorimeter [2].

1.1.2 The Particle Flow Approach

The particle flow (or PFlow) approach is a new method that has been recently proposed to fulfill the requirements of the ILC for the invariant mass reconstruction of hadronic jets. Precise measurements performed at LEP provided detailed information on the composition of the hadronic jets. In particular, it has been found that after the decay of the short-lived particles, the jet total energy is shared among several carriers [10]:

- $\sim$62% in charged particles;
- $\sim$27% in photons;
- $\sim$10% in neutral hadrons (neutrons and K_L);
- $\sim$1% in neutrinos.

In the traditional calorimetric approach, the energy of the jet is measured using only the information provided by the electromagnetic and hadronic calorimeters, thus being limited by the poor performance of the HCAL, whose energy resolution

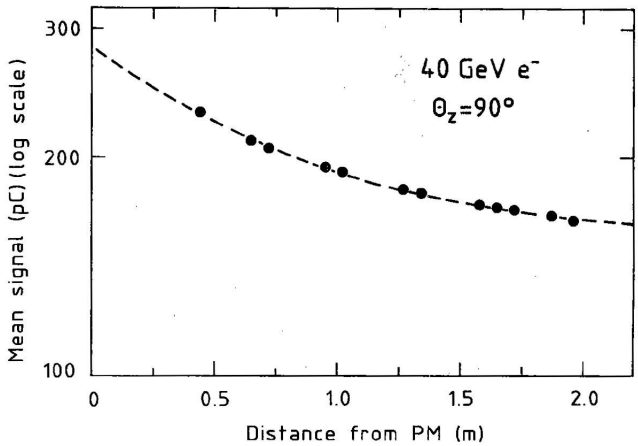

(a)

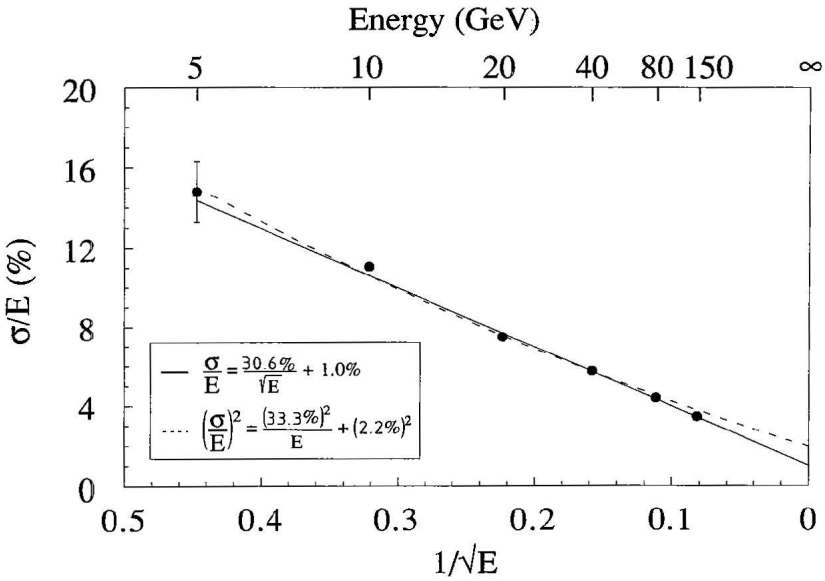

(b)

Figure 1.7: Light attenuation in the scintillating fibers of the SPACAL calorimeter measured with an electron beam impinging on different positions of the calorimeter, tilted of 90° (a) and energy resolution for pions after the attenuation correction (b) with a linear and quadratic fit [9].

is typically $> 60\%/\sqrt{E}$. The idea of the particle flow method is to reconstruct the energy of the charged particles composing the jet using the tracker system, limiting the use of the two calorimeters to the reconstruction of the neutral particles (γs and neutral hadrons). With this approach, the HCAL is used only to reconstruct a small fraction (10%) of the jet total energy, thus improving the final energy res-

olution. Assuming a photon energy resolution of $15\%/\sqrt{E}$, a hadronic energy resolution of $55\%/\sqrt{E}$ and a tracker energy resolution of $\sim 10^{-4}E^2$, a jet energy resolution of $19\%/\sqrt{E}$ can be theoretically obtained [10]. From the practical point of view, such a performance cannot be reached because it is not possible to perfectly associate all the energy deposits detected by the calorimeters to the correct particles, due to the finite *granularity* of the calorimeter itself.

The PFlow method has been used for the first time by the ALEPH experiment at LEP [11], obtaining a jet energy resolution for $\sqrt{s} = M_z$ of $\sigma_E/E = \sim 59\%/\sqrt{E} + 0.6\%$ (starting from a value of roughly $\sim 85\%/\sqrt{E}$ with no PFlow correction). This was the best jet energy resolution of the four LEP experiments, but is roughly a factor two worse than what needed by the ILC. The main limiting factor in the ALEPH case was the low granularity of the calorimeters.

The reliability of the PFlow approach strictly depends on the ability to correctly assign a calorimeter energy deposit to the corresponding reconstructed particle:

- from the tracker point of view, it is necessary to develop a complex pattern recognition software able to track and measure the energy of all the charged particles involved in the interaction; a large magnetic field is also necessary to curve the charged tracks and to separate the particles composing the jets as much as possible;

- from the calorimeter point of view, the PFlow approach places stringent requirements on the granularity of the ECAL and HCAL, which becomes the most important feature to be taken into account in the calorimeter design.

The high granularity (which means a large number of readout channels) and the need to use the calorimeters inside intense magnetic fields (thus needing magnetic field-insensitive detectors for their readout) can be considered the main technological challenges for the development of PFlow-optimized calorimeters, both in terms of the channel calibration/equalization and the readout systems. In this context, silicon photodetectors can play a very important role: these devices are intrinsically insensitive to magnetic fields, they have small dimensions (thus allowing the construction of very compact multichannel readout systems, avoiding cracks inside the calorimeter) and are cheaper than standard PMTs. In other words, silicon photodetectors are the perfect candidates for the readout of highly-segmented scintillator based calorimeters.

In recent years, the CALICE [12] collaboration has started the development of high granularity calorimeters for the future ILC collider, focusing on the PFlow approach to obtain the required detector performance. The CALICE collaboration follows different technological options for the development of both the electromagnetic and hadronic calorimeters. In particular, it successfully developed and

tested two prototypes of calorimeters (an electromagnetic and a hadronic one) based on plastic scintillator as the active material, readout with silicon photomultipliers.

1.1.2.1 The Scintillator-Tungsten ECAL

Electromagnetic showers are characterized by a much smaller spatial extension (and thus a much larger particle density) with respect to the hadronic ones. Thus, a very fine granularity of the order of 1 cm is needed to exploit the PFlow approach. The ECAL prototype built by the CALICE collaboration is a sampling calorimeter with 26 3 mm thick tiles of tungsten alloy (88% W, 11.5% Co and 0.5% C) and 26 3.5 mm thick tiles of plastic scintillator with an area of 9x9 cm^2 [13] for a total of 18.5 X_0. The plastic scintillator tiles were machined and segmented in 9x2 strips with an area of 4.5x1 cm^2 (Fig. 1.8); the strips were then drilled in order to host a 1 mm diameter WLS fiber to collect the scintillation light (Fig. 1.9).

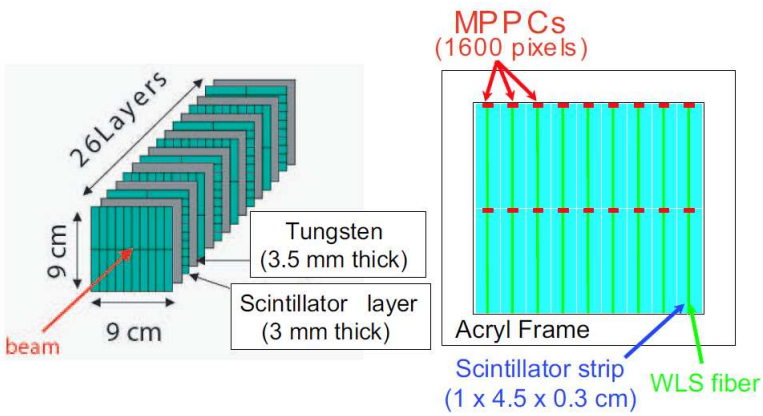

Figure 1.8: Sketch of the CALICE ECAL structure.

The scintillator layers are then arranged to form a x-y readout scheme: the strip approach has the advantage to fulfill the 1 cm granularity requirement, minimizing the number of readout channels with respect to a “pixel” scheme.

The use of the tungsten alloy as the absorber material has the advantage to reduce the Molière radius of the calorimeter, which is 29 mm; this means that about 5 strips in each layer will be triggered in each EM shower. The scintillation light collected by each WLS fiber is readout using a silicon photomultiplier (manufactured by Hamamatsu), with 1600 pixels of 25x25 μm^2, for a total active area of 1 mm^2. The silicon photomultipliers are assembled in a hole at the end of each scintillator strip and soldered to a flat signal cable. Fig. 1.10 presents a picture of the assembled calorimeter: the size of the entire module is about 9x9x20 cm^3, for a total of 468 readout channels.

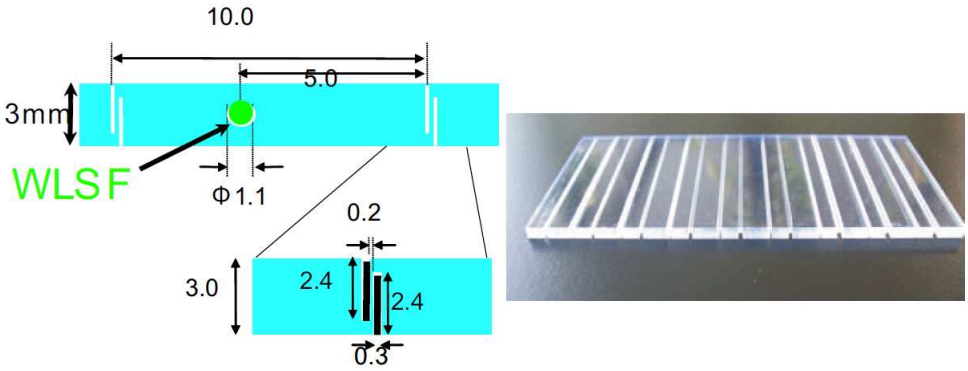

Figure 1.9: Sketch of the CALICE ECAL scintillator tiles. The WLS fiber hole and the trenches used to divide the scintillator tiles in strips are also depicted.

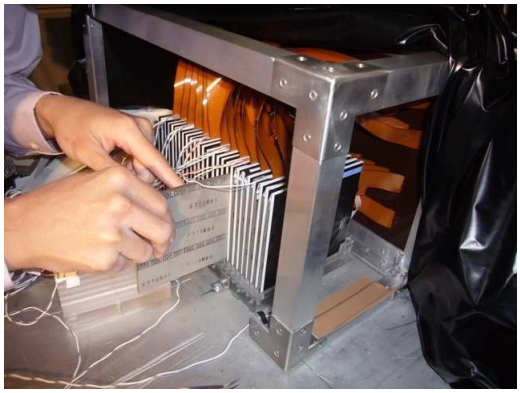

Figure 1.10: Picture of the CALICE ECAL module during the DESY 2007 beamtest.

The calorimeter has been tested at DESY in 2007 using a positron beam with an energy in the range 1–6 GeV. The response of each scintillator strip has been calibrated using MIPs, and the performance of the calorimeter has been evaluated in terms of linearity and energy resolution: the results are presented in Fig. 1.11. The linearity is quite good, with maximum deviations smaller than 4%, while the energy resolution features a stochastic term of 13.5%, and a constant term of the order of 2.9%. This large constant term has been ascribed to the calorimeter leakage and to non-uniformities in the strip response, even after the calibration with the MIPs.

After the DESY beamtest, the CALICE collaboration decided to modify the prototype, increasing both its lateral and longitudinal dimensions (thus reducing the leakage). The new prototype consists of 30 3.5 mm thick tungsten alloy layers and 30 3 mm thick scintillator layers with an area of 18x18 cm^2, for a total of

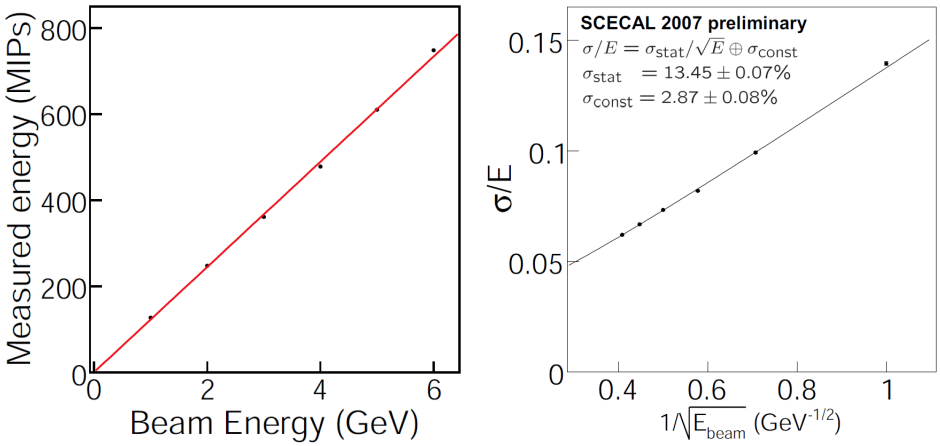

(a) (b)

Figure 1.11: Linearity (a) and energy resolution (b) obtained on the DESY 2007 beamtest with the first prototype of the CALICE ECAL [13].

21.3 X_0 [14]. Differently from the first prototype, the scintillator strips have been manufactured using an extrusion method and each strip is covered with a reflective film. Each scintillator layer is composed of 18x4 strips; as in the first prototype, the area of the strips is 4.5x1 cm^2, the scintillation light is collected using a double cladding WLS fiber and the readout is performed using SiPMs with 1600 pixels, glued in a hole at the end of each strip. The new prototype has been tested at FNAL between August and September 2008 using an electron beam with an energy up to 32 GeV. During the test, both a MIP calibration procedure and a SiPM saturation correction have been implemented. The results are shown in Fig. 1.12.

As far as the linearity is concerned, maximum deviations below 6% have been obtained, thus confirming the good results achieved by the first prototype even on a larger energy range. The energy resolution scan presents a stochastic term of 15.2% and a constant term of 1.4%: compared to the first prototype, the constant term is reduced to half of its previous value, indicating that the response uniformity and the leakage were effectively the limiting factors. On the other hand, the stochastic term is worse, a result which is still under study.

1.1.2.2 The Scintillator-Steel HCAL

The hadron calorimeter developed by the CALICE collaboration is conceptually similar to the electromagnetic one. It is composed of 38 17.4 mm thick steel plates (the absorber) and 38 active layers, which contain both the sensitive material (plastic scintillator) and the readout electronics [15]. This layout has been chosen to allow the integration of the readout electronics inside the calorimeter, maximiz-

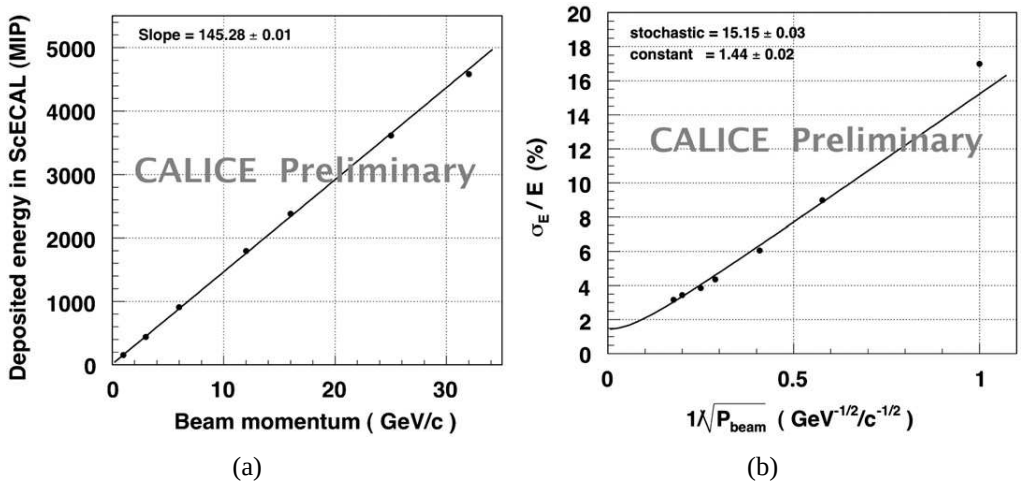

(a) (b)

Figure 1.12: Linearity (a) and energy resolution (b) obtained on the FNAL 2008 beamtest with the second prototype of the CALICE ECAL [14].

ing the compactness of the calorimeter itself. The high granularity required by the PFlow approach is ensured by the segmentation of the active scintillator layer in tiles with different dimensions according to their position in the layer itself: 3x3 cm^2 tiles have been used in the central part of the calorimeter, while a coarser granularity of 6x6 cm^2 and 12x12 cm^2 has been chosen moving towards the edges of the module (Fig. 1.13(a)). The thickness of the scintillator tiles is 0.5 cm.

A 1 mm WLS fiber has been embedded in each tile (Fig. 1.13(b)) to collect the scintillation light. In the smallest tiles a full circle is not possible (due to the small bending radius), thus a quarter of radius has been used. As in the ECAL, the light readout is performed using silicon photomultipliers directly embedded inside the edge of the scintillator tiles. The SiPMs have been manufactured by the MEPhI/PULSAR group; they have an active area of 1.1x1.1 mm^2 for a total of 1156 pixels. Considering the number of scintillator tiles, a total of 7608 SiPMs have been used for the HCAL prototype.

The scintillator tiles are sandwiched between two reflective sheets (manufactured by 3M) in order to improve the light collection. Micro-coax cables have been used to connect the SiPMs to the readout electronics, which is directly integrated at the front of the scintillator plate. The stability of the SiPMs is checked using a LED light distribution system and monitoring the temperature of the active layers by means of temperature sensors. The active layers are then assembled in “cassettes” (Fig. 1.14) that can be easily removed from the main calorimeter support in case of problems of the SiPMs or the readout electronics.

The HCAL has been tested in different beamtests at CERN in 2007 and at FNAL in 2008 and 2009 using both electron and pion beams with an energy be-

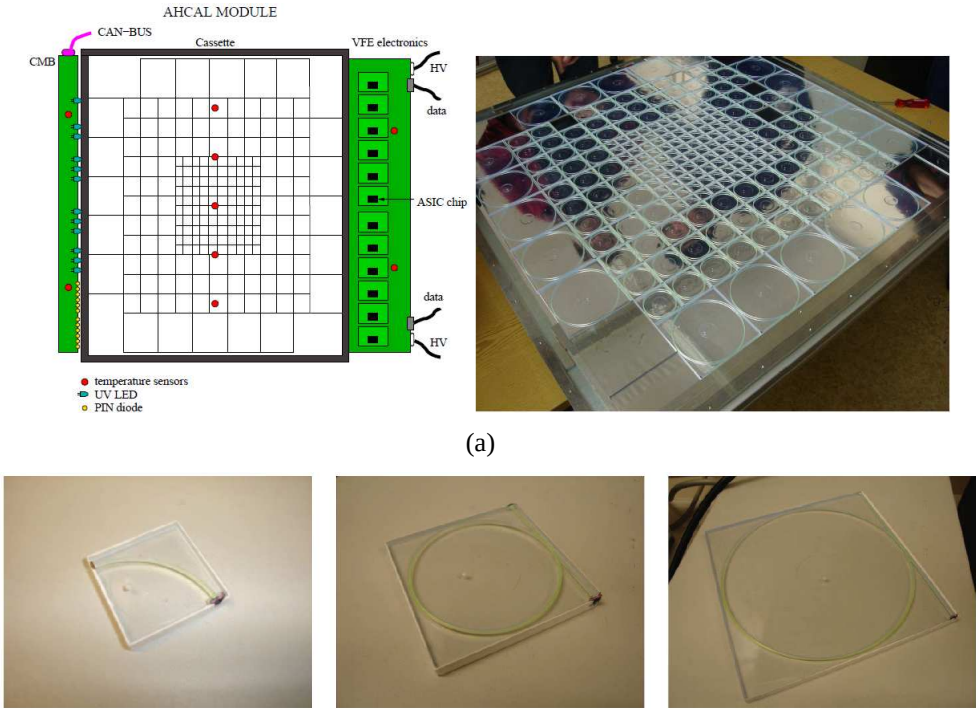

(a)

(b)

Figure 1.13: Layout of the scintillator tiles (a) and picture of the different tiles with the embedded WLS fibers (b).

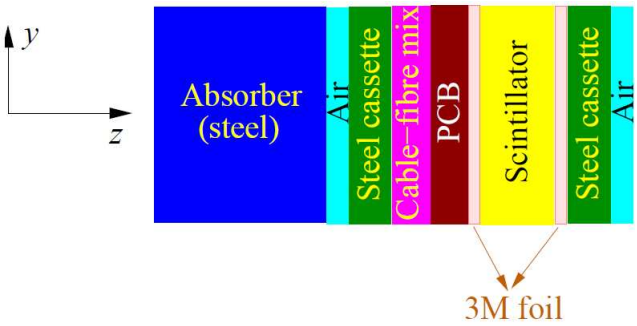

Figure 1.14: Schematic representation of one of the 38 cassettes (not to scale) of the CALICE HCAL, containing both the scintillator and electronics layers.

tween 1 and 50 GeV. The aim of these tests was twofold:

- to evaluate the response of the calorimeter to electromagnetic and hadronic showers for calibration purposes;
- to check the validity of different hadronic models used for the Monte-Carlo

simulation of the calorimeter.

As far as the electron test is concerned, the calorimeter performance has been evaluated in terms of linearity and energy resolution. The linearity is quite good in the 1-50 GeV range, with a good agreement between the CERN and FNAL datasets. The energy resolution has been measured to have a stochastic term of 21.7% and a constant term compatible with zero. The electron results are presented in Fig. 1.15.

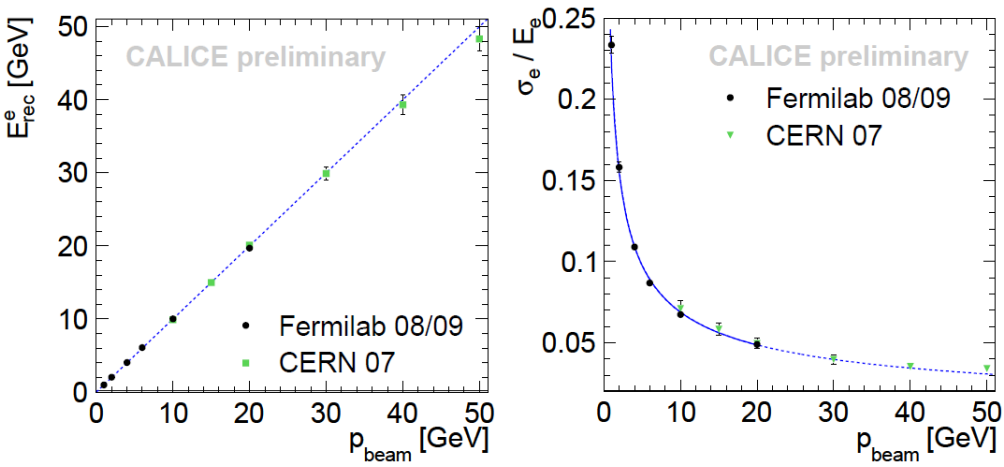

(a) (b)

Figure 1.15: Electron linearity (a) and energy resolution (b) of the CALICE HCAL. The different datasets acquired at CERN and FNAL are indicated with green and black dots [16].

Going to the hadronic tests, a non-linear response to pions was expected. This is due to the fact that the HCAL is not compensated, in the sense that the π/e[3] ratio is smaller than one. This effect is clearly visible in the plot of Fig. 1.16(a) where the pion mean energy (rescaled in units of MIPs to be compared with the electron data) at different momenta is presented.

The pion energy is underestimated with respect to the electron one, a clear indication of a non-compensation. Moreover, as can be seen in Fig. 1.16(b), the π/e ratio varies with energy, thus deteriorating the energy resolution.

Even in intrinsically non-compensating calorimeters, compensation can be achieved analyzing the contribution of the different energy deposits (electromagnetic or hadronic) and by weighting them with different factors in the off-line analysis. To discriminate between two components, it is necessary to evaluate the

[3]The π/e ratio is an alternative way to describe the compensation parameter, usually expressed as the e/*h* ratio.

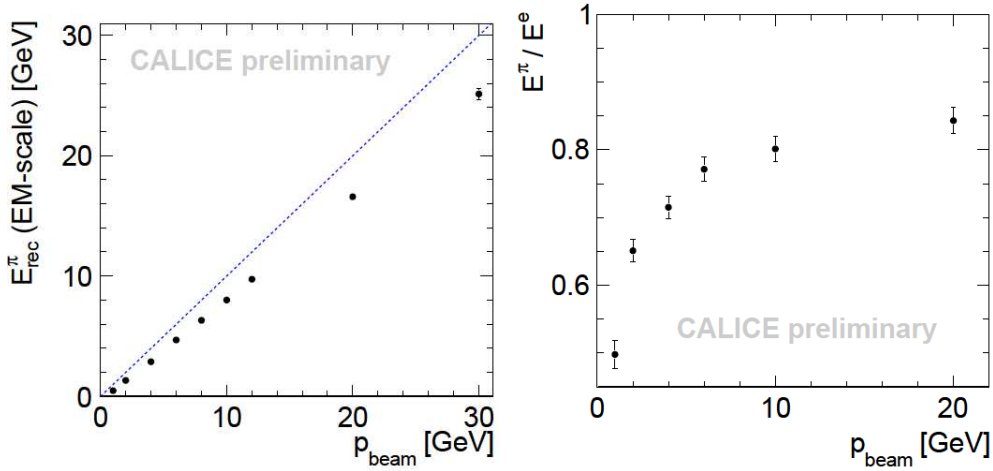

(a) (b)

Figure 1.16: Energy response to pions (a) and π/e value at different energies (b) obtained with the CALICE HCAL [16].

local energy density in the detector, exploiting the fact that electromagnetic showers are denser than the purely hadronic ones. This procedure can be used with the HCAL, analyzing the energy deposit inside each calorimeter cell: the large energy deposits are associated to the core of the shower, and thus a small weighting factor is used. Since the composition and the density of the shower vary with the energy, the weighting factors are usually energy dependent. Fig. 1.17 presents the energy resolution of the HCAL computed using different analysis approaches for pions with an energy up to 80 GeV.

The single weight method is the simplest one, but also the less optimized: it consists in the sum of the contributions of the different cells, multiplied by an average GeV/MIP correction factor. The energy resolution can be improved using multiple energy dependent weights for the electromagnetic and hadronic showers, selected according to the energy density of each calorimeter cell, obtaining a stochastic term smaller than $50\%/\sqrt{E}$. The results of this analysis are still preliminary.

1.1.3 The Dual Readout Technique

The dual readout technique is an evolution of the compensation technique. As previously explained, the main problem of the hadronic showers is that the EM component fluctuates on an event by event basis, with a relative importance that varies with the energy. In compensating calorimeters these fluctuations are eliminated by design, and the calorimeter has the same response to the EM and non-EM

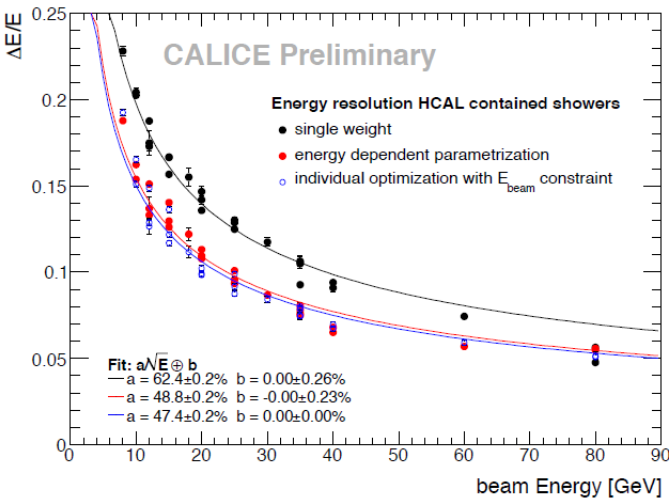

Figure 1.17: Energy resolution of the HCAL using a simple single weighting method (black dots), multiple energy dependent weights (red dots) and multiple weights with beam energy constraints (blue dots) [17]. The analysis is based on the 2007 CERN data.

component. These calorimeters are however limited by the poor EM resolution, due to the small sampling fraction that has to be adopted to fulfill the compensation requirement.

The goal of the dual readout technique is to measure the fraction of the EM component event by event using a non-compensated calorimeter (*i.e.* with an electromagnetic resolution $< 15\%/\sqrt{E}$), thus eliminating the main source of fluctuations. The dual readout approach takes advantage from the fact that the energy carried by the non-EM component is deposited mainly through non-relativistic particles (protons and neutrons), while relativistic electrons are the responsible of the EM part [2]. This means that it is possible to evaluate the EM and non-EM components of a hadronic shower measuring at the same time:

- the Cherenkov emission, which is sensitive only to the relativistic EM part;
- the total dE/dx inside the detector, for example measuring the scintillation light emitted by a standard scintillator, which is sensitive to both the EM and non-EM part.

The feasibility of the dual readout method was first experimentally demonstrated by the DREAM (Dual REAdout Method) collaboration [18]. The basic element of the DREAM detector is a 2 m long extruded rod of copper with a cross section of 4x4 mm^2. The central part of the rod is hollow, with a hole with a diameter of 2.5 mm filled with seven 0.8 mm diameter optical fibers (Fig. 1.18). The

effective nuclear interaction radiation length is ∼200 mm, thus the whole detector corresponds to 10 λ_{int}.

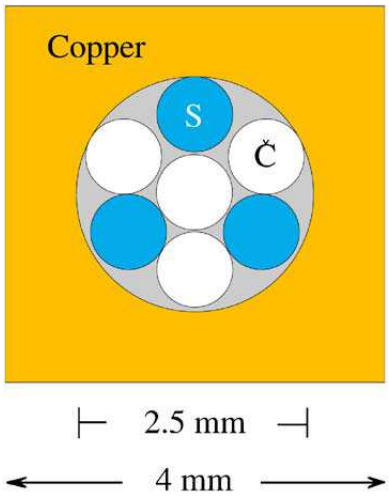

Figure 1.18: Basic module of the DREAM calorimeter. The Cherenkov fibers are depicted in white, while the plastic scintillating fibers are depicted in blue [18].

Three of the seven fibers are standard plastic scintillating fibers, while the other four are made of high purity quartz or undoped plastic and are used as Cherenkov radiators. The complete DREAM calorimeter consists of 5580 copper rods, 5130 of which equipped with fibers, while the remaining are left empty and used in the external region of the detector to improve the mechanical stability. The central rods of the assembly have been equipped with the quartz fibers, while the external ones with the clear plastic fibers. The rods have been divided into 19 hexagonal towers, as schematically shown in Fig. 1.19(a). The fibers of each tower are also divided in different bunches (Fig. 1.19(b)) for the scintillating and Cherenkov ones, for a total of 38 bunches. Each bunch of fibers is coupled to a PMT, using a yellow filter for the scintillating fibers and no filter for the Cherenkov ones. The yellow filter is used both to reduce the light attenuation effect along the fibers (the yellow wavelength is less attenuated inside the plastic material) and the amount of light impinging on the PMT, thus avoiding saturation effects.

The DREAM calorimeter has been tested at CERN on the H4 beamline using high energy electrons, pions and jets between 20 and 300 GeV. The electron events have been used for calibration purposes, to evaluate the e/h ratio and to study the light attenuation inside the fibers. In order to avoid the tunneling of the particles inside the fibers, the calorimeter has been tested in a slightly tilted position with respect to the beam axis (2° in the horizontal plane and 0.7° in the vertical one).

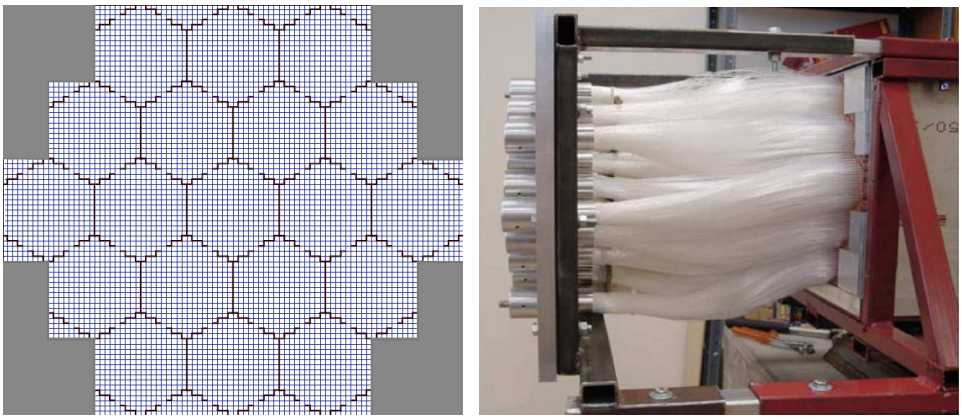

(a) (b)

Figure 1.19: Sketch of the DREAM calorimeter tower structure (a) and bundles of fibers exiting from the back of the calorimeter coupled to the PMTs (b) [18].

As far as the pion events are concerned, their signal is characterized by the typical shape of non-compensating calorimeters (Fig. 1.20(a)):

- the presence of asymmetric tails both in the Cherenkov and scintillator signals;
- very broad distributions, with σ_E/E values of 12.3 and 19% at 100 GeV;
- mean values considerably smaller than the ones obtained with electrons of the same energy.

Thus, the calorimeter is non-linear for pion detection, and is characterized by a poor energy resolution (Fig. 1.20(b)), especially when using the Cherenkov readout.

On the other hand, the power of the dual readout technique can be exploited combining the information collected by the Cherenkov and scintillating fibers. In general, the hadronic response of the calorimeter can be expressed as a function of the EM shower fraction according to the following relation [18]:

$$R(f_{em}) = f_{em} + \frac{1}{e/h}(1 - f_{em}) \tag{1.1}$$

where f_{em} is the EM shower fraction and e/h is the compensation ratio. This equation holds separately both for the Cherenkov and scintillating components, which are characterized by a different e/h value. In particular, the compensation ratio of a copper/quartz fiber module is $\sim$5, while the one of a copper/plastic

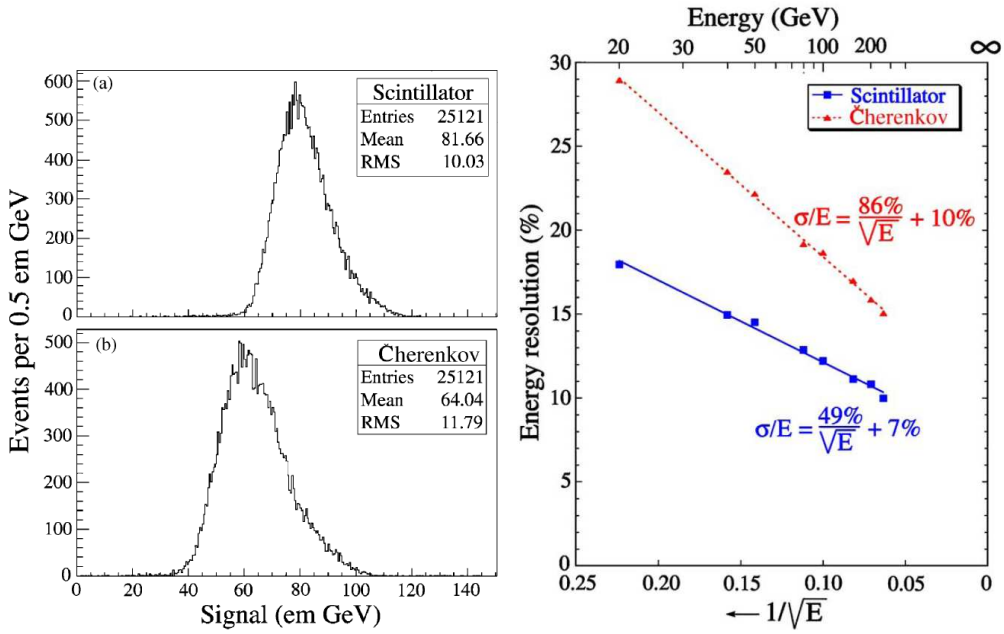

(a) (b)

Figure 1.20: Signal distributions of 100 GeV pions using the scintillating and Cherenkov fibers (a) and corresponding energy resolution fitted with a linear sum (b) [18].

structure is ∼1.4. Thus, equation 1.1 can be written in two separate ways for the scintillator and Cherenkov components:

$$Q = f_{em} + 0.20(1 - f_{em}) \tag{1.2}$$
$$S = f_{em} + 0.71(1 - f_{em}) \tag{1.3}$$

where 0.20 and 0.71 are the $(e/h)^{-1}$ values of the Cherenkov (Q) and scintillator (S) components. Two variables can be defined to relate Q and S to the EM fraction: the Q/S and the $(Q+S)/E$ ratio. The first one is the ratio of the scintillator and Cherenkov response to hadrons:

$$\frac{Q}{S} = \frac{f_{em} + 0.20(1 - f_{em})}{f_{em} + 0.71(1 - f_{em})} \tag{1.4}$$

The Q/S ratio can be used to evaluate the f_{em} parameter event by event (Fig. 1.21(a)) and a correction procedure for each of the two components can be applied using the following:

$$S(Q)_{final} = S(Q)\left[\frac{1 + p1/p0}{1 + f_{em}p1/p0}\right] \tag{1.5}$$

where $S(Q)_{final}$ is the corrected scintillator (Cherenkov) signal and $S(Q)$ is the uncorrected scintillator (Cherenkov) signal. $p1/p0$ is defined as $e/h-1$ and the exact value of this ratio can be obtained performing a linear fit on the scintillator signal as a function of the f_{em} variable (Fig. 1.21(b)).

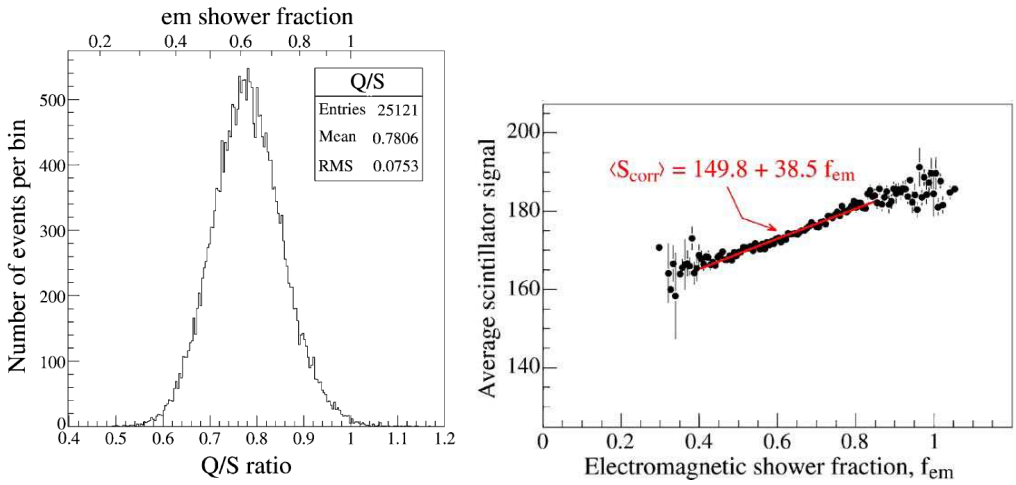

(a) (b)

Figure 1.21: Value of the Q/S ratio with the corresponding f_{em} value (a); linear fit of the scintillator signal versus the f_{em} value (b) [18].

Fig. 1.22(a) presents the energy resolution for pions before and after the correction. The energy resolution improves from the $86\%/\sqrt{E}$ and $49\%/\sqrt{E}$ of the Cherenkov and scintillator component to $41\%/\sqrt{E}$ for both the components. Moreover, the correction procedure improves also the linearity, with maximum deviations after the correction of the order of 3% (Fig. 1.22(b)), and substantially reduces the asymmetric tails of the signals.

The efficacy of the Q/S correction procedure could be improved reducing the shower longitudinal leakage, which affected the calorimeter at very high energy. The presence of the longitudinal leakage can be confirmed looking at the high energy signal distributions, which are still characterized by asymmetric tails also after the correction. Nevertheless, the efficacy of this procedure was remarkable.

Even better results can be obtained using the second correction method, based on the $(Q+S)/E$ variable:

$$\frac{(Q+S)}{E} = 0.91 + 1.09 f_{em} \tag{1.6}$$

This variable is defined starting from equations 1.2 and 1.3, including the beam energy E. Similarly to the Q/S method, the correction is applied to a single component (the scintillator or the Cherenkov one) after a linear fit of the $(Q+S)/E$

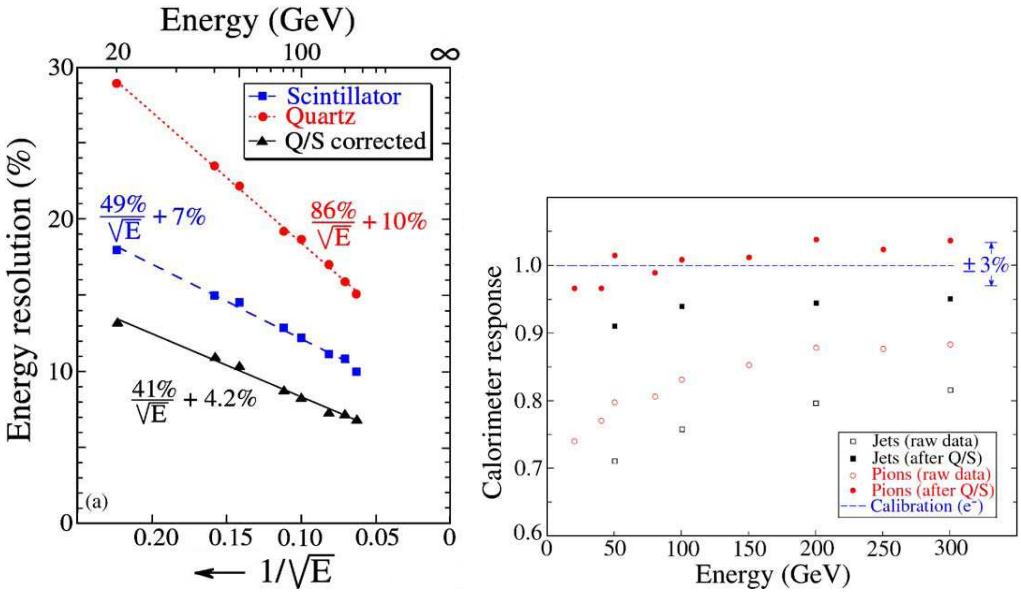

(a) (b)

Figure 1.22: Energy resolution (a) and linearity (b) before and after the Q/S correction procedure [18].

dependence. The results in terms of energy resolution and linearity are presented in Fig. 1.23.

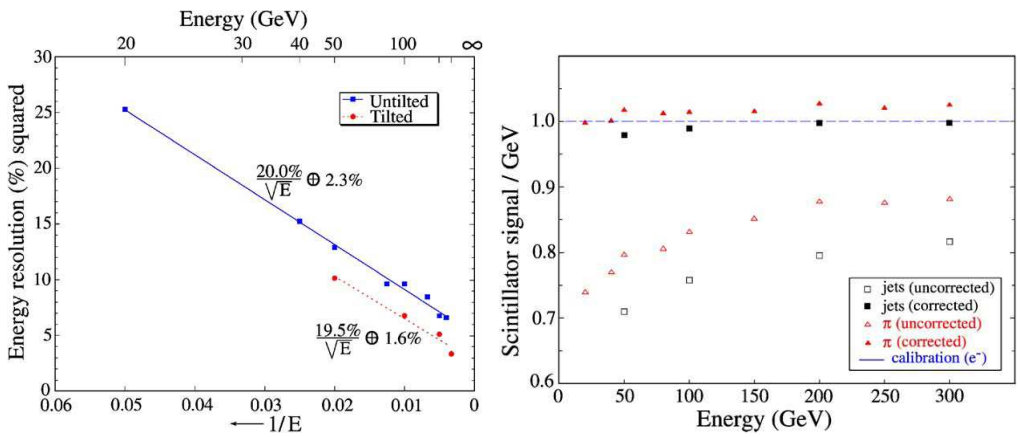

(a) (b)

Figure 1.23: Energy resolution after the $(Q+S)/E$ correction (both in the tilted and untilted position) (a) and linearity (b) before and after the $(Q+S)/E$ correction procedure [18].

As can be seen, the energy resolution is greatly improved with respect to the

simple Q/S method reaching a value of $20\%/\sqrt{E}$. Even better results can be obtained tilting the calorimeter, thus minimizing the particles tunneling into the fibers. The new correction method improves also the linearity of the calorimeter to pions and jets. However, this method is based on an information which is usually not available in a real calorimeter: the knowledge of the impinging particle energy. Thus, this correction method cannot be applied in a real collider experiment. However, these results can be considered as the best estimate of the dual readout capabilities, which can anyway be achieved with the Q/S method minimizing the longitudinal leakage.

It has been shown recently that the dual readout method can be applied also to crystal calorimeters, in particular to $PbWO_4$ and BGO [19] crystals, which are used simultaneously as scintillators and Cherenkov radiators. In this case the discrimination between the scintillation and Cherenkov light is performed exploiting the time structure of the two signals. In particular, the Cherenkov radiation is emitted promptly with a very fast emission of the order of a few ns, while the scintillation light is emitted with a timescale of tens or hundreds of ns, with a well defined exponential attenuation law. Thus, also in this case the use of new and fast silicon photodetectors like the silicon photomultipliers offers many advantages with respect to the standard PMTs.

1.2 Calorimetry in Space Physics

Since their discovery in 1912, cosmic rays played a fundamental role both in particle physics and astrophysics [20]. Composed of charged and neutral particles, their energy spectrum covers more than 20 orders of magnitude up to 10^{20} eV [21], an energy far beyond the one achieved in modern particle accelerators. These particles are emitted by the most powerful astrophysical and cosmological objects in the universe, but the models describing the acceleration processes of the most energetic cosmic rays ($E > 10^{18}$eV) are still unknown.

Even if the energy of primary cosmic rays can be studied on the Earth surface, detecting the particle showers produced inside the atmosphere, direct measurements performed outside the atmosphere are needed to better identify their emission sources. Moreover, the Earth atmosphere is opaque to high energy photons (in the X and gamma band), thus satellite-based experiments are mandatory to study this component of the cosmic rays. All these demands led to the development of particular types of calorimeters specifically designed to operate in the space environment.

The calorimeters used in space physics experiments have to face a large number of constraints:

- compactness and robustness, in order to comply with the stringent dimension and weight requirements of the payloads and to reduce the launch costs;
- low power consumption and heat dissipation;
- spatial and angular discrimination to identify the emission sources with a good enough resolution;
- large dynamic range in order to cover a large energy interval.

Due to the large spatial extension of the hadronic showers, the dimension constraints particularly affect the hadronic capabilities of the calorimeter. For this reason, space calorimeters are usually used to study the electromagnetic component of the cosmic rays, that is electrons, positrons and high energy γs. Nevertheless, topological constraints on the shower development inside the calorimeter can be used to discriminate between hadrons and leptons: for this reason, silicon based detectors (mainly strips or small scintillators coupled to silicon photodetectors) are usually used to build finely-segmented calorimeters in both the lateral and longitudinal direction in order to reconstruct the shape of the shower.

1.2.1 Cosmic Ray Satellites

These experiments are designed to study the charged component of the cosmic rays in terms of energy spectrum and composition, with particular attention to the anti-matter research. The two most recent experiments of this type are PAMELA (Payload for Antimatter Matter Exploration and Light-nuclei Astrophysics) [22] on board of the Russian Resurs DK-1 earth-observation satellite, and AMS-02 (Alpha Magnetic Spectrometer-2) [23], installed on the International Space Station in 2011. The main goals of both these experiments are:

- the search for anti-matter, in particular anti-helium nuclei;
- the search for dark matter candidates;
- the precise measurement of the cosmic ray flux and energy spectrum up to several TeVs.

A sketch of the experiments layout is presented in Fig. 1.24.

The central part of both the detectors is a magnetic spectrometer, to measure the momentum of the incoming particles by their bending inside the magnetic field. The calorimeter is used to precisely measure the energy of the incoming particle and to discriminate between electrons/positrons and hadrons. In particular, positrons have to be identified from a background of protons that is about 10^3

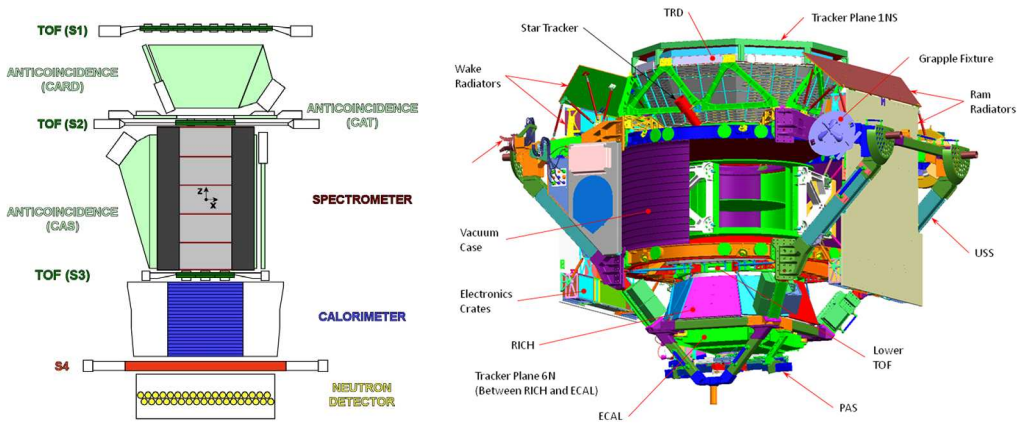

(a) (b)

Figure 1.24: Layout of the PAMELA (a) [22] and AMS-02 (b) [24] experiments.

times the positrons component at 1 GeV, while anti-protons have to be selected from a background of electrons $\sim$5x10^3 times larger [22]. In both the experiments, the particle identification (PID) is performed exploiting the different shape of the electromagnetic and hadronic showers, using a fine grained calorimeter, able to image the shower development in 3D[4].

The PAMELA calorimeter section is composed of 22 2.6 mm thick layers of tungsten and 44 layers of silicon strip detectors, for a total of 16.3 X_0. The silicon layers are arranged in a x-y geometry, thus providing a 2D spatial information of the shower development. Each silicon plane consists of two single sided 3x3, 380 μm thick, 8x8 cm^2 detectors, segmented into 32 strips with a pitch of 2.4 mm [22]. Two pictures of the PAMELA calorimeter are presented in Fig. 1.25.

A prototype version of the calorimeter has been tested at the CERN SPS with electrons and pions up to 200 GeV, which corresponds to the maximum energy sensitivity of the spectrometer. The results showed that an energy resolution of the order of 5.5% could be achieved in the energy range 20–200 GeV, with a very good electron-pion separation (Fig. 1.26). An important feature of the PAMELA calorimeter is the ability to work in self triggering mode up to an energy of 2 TeV, overcoming the limit imposed by the magnetic spectrometer. The performance of the calorimeter in the self triggering configuration has been simulated above 200 GeV, obtaining an energy resolution of the order of 12% in the 200–700 GeV range, which deteriorates to 16% above 1 TeV, due to the large shower leakage (open circles in Fig. 1.26(a)).

[4]The PID task in the AMS-02 detector is accomplished using also a Transition Radiation Detector and a Ring Imaging Cherenkov Detector, installed before the calorimeter section.

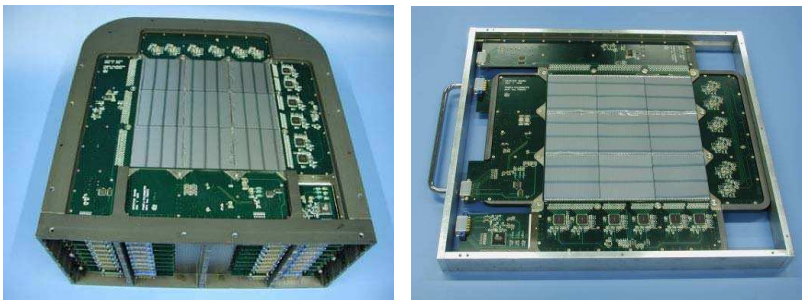

(a) (b)

Figure 1.25: Layout of the complete PAMELA calorimeter module (a) and a detail of a single layer (b) [22].

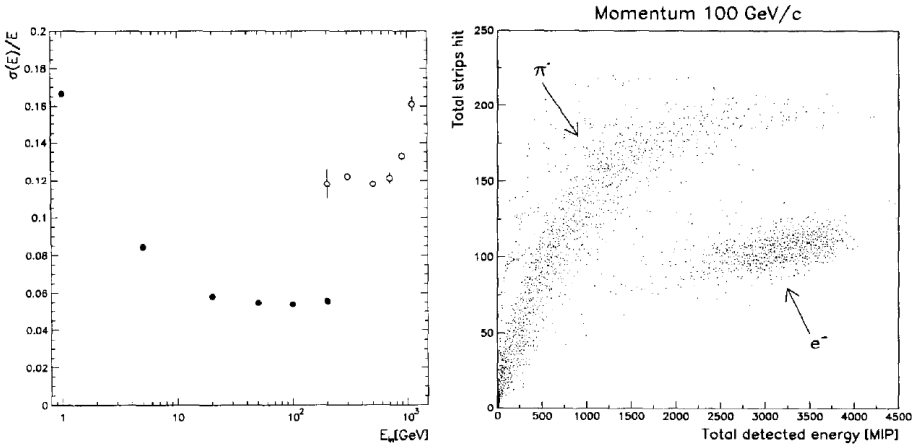

(a) (b)

Figure 1.26: Energy resolution (a) and electron/pion discrimination (b) of the PAMELA calorimeter [25]. The open circles in (a) are the simulated data obtained with the calorimeter in self triggering mode.

After a brief commissioning phase, the instrument has entered the data taking mode in July 2006. Fig. 1.27 presents an example of event discrimination performed with the calorimeter on real in flight data. The events have been selected by the magnetic spectrometer with a momentum between 20 and 30 GeV/c. The plots of Fig. 1.27(a) have been obtained exploiting the shower tracking capability of the calorimeter. The x axis represents the ratio between the charge released along the track in the calorimeter (obtained by summing the signal in the hit strip and the signals in the left and right neighboring strips) and the total charge measured in the calorimeter itself. Thus, this quantity is equal to one in the case of non interacting hadrons (protons or anti-protons). In the negative par-

ticles plot, the peak corresponding to the electrons can be clearly seen, while in the positive particle plot the positron sample, expected to be peaked in the same position of the electron one, is completely overwhelmed by the background of protons. Fig. 1.27(b) presents the same plots after some topological cuts on the shower profile, the starting point and energy-momentum matching with the magnetic spectrometer. The positron peak can be clearly seen, demonstrating the good PID capabilities of the calorimeter.

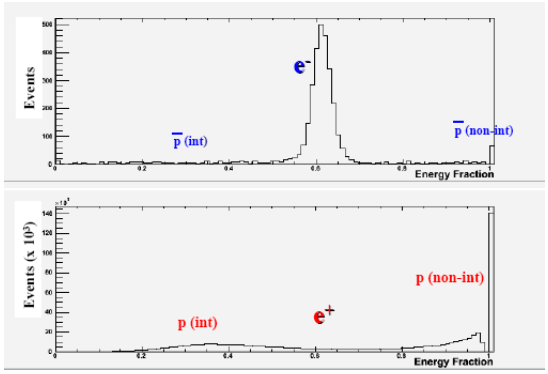

(a)

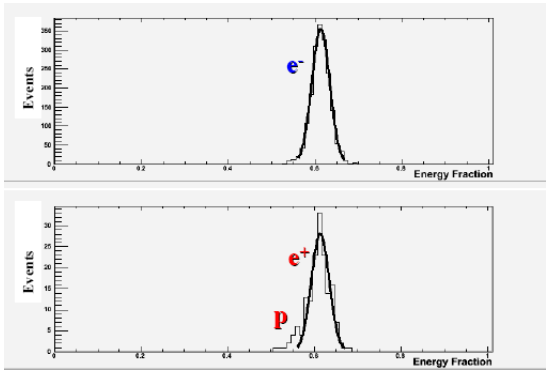

(b)

Figure 1.27: Energy fraction released along the track in the calorimeter for both negative (top) and positive (bottom) particles before (a) and after the energy-momentum match correction (b) [22].

As far as the AMS-02 calorimeter is concerned, a completely different design has been chosen with respect to the PAMELA one. The AMS-02 calorimeter is a sampling device composed of lead as the absorber and 1 mm plastic scintillating fibers embedded in the lead structure as the active medium. The orientation of the fibers is rotated by 90° every 10 planes of lead and fibers, forming a so-called superlayer. In total, 9 superlayers are present, 4 in the x direction and 5 in the y one. The dimensions of the calorimeter are 65.8x65.8x16.65 cm^3 for a

total of ∼16.8 X_0 [26]. A sketch of the fiber-lead structure and a picture of three superlayers are presented in Fig. 1.28.

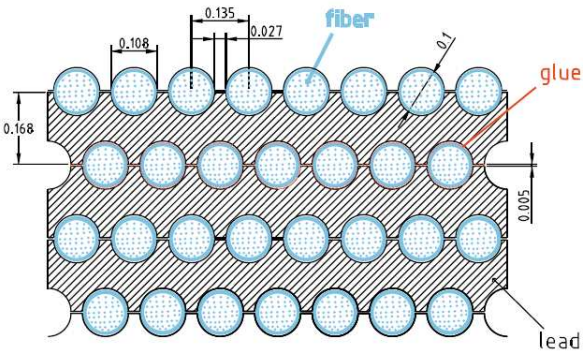

(a)

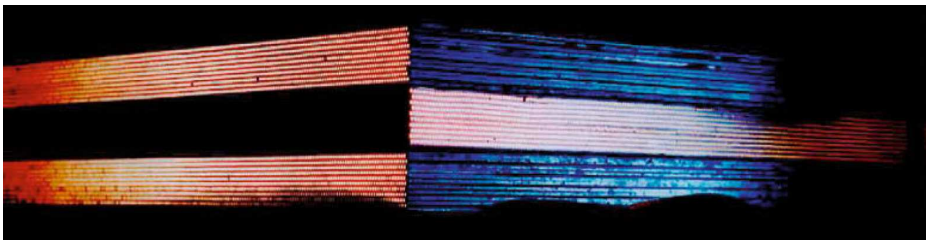

(b)

Figure 1.28: Sketch (a) and picture (b) of the AMS-02 calorimeter [26].

The light readout is performed using 324 Hamamatsu multianode PMTs (MAPMTs). Each MAPMT is composed of 4 9x9 mm^2 pixels. The MAPMT cells are coupled to groups of fibers by means of light guides. The MAPMTs located in the central superlayers are also used to provide a standalone trigger for electron/positron or gamma events. The complete calorimeter module has been tested at the CERN H4 beamline using 100 GeV protons and electrons in the 6–250 GeV range. Considering the fiber structure of the calorimeter, different corrections have to be implemented to improve the angular and energy resolution:

- a gain equalization of the different channels using a dedicated MIP beam;
- a correction of the light attenuation along the fibers;
- a correction of the energy deposit with respect to the particle impact point;
- a correction of the longitudinal energy leakage.

In particular, the leakage correction considerably improves the linearity and energy resolution at high energies: Figs. 1.29(a) and 1.29(b) present a maximum

deviation from linearity of the order of 1%, with an energy resolution (for an incidence angle of 0°) of $\frac{9.9\%}{\sqrt{E}} \oplus 1.5\%$. The energy resolution improves increasing the impinging angle due to the larger number of radiation lengths crossed by the particle. As far as the angular resolution is concerned, a value below 1° has been obtained for particles above 50 GeV (Fig. 1.29(c)).

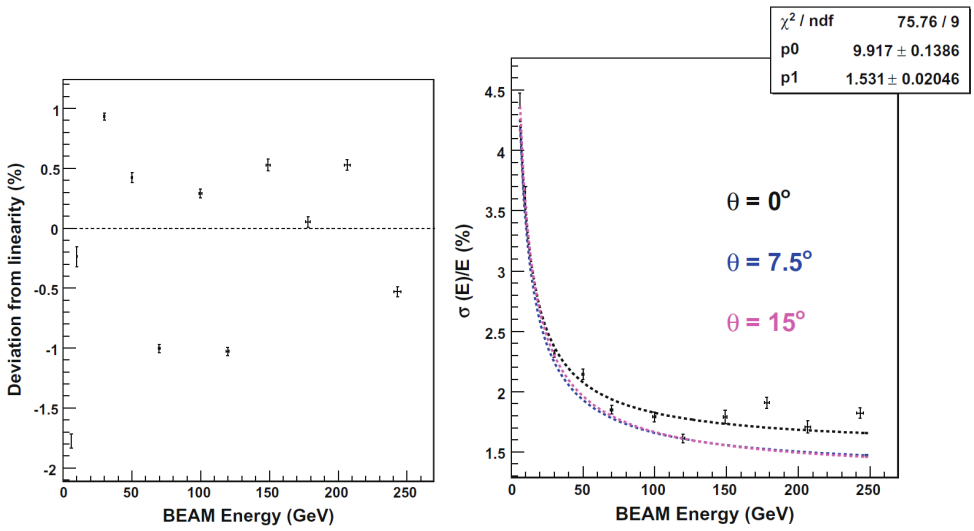

(a)

(b)

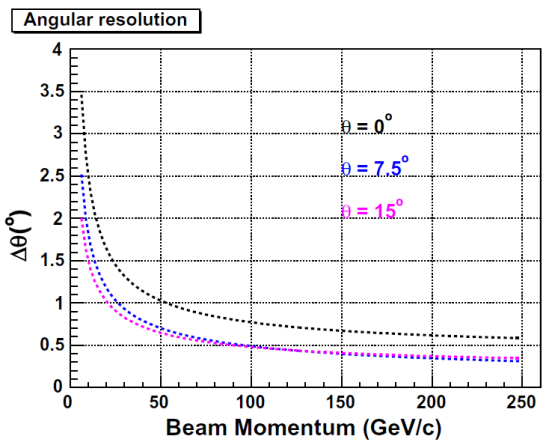

(c)

Figure 1.29: Linearity (a), energy (b) and angular resolution (c) of the AMS-02 calorimeter [26].

1.2.2 Gamma Ray Satellites

The first observations of gamma rays coming from outside the Earth atmosphere were performed using very simple detectors mounted on air balloons or rockets originally developed to monitor the atomic tests of USA and USSR [27]. Unexpectedly, most of the gamma ray sources identified during these surveys were located outside the Earth atmosphere: gamma ray astronomy was born.

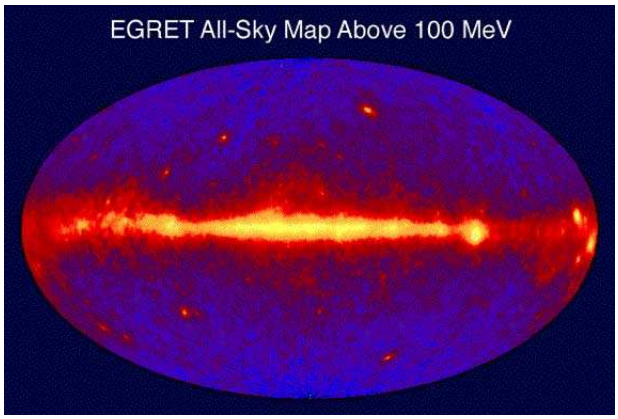

Figure 1.30: Map of the sky obtained by the EGRET telescope with gamma rays above 100 MeV.

Since the ’60s, many satellite-based experiments have been sent in orbit to study the gamma and X ray emission starting from a few hundreds of keV up the multi-GeV scale. Among them, EGRET (Energetic Gamma-Ray Telescope Experiment), mounted on the Compton Gamma-Ray Observatory [28] in 1991, discovered a large number of new sources and studied in great detail the diffused galactic gamma ray emission (Fig. 1.30).

The study of high energy photons is the primary interest also of the recent space physics experiments, like AGILE [29] and FERMI-LAT [30]. Due to the fact that gamma rays are neutral particles, their path is not modified by the galactic magnetic field and thus can be considered as a direct probe to study their production sites, like supernova remnants, active galactic nuclei and gamma ray bursts. The typical layout of a gamma ray telescope is the following (Fig. 1.31):

- a gamma ray tracker;
- an electromagnetic calorimeter;
- an anticoincidence system.

The gamma ray tracker is the heart of the experiment: it is composed of alternate layers of high Z material (called converters) and silicon microstrip detectors.

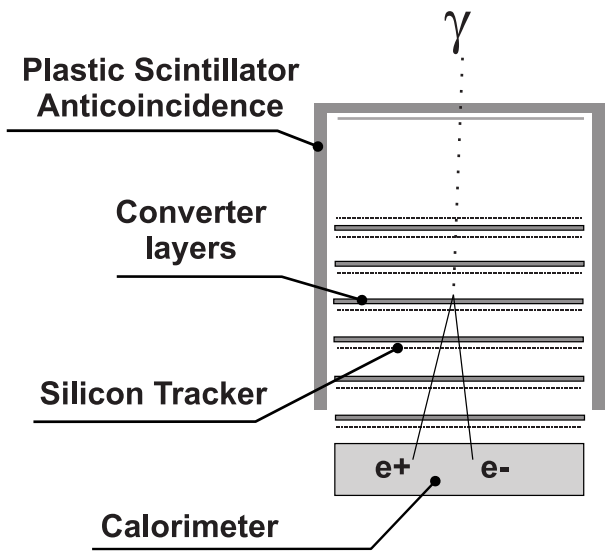

Figure 1.31: Layout of the structure of a gamma telescope.

The high energy γs interact with the converters creating electron-positron pairs. The tracks of the two charged particles are then sampled by the silicon strip detectors in order to estimate the direction of the primary photon, while the opening angle between the tracks is used to measure its energy. The calorimeter can be combined with the tracker to measure the energy of the electron-positron pair, or as a standalone detector to perform an independent measurement of the energy of non-converted γs. For both these tasks, the main requirement of the calorimeter is a good energy resolution. Among the alternatives, inorganic scintillator crystals are well suited to fulfill the requirements of good energy resolution, compactness and easy segmentation. Moreover, considering the weight, dimension and power consumption constraints of space calorimeters, silicon photodetectors are the best candidates for the readout of the scintillation light. In fact, the three most important telescopes sent in orbit in the last two decades (EGRET [28], AGILE [31] and FERMI-LAT [30]), use NaI(Tl) or CsI(Tl) crystals as the calorimeter active material and two of them (AGILE and FERMI-LAT) use PIN photodiodes [5] as the readout detectors.

The calorimeter sensitivity to high energy γs is limited by the number of radiation lengths of the calorimeter itself. As an example, the FERMI calorimeter, which is 8.4 X_0 can measure a maximum gamma energy of 70 GeV [30], while the AGILE equivalent one (MCAL, 1.5 X_0) is limited only to 100 MeV [31]. Thus, to enhance the energy sensitivity of the next generation telescopes, larger calorimeters are needed.

[5] Described in detail in the next chapter.

1.2.2.1 The Gamma-400 Experiment

The Gamma-400 experiment is one of the most promising and challenging next generation projects in the field of gamma ray physics. Supported by the Russian Space Agency in collaboration with many other institutions, including the Trieste, Roma and Florence sections of the Italian Institute of Nuclear Physics (INFN), the aim of the project is to further increase the energy range with respect to the FERMI-LAT experiment. This task is obtained with the construction of a very large and deep calorimeter, comparable in terms of radiation lengths with the typical calorimeters of high energy physics experiments. The main goals of the Gamma-400 mission can be summarized as follows [32]:

- to extend the gamma energy range up to 3 TeV;
- to improve the angular resolution up to 0.01° to identify discrete sources;
- to improve the energy resolution up to 1% to enhance the sensitivity to dark matter candidates.

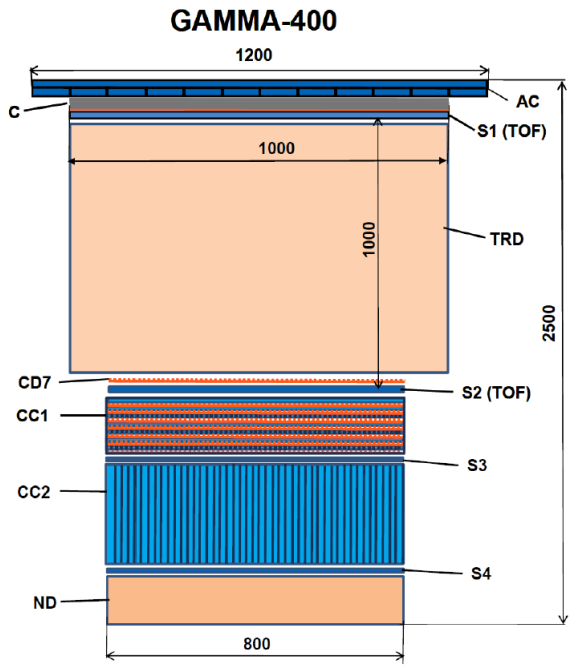

Figure 1.32: Layout of the Gamma-400 observatory [32].

A sketch of the Gamma-400 telescope is presented in Fig. 1.32. The complete space observatory is composed of:

- an anticoincidence (AC) detector;
- the multilayer converter (C), which consists of 6 0.14 X_0 layers of tungsten (CD1-6) interleaved with x-y silicon strip detectors with a 100 μm readout pitch and an active area of 1x1 m^2. A 7th layer (CD7) is positioned $\sim$1 m below the first six layers for a more precise measurement of the electron-positron opening angle;
- a Time-Of-Flight (TOF) system, composed of two plastic scintillators (S1-2), used to identify the particle direction;
- a Transition Radiation Detector (TRD) and a Neutron Detector (ND) to improve the proton rejection efficiency;
- two scintillation detectors (S3-4) used as additional trigger;
- the calorimeter system (CC).

The calorimeter system is divided in two parts: the imaging (CC1) and the electromagnetic one (CC2). The imaging calorimeter consists of 10 1 cm thick layers of BGO crystals interleaved with silicon strip detectors with a readout pitch of 500 μm, for a total of $\sim$9 X_0. This calorimeter is used to perform high precision measurements of the shower axis in order to enhance the angular resolution. The electromagnetic section is composed of BGO crystals arranged in towers, for a total of 21 X_0; this section of the calorimeter is used to enhance the sensitivity of the calorimeter itself to high energy γs and to fulfill the σ_E/E=1% requirement. The BGO crystals might be readout using large area SiPMs, characterized by a very large dynamic range to fulfill the large energy range requirement of the experiment. In particular, the Gamma-400 project could be the first to introduce the SiPM technology for the light readout in a space environment.

Chapter 2

Silicon PhotoMultipliers

This chapter is devoted to the description of Silicon PhotoMultipliers, a new type of silicon photodetectors recently proposed as an alternative to the widespread photomultiplier tubes (PMTs) in many applications. The first part of the chapter is dedicated to the description of the basic principles of silicon photodetectors and to the different available devices. The second part analyzes SiPMs and the main parameters used to characterize them, while in the last part the attention will be focused on the SiPMs manufactured by FBK-irst, the devices at the basis of this thesis work.

2.1 The Basic Principles of Silicon Photodetectors

Silicon photodetectors are semiconductor devices that can convert optical signals into electrical ones. These devices are produced joining together two doped semiconductors of the *p* (with a majority of positive carriers) and *n* (with a majority of negative carriers) type, obtaining a so-called *p*-*n* junction: a complete and more detailed description of this topic can be found in [33, 34]. When the junction is formed, the large carrier concentration gradient causes the diffusion of the electrons from the *n*-side into the *p*-side and the diffusion of the holes from the *p*-side into the *n*-side. With the charge carriers flowing from one side to the other, some of the ions fixed in the semiconductor lattice are left uncompensated: due to this effect, two spatial charges form near the junction zone and an electric field with an opposite direction with respect to the carrier diffusion stops the diffusion itself (see Fig. 2.1). If no external bias is applied to the semiconductor, an equilibrium condition is reached: near the junction all the majority carriers of the *p*-side have recombined with the majority carriers of the *n*-side generating the spatial charge; the region is known as *depleted region*. At the thermal equilibrium, the width W of the depletion zone depends mainly on the doping concentration of the *p* and *n*

side of the semiconductor according to the equation:

$$W = \sqrt{\frac{2\varepsilon_s}{q}\left[\frac{N_A + N_D}{N_A N_D}\right] V_{bi}} \tag{2.1}$$

where N_A is the number of acceptor (p) ions, N_D the number of donor (n) ions, ε_s the semiconductor dielectric permittivity and V_{bi} the total electrostatic potential across the junction defined as:

$$V_{bi} = \frac{kT}{q} \ln \frac{N_A N_D}{n_i^2} \tag{2.2}$$

where k is the Boltzman's constant, q is the electric charge and n_i the intrinsic concentration of free carriers.

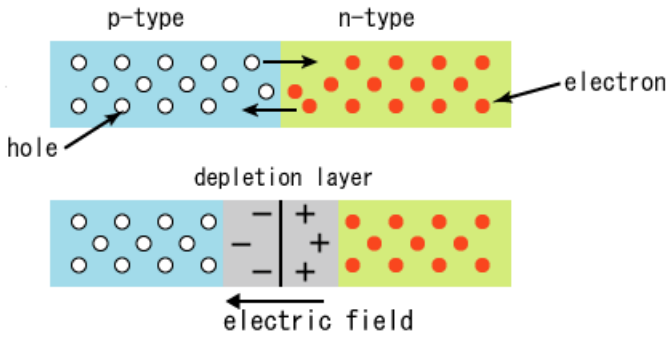

Figure 2.1: A p-n junction.

If an external bias is applied to the junction, the system is no longer at equilibrium and the depletion zone is modified. Two cases can be defined:

- forward bias: a positive voltage is applied on the p side of the junction and a negative voltage on the n side;
- reverse bias: a negative voltage is applied on the p side of the junction and a positive voltage on the n side.

In the forward bias configuration the total electrostatic potential across the junction decreases, reducing the depletion layer width; on the contrary, in the reverse bias configuration the total electrostatic potential increases, enlarging the depletion layer width. It can be shown that the width W of the depletion layer follows the relation:

$$W = \sqrt{\frac{2\varepsilon_s (V_{bi} - V)}{q N_B}} \tag{2.3}$$

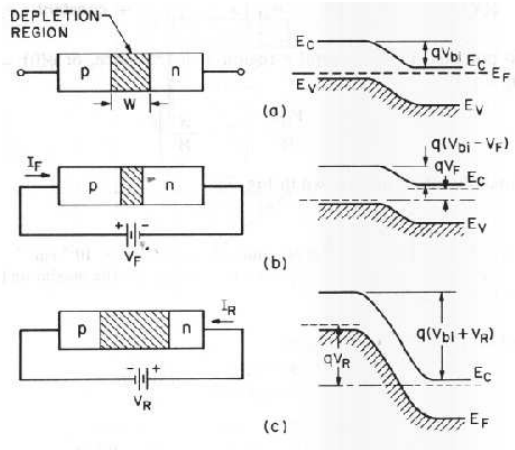

Figure 2.2: The *p-n* junction with different bias configurations: (a) no bias, (b) forward bias and (c) reverse bias. E_F, E_C and E_V are the Fermi, conduction and valence energy levels.

where N_B is the bulk doping concentration; Fig. 2.2 presents the behavior of the depletion region as a function of the bias configuration.

The typical I-V curve of a *p-n* junction can be divided in two regions corresponding to the forward and to the reverse bias configuration: an example is shown in Fig. 2.3. When forward biased, there is no current flowing through the junction up to a voltage threshold. In common diodes this threshold is called *diode drop* or *voltage drop* and is equal to ∼0.6 V (∼0.2 V for Schottky diodes): this drop corresponds to the bias needed to overcome the junction built-in potential. When the bias becomes larger than the voltage drop, the current starts flowing in the junction following an exponential law:

$$I = e^{\frac{V}{nV_T}} \tag{2.4}$$

where I is the diode current, V is the applied voltage, $V_T = \frac{kT}{e}$ is the thermal voltage (∼26 mV at 300 K) and n is the quality factor which varies from 1 to 2 depending on the diode manufacturing process.

As far as the reverse bias configuration is concerned, ideally no carrier should cross the depleted region, and the current should be equal to zero. As can be seen in Fig. 2.3, this assumption is not completely true because inside the depleted region electron-hole pairs are continuously generated by thermal excitations. The presence of the external field makes the carriers drift through the junction generating the so-called *inverse saturation* current. This effect can be introduced in equation 2.4:

$$I = I_s(e^{\frac{V}{nV_T}} - 1) \tag{2.5}$$

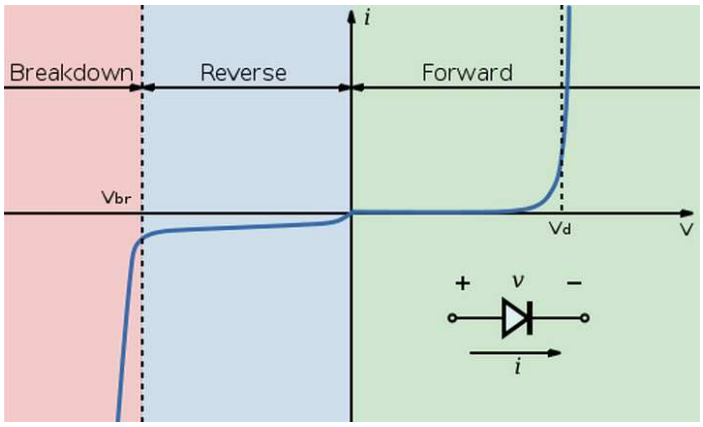

Figure 2.3: I-V characteristic curve for a *p-n* junction in the forward and reverse bias configuration. The scale of the y axis is not the same in the forward and reverse bias regions.

where I_s is the inverse saturation current. Equation 2.5 is known as the *Shockley diode equation* or the *ideal diode equation*.

The inverse saturation current remains almost constant until the reverse bias is so large that the majority carriers have enough kinetic energy to create another electron-hole pair before their collection on the electrodes. When this phenomenon occurs, the inverse saturation current quickly increases and, if the reverse bias is further increased or the maximum current is not limited, it can lead to the destruction of the device. The bias which corresponds to the start of the uncontrolled multiplication process is known as *breakdown* voltage, or V_{BD} and, as will be shown in section 2.1.3, is the principle at the basis of avalanche photodetectors like the Silicon PhotoMultipliers.

Besides thermal excitation, other two mechanisms can create electron-hole pairs inside the depleted region: ionization effects induced by penetrating charged particles and optical excitation induced by visible, UV or infrared light. Both these phenomena make reverse biased *p-n* junctions suitable to be used as particle and light detectors.

2.1.1 Ionization Processes

Charged particles crossing matter lose part of their energy through elastic collisions with electrons. The theory of radiation-matter interactions has been developed first by Bohr using classical arguments, and later in a quantum mechanical way by Bethe and Bloch; a complete discussion of the subject can be found in [35]. The basic calculation performed by Bohr considers the momentum transfer to a free electron by the ionizing particle when passing at its closest distance *b* (the

impact parameter). To obtain the transferred energy, which is proportional to the square of the momentum transfer, an integration over the kinematic variables is then performed. The resulting formula is called the Bethe-Bloch formula:

$$\frac{dE}{dx} = 2\pi N_0 r_e^2 m_e c^2 \rho \frac{Z}{A}\frac{z^2}{\beta^2}\left[\ln\left(\frac{2m_e\gamma^2 v^2 W_{max}}{I^2}\right) - 2\beta^2 - \delta - 2\frac{C}{Z}\right] \tag{2.6}$$

The main parameters of the formula are the following:

- $2\pi N_0 r_e^2 m_e c^2$ = 0.1535 MeV cm^2/g;
- r_e = electron classical radius = 2.8717 $\times 10^{-3}$cm;
- N_0 = Avogadro's number;
- I = mean excitation potential;
- Z = atomic number of the absorbing material;
- A = atomic weight of the absorbing material;
- ρ = density of the absorbing material;
- z = charge of the incident particle in units of e;
- v = particle relative velocity;
- $\beta = v/c$ of the incident particle;
- γ = Lorentz factor;
- δ = density correction factor (high energy correction);
- C = shell correction factor (low energy correction);
- W_{max} = maximum energy transfer in a single collision.

An example of the ionization rate of a charged pion passing through silicon computed with equation 2.6 is shown in Fig. 2.4.

In semiconductors, only a part of the energy loss is used for the creation of electron-hole pairs. In particular for silicon the average energy used for the creation of a pair is 3.6 eV, three times larger than the band gap of 1.12 eV. In fact part of the deposited energy is dissipated through lattice vibrations (phonons). Considering the example shown in Fig. 2.4, a 200 MeV pion (at the minimum of the ionization rate) deposits $\sim$200 keV in a 500 μm thick silicon detector, which

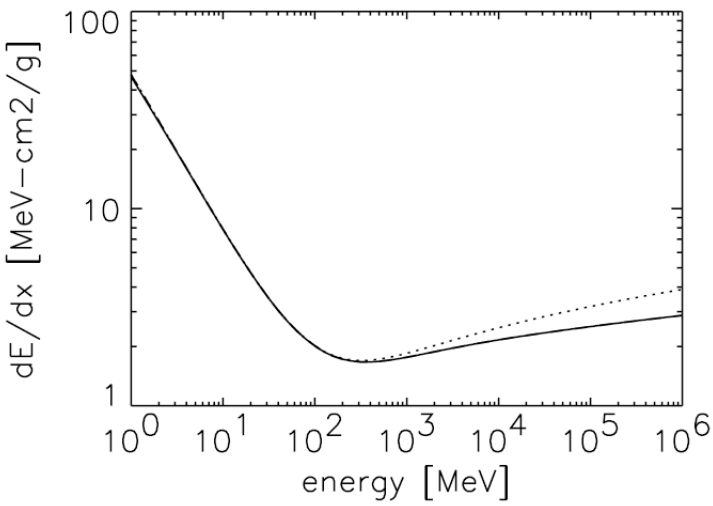

Figure 2.4: Rate of energy loss due to ionization as a function of the kinetic energy of a charged pion crossing silicon (effective ionization potential I = 173 eV) with (continuous line) and without (dotted line) the density and shell corrections.

corresponds to more than 60000 electron-hole pairs created inside the depleted region.

Electron-hole pairs produced by ionization processes inside silicon photodetectors are usually referred to as *nuclear counter effects*: these effects create spurious signals, therefore contributing to the noise of the photodetector. In order to minimize these contributions, the geometry of the detector, the doping profiles and the width of the junction should be carefully analyzed.

2.1.2 Optical Excitations

Electron-hole pairs can be produced inside the depleted region by light if the energy of the impinging photons is large enough to bring the electron from the valence band to the conduction band. In other words, in silicon at least 1.12 eV are needed and the wavelength of the incoming photons has to be smaller than 1100 nm [36]. A sketch of the phenomenon is presented in Fig. 2.5.

For light to be detected, it first has to enter through the surface of the *p-n* junction and then to be absorbed in the depletion region. Two effects must be taken into consideration:

- the Fresnel reflection of the light at the surface of the device (due to the large refractive index of silicon) must be kept as low as possible, introducing an anti reflective coating;

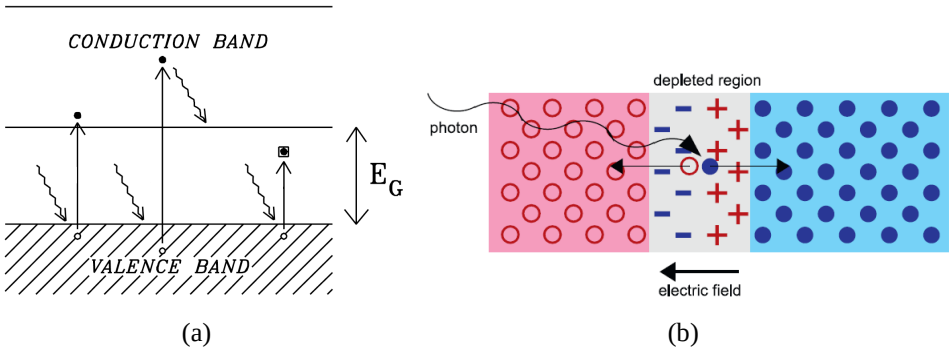

Figure 2.5: Detection of light inside a reverse biased *p-n* junction; if the energy of the incident photons is larger than 1.12 eV, electron-hole pairs are created inside the depleted region and are then collected by the electrodes.

- the thickness of the depleted region must be larger than the absorption length otherwise the electron-hole pairs will be created outside the sensitive region.

The second requirement is particularly challenging considering that the absorption length of optical photons varies from a few nm for UV light up to ∼1 mm for infrared light. The absorption length of optical photons inside silicon as a function of the wavelength is shown in Fig. 2.6.

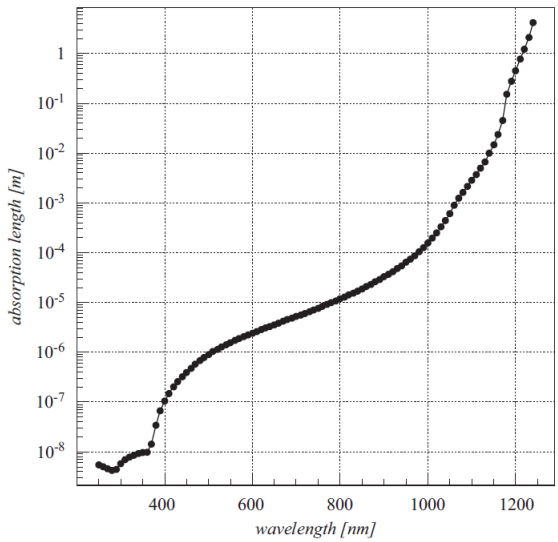

Figure 2.6: Absorption length in silicon as a function of the photon wavelength [36].

Due to the technological constraints in the production of the *p-n* junction, it is not possible to build a detector with high sensitivity from infrared up to UV wavelengths. The sensitivity of the device is called *quantum efficiency* and will be described together with other characterizing parameters in the next section.

2.1.3 Junction Breakdown

As can be seen in Fig. 2.3, when a reverse bias large enough is applied to the *p-n* junction, the junction starts to draw a large amount of current: this phenomenon is called *breakdown*. If the current is not limited by an external circuit, the junction can be damaged by the excessive heat. Two main processes are responsible of the breakdown effect: the *tunneling effect* and the *avalanche multiplication*.

The tunneling effect consists of electrons of the valence band that are extracted into the conduction band by the large electric field. This process is usually prevented by the presence of a potential barrier, whose height is proportional to the energy gap, which in fact can be overcome by the quantum mechanical tunnel effect. The probability of this process has an exponential behavior proportional to the electric field and to the inverse of the barrier width. For these reasons this process occurs only when the electric field is very high and the doping concentrations of the *p* and *n* regions are larger than 5×10^{17} cm^{-3}, in order to maximize the number of carriers able to cross the barrier.

The second and most important process responsible of the breakdown is the avalanche multiplication. In this process the kinetic energy acquired by the carriers drifting in the junction is large enough to trigger the generation of a second electron-hole pair by impact ionization. If the electric field is large enough, the secondary generated carriers are also capable to trigger other pairs and so on, resulting in a self sustained avalanche of carriers. A representation of the process is sketched in Fig. 2.7.

The ionization rate can be expressed using the ionization constants of electrons and holes, a_n and a_p. These ionization constants are defined through the relation:

$$dn = a_n n dx \qquad dp = a_p p dx \tag{2.7}$$

where n and p are the number of n-type and p-type free carriers and dx identifies the movement along the drift direction. The ionization causes the generation of additional electrons and holes. Assuming that the ionization coefficients of electrons and holes are the same, the multiplication factor M can be calculated as:

$$M = \frac{1}{1 - \int_{x_1}^{x_2} \alpha dx} \tag{2.8}$$

where the integral interval defines the region within the depletion layer where the electric field is large enough to cause impact ionization. Outside this range, the

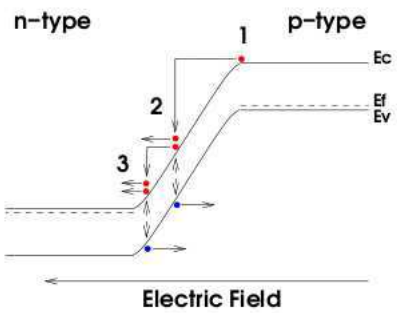

Figure 2.7: Qualitative explanation of the avalanche multiplication: the first free carrier in (1) is accelerated by the external field and in (2) generates another electron-hole pair by impact ionization. The free carriers in (2) are accelerated again by the external field and in (3) generate other pairs and so on, self sustaining an avalanche process.

electric field is assumed to be too small to cause impact ionization. Equation 2.8 holds if the electric field is assumed constant in the x_1 - x_2 interval. As will be shown in the next sections, one of the main parameters characterizing the different types of silicon photodetectors is the multiplication factor, *i.e.* the *gain* of the devices.

If the integral in equation 2.8 equals one, then the multiplication factor reaches infinity. This means that for each electron arriving in the high field at the x_1 point, one additional electron-hole pair is generated at the x_2 point. This hole then drifts in the opposite direction and generates an additional electron-hole pair at the starting x_1 point. One initial electron therefore yields an infinite number of electrons arriving at x_2, hence an infinite multiplication factor. When this condition is satisfied, the creation of a single electron-hole pair inside the depleted region is sufficient to start a self sustained and virtually *unlimited* [1] avalanche process which is called *Geiger-Muller avalanche*. Silicon PhotoMultipliers operate in this regime.

2.2 Silicon Photodetectors

As explained in the previous section, silicon photodetectors are silicon devices based on *p-n* junctions specifically designed to detect light. Silicon photodetectors can be characterized by three main parameters: *Quantum Efficiency* (QE), *PhotoDetection Efficiency* (PDE) and *Gain*.

[1] An unlimited multiplication process should lead to an unlimited current through the junction and to a damage due to heat dissipation; to avoid this problem active or passive quenching circuits are usually implemented to limit the maximum current crossing the device [36].

The quantum efficiency is defined as the ratio of photons hitting the sensitive area of the photodetector which produce an electron-hole pair over the total number of impinging photons. Due to the small energy of the band gap, the quantum efficiency in silicon based photodetectors is usually very high, of the order of 90% in a wide range of wavelengths. To perform a comparison, the maximum QE of recently introduced multialkali PMTs is of the order of 60% [37] (Fig. 2.8).

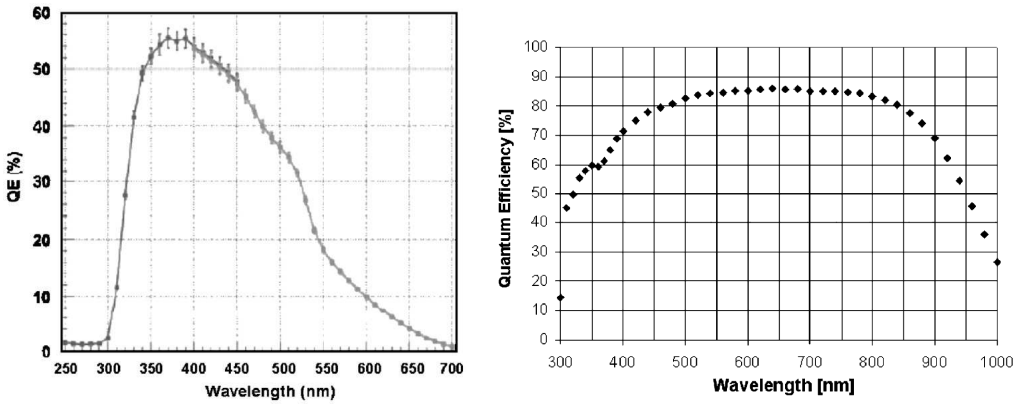

(a) (b)

Figure 2.8: Comparison of the typical QE of PMTs (a) and PIN diodes (b) [37].

QE depends on the structure of the junction: the undepleted layer should be thin enough to be crossed by the short-wavelength photons and the depleted layer should be thick enough to allow the absorption of long-wavelength photons. QE describes the efficiency of conversion from optical photons to pairs, but this value does not represent the detection efficiency of the whole device. This parameter is represented by PDE, which is the probability that an impinging photon is detected by the photodetector.

The PDE definition varies according to the different types of photodetectors:

- for single pixel non-amplifying photodetectors (like PIN diodes), PDE is essentially equal to the QE of the device, multiplied by the inverse of the recombination probability of the carriers during the drift (which can be reduced increasing the reverse bias);

- for single pixel amplifying photodetectors (like APDs, Avalanche Photo Diodes), the PDE is equal to the QE multiplied by the avalanche trigger probability. When a pair is created, the carriers start to drift inside the junction. As shown in the previous sections, if the electric field is intense enough, the carriers can start an avalanche process which multiplies the charge collected at the ends of the junction. Two avalanche trigger proba-

bilities can be defined, one for the electrons and one for the holes, being the first usually larger [38];

- for multipixel amplifying photodetectors (like SiPMs) PDE depends on one more parameter with respect to single pixel amplifying photodetectors, called the geometrical (fill) factor, that is the ratio of the sensitive to the total area of the device [39]. More details on the SiPM PDE will be discussed in section 2.3.3.

The third parameter that characterizes the photodetectors is the gain. It represents the multiplication factor of the photodetectors working in avalanche or in Geiger-Muller regime. This parameter is also used to sort the different devices available on the market: in Table 2.1 the different photodetectors are listed according to their gain factor.

Gain	Device
1	PN and PIN photodiode
10	Vacuum PhotoTriode (VPT)
>100	Hybrid PhotoDetector (HPD)
~ 100	Avalanche PhotoDiode (APD)
$\sim 10^6$	Single Photon Avalanche Diode (SPAD)
$\sim 10^6$	Silicon PhotoMultiplier (SiPM)

Table 2.1: Different photodetectors available on the market listed according to their gain factor.

A more detailed description of these devices is given in the following sections.

2.2.1 PIN Diodes

The PIN photodiode is one of the simplest types of photodetectors. It is an intrinsic piece of ohmic semiconductor sandwiched between two heavily doped $n+$ and $p+$ regions. The layer of intrinsic silicon reduces the capacitance of the diode and thus the noise and makes it sensitive to red and infrared light (which has a rather long absorption length) [37]. A picture and a sketch of the structure of a PIN diode are shown in Fig. 2.9.

The development of PIN diodes was driven by the need to find an alternative to the photomultiplier tubes in high energy physics (HEP) experiments, where solid state detectors are needed to fulfill the constraints of dimensions and insensitivity to magnetic fields. The breakthrough came with the evolution of the technological

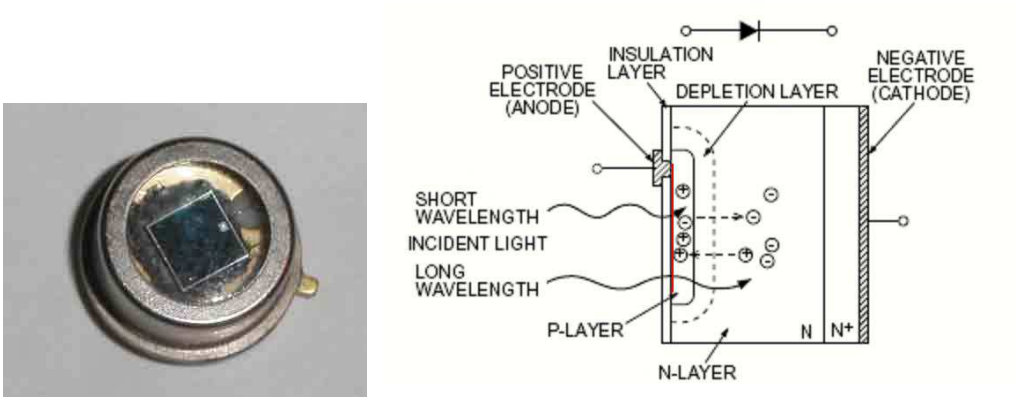

(a) (b)

Figure 2.9: Picture (a) and schematic representation (b) of the structure of a PIN diode [38].

processes in semiconductor devices during the ’80s, which allowed the construction of new types of PIN diodes with very low leakage currents, low noise and enhanced sensitivity for blue light.

PIN diodes were used for the first time in HEP for the readout of the L3 and CLEO crystal calorimeters at the end of the ’80s. In recent years, PIN diodes have been used as the readout system of the scintillator calorimeters of the Belle and BaBar B-factories [38]. Considering the lack of charge multiplication of these devices, their use is limited to scintillators with a large light yield and to the presence of a low noise signal amplification. Just to give an example, in the BaBar experiment, two PIN diodes were used to read the light coming from each of the 6580 CsI(Tl) crystals composing the electromagnetic calorimeter (Fig 2.10(a)). The signals of the two diodes were then amplified and shaped separately by a dual range pre-amplifier mounted in the rear of the crystals. Beamtest results on a module composed of 25 crystals showed that the average number of collected photons per deposited MeV was of the order of 6600, while the energy resolution (Fig. 2.10(b)) was of the order of $1\%/\sqrt{E}$ [40].

2.2.2 Hybrid PhotoDetectors

Hybrid PhotoDetectors (HPDs) are the link between PMTs and silicon photodetectors. Like any PMT, HPDs are composed of a photocathode with high sensitivity for photons in the visible and near UV range. The electrons extracted by the impinging photons via the photoelectric effect are then accelerated by an electrostatic potential of the order of 10 kV in a vacuum tube and collected by a silicon detector, used as an anode. The accelerated electrons penetrate in silicon for a

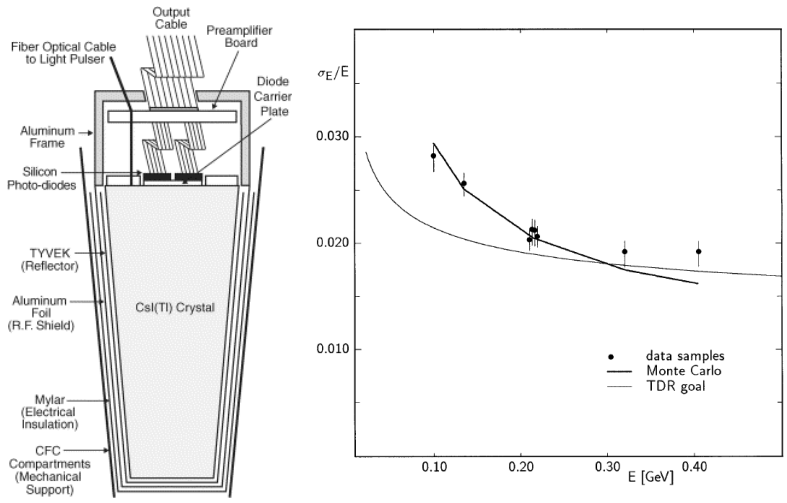

(a) (b)

Figure 2.10: Sketch of a crystal (a) [41] and energy resolution as a function of the electron beam momentum (b) of a prototype module of the BaBar calorimeter [40].

mean path of 3 μm, creating electron-hole pairs. Considering the kinetic energy of the electrons (few keV), a gain factor of 1000 or more (linearly proportional to the intensity of the field) is normally achieved [42]. A sketch of the working principle of a HPD is presented in Fig. 2.11.

HPDs have some of the limits characterizing PMTs: a low QE ($\sim$30%), the need of high voltages to work properly and a performance weakly affected by intense magnetic fields. These drawbacks are compensated by several advantages: small dimensions, low noise, stable gain, single photoelectron capability and the possibility to easily segment the anode into pads or pixels [43]. HPDs have been chosen by the LHCb collaboration for the readout of the RICH Cherenkov detector [44], which requires a large area coverage (2.6 m^2) with a large active area fraction, high granularity, single photoelectron sensitivity and high speed. The HPDs used by the RICH are devices with a diameter of 83 mm, biased at 20 kV for a total gain of $\sim$5000 and with a QE of the order of 20% at 400 nm; the anode is segmented in 1024 pixels of 0.5$\times$0.5 mm^2, bump-bonded to a readout chip housed directly inside the vacuum tube. A sketch of the LHCb HPDs is presented in Fig. 2.12(a), together with an example of the beamtest result of the prototypes [44] (Fig. 2.12(b)).

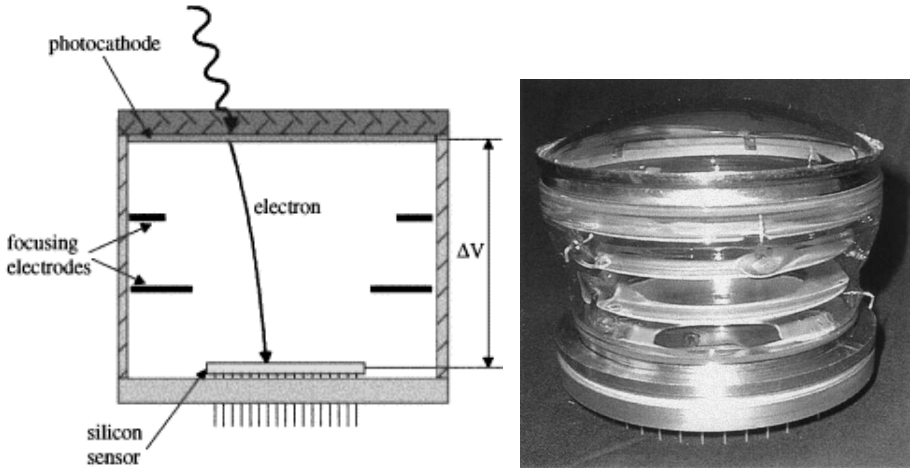

(a) (b)

Figure 2.11: Sketch (a) and picture (b) of a HPD and its working principle [42]: optical photons impinge on the surface of the photocathode, generating electrons which are then accelerated by the electrostatic potential and collected by a silicon detector.

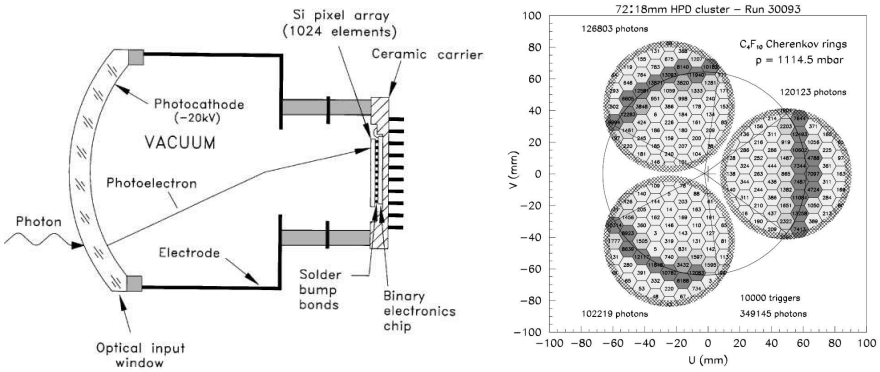

(a) (b)

Figure 2.12: Sketch of the final prototype of the HPD detector (a) and light cone of a 120 GeV/c pion detected during a LHC-b RICH beamtest (b) [44].

2.2.3 Avalanche PhotoDiodes

Avalanche PhotoDiodes (APDs) are particular types of PN diodes reverse biased near the breakdown voltage working in the charge multiplication regime. The multiplication factor is moderate and varies between 50 and ∼1000. According to [38], three types of APD structures are available (Fig. 2.13): beveled edge, reach-through and reverse or buried junction. The differences between these struc-

tures are mainly due to the electric field profile and to the region where the multiplication process occurs. In particular, in the beveled edge and reach-through configurations, the electrons have high multiplication rates throughout almost the entire device structure while hole multiplication is kept to a minimum. These types of APDs are sensitive to a large part of the visible spectrum, but suffer of radiation damage and of large nuclear counter effects.

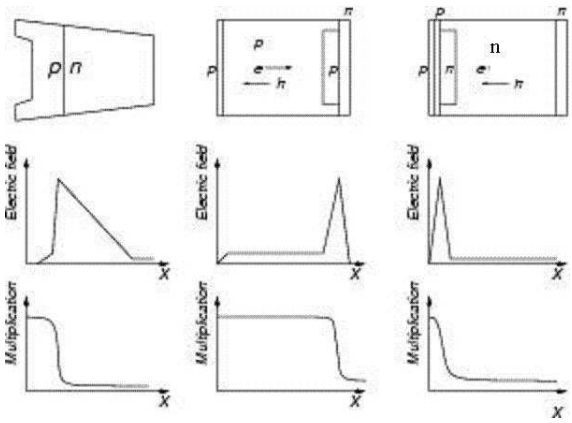

Figure 2.13: Device structures, electric field profiles and electron-hole multiplication for (left) beveled-edge, (center) reach-through and (right) buried junction APDs [38].

A breakthrough in the development of APD sensors is represented by the third type of geometry, the reverse or buried junction, specifically developed by Hamamatsu (with the S8141 model) for the readout of the lead-tungstate ($PbWO_4$) crystals of the CMS electromagnetic calorimeter [45]. In this type of geometry, the *p-n* junction is very close to the front surface: the multiplication region is only $\sim$5 μm thick, and the rest of the junction acts only as a drift region. A sketch of this geometry and two devices are shown in Fig. 2.14.

The advantages of the buried junction, mainly due to the very thin multiplication layer, are a low nuclear counter effect, a very good radiation hardness, a fast response, small dark currents and a better temperature stability. The main disadvantage is the poor sensitivity to long wavelength photons, due to the fact that their mean path in silicon is too long thus causing their absorption beyond the multiplication region. In the CMS experiment this is not a problem because the peak emission of the lead-tungstate crystals is at 420 nm, where the APDs have a QE of 72% [45].

Even if the buried junction improves the APD stability, these devices are very sensitive to gain variations due to bias or temperature changes. For example, the S8141 APDs are operated at a low gain value of 50 in order to maintain the bias and temperature stability in the 3.3 (-2.3)%/V (°C) range [45]; if operated at a

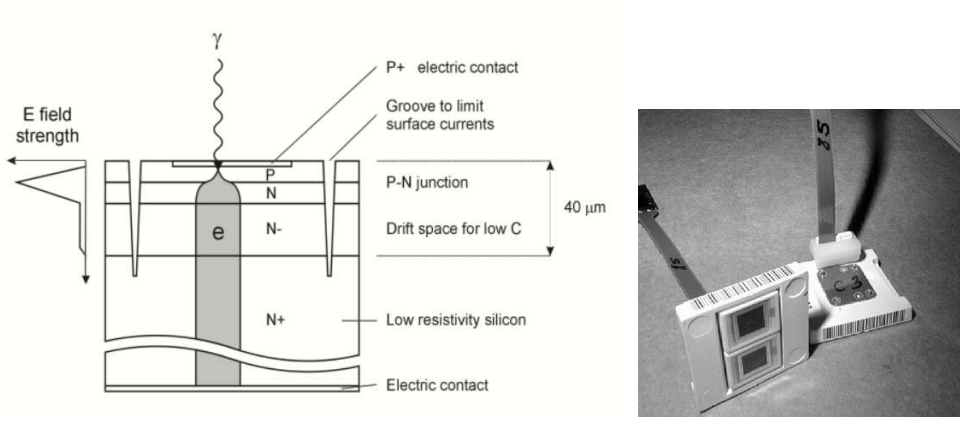

(a) (b)

Figure 2.14: Sketch of the buried junction CMS APDs (a) and an image of two APDs in their plastic package ready to be glued on a crystal (b).

gain of 1000, the stability would worsen to an unacceptable value of 30 (-15)%/V (°C).

Considering the low multiplication factor of APDs, the avalanche fluctuations become important and contribute to the noise effects with the so-called *Excess Noise Factor* (ENF). ENF is a measurement of the fluctuations in the total number of secondary charge carriers generated by each primary carrier entering in the avalanche region and can be expressed as [46]:

$$ENF = 1 + \frac{\sigma_M^2}{M^2} \tag{2.9}$$

where M is the avalanche gain and σ_M^2 is the avalanche gain fluctuation, whose primary sources are due to [46]:

- random fluctuations in the distance crossed by carriers between successive ionizing collisions;
- fluctuations of the avalanche gain due to the different depths at which primary photons are absorbed;
- fluctuations of the electrons and holes contribution to the avalanche at different absorption depths;
- electric field variations with the profile of the avalanche region.

For the APDs used in the CMS experiment, ENF is equal to 2 for a gain of $\sim$50 [45].

2.3 Silicon PhotoMultipliers

Silicon PhotoMultipliers (SiPMs) are passively quenched multipixel silicon detectors, biased above the breakdown voltage, working in Geiger-Muller avalanche mode and readout in parallel via a common substrate. While each pixel operates in digital mode, the analog information can be inferred considering the number of fired pixels.

Their development started at the beginning of 1960 when single photon detectors and the theoretical description of the avalanche processes inside silicon were under study at the RCA (Radio Corporation of America) and Shockley laboratories in the USA [47, 48]. Even if the performances of the first test devices were poor (mainly due to the silicon technology limits at the time), single photons were observed. The main problem was that only very small volumes of silicon could be kept depleted above the breakdown voltage for a time long enough for the diodes to be sensitive. In most cases, the large internal bulk current in the depleted volume triggered an instant breakdown when the diode bias rose just above the breakdown voltage. The development phase of these devices led to the production of the first Single Photon Avalanche Diode (SPAD) [38].

No important step forward took place until 1990, when the first Metal-Resistor-Semiconductor (MRS) APDs were invented in Russia [49]. In these devices a very thin metal layer and a layer of SiC (or Si_XO_Y with high resistivity) limits the Geiger breakdown thanks to a local reduction of the electric field. The result is that high multiplication values (of the order of 10^6) can be reached without an uncontrolled breakdown, simply raising the bias voltage [50]. The next step was to divide the MRS structure into many cells and connect them all in parallel through an individual quenching resistor, creating the first SiPM: in Fig. 2.15 one of the basic SiPM structures and a typical electric field profile are presented.

Nowadays different structures have been developed in order to optimize the SiPMs performance. State of the art devices consist of 500-4000 pixels/mm^2, with a typical pixel dimension in the 20-100 μm range [52]. The discharge is quenched with a polysilicon resistor embedded in the silicon wafer thus limiting the current flowing in each pixel. The most important advantages of SiPMs can be listed as follows:

- a high gain, of the order of 10^6, comparable with the PMTs one: no or very simple amplification of the output signal is thus required [38];
- the insensitivity to magnetic fields;
- a low bias voltage, usually of the order of $\sim$50 V;
- a compact and easy to handle (*e.g.* no vacuum) structure;

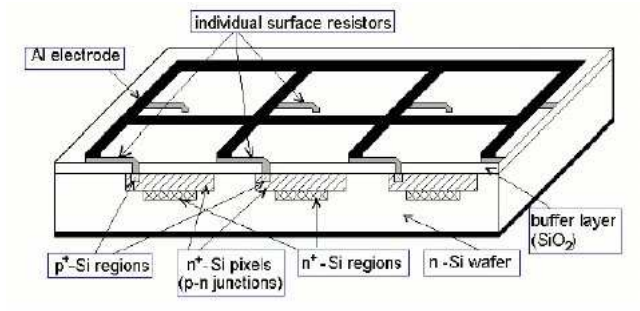

(a)

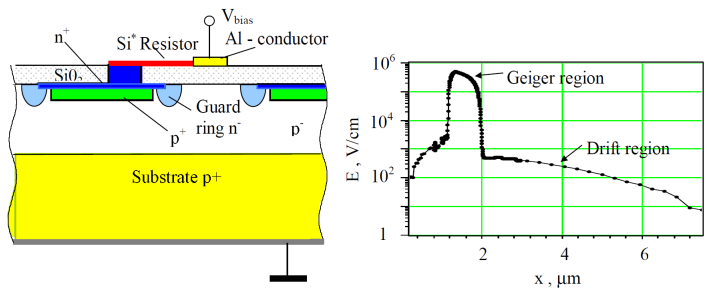

(b)

Figure 2.15: Basic structure of a Geiger-mode avalanche photodiode developed by Sadygov (a) [38] and electric field distribution inside the junction (b) [51].

- a very small excess noise factor, due to the fact that no fluctuations in the avalanche process are present;
- the single photoelectron sensitivity.

The drawbacks of these devices are mainly a large (temperature dependent) dark noise and a low radiation hardness; the most important properties of SiPMs will be discussed in detail in the following sections.

2.3.1 Gain and Linearity

SiPMs are characterized by a very high gain, of the order of 10^6, comparable with the PMTs one. When a cell goes into breakdown, it produces a signal (A_i) which is linearly proportional to the capacitance of the cell. When many cells are fired at the same time, the output (A) is the sum of the single pulses [53]. Thus:

$$A_i \sim \frac{C}{e}(V - V_b) \qquad A = \sum_i A_i \tag{2.10}$$

where V is the bias voltage, V_b is the breakdown one and C the cell capacitance. The typical pulse height spectrum of a SiPM together with the linear dependence of the gain on the overvoltage are presented in Fig. 2.16.

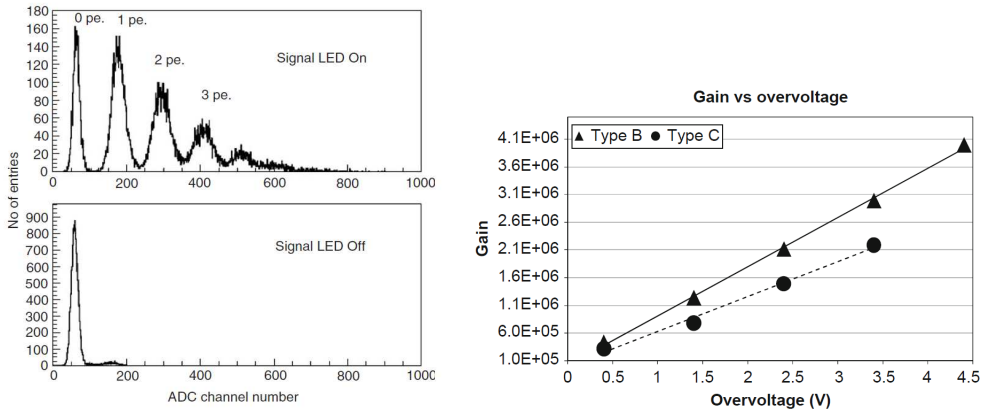

(a) (b)

Figure 2.16: (a) Pulse height spectrum of a SiPM with and without a LED illumination [53] and (b) linear dependence of the gain as a function of the overvoltage [54] for two types (labeled B and C) of SiPMs.

Considering the high density of cells, SiPMs are linear over a wide range of light intensities. The linearity limit is due to the finite number of cells because two or more photons that impinge on one cell produce exactly the same signal as one single photon. It can be shown that the number of fired cells depends on the incoming photon flux and on the PDE of the device [37]:

$$N_{firedCells} = N_{total}\left[1 - \exp\left(\frac{-N_{photon} \times PDE}{N_{total}}\right)\right] \tag{2.11}$$

where N_{total} is the number of available pixels in the device, N_{photon} is the number of impinging photons, $N_{firedCells}$ is the number of cells effectively fired by the impinging photons and PDE is the PhotoDetection Efficiency of the SiPM (which will be discussed in detail in section 2.3.3). Due to the finite number of available cells (N_{total}), deviations from linearity occur when the number of photons (*i.e.* the light intensity) is comparable to the number of available pixels. A plot showing the non-linear response to a 40 ps laser light signal for SiPMs with different number of cells is presented in Fig. 2.17 [38].

As can be seen in Fig. 2.17, the deviations from linearity start to appear when the $\frac{N_{photon} \times PDE}{N_{total}}$ ratio is larger than 0.6. It has to be noted that equation 2.11 holds considering an infinite recovery time of each cell, while the typical recovery time of a SiPM cell is of the order of $\sim$10 ns. This means that photon signals longer

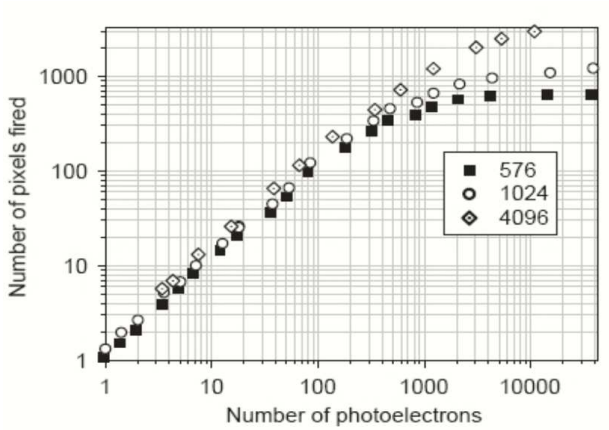

Figure 2.17: SiPM non-linear response to a 40 ps laser light signal [38]: the number of cells of each SiPM is indicated.

than the cell recovery time result in an increase of the effective dynamic range of the SiPM, which can be linear or not according to the incident photon flux [55].

2.3.2 Dark Counts

SiPMs are affected by a large number of dark count events, varying from a few kHz up to several MHz per mm^2. The large dark count rate is one of the most important disadvantages of SiPMs and represents a limit to the sensitivity of these devices to very low photon fluxes (down to the single photon case). Besides the ones due to incident photons, avalanches inside the SiPM cells can be triggered by any generation of free carriers in the depleted layer. Two main processes are responsible of the dark count rate [38]:

- the thermal generation of *e*-*h* pairs;
- the field-assisted generation of free electrons.

A sketch of the two processes is presented in Fig. 2.18.

The first process is temperature driven and can be substantially reduced cooling the device; the same effect can be obtained reducing the volume of the depleted region, *i.e.* reducing the dimensions of the SiPM cells. The second phenomenon is due to the large electric field inside the depleted region: as explained in section 2.1.3, the free carriers have a probability proportional to the electric field to overcome the potential barrier through the quantum mechanical tunnel effect. This process can be reduced decreasing the bias voltage and, consequently, the electric field inside the junction. In Fig. 2.19 the dark count rate as a function of bias and temperature is shown, confirming the expected behavior.

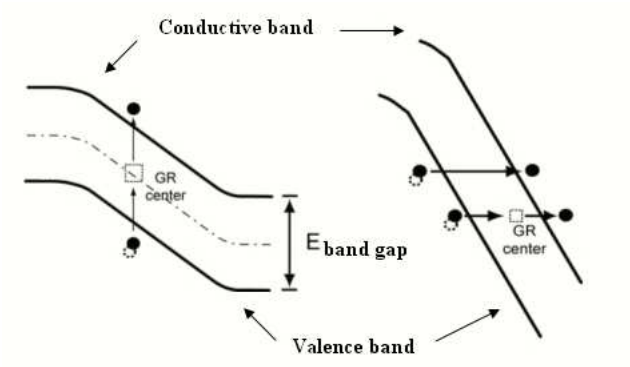

Figure 2.18: Thermal (left) and field-assisted generation (right) of free carriers [53].

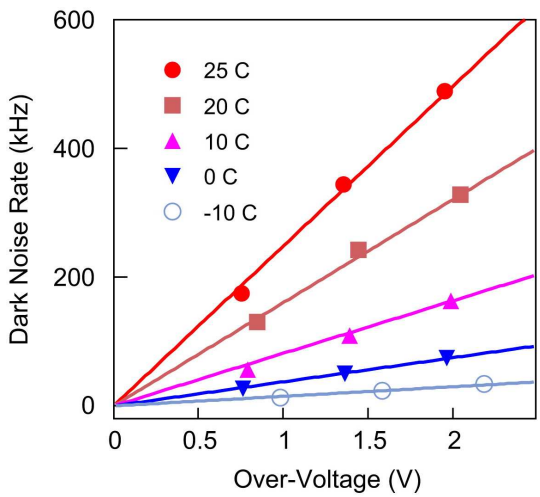

Figure 2.19: Dark count rate as a function of bias and temperature [56].

Both the thermal and field-assisted processes are mediated by impurities inside the *p-n* junction which act as generation-recombination centers (indicated as "GR" in Fig. 2.18). This means that another way to reduce dark counts is to use a very pure and defect-free silicon technology [53]. The dark count rate can be substantially reduced increasing the threshold of the readout electronics to values larger than the amplitude of the single photoelectron signal. A threshold scan can be performed, increasing the threshold by the equivalent of one photoelectron at each step: the resulting plot is presented in Fig. 2.20.

The trend of Fig. 2.20 is known as *staircase curve* and is used to characterize the dark counts of SiPMs. As can be seen, a substantial drop in the dark count rate is achieved at each threshold step: a threshold equivalent to four photoelectrons is

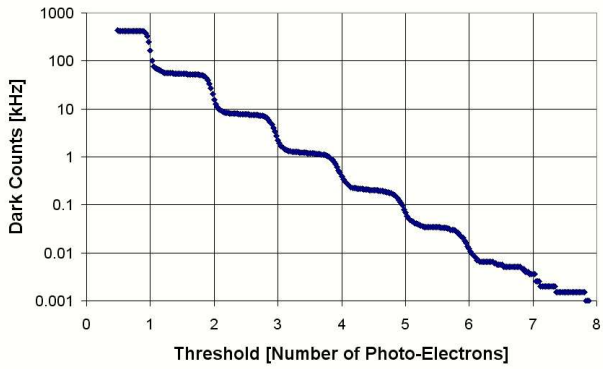

Figure 2.20: Dark count rate as a function of the electronics threshold [38].

normally enough to reduce the dark counts to a rate of the order of a few kHz. The presence in the dark count events of signals with amplitude larger than the single photoelectron is due to the *optical crosstalk* phenomenon that will be discussed in section 2.3.4.

2.3.3 PhotoDetection Efficiency

The PhotoDetection Efficiency or PDE has been introduced in section 2.2 and is defined as the probability that a single impinging photon has to trigger a SiPM cell. PDE is defined as

$$PDE = QE \times P_t \times \varepsilon_f \tag{2.12}$$

where QE is the quantum efficiency, P_t the avalanche trigger probability and ε_f the geometrical fill factor. QE is normally very high and typical values of 80-90% can be achieved at different wavelengths depending on the structure of the junction. The avalanche trigger probability is the probability that a free carrier (electron or hole) starts the avalanche process inside the cells: two trigger probabilities must be defined separately for electrons and holes, being the first generally larger. P_t increases almost linearly with the bias until a saturation at the 100% level occurs for very high voltages [57]: this phenomenon is responsible of the PDE behavior with respect to the bias voltage shown in Fig. 2.21.

The geometrical fill factor is defined as the sensitive to total area ratio and has to be optimized as a function of the application. ε_f depends on how much space is needed between the cells to place the quenching resistors, the cell bondings and the trench regions (to reduce the optical crosstalk). Thus the best filling factor can be achieved using a small number of big cells: in this way a factor of the order of 70% or more can be obtained. However, a small number of too large cells has the disadvantage of a low dynamic range, larger dead-times and high dark count rates

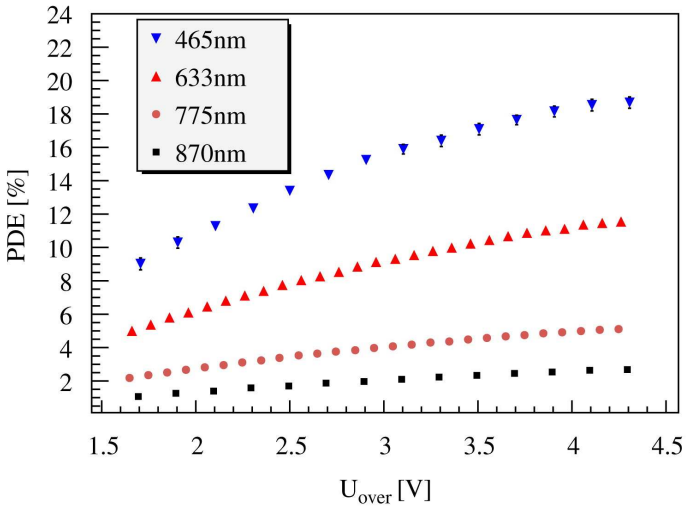

Figure 2.21: PDE as a function of the wavelength (due to the QE variations) and the bias voltage (due to the trigger probability variations) [58].

due to the larger depleted volume [38].

2.3.4 Optical Crosstalk

The optical crosstalk phenomenon is due to photons emitted during the avalanche breakdown in one cell that travel to the neighboring cells and trigger a second avalanche exactly in the same way of an external photon. During an avalanche, an average of 3 photons per 10^5 carriers are emitted. The photons in the 850-1100 nm range are particularly critical because shorter wavelength photons are absorbed in the cell in which they are emitted, while longer wavelength photons travel longer distances and are not absorbed [38] (Fig. 2.22).

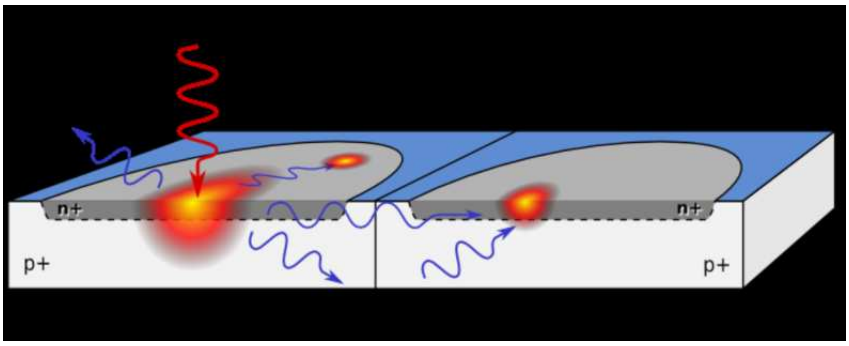

Figure 2.22: Sketch of the optical crosstalk phenomenon.

The optical crosstalk can be reduced in three ways:

- modifying the structural parameters of the SiPM, placing the cells at a larger distance;
- introducing trenches and grooves between the cells which act as optical isolation;
- reducing the bias in order to reduce the avalanche trigger probability and consequently the crosstalk effects.

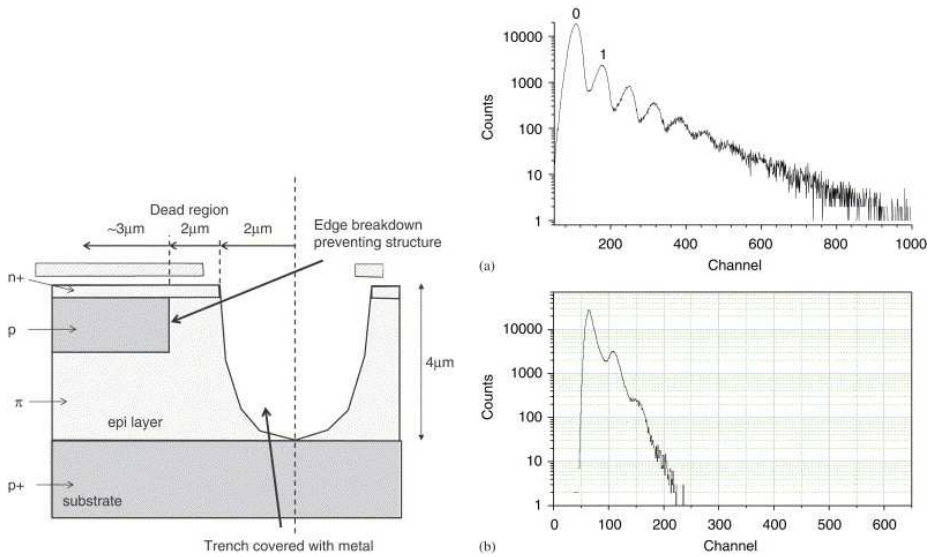

(a) (b)

Figure 2.23: (a) SiPM structure with optical grooves [59] and (b) pulse height distribution of the same SiPM with and without the optical grooves [60].

With the first solution the optical crosstalk is reduced at the expense of the geometrical fill factor, while the third solution reduces the avalanche trigger probability: in both cases the resulting effect is a much lower PDE. The second solution is the most convenient one and is used by many SiPM manufacturers. The optical groove is usually covered with a metal layer in order to enhance the reflection probability of the photons inside the cell. To minimize their impact, these structures should overlap the existing dead border region of the pixel as much as possible [59]. An example of a SiPM structure with optical trenches and the results of this layout in terms of optical crosstalk suppression are shown in Fig. 2.23.

The optical crosstalk events violate the pixel independence and the Poisson statistics of fired pixels, thus acting as shower fluctuations (as in APDs) and increasing the Excess Noise Factor [60]. Neglecting the second order effects, in

SiPMs ENF can be approximated as:

$$ENF \approx 1 + P_{Ct} \tag{2.13}$$

where P_{Ct} is the probability of optical crosstalk events defined as the rate of dark count events with crosstalk (setting a threshold of 1.5 fired cells) divided by the total dark count rate (setting a threshold of 0.5 fired cells) [38]. With the use of optical grooves, the optical crosstalk probability can be reduced from a ∼20% value down to a few % [60].

2.3.5 Temperature Stability

As shown in the previous sections, all the SiPM parameters depend on the bias voltage and in particular on the overvoltage with respect to the breakdown voltage. In silicon detectors the breakdown voltage varies with temperature because of the different interactions of the free carriers with the lattice phonons [38]. This means that all the overvoltage-dependent SiPM parameters (gain, dark counts, PDE and optical crosstalk) are also temperature dependent. In Fig. 2.24 the temperature dependence of the breakdown voltage of a FBK-irst SiPM down to cryogenic temperatures is presented.

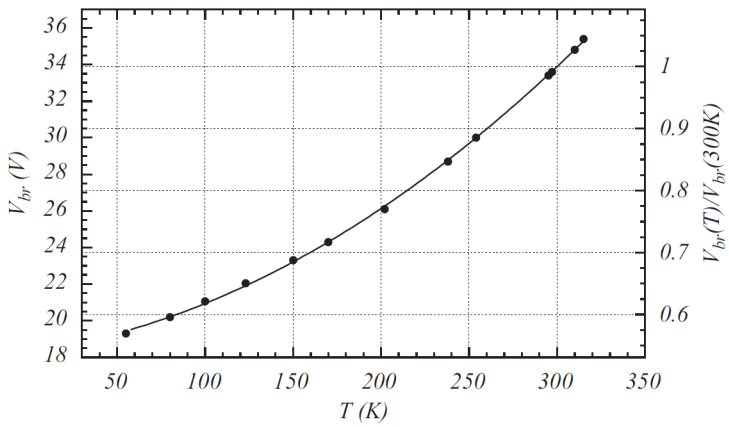

Figure 2.24: Breakdown voltage as a function of temperature of a FBK-irst SiPM [61].

The dark count rate trend as a function of temperature has been already introduced in section 2.3.2. As far as the gain is concerned, fixing the bias voltage, a higher gain corresponds to a lower temperature, as confirmed by the plot of Fig. 2.25.

The typical temperature coefficient ($\frac{\Delta V_{bd}}{\Delta T}$) is of the order of a few tens of mV per degree: this means that for a stable operation the temperature needs to be

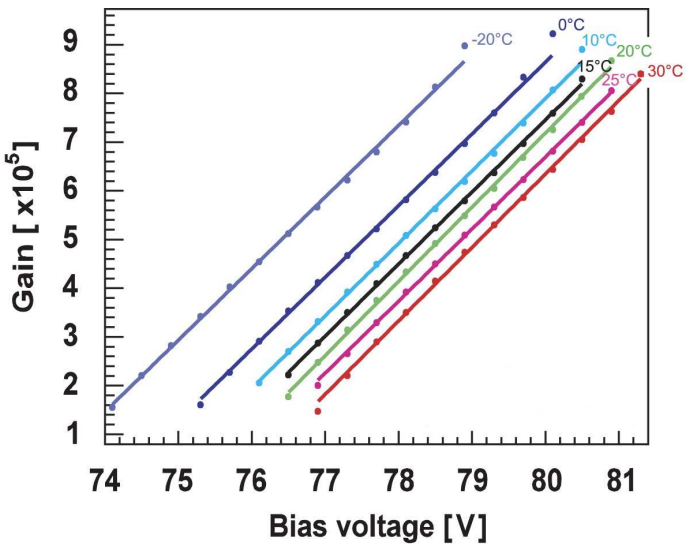

Figure 2.25: Gain as a function of the bias voltage for different temperatures [62].

controlled with a precision of a fraction of a degree. Another possibility is to correct the bias voltage as a function of temperature to compensate for the shift of the breakdown voltage [38].

2.3.6 Timing Performances

Silicon PhotoMultipliers are very fast devices thanks to the very thin (2-4 μm) charge multiplication volume and to the intrinsic high speed of the avalanche process [53]. Timing measurements have been performed in [63] using a very fast red laser diode (λ=670 nm) with a light pulse of 40 ps FWHM. The single photoelectron timing resolution for a very low intensity pulse is shown in Fig. 2.26.

The measured value is 123 ps FWHM and includes the laser pulse width and the electronics contribution. The intrinsic SiPM timing resolution after the subtraction of these contributions is of the order of $\sim$100 ps FWHM, that is $\sim$50 ps RMS. The tail events in Fig. 2.26 can be explained as events triggered by carriers created in the low electric field region that have to diffuse into the high field region to trigger the avalanche [53]. As shown in Fig. 2.27, the tail events can take up to a few tens of nanoseconds to reach the high field region.

At low gain, the lateral spread of the depleted volume can be incomplete, enhancing the diffusion tail: the contribution of these events can be reduced increasing the SiPM overvoltage (Fig. 2.28).

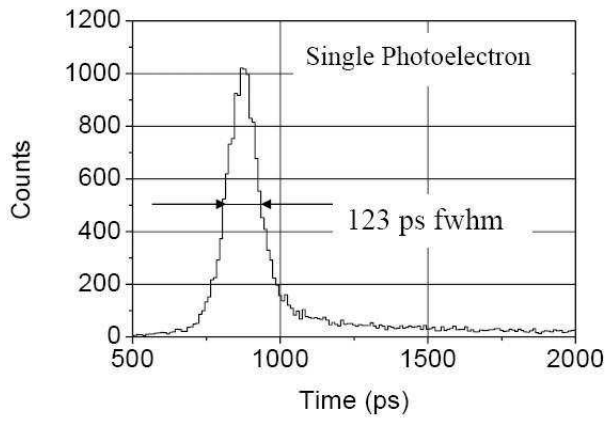

Figure 2.26: Single photoelectron timing resolution [63].

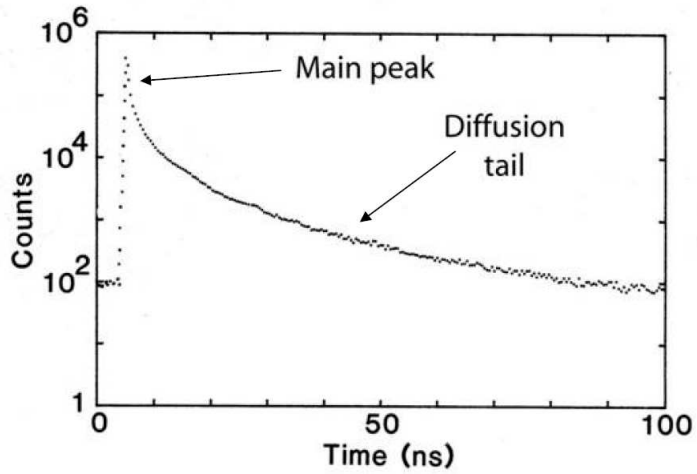

Figure 2.27: Single photoelectron timing resolution with diffusion tail events [53].

2.3.7 Radiation Damage

In order to use the SiPMs in HEP experiments, their resistance to radiation is a critical issue. The general effect of radiation (gammas, protons, neutrons and electrons) in silicon is the creation of defects in the bulk or in the Si/SiO_2 interface [34] thus causing an increase of the leakage current and, because of the avalanche multiplication process, of the dark count rate. In recent years many studies have been performed in order to investigate the radiation tolerance of SiPMs: the fundamental results are presented in the next paragraphs.

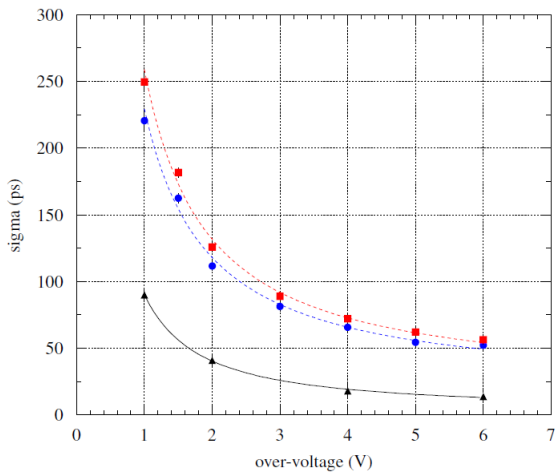

Figure 2.28: Time resolution as a function of the overvoltage at 400 nm (circles) and at 800 nm (squares) of a FBK-irst SiPM prototype (triangles indicate the electronics noise contribution) [64].

2.3.7.1 Gamma Irradiation

Interesting tests have been performed in [65] using devices produced by Hamamatsu with 100 μm cell sizes, irradiated with a high intensity ^{60}Co source. During the irradiation, performed in six steps of 40 Gy each for a total of 240 Gy, the devices were biased with an overvoltage of 1.2 V. The main parameters of the devices have been measured after each irradiation step and after one hour to detect the possible presence of an annealing effect. The main results are shown in Fig. 2.29.

As can be seen, no evident changes in the gain and in the optical crosstalk are present. As anticipated, there is an increase in the dark count rate of a factor 1.5 due to the increased number of defects induced by gamma radiation. Anyway, the SiPMs performances are only slightly reduced by the γ irradiation and, with some modifications to the silicon design, γ-hard SiPMs could be developed [38].

2.3.7.2 Neutron Irradiation

The performances of two types of Hamamatsu devices (with an area of 1 mm^2 and a cell size of 50 and 100 μm) have been tested after neutron irradiation in [66]. The SiPMs have been irradiated using a nuclear reactor facility with a fluence of 10^{12} neutrons/cm^2. The devices were unbiased during the irradiation and their performances have been characterized before and after the irradiation in a 20° C thermostatic chamber in order to avoid temperature dependent differences. The first detrimental effect of neutron irradiation is the increased noise in the SiPM

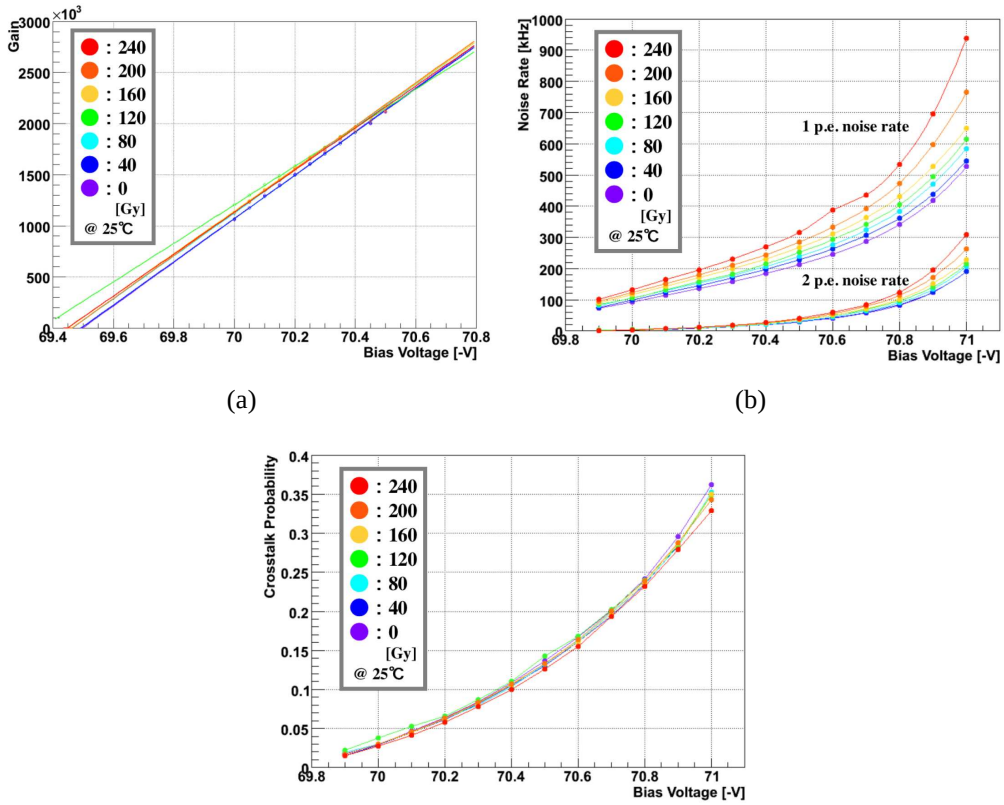

(a) (b)

(c)

Figure 2.29: Gain (a), dark count rate (b) and optical crosstalk (c) variation after each step of the irradiation with a ^{60}Co gamma source.

signal output. Fig. 2.30 presents the response in ADC to a LED signal before and up to two months after the irradiation.

The single photoelectron resolution is lost due to the increased noise effects. The situation partially recovers after a few days thanks to the annealing, but at higher irradiation levels (more than 10^{11} neutrons/cm^2) the single photon resolution is completely lost. Other two parameters affected by the neutron irradiation are the dark count rate (as in gamma irradiation) and the breakdown voltage: both these variations are due to the increased number of defects in the silicon structure. In particular, the small breakdown voltage change ($\sim$50 mV) is a symptom of a variation in the doping concentration induced by radiation. The results for the dark count rate and the breakdown voltage are shown in Fig. 2.31.

The single photoelectron dark count rate grows up to 10 MHz. Moreover, it has to be noted that no measurement has been performed above a few 10^{10} neutrons/cm^2 because the noise of the devices was too high to fit the pulse height distributions

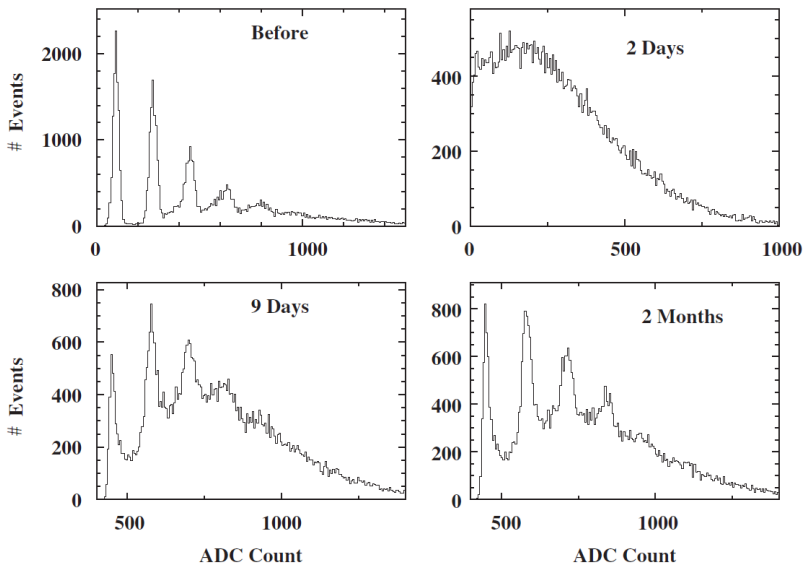

Figure 2.30: Pulse height distribution of the 100 μm Hamamatsu devices before and after the neutron irradiation with 2×10^{10} neutrons/cm^2.

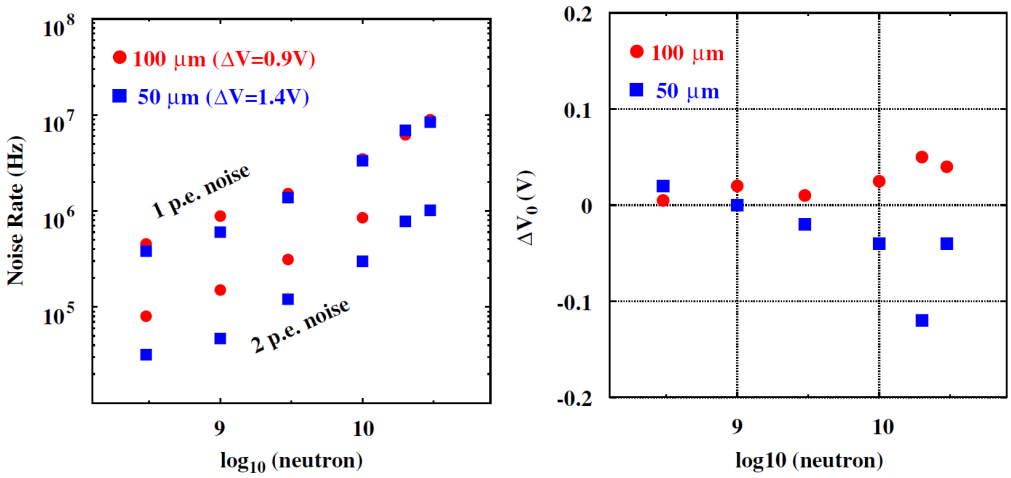

(a) (b)

Figure 2.31: Dark count rate (a) and breakdown voltage (b) as a function of the neutron fluence for both the 50 and 100 μm Hamamatsu devices.

and to discriminate the single photoelectron peaks. For what concerns the PDE and the optical crosstalk probability, no variations have been measured. These results show that, with the present technology, the use of SiPMs should be avoided in environments where the expected neutron fluence is more than 10^{10} neutrons/cm^2.

2.3.7.3 Proton Irradiation

A complete analysis of the effects of proton irradiation on five devices produced by different SiPM manufacturers (Hamamatsu, FBK, Zecotek and CPTA) has been performed in [67]. The devices have been irradiated with a 82 MeV proton beam, equivalent to a fluence of 10^{10} neutrons/cm^2 with an energy of 1 MeV. During the irradiation the devices have been biased with a 10 V reverse voltage. The performances of the devices have been measured before and 90 days after the irradiation using a thermostatic chamber. As in the gamma and neutron irradiation cases, an increase in the dark count rate has been observed in all the devices up to a few tens of MHz as shown in Fig. 2.32.

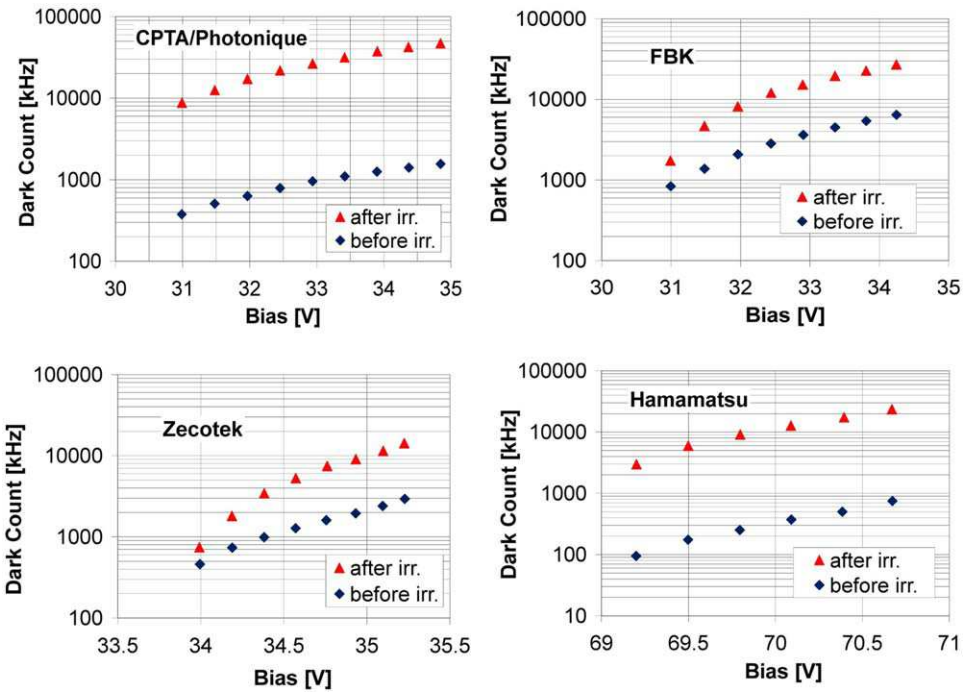

Figure 2.32: Dark count rate before and after the proton irradiation of four SiPM devices produced by different manufacturers.

As far as the gain is concerned, the response of the SiPMs has been tested with a calibrated 50 photons LED pulse before and after the irradiation: the signal waveforms have been recorded and then integrated in a 120 ns gate.

As can be seen in Fig. 2.33, at low overvoltages the changes in the measured LED signals are small; however, significant deviations (more than 10%) appear at high (>4 V) overvoltages. Similarly to the neutron irradiation results, a variation of ∼50 mV in the breakdown voltage has been observed in all the tested devices.

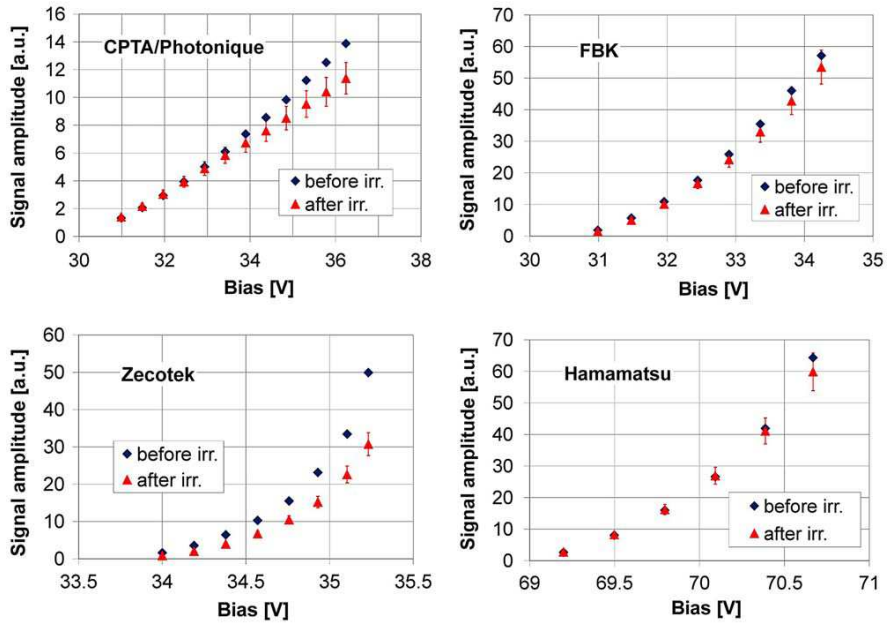

Figure 2.33: SiPM response to a calibrated LED signal before and after the proton irradiation of four devices produced by different manufacturers.

No variations have been measured for the PDE even if an accurate measurement is difficult due to the high noise levels.

2.4 The FBK-irst Silicon PhotoMultipliers

The SiPMs used for most of the tests described in this thesis work are manufactured by FBK-irst (Fondazione Bruno Kessler), former known as ITC-irst; at the end of 2010 a joint venture between FBK-irst and two other companies specialized in packaging and marketing led to the creation of Advansid[2], which now sells FBK-irst SiPMs on the market.

The research of FBK-irst in the field of SiPMs started in 2005 within a collaboration with INFN: the aim of the project was to develop the SiPM technology for applications in high energy, space and medical physics. FBK-irst SiPMs are made of arrays of micro-cells, ranging from 25x25 μm^2 to 100x100 μm^2 in size, arranged in circular (1.2 and 2.8 mm diameter) or squared (1, 4, 9 and 16 mm^2) geometries; recently, linear and 4x4-matrix packages have been also developed [68]. A sketch of the section of one micro-cell is presented in Fig. 2.34.

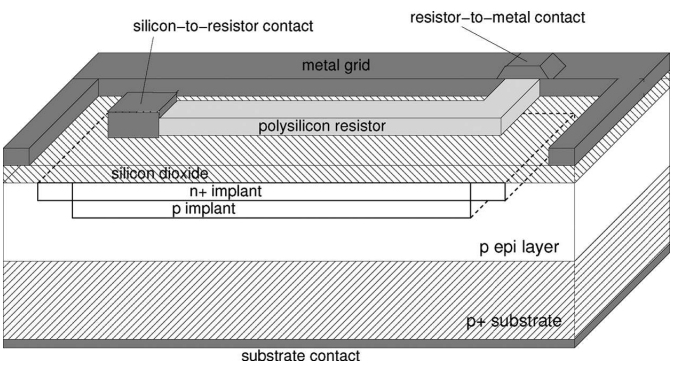

Figure 2.34: Sketch of the typical FBK-irst micro-cell composing the SiPM. The substrate is an epitaxial $p+$-type silicon with an epi (π) layer thickness of 4 μm; the second p implantation is used to fix the breakdown voltage to the desired value. The n^+ zone creating the junction is obtained using arsenic implantations and is located $\sim$100 nm from the top silicon surface [69].

Going from top to bottom, the structure of the cell is a $n^+/p/\pi/p^+$ sequence; the doping profiles and the dielectric layers deposited on the silicon surface are designed to enhance the PDE in the 420-450 nm region. After the first prototypes, produced to evaluate the functionalities of the devices, many improvements have been introduced in the technological process (especially in the geometrical fill factor) to increase the PDE and reduce the dark count rate. The typical signal shape and pulse height distribution of a 1 mm^2 area SiPM with 400 50x50 μm^2 cells are presented in Fig. 2.35.

[2] Advansid web-site: www.advansid.com

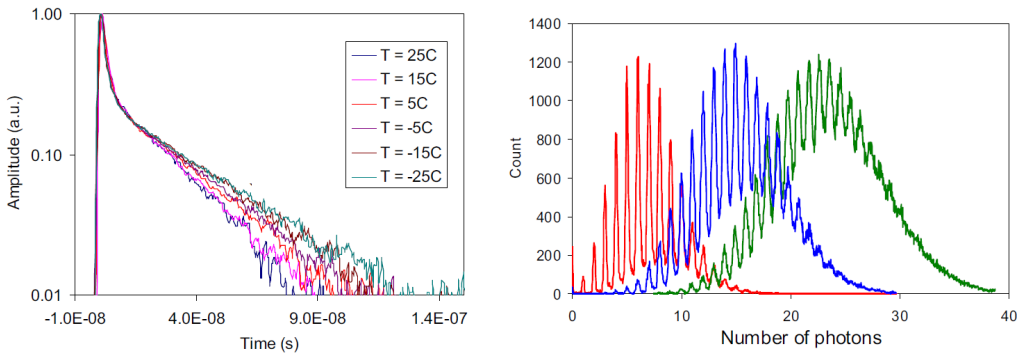

(a) (b)

Figure 2.35: Signal shape (a) and pulse height distribution (b) under illumination with variable light pulses of a 1 mm^2 area, 400 50x50 μm^2 cells FBK-irst SiPM [69].

The breakdown voltage of the basic cell is of the order of 30 V and a very high gain of the order of $\sim 10^6$ can be achieved with a moderate ($\sim$4 V) overvoltage (Fig. 2.36(a)) [69]. In particular, Fig. 2.35(b) shows that the cell uniformity response is extremely good, considering the fact that the photoelectron peaks perfectly overlap between different measurements performed with short light pulses.

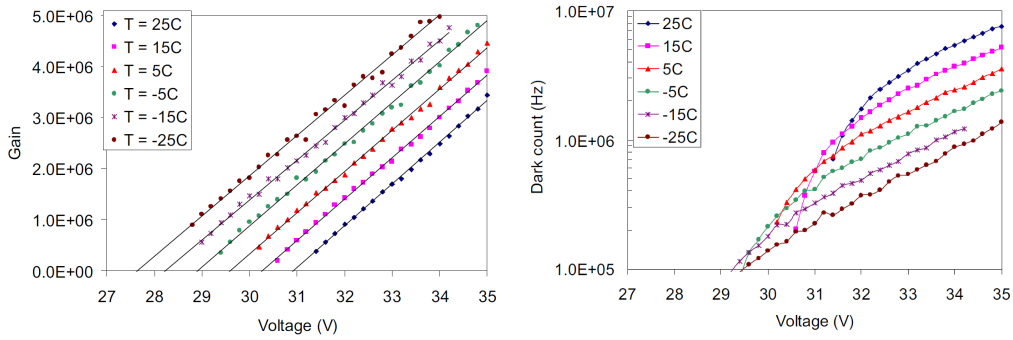

(a) (b)

Figure 2.36: Gain as a function of temperature and bias voltage (a) and dark count rate as a function of bias voltage and temperature (b) of a FBK-irst device with an area of 1 mm^2 and 400 50x50 μm^2 cells [69].

Fig. 2.36(b) presents the measured dark count rate as a function of temperature and bias voltage: in standard conditions (25° C and $\sim$4 V overvoltage) the 400 cells devices are characterized by dark count rates of a few MHz. Dark noise values of the order of 100 kHz can be achieved only biasing the device at very low overvoltages or operating it at very low temperatures. It has to be noted that the

dark count rate in Fig. 2.36(b) has been computed counting the number of pulses with a threshold level set at a half of the signal amplitude corresponding to one photoelectron, thus including also the optical crosstalk events. Modifications in the technological process are under study in order to reduce even further the dark noise [69].

As far as the PDE is concerned, many improvements have been obtained since the first prototype batch run, doubling the geometrical fill factor. A comparison between the old and new values of PDE is presented in Fig. 2.37.

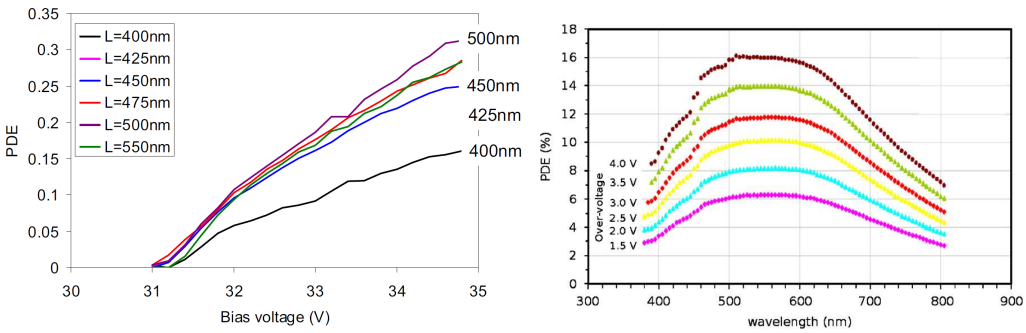

(a) (b)

Figure 2.37: Comparison between the PDE of the new devices with improved fill factor (a) [68] and the first prototypes (b) of the FBK-irst SiPMs [64].

The PDE values have been obtained using a photon counting technique: the SiPMs have been illuminated with a constant and low rate calibrated flux of photons, and the PDE is obtained dividing the detected pulses (corrected by the dark count rate) by the number of incident photons. The maximum PDE value in the new devices is $>$30% at 500 nm with a 4 V overvoltage, to be compared with a value of $\sim$16% obtained with the first prototypes.

The timing resolution of the FBK-irst devices with different cell sizes at different overvoltages has been analyzed in [70] using a 470 nm laser with an emission time window of 80 ps FWHM; both single-cell SPAD and SiPMs have been tested. The obtained results are shown in Fig. 2.38 after the subtraction of the laser and its electronics contributions from the time resolution.

As stated in section 2.3.6, the time resolution improves with the overvoltage: according to the number of fired cells and to the overvoltage, time resolutions of the order of 100 ps can be easily achieved with the FBK-irst SiPMs.

The main characteristics of the FBK-irst SiPMs are summarized in Table 2.2.

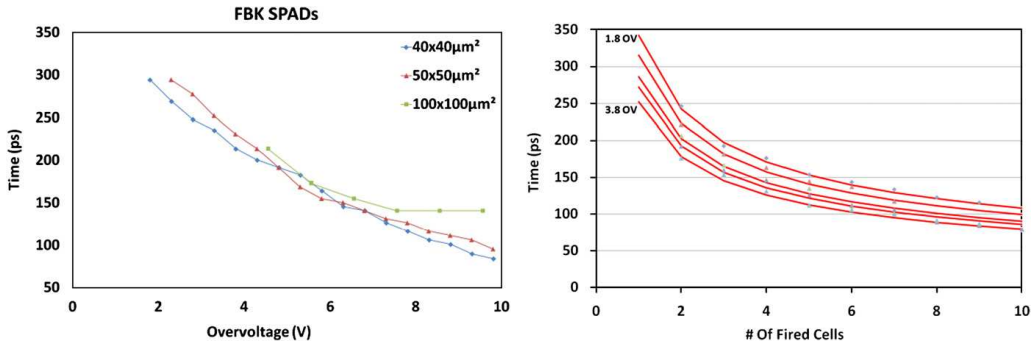

(a) (b)

Figure 2.38: Timing resolution as a function of the overvoltage obtained for SPADs with different cell sizes (a) and for 50x50 μm^2 cells SiPMs (b) [70].

Breakdown voltage	Time resolution [64, 70]	Gain [68]	PDE (500 nm, 4 V overvoltage)	Temperature coefficient $\Delta V_{BD}/\Delta T$
∼30 V	80-250 ps	$\sim 10^6$	∼30% [68]	65 mV/°C [68]

Table 2.2: FBK-irst SiPM specifications: the breakdown voltage is an indicative value.

Chapter 3

Performance of SiPMs with scintillating bars

Silicon PhotoMultipliers are a new type of detector that only recently started to gain importance in the field of high energy physics. Even if their working principles and their characteristics (described in detail in section 2.3) are well known, only a few SiPM based acquisition systems are currently in an advanced test phase. Among them, the readout system developed for the electromagnetic and hadron calorimeters of the CALICE collaboration [12] (described in section 1.1.2), the near detector system of the T2K experiment [71] and the scintillating fiber tracker of the PEBS (Positron Electron Balloon Spectrometer) experiment [72] have to be mentioned. This chapter is dedicated to the preliminary studies of the Silicon PhotoMultipliers coupled to a well known detector (a scintillating bar tracker) to compare their performance with a standard readout system based on multianode photomultiplier tubes. The experience acquired with these tests has helped in the definition of the SiPM readout system for the electromagnetic calorimeters described in the following chapters. The scintillating bar tracker used for the preliminary studies is the prototype of the Electron Muon Ranger (EMR) detector of the MICE experiment [73]. Two different tests have been performed using this detector: the first one, described in the first part of the chapter, took place on the CERN T9 beamline in summer 2008, using Hamamatsu and FBK-irst devices before and after the irradiation with neutrons and gammas. The second part of the chapter is devoted to the description of the second test, performed using cosmic rays in winter 2011 to evaluate the performances of an innovative SiPM readout system based on the MAROC3 ASIC.

3.1 The 2008 CERN Test

The purpose of the 2008 CERN test was to compare the performance of SiPMs and PMTs in a typical high energy physics application: a scintillating bar tracker. The main advantages of such a type of detector are a large area coverage, low costs (compared to the ones of silicon detectors), spatial resolutions of a few millimeters and mechanical durability. These detectors are usually readout with multianode PMTs (MAPMTs), as in the Minerva experiment at Fermilab [74] or in the EMR detector [73]. The impossibility of using scintillating bar trackers inside intense magnetic fields and other problems such as the crosstalk effect between the neighboring pads of MAPMTs can be overcome with the use of SiPMs.

The 2008 test had a twofold purpose: the first was to evaluate the performance of the whole detector in terms of efficiency, compared to the one obtained with a standard readout based on MAPMTs; the second was to characterize five different SiPMs, manufactured by Hamamatsu and FBK-irst, in terms of signal to noise ratio and time resolution, before and after the irradiation with gammas and neutrons. The results of this analysis have been published in [75].

3.1.1 The T9 Beamline

The SiPM test with the EMR prototype has been performed on the T9 beamline, located in the East Hall of the PS complex. The beam delivered to the T9 beamline is obtained from the interaction of the primary 24 GeV protons of the PS accelerator with a fixed target; different targets can be chosen in order to maximize the production of secondary electrons or hadrons. The momentum of the extracted beam is selected through primary collimators and dipole magnets near the target zone in a momentum range between 0.5 and 15 GeV/c. Additional focusing and tuning of the beam can be performed both in the horizontal and vertical directions by means of the collimators, the dipole and quadrupole magnets installed along the beamline. According to [76], the momentum resolution $\frac{\delta p}{p}$ can be set in steps of 1% varying the aperture of the horizontal collimators. A sketch of the East Hall complex is presented in Fig. 3.1.

The typical beam structure is characterized by the so-called *spills*, bunches of particles with intensities of the order of 10^4 and with a typical duration of 400 ms. The spill repetition period can vary from a few seconds up to 45 s. The T9 beamline is also equipped with two Cherenkov counters for the particle identification and two beam monitors. The beam dimension can be tuned using the secondary collimators and the quadrupole magnets, obtaining values of the order of a few centimeters RMS. The typical beam profile and divergence for a 2 GeV electron beam is presented in Fig. 3.2.

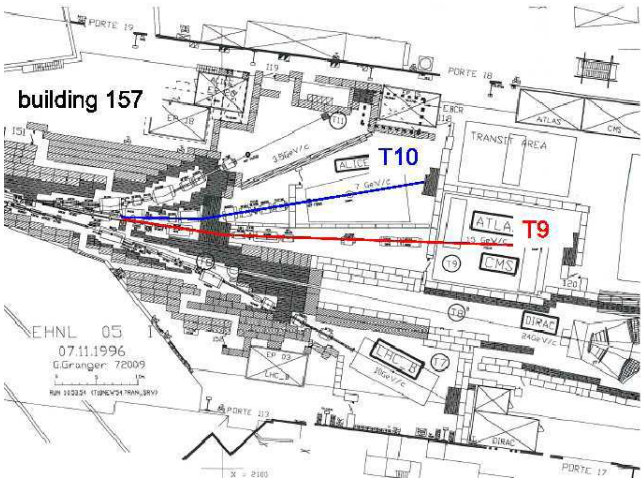

Figure 3.1: The East Hall of the PS complex: the T9 and T10 beamlines are highlighted.

3.1.2 Experimental Setup

The experimental setup on the T9 beamline is presented in Fig. 3.3. It consists of:

- a 10x10 cm^2 plastic scintillator for the trigger generation;
- two silicon beam chambers for the track reconstruction;
- the EMR prototype;
- a scintillator-lead sampling calorimeter (called DEVA);
- four 1 m long scintillating bars.

More details on the different parts of the experimental setup will be presented in the following sections. The DEVA electromagnetic calorimeter and the four 1 m long bars were under study during the beamtest but are not part of the SiPM test.

3.1.2.1 The Silicon Beam Chambers

The silicon beam chambers used for the particle tracking are based on the silicon detectors developed for the AGILE satellite [77]. Each chamber is composed of two single side silicon microstrip detectors manufactured by Hamamatsu, arranged in a x-y geometry and glued on an epoxy fiberglass support (Fig. 3.4(a)). Each silicon tile is 410 μm thick and has an active area of 9.5x9.5 cm^2 for a total of 768 strips. The strip physical pitch is 121 μm, while the readout one is

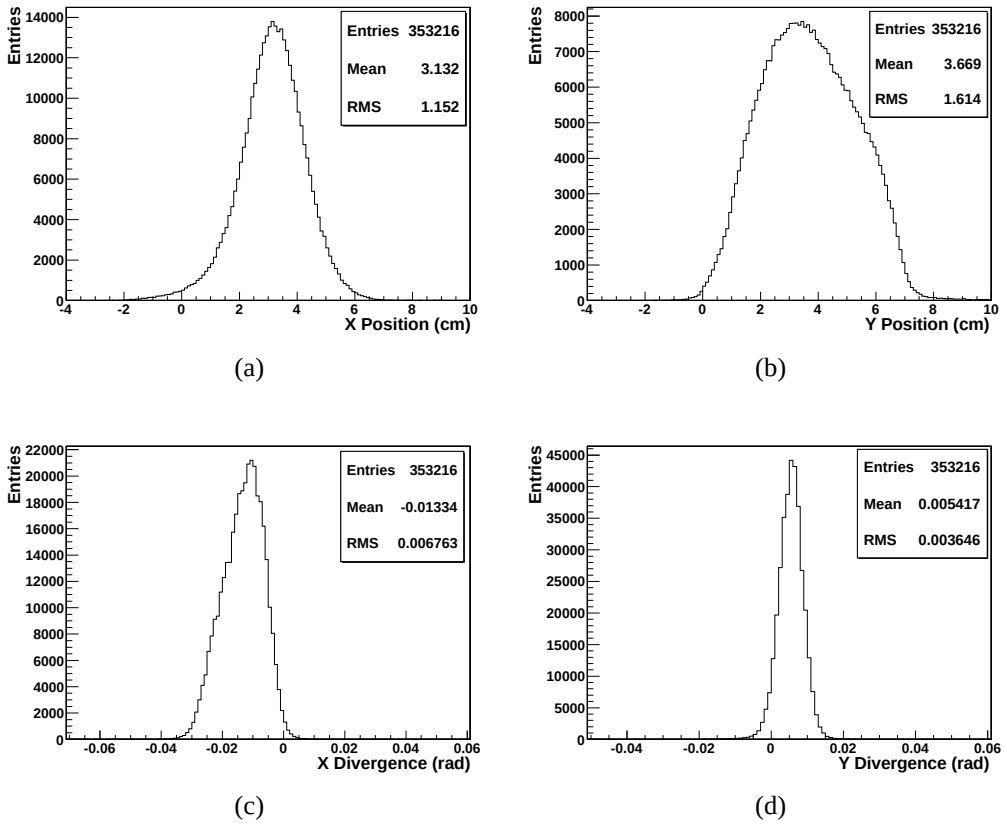

Figure 3.2: Beam profile in the x (a) and y (b) directions and beam divergence in the x (c) and y (d) directions on the T9 beamline.

242 μm (floating strip readout) allowing to obtain a spatial resolution of the order of $\sim$40 μm.

Each silicon layer is readout by three 128 channel self-triggering TA1 ASICs manufactured by Gamma Medica - IDEAS. The analog readout is a multiplexed one with a maximum clock frequency of 10 MHz. The detectors are installed inside an aluminum box (Fig. 3.4(b)) with part of the front-end electronics: a PCB housing the ASICs and a repeater board which generates the bias voltages for the ASICs, transforms the digital input signals from RS422 to single ended and amplifies the multiplexed analog signals. The readout sequence is generated by a VME Sequencer (INFN Ts) while the analog digitization is provided by a custom ADC Board or by the CAEN V550 ADC modules.

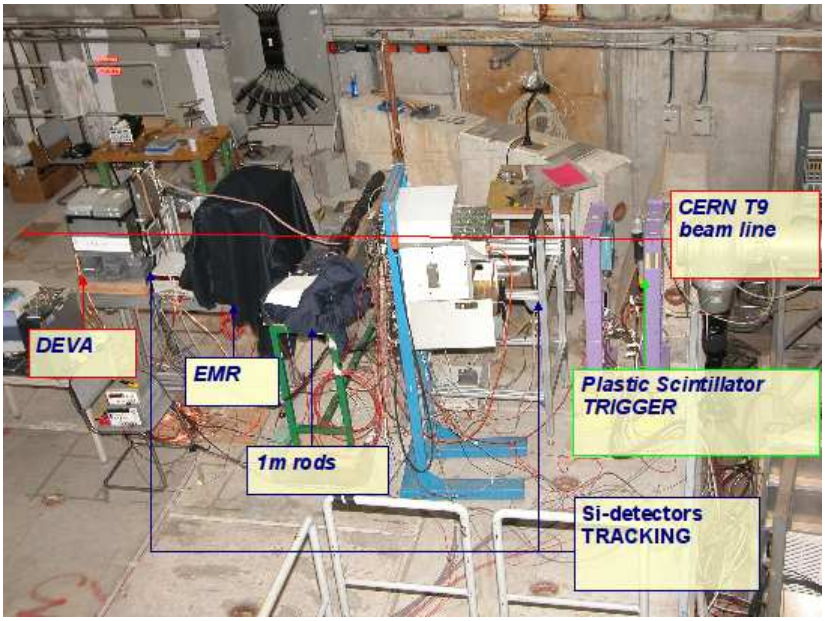

Figure 3.3: The experimental setup on the PS T9 beamline.

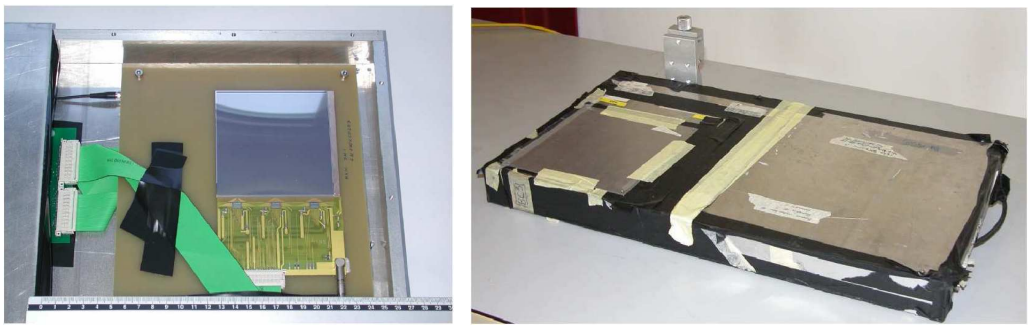

(a) (b)

Figure 3.4: Pictures of the single side silicon microstrip detector used for the tracking system (a) and aluminum box housing the microstrip detector and the readout electronics (b).

3.1.2.2 The EMR Prototype

The EMR prototype has been assembled by the mechanical workshop of INFN-Trieste as a proof of concept for the final detector that is now in the assembly phase at RAL (Rutherford Appleton Laboratory). The EMR prototype consists of 8 planes divided in x and y layers. The layers are arranged to form two blocks with 4 layers each, separated by a 3 cm air gap. Each layer consists of ten 19 cm long extruded scintillator bars with a cross section of 1.5x1.9 cm^2, manufactured

by the Fermilab scintillator workshop [78]; a drawing of the mechanical layout and a picture of the EMR prototype are presented in Fig 3.5.

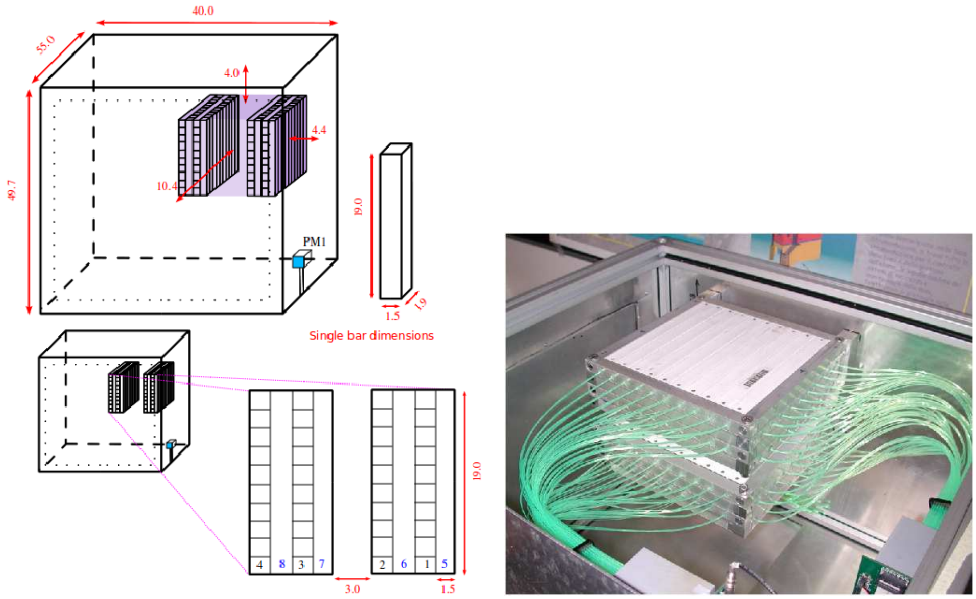

(a) (b)

Figure 3.5: Sketch of the EMR prototype (a) and photo of the detector inside its aluminum box (b).

The scintillation light of the bar is collected using four wavelength shifter (WLS) fibers with a diameter of 0.8 mm (Kuraray Y11) inserted and glued in the bar hole. In one plane the fibers come out from both sides of the scintillating bars: one side is connected to a PMT array, while SiPMs are connected to the other side, to perform correlated measurements on the same bar. On the PMT side, the fibers are readout by two 64 channels multianode PMTs (R7600-M64 by Hamamatsu), positioned inside the aluminum box which contains the whole detector. To align the PMTs and the fibers a plastic mask divided in two parts has been used: the first part holds the fibers, while the second one is positioned in front of the PMT to direct the fibers to the photocathodes. On the other side, the SiPMs are also connected to the fibers using a plastic mask divided in two parts: the first part (Fig. 3.6(a)) holds the SiPMs in position, while the fibers are fixed with optical glue to the second part of the mask (Fig. 3.6(b)). The SiPMs under test were connected to two bars (number 5 and number 6) of the first y plane of the EMR prototype.

The MAPMTs front-end electronics is based on two ASICs: the VA64TAP3 and the LS64_2 (Gamma Medica-IDEAS). The VA64TAP3 is a 64 channel low noise ASIC built in 0.35 μm N-well CMOS technology. Each channel is com-

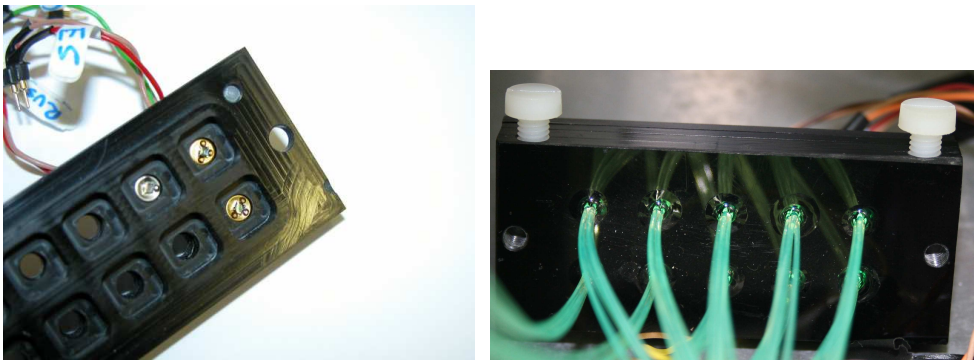

(a) (b)

Figure 3.6: The two parts of the plastic mask used to connect the SiPMs to the WLS fibers.

posed by a low gain pre-amplifier, a fast shaper and a tunable threshold discriminator. The analog signals are fed to a sample-and-hold circuit and the readout is multiplexed with a maximum readout clock of 10 MHz; moreover, 64 parallel digital outputs are available. The LS64_2 ASIC is used to shift to a low voltage TTL standard the open drain parallel trigger outputs which are then processed by an ALTERA Cyclone II FPGA. The front-end board houses two complete electronics chains [78].

As far as the SiPMs are concerned, their output signal is amplified (with a fixed gain factor of 10x) with an AMP_0604[1] Photonique amplifier, delayed of 150 ns and then integrated by a CAEN V792 12 bit QDC. The SiPM bias voltage is provided by an Agilent 3412 power supply. For the time resolution measurements, the SiPM signal is discriminated and then sampled by a CAEN V775 TDC unit.

3.1.2.3 The DAQ System

The DAQ system is a standard VME system controlled by a SBS Bit3 model 620 bridge[2], optically linked to a Linux PC-system. A schematic view of the DAQ chain is presented in Fig. 3.7(a): the blue lines represent the input signals while the pink ones the output signals from each detector.

The trigger signal is generated by the coincidence of the scintillator counter and the spill signal provided by the PS accelerator. The conditioning of the trigger signal is performed by a custom VME board (the trigger board) and the signals are then sent to a VME Control Board (INFN Ts) to generate the DAQ trigger and the readout sequence; the board is also responsible of the ASICs configuration before

[1] Photonique AMP_0604 specification internet page: *http://www.photonique.ch/Prod_AMP_0600.html*.
[2] SBS Technologies Inc., US, *http://www.ge-ip.com*

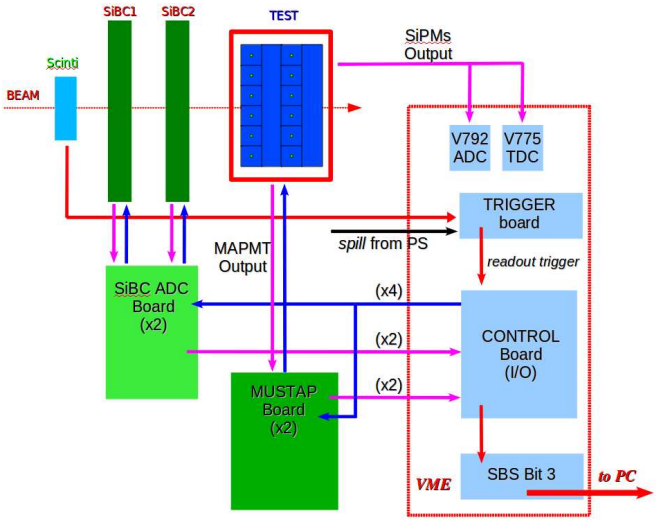

(a)

(b)

Figure 3.7: Sketch of the DAQ chain (a) and example of the DAQ graphical user interface based on Tcl/Tk (b). In (a) the blue arrows represent the configuration and control signals, while the pink and red arrows represent the detector outputs.

the start of the run. The signals of the silicon beam chambers and of the MAPMTs are digitized by two dedicated boards (the ADC board and the MUSTAP one,

respectively) and sent to the Control Board that is also responsible of the zero suppression[3] of the silicon beam chamber data. The analog data of the SiPMs are digitized by the CAEN V792 and V775 modules to obtain the pulse height and the timing information.

The DAQ software is written in C with Tcl/Tk[4] for the graphical user interface (Fig. 3.7(b)); the output data are stored in binary files (PAW ntuples) and processed off-line to obtain ASCII DST (Data Summary Tape) output files with all the relevant information. The data analysis is performed with the ROOT[5] software tool.

3.1.3 SiPM Characterization

Five SiPMs have been used for this analysis: four manufactured by Hamamatsu and one by FBK-irst. The Hamamatsu devices are a off-the-shelf model (S10362-050U metallic). Their features are the following [79]:

- 400 pixels with a cell area of 50x50 μm^2;
- a breakdown voltage of $\sim$70 V;
- a gain of 7.5x10^5;
- a PDE of 50% at 400 nm;
- a 220 ps FWHM for the time resolution.

The FBK-irst SiPM used in this test is a pre-production device belonging to the batch with enhanced fill factor and reduced dark count rate: it is composed of 688 pixels with 40x40 μm^2 cells arranged in a circular geometry. The main features of this device are listed in section 2.4. In order to evaluate the performances of SiPMs after the irradiation, two Hamamatsu devices have been irradiated with gammas (up to 3 kGy) and neutrons (4.5x10^{10} cm^{-2} of total fluence). The pictures of the Hamamatsu and FBK-irst devices are shown in Fig. 3.8.

As can be seen in Fig. 3.8, the Hamamatsu devices are encapsulated under a quartz window, while in the FBK-irst device no protection is present. Table 3.1 presents the working voltages, the criterion for the event selection and the irradiation type (if present) of the SiPMs used in the analysis.

[3] In the zero suppression mode only the strips with a signal above a given threshold are stored, thus increasing the readout speed; the threshold is set considering the noise RMS.

[4] Tcl (Tool Command Language) is a dynamic programming language and Tk is its graphical user interface toolkit, *http://www.tcl.tk*

[5] ROOT analysis software: *root.cern.ch*

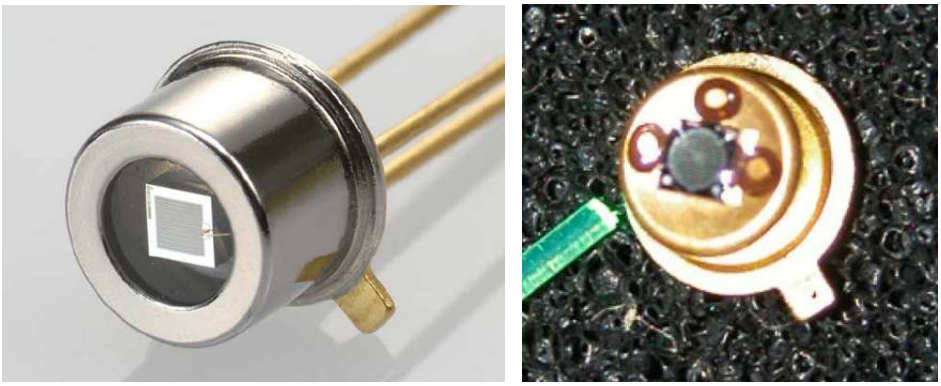

(a) (b)

Figure 3.8: The Hamamatsu S10362-050U (a) and FBK-irst (b) devices.

Model	Irradiation	Voltage (V) (breakdown)	Voltage (V) (bias)	ADC Signal Threshold	ADC Eff. Threshold
Hama. 199	∅	68.3	70.2	>450	>450
Hama. 200	∅	68.1	70.2	>450	>450
Hama. 209	Photons 3 kGy	68.3	70.2	>400	>400
Hama. 212	Neutrons $4.5\text{x}10^{10}\text{cm}^{-2}$	68.2	69.4	>50	>200
FBK-irst	∅	30.5	34.0	>400	>400

Table 3.1: SiPMs used in the test, their breakdown and bias voltages and the ADC cuts used to select the signal events and to compute the efficiency.

The ADC signal and efficiency thresholds are the cuts used in the analysis to discriminate between the signal and noise events or to define a threshold for the bar efficiency calculation. The cuts are usually the same for all the runs and for all the SiPMs, with the exception of the neutron irradiated and heavily damaged SiPMs, where two different cuts have been chosen in order to correctly evaluate the signal to noise ratio and the bar efficiency. The details of the analysis are presented in the next sections.

3.1.3.1 FBK-irst SiPM Results

The behavior of the FBK-irst device has been studied with a high statistics run with a 2 GeV beam. The first event selection is performed using the information provided by the silicon chambers, selecting only the single track events. After this selection, the events have been divided in *signal* and *noise* events using the hit

projections of the silicon chambers on the EMR plane and the SiPM signal amplitudes. An event is considered a signal if the particle hit projection corresponds to the coordinates of the bar connected to the SiPM and if the ADC value of the SiPM overcomes a given threshold (the *ADC Signal Threshold* parameter of Table 3.1). The multiple scattering contribution has been included in this selection introducing a spread in the bar dimension. All the other events are considered noise events: these events represent either those in which the particle has hit a bar without the SiPM or those in which the signal amplitude is below the threshold.

Fig 3.9(a) presents the typical SiPM pulse height spectrum of the signal events. In this plot up to 19 peaks are clearly visible corresponding to the different numbers of fired pixels. The peaks have been fitted with a Gaussian function and the linearity of the response is fitted in the plot presented in Fig. 3.9(b).

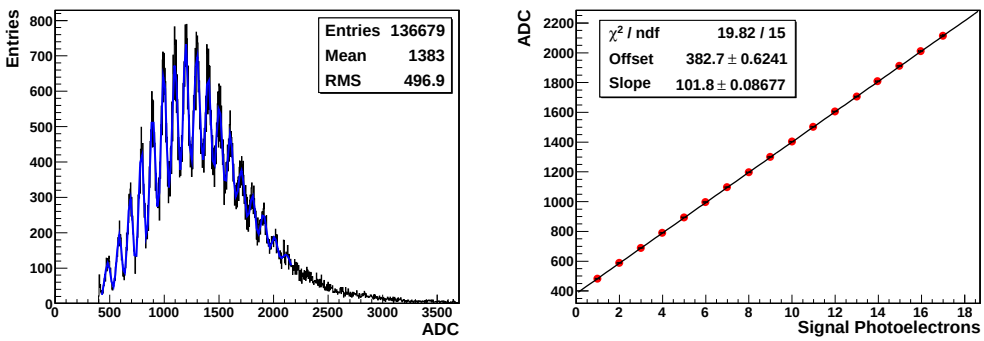

(a) (b)

Figure 3.9: Multi-peak distribution of the signal events (a) and linearity plot of the ADC signal peaks (b).

The multi-peak distribution can be observed also in the noise events, presented in Fig. 3.10(a): in this case up to 4 peaks can be identified. To define the signal to noise ratio value, the signal distribution is fitted using a user-defined function to evaluate the ADC value of the peak of the histogram, as shown in Fig. 3.10(b) (the multi-peak behavior is no more visible due to a larger bin width). The function used for the fit is obtained convolving a Landau[6] with a Gaussian function. The signal to noise ratio is then computed dividing the ADC value of the peak by the RMS value of the noise distribution.

The signal events distribution superimposed on the total events distribution is shown in Fig. 3.11(a); Fig. 3.11(b) presents the same plot zoomed in the region near the ADC cut. The non-signal events above the ADC cut are the ones in which the reconstructed track does not hit the bar readout by the SiPM. The fraction of

[6]CERN-Root package reference internet page *http://root.cern.ch/root/html/TMath.html#TMath:Landau*.

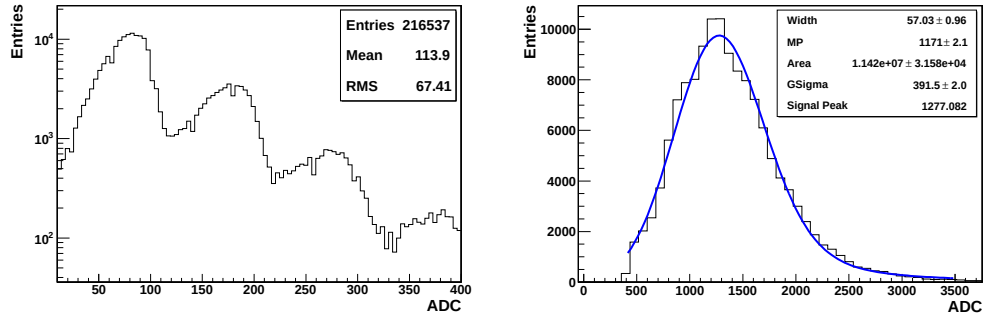

(a) (b)

Figure 3.10: Multi-peak distribution of noise events in logarithmic scale (a) and signal events distribution fitted with a Landau convolved with a Gaussian function (b): *width* is the scale parameter of the Landau; *MP* the most probable value of the Landau; *Area* the normalization constant; *GSigma* the sigma value of the convolved gaussian function.

these events with respect to the signal events represents the ”purity” parameter, described at the end of this section.

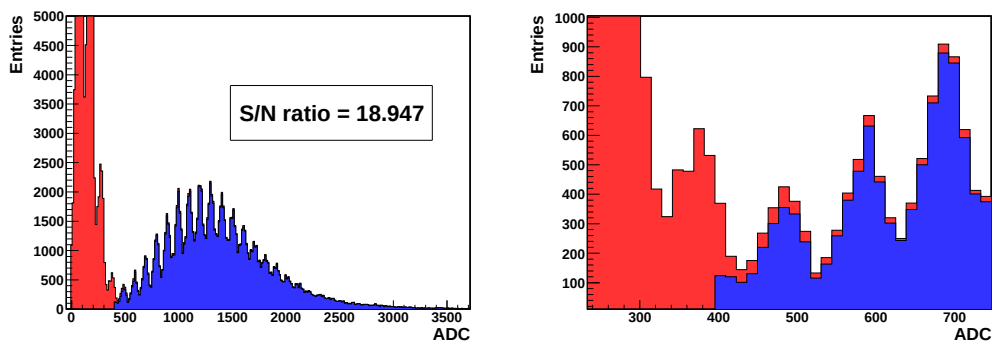

(a) (b)

Figure 3.11: Total (red) and signal (blue) events superposition (a) and zoom near the ADC cut (b).

The efficiency of the whole detector (bar, WLS fibers and SiPM) has been evaluated using the information provided by the two silicon chambers, selecting the tracks crossing the bar connected to the SiPM. A profile histogram has been filled with 1 if the SiPM pulse exceeds a given ADC threshold (the *ADC Efficiency Threshold* parameter of Table 3.1), with 0 otherwise. The same procedure has been applied to the MAPMT pulse height. Fig. 3.12(a) shows the resulting ef-

ficiencies; the multiple scattering contribution has not been included in the mean efficiency calculation.

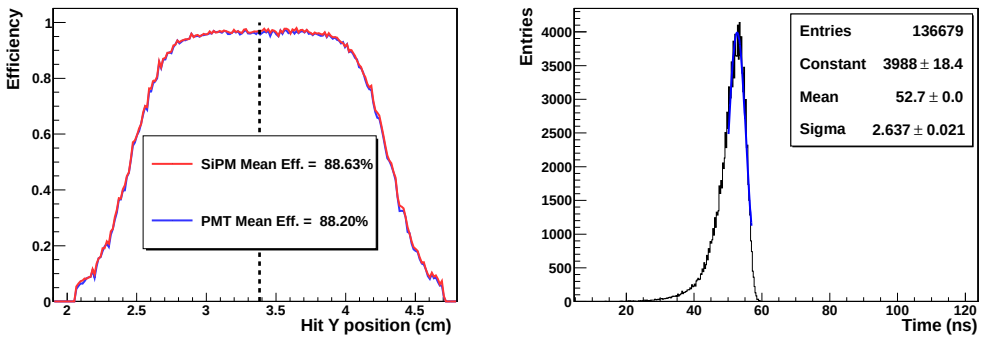

(a) (b)

Figure 3.12: Total bar efficiency for the PMT and SiPM readout configuration (the dotted line represents the bar center) (a) and time distribution of the FBK-irst SiPM fitted with a Gaussian function (b).

The time resolution value has been computed plotting the time difference between the incoming signal from the trigger plastic scintillator and the over-threshold signal of the SiPM after a discriminator. The time distribution, presented in Fig. 3.12(b), is then fitted with a Gaussian function whose standard deviation is the time resolution: the Gaussian fit has been performed in the $[-0.5\sigma, 2\sigma]$ range. This resolution value is an upper limit because it sums the intrinsic time resolution of the SiPM, the timewalk of the discriminators used in the trigger and in the sampling, the different impact point of the particle in the trigger counter and in the bar and the possible spread at the point where the scintillating light is collected by the WLS fiber. The obtained time resolution is $\sim$2.6 ns, so the 100-200 ps contribution due to the SiPM can be considered negligible.

In conclusion, the following parameters summarize the FBK-irst SiPM performances:

- signal to noise ratio: 18.947;
- mean (Max) efficiency: 88.63% (97.97%);
- time resolution: 2.637 ns;
- purity: 97.44%;
- plateau region width: 0.35-1.51 cm.

The purity parameter is computed as the ratio between the signal events (selected using the pulse height and the tracker information) and the total ones which overcome the efficiency threshold. In other words, the purity parameter represents the efficiency in selecting the signal events using only the SiPM pulse height information. Concerning the plateau region, it is defined as the bar region where the detection efficiency remains stable, with a deviation from the maximum value smaller than 5%.

3.1.3.2 Hamamatsu SiPMs Results

The same event selection and analysis procedure used for the FBK-irst device has been applied to the SiPMs manufactured by Hamamatsu. Four devices have been tested with a 2 GeV beam: two non irradiated devices (labeled 199 and 200), a gamma irradiated (3 kGy) device (labeled 209) and a neutron irradiated one (with a fluence of 4.5x10^{10}cm^{-2}, labeled 212).

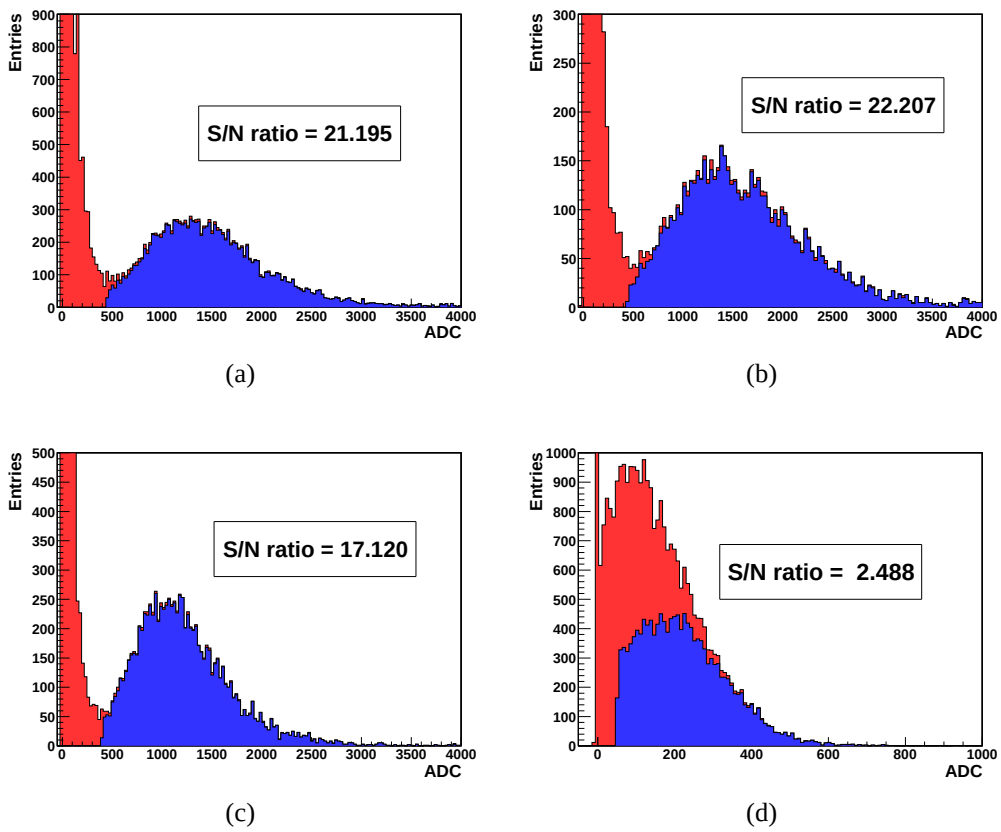

Figure 3.13: Signal to noise ratio for the Hamamatsu 199 (a), 200 (b), 209 (c) and 212 (d) devices.

The signal to noise ratio value obtained with the four Hamamatsu devices is presented in Fig. 3.13. The one of the non-irradiated SiPMs is very good (21.2 and 22.2 for the 199 and 200 models, respectively), even higher than the value obtained with the FBK-irst device. As far as the irradiated devices are concerned, the situation is quite different: the gamma irradiation worsens slightly the S/N ratio to 17.1, while the neutron irradiation has a larger impact, reducing the S/N ratio to an even smaller value of 2.5. In particular, looking at the plot in Fig. 3.13(d), it can be seen that the noise and the signal events are practically superimposed: this means that without the information provided by the silicon chambers, the discrimination between signal and noise events is very difficult. To correctly fit the signal events distribution of the neutron irradiated SiPM, the ADC cut used to select the signal events has been set to the very low value of 50 ADCs (see Table 3.1): the noise events rejection efficiency (the *purity* parameter) of this cut is only ∼60%.

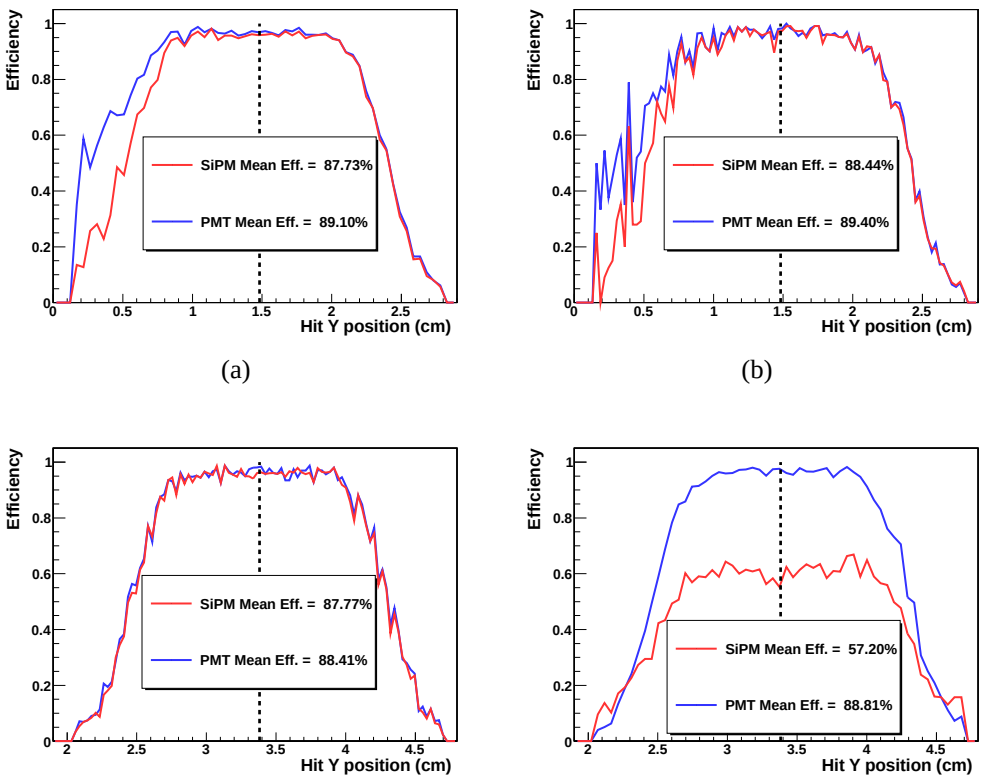

Figure 3.14: Bar overall efficiency for the PMT and SiPM readout configurations for the Hamamatsu 199 (a), 200 (b), 209 (c) and 212 (d) devices. The dotted line represents the bar center.

The parameter most affected by the worsening of the signal to noise ratio is the mean detection efficiency, presented in Fig. 3.14. Using the neutron-irradiated device, the mean detection efficiency is reduced to 60%, while the results obtained with the gamma-irradiated device are quite good, with a mean detection efficiency still of the order of 90% and comparable with the efficiency obtained with the non-irradiated devices. The rugged profile on the left of Figs. 3.14(a) and 3.14(b) is due to the poor statistics on that side of the bar. The efficiency with the neutron-irradiated SiPM has been obtained increasing the ADC cut to 200 ADCs to better reject the noise events.

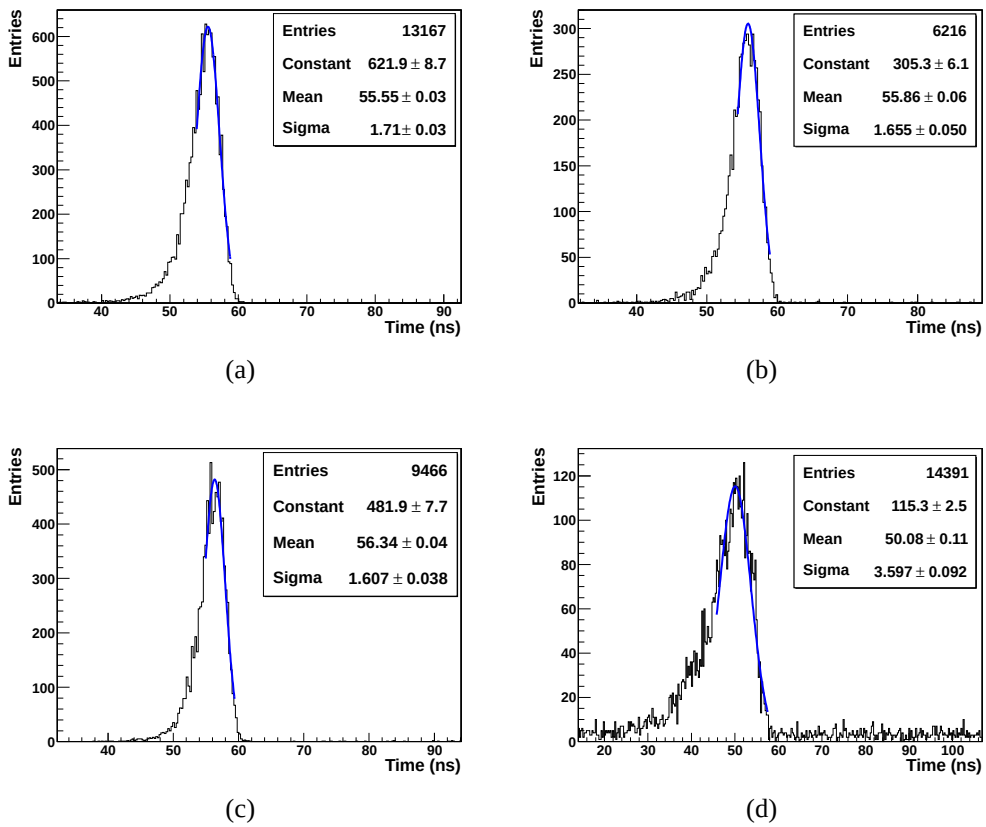

Figure 3.15: Time resolution for the Hamamatsu 199 (a), 200 (b), 209 (c) and 212 (d) devices.

The neutron irradiation also affects the SiPM time resolution (see Fig. 3.15) which varies from ∼1.7 ns for the non-irradiated or gamma-irradiated devices to 3.6 ns. The performances of the four Hamamatsu devices are summarized in Table 3.2.

As in the FBK-irst device case, the plateau region is defined as the bar region

Model	S/N Ratio	Time Res. (ns)	Mean (Max) Efficiency (%)	Purity (%)	5% Plateau Region (cm)
Hama. 199	21.195	1.751	87.73 (98.18)	96.26	0.39-1.59
Hama. 200	22.207	1.711	88.44 (99.16)	96.01	0.6-1.47
Hama. 209	17.120	1.756	87.77 (98.75)	98.28	0.43-1.59
Hama. 212	2.488	3.775	57.2 (66.89)	84.52	0.29-1.74*

Table 3.2: Performances obtained with the Hamamatsu SiPMs in terms of signal to noise ratio, time resolution, efficiency and purity of selected events. The plateau regions marked with * are defined for a 20% deviation from the maximum value.

where the detection efficiency remains stable, with a deviation from the maximum value smaller than 5% (or 20% for the neutron irradiated device.). The maximum efficiency values are extracted from the plots of Fig. 3.14, taking the maximum efficiency points.

3.2 The 2011 Cosmic Ray Test

In winter 2011 the EMR prototype has been used to test a new readout system based on the MAROC3 (Multi Anode ReadOut Chip) ASIC (Application Specific Integrated Circuit) [80]. Originally designed for the readout of MAPMTs, this ASIC can be used also for the readout of SiPMs, as proven in [81] using a matrix of SiPMs coupled to LYSO crystals. Two differences characterize the 2011 test with respect to the 2008 one: the first one is that in the new test eight SiPMs have been used to read almost an entire EMR plane, allowing a complete spatial resolution, efficiency and timing study of the EMR detector used as a tracker. The second difference is that both the MAPMTs and the SiPMs are readout using the same readout system, based on a MAROC3 board, allowing a better comparison.

3.2.1 Experimental Setup and DAQ

The experimental setup (Fig. 3.16) for the cosmic rays is essentially the same used in the 2008 CERN test, rotated of 90°. It is composed of:

- two plastic scintillators to generate a trigger;
- two silicon beam chambers for the track reconstruction;
- the EMR prototype.

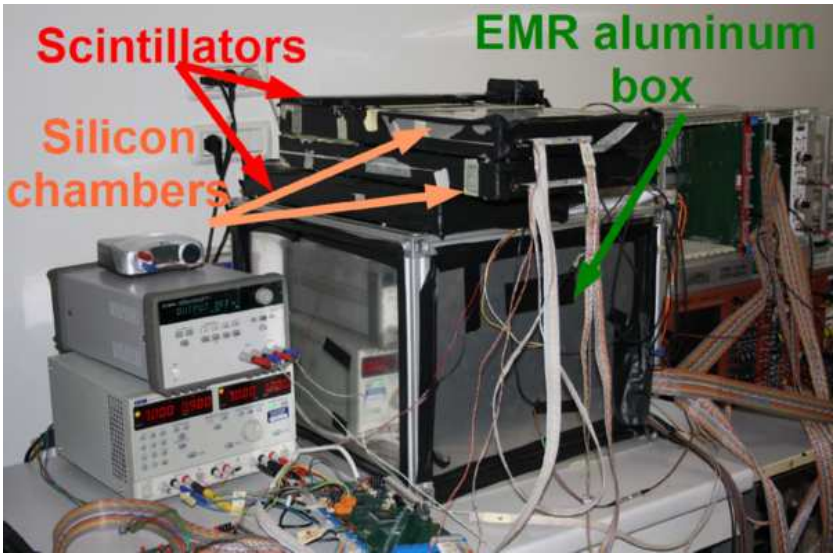

Figure 3.16: Picture of the experimental setup of the 2011 cosmic ray test.

The details of the silicon beam chambers and of the EMR prototype have been discussed in sections 3.1.2.1 and 3.1.2.2. During this test, only one MAPMT has been used for the readout of the EMR prototype, thus only 4 planes (2 x and 2 y) were active. Eight SiPMs manufactured by FBK-irst have been used for the readout of the SiPM plane of the EMR prototype. The SiPMs are the same model of the one tested in 2008, composed of 688 40x40 μm^2 pixels arranged in a circular geometry with a diameter of $\sim$1 mm. The main difference with respect to the device tested in 2008 is that in the new test the SiPMs are covered with an epoxy resin to protect the sensors themselves.

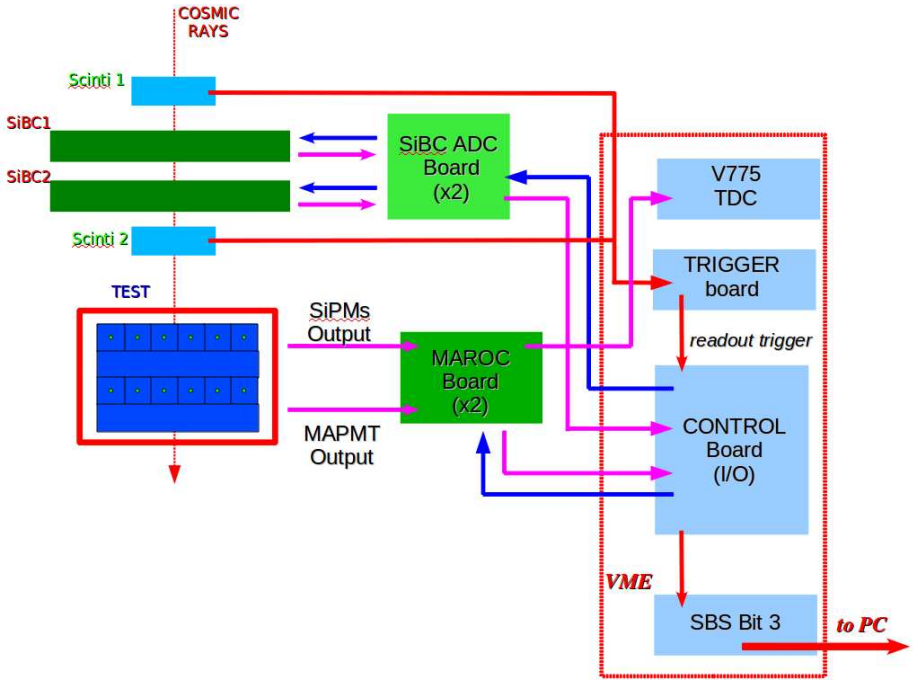

Figure 3.17: Sketch of the DAQ scheme of the 2011 cosmic ray test. The blue arrows represent the configuration and control signals, while the pink and red arrows represent the detector outputs.

The DAQ system is sketched in Fig. 3.17: it is similar to the one used in the 2008 CERN test, with the difference that the trigger signal is provided by the coincidence of the two scintillator counters. The signals coming from the MAPMT and the SiPMs are digitized by two boards based on the MAROC ASIC (see section 3.2.1.1), controlled by a VME control board, responsible of the initial configuration and of the storage of the data coming from the MAROC. The data are then sent to the PC through an optical link. As will be shown, the MAROC ASIC can operate both in the analog and digital mode: in particular, the digital outputs have been sampled by the V775 TDC module for the timing measurements.

3.2.1.1 The MAROC3 Board

The MAROC3 board is based on the third revision of the MAROC chip, a 64 channel ASIC designed in AMS SiGe 0.35 μm technology; the chip has an effective area of 4x4 mm^2 and is powered with a 3.5 V bias for a power consumption of 350 mW [80]. The 64 channels work in parallel and each of them consists of (Fig. 3.18):

- a 5 pF input capacitor;
- a pre-amplifier with a variable gain up to 4x, adjustable with a 8 bit resolution (the unitary gain corresponds to 64);
- a tunable slow shaper and a sample & hold circuit for the analog readout;
- a tunable fast shaper and a discriminator for the digital readout.

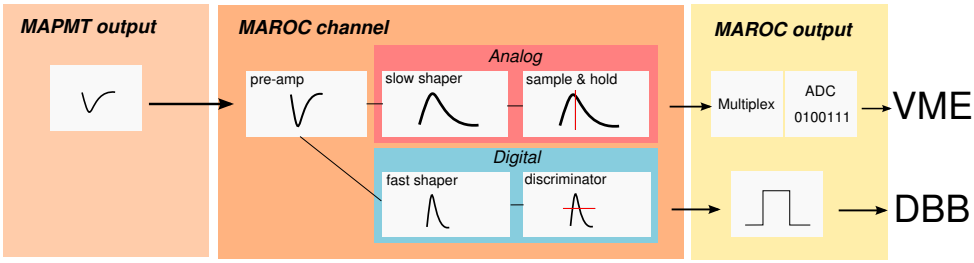

Figure 3.18: Scheme of one of the MAROC3 channels.

Each MAPMT anode or SiPM output signal is sent to the input capacitor of the MAROC channel and amplified in the pre-amplifier stage. A current mirror feeds then the analog and the digital circuit with a copy of the amplified signal. In the analog mode the slow shapers outputs are addressed to the sample & hold circuit and then multiplexed with a maximum clock frequency of 10 MHz by an external 12 bit ADC (AD9220, Analog Devices[7]). In the digital mode the fast shaper outputs are discriminated to generate 64 digital outputs whose width is a function of the input amplitude, thanks to a Time over Threshold (ToT) architecture [73]. All the ASIC settings, like the pre-amplifier gain and the shaping time (varying the feedback capacitors and resistors) can be selected sending a string of 829 bits to the ASIC during the configuration phase.

The MAROC ASIC is hosted on a custom board (Fig. 3.19) whose main parts are:

- the MAROC ASIC;

[7] Analog Devices Inc.; *www.analog.com*

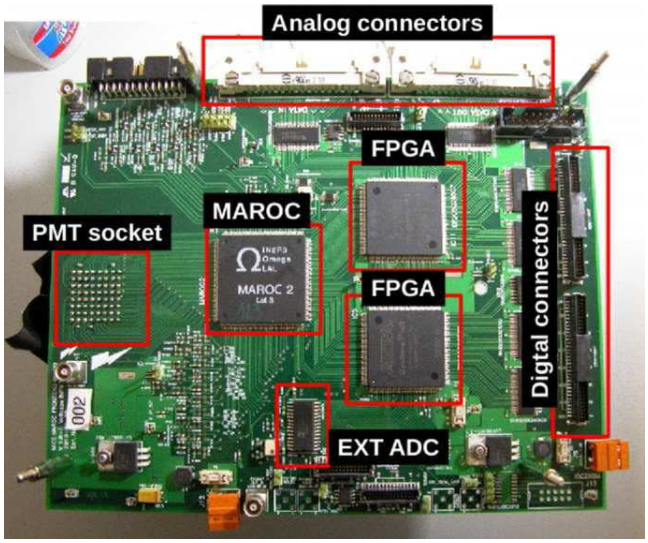

Figure 3.19: Picture of the MAROC3 board.

- the PMT socket, used to directly connect the MAPMT to the board (thus reducing the electronics noise) and to provide the high voltage bias for the MAPMT;
- two Altera Cyclone II[8] FPGAs (Field Programmable Gate Array), responsible of the ASIC configuration and of the generation of the readout sequence;
- the 12 bit AD9220 ADC;
- two analog connectors, used for the configuration and the analog readout;
- two digital connectors, where the digital signals coming from the ASIC are addressed to.

3.2.2 Results

The performances of the SiPMs have been compared to the MAPMT ones in terms of signal to noise ratio, detection efficiency, spatial and timing resolution. As in the 2008 CERN test, the information provided by the silicon beam chambers has been used to select only the single track events. The final analysis is based on a run of ∼310000 cosmic rays. The cosmic rays distribution obtained with the silicon beam chambers projected on the EMR detector is shown in Fig. 3.20.

During the run, the SiPMs have been biased at 38 V, while the high voltage of the MAPMT was set to 850 V. The gain of the MAROC3 pre-amplifier has

[8] Altera Corporation; *www.altera.com*

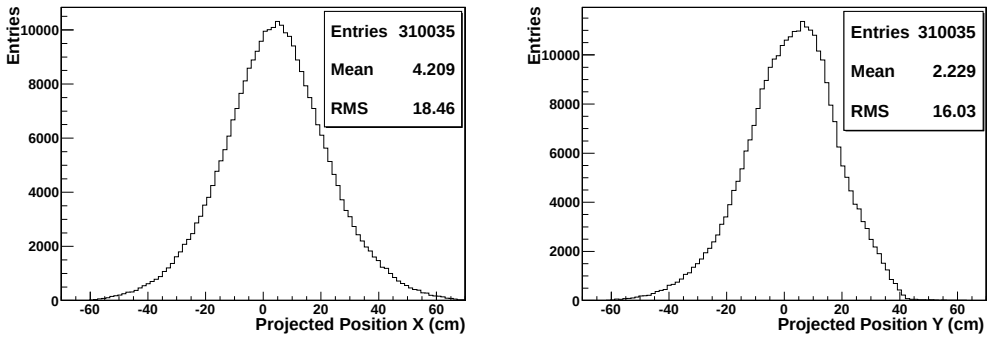

(a) (b)

Figure 3.20: Silicon beam chambers cosmic ray distribution once projected on the EMR tracker for the x (a) and y (b) directions.

been set to 64, corresponding to the unitary gain, for both the MAPMT and the SiPM readout. The MAPMT has been connected directly to the PMT socket of the MAROC3 board, while the connection of the eight SiPMs was performed using eight 8 ns long cables soldered to a custom board which was then coupled to the standard PMT socket.

3.2.2.1 Signal to Noise Ratio

The signal to noise ratio has been evaluated fitting the PMT/SiPM pulse height distribution with a Landau function convolved with a Gaussian one. The signal events distribution has been obtained for each bar using the information provided by the silicon beam chambers, selecting only the events corresponding to the crossing of a bar by a particle. The S/N ratio value has then been computed dividing the signal peak position by the RMS value of the pedestal distribution. An example of one SiPM and one PMT channel pulse height distribution with the corresponding S/N ratio value is presented in Fig. 3.21: the signal to noise ratio value of this bar is 8.8 for the SiPM readout and 109.6 for the PMT readout.

Considering all the bars, the mean S/N ratio for the SiPM readout is 8.13 and 108.33 for the PMT readout. The huge difference between these two values is due to the noise RMS, which in the SiPM case is larger than 100 ADC, compared to the $\sim$2 ADC of the PMT. The large RMS is due to the electromagnetic noise induced by the cables connecting the SiPMs outputs to the MAROC inputs. This is the reason why for the calorimeter test described in the next chapters, a custom board to plug the SiPM output directly to the PMT socket of the MAROC3 board has been designed.

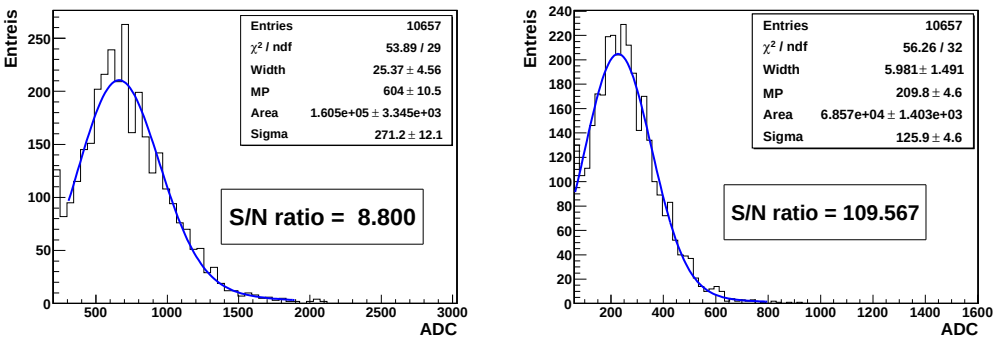

(a) (b)

Figure 3.21: Pulse height and signal to noise ratio for a SiPM (a) and one channel of the PMT (b).

3.2.2.2 Detection Efficiency

The detection efficiency for the SiPM and MAPMT readout has been evaluated as the ratio between the beam profile reconstructed by the SiPMs/MAPMT and the one reconstructed by the silicon beam chambers, projected on the reference layer. The EMR layer beam profile has been reconstructed with the following procedure:

- definition of the signal cluster: a cluster is a group of bars detecting the same particle. Their pulse height has to overcome a threshold which has been set to 3σ for the SiPM and 50σ for the MAPMT;
- selection of the single cluster events;
- definition of the impact point coordinate of the particle using a center of gravity algorithm based on the pulse height of the bars in the cluster.

In order to be sure that the particle has crossed the reference layer, the good events are defined as those which have a single cluster hit also on the plane below the reference layer. The ratio between the EMR and silicon chamber beam profiles is presented in Fig. 3.22.

The mean detection efficiency has been obtained slicing the plots in Fig. 3.22 along the x direction and fitting them with a constant function: an example of a slice is shown in Fig. 3.23.

As can be seen in Figs. 3.22 and 3.23, the mean detection efficiency is above 90%, with a mean value of $\sim$94%, for both the SiPM and MAPMT. Better results with the SiPMs can be in principle obtained removing the tiny air gap between the SiPM and the WLS fibers inside the SiPM mask, for example using optical grease.

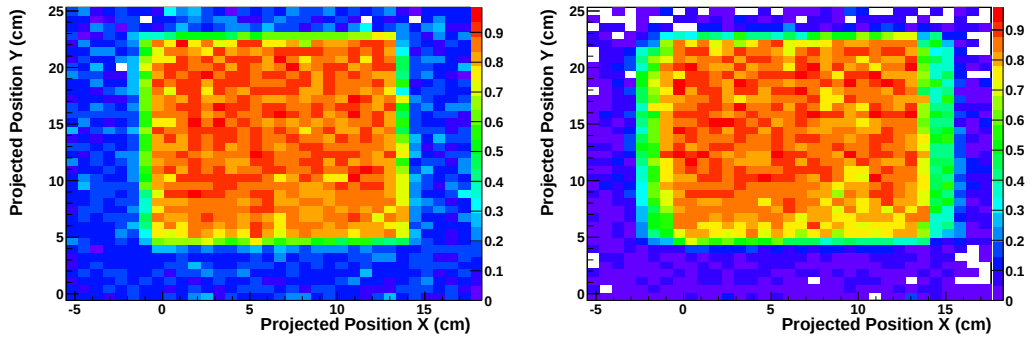

(a) (b)

Figure 3.22: 2D detector efficiency obtained with the SiPM (a) and MAPMT (b) readout. Eight bars have been used to define the 2D profile for both the SiPM and the MAPMT: the larger plane shadow in the MAPMT plot is due to the optical crosstalk effect.

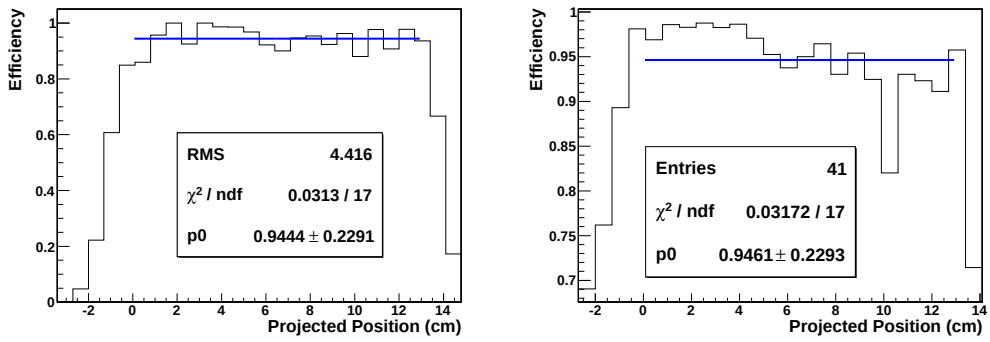

(a) (b)

Figure 3.23: Fitted efficiency slices obtained with the SiPM (a) and MAPMT (b) readout.

3.2.2.3 Optical Crosstalk

The optical crosstalk phenomenon is due to a misalignment between the WLS fibers and the pads of the MAPMT. In presence of a misalignment, the light coming from a bar can hit two (or more) neighboring pads, thus resulting in a misidentification of the bar itself. This effect is obviously absent in the SiPM readout because the SiPM and its corresponding WLS fiber are optically isolated from the neighboring ones. The effect of the optical crosstalk can be highlighted defining an efficiency plot using only the signal coming from a single pad of the MAPMT or from a single SiPM: the plots obtained selecting the pad and the SiPM

corresponding to the same bar are shown in Fig. 3.24.

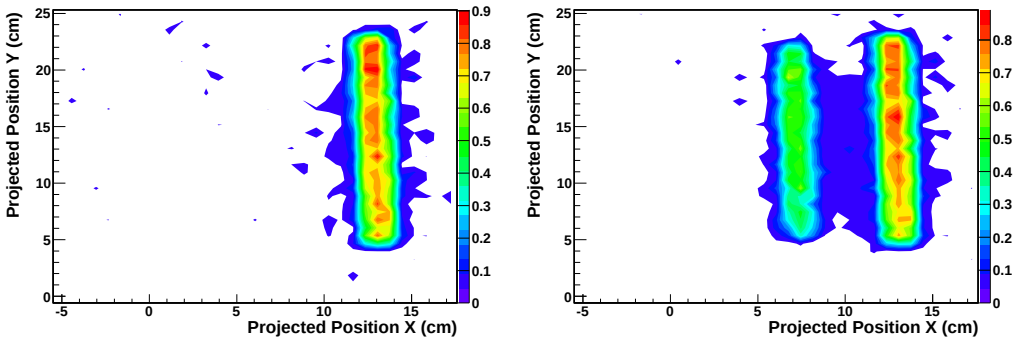

(a) (b)

Figure 3.24: Contour plot of a single bar efficiency obtained with the SiPM (a) and MAPMT (b) readout to highlight the crosstalk effect.

The selected pad of the MAPMT is partially illuminated by a second bar, while no crosstalk effect can be seen in the SiPM readout. The optical crosstalk is very difficult to avoid: even with a perfect alignment between the fibers and the pads, a small amount of light can still hit a wrong pad due to the refraction processes in the glass that covers the MAPMT. As will be shown in the following, the optical crosstalk effect can affect also the position reconstruction of the incoming particles, thus worsening the spatial resolution.

3.2.2.4 Spatial Resolution

The spatial resolution has been computed using the residuals, that is the difference between the particle position reconstructed with the beam chambers and with the EMR layer. The position of the particle in the EMR layer has been obtained using the procedure described for the efficiency, selecting the single cluster events and calculating the impact coordinate inside the cluster with the center of gravity method. The residual histograms for the SiPM and MAPMT readout are presented in Fig. 3.25. They are fitted with a Gaussian function: the spatial resolution is defined as the σ parameter of the fit. A value of 0.7 cm has been obtained for both the SiPM and MAPMT readout. However, the MAPMT residuals are affected by the presence of a second peak, due to the optical crosstalk.

3.2.2.5 Timing Resolution

The timing resolution value has been computed plotting the time difference between the incoming signal from the trigger plastic scintillators and the digital

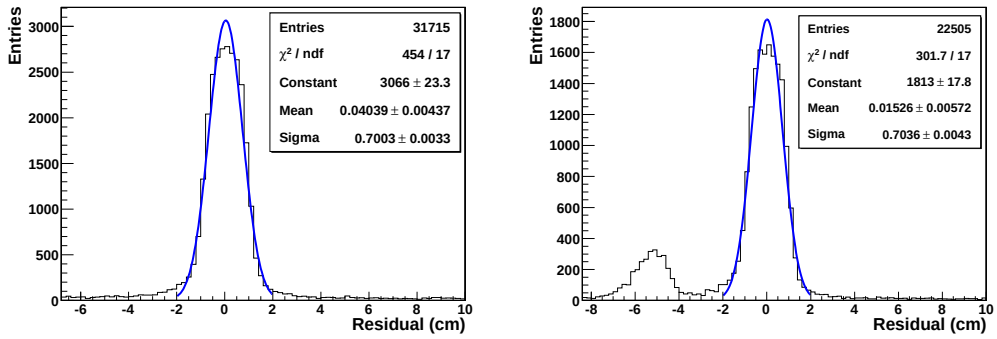

(a) (b)

Figure 3.25: Spatial resolution obtained with the SiPM (a) and MAPMT (b) readout. The second peak in the MAPMT plot is due to the mis-reconstructed hit positions deriving from the optical crosstalk effect.

output of the MAROC3 board. The histogram is fitted with a Gaussian function in the $[-\sigma, 2\sigma]$ range, and the timing resolution parameter is defined as the σ of the fit. An example of the TDC spectrum obtained for the SiPM and MAPMT readout is presented in Fig. 3.26.

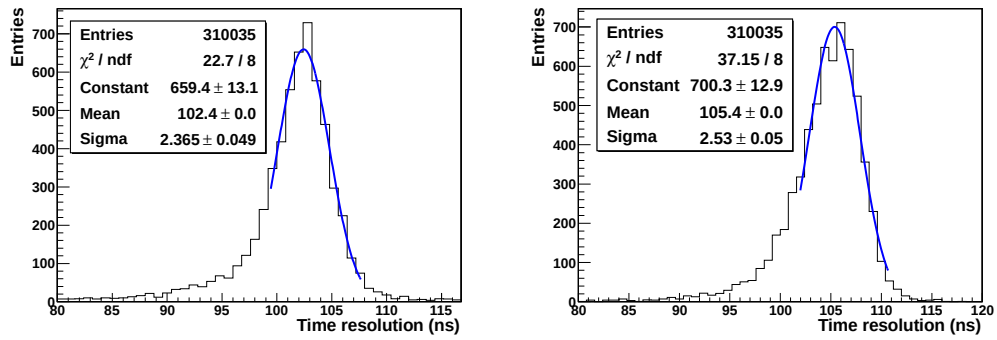

(a) (b)

Figure 3.26: Example of TDC spectrum for the SiPM (a) and MAPMT (b) readout.

The timing resolution of the selected channel is equal to 2.37 ns for the SiPM readout and to 2.53 ns for the MAPMT one. The mean values obtained considering the eight channels are 2.62 ns and 2.75 ns for the SiPM and MAPMT systems respectively. As in the 2008 CERN test, these results can be considered as an upper limit because they are the sum of different effects, like the timewalk of the electronics chain, the characteristic timing of the scintillator light emission and

the intrinsic timing response of the SiPM.

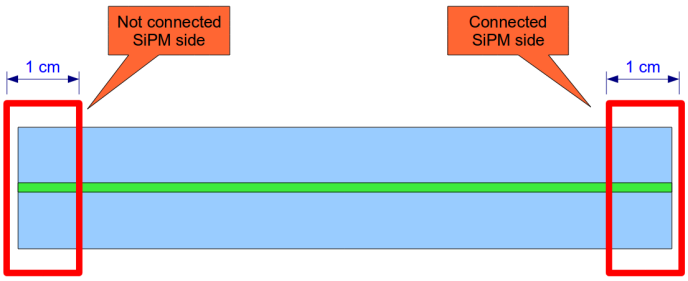

Figure 3.27: Sketch of the event selection at the two ends of the bars. The selected regions are 1 cm large.

Using the information provided by the silicon beam chambers and the fact that the cosmic rays span the whole bar length, it is possible to select only the events hitting a bar on the opposite ends, thus computing the different timewalk of the scintillator light. The light speed inside polystyrene, considering a refraction index $n = 1.59$, is $\sim$19 cm/ns; this means that, given the bars are 19 cm long, the signals coming from the not connected end of the bar should be delayed of $\sim$1 ns with respect to the ones coming from the connected end. The TDC spectrum obtained with the SiPM selecting only the events in the last cm of the two ends of the bar (Fig. 3.27) is presented in Fig. 3.28.

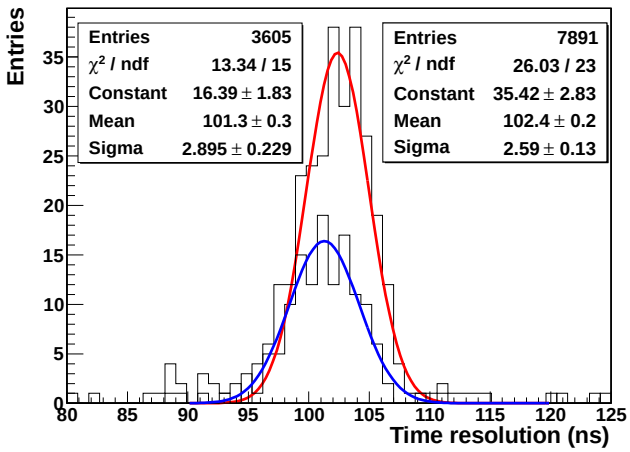

Figure 3.28: Comparison between the SiPM TDC spectrum obtained for the two ends of the bar. The histograms are fitted with a Gaussian function.

As can be seen from the Gaussian fit, the two peaks are separated by $\sim$1 ns, thus confirming the expected behavior. This analysis is possible because, as

explained in section 3.1.3, the intrinsic timing resolution of the SiPM is much smaller than 1 ns, being of the order of 200 ps. On the contrary, the intrinsic resolution of the MAPMT is not good enough and the same analysis approach gives two broad distributions in which no time separation is present.

Chapter 4

Shashlik Calorimeters and SiPMs - Prototype 0

This chapter is devoted to the description of the performance of a SiPM based readout system for an electromagnetic shashlik calorimeter, defined as “Prototype 0” or with its nickname “Willie”. More details on the electromagnetic calorimeters and in particular on the shashlik structure can be found in appendix A. The calorimeter under test, originally built for the development of the STIC calorimeter [82], has been reconditioned by the mechanical workshop of INFN-Trieste and equipped with a versatile readout system which can be coupled to either a MAPMT or an array of SiPMs. All the tests described in this chapter are performed within the framework of the FACTOR (Fiber Apparatus for Calorimetry and Tracking with Optoelectronic Read-out) collaboration, a three years INFN R&D project in collaboration with FBK-irst. The main goals of the FACTOR collaboration are the following:

- the development and optimization of the SiPM technology;
- the tests of the performance of these devices as a readout system for fiber calorimeters or scintillators, with particular attention to the high energy physics and space fields.

The prototype 0 calorimeter has been tested in two separate beamtest campaigns. The first one, described in the first part of the chapter, has been performed at CERN in summer 2009, using electrons up to 6 GeV and tagged photons up to 120 GeV. The aim of this test was to evaluate and compare the performance of the calorimeter using both a SiPM and a MAPMT based readout system. The second test, performed at CERN at the end of 2010, represents the first attempt to use a MAROC3 ASIC readout system, originally developed for the readout of MAPMTs, for an array of SiPMs.

4.1 The 2009 CERN Beamtests

In summer 2009 the calorimeter prototype has been tested in two separate beamtests at CERN in order to evaluate its performance in terms of linearity, energy and spatial resolution, using both a standard (MAPMT) and a SiPM based readout system. The tests have been performed on the T10 and H4 beamlines using electrons up to 6 GeV and tagged photons up to 120 GeV. In order to simplify as much as possible the readout chain, the signals coming from the MAPMT or the SiPMs have not been amplified before being sampled by a charge integrating ADC. The results described in the following are a refined version of the analysis published in [83].

4.1.1 The Prototype 0 Shashlik Calorimeter

The shashlik calorimeter prototype under test has been built by the mechanical workshop of INFN-Trieste and is composed of 41 3.27 mm thick tiles of plastic scintillator and 40 3.1 mm thick tiles of lead, for a total of $\sim$22.4 radiation lengths and a Molière radius of $\sim$4.5 cm; each tile has an area of 8×8 cm^2. The readout is performed using 64 0.8 mm WLS fibers (Kuraray Y11 [84]) and the sensitive part of the calorimeter is contained in a 1 cm thick aluminum vessel. Aluminized reflective sheets have been used as an interface between the scintillator and lead tiles in order to improve the light output. A sketch of the calorimeter is shown in Fig. 4.1.

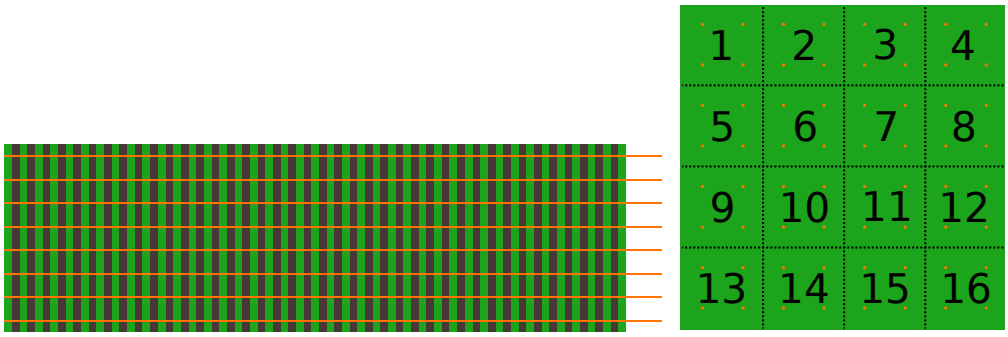

(a) (b)

Figure 4.1: Lateral (a) and frontal sketch (b) of the calorimeter with the scintillator tiles, the lead tiles and the WLS fibers. The numbers of the readout channels are also indicated. The dotted lines in (b) have no physical meaning and are depicted only to define the fibers that are bundled together.

The WLS fibers cross the whole calorimeter, so each fiber collects the light of all the scintillator tiles. As sketched in Figs. 4.1(a) and 4.1(b), the fibers are placed

in a 8x8 matrix of 1 cm spaced holes in the scintillator and lead tiles; the fibers are then grouped and glued in bundles of four using 16 plastic holders (Fig. 4.2(b)) and plugged into a plastic support (Fig. 4.2(c)) designed to hold both an array of 16 SiPMs (Fig. 4.3(b)) or a multichannel PMT (Fig. 4.3(a)) manufactured by Hamamatsu (model H8711), which has been used for the preliminary tests. A few pictures of the calorimeter during the assembly are shown in Fig. 4.2.

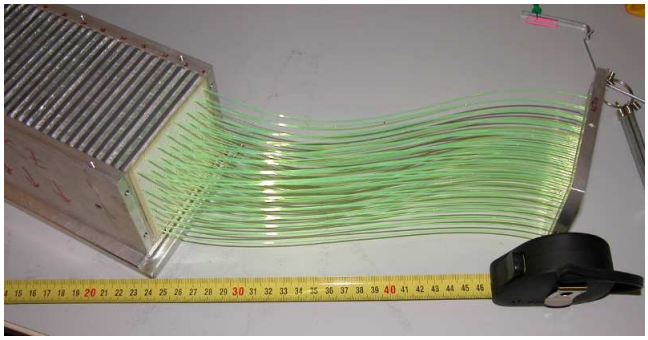

(a)

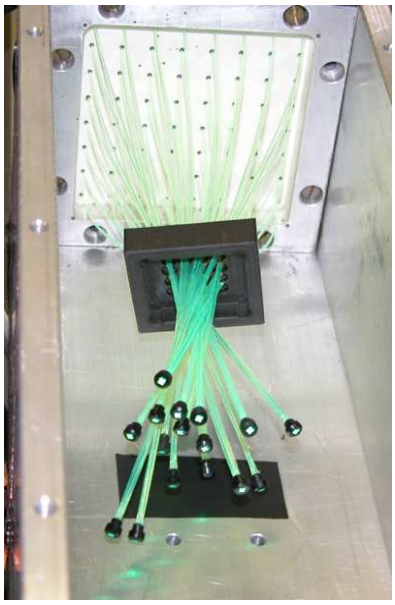

(b)

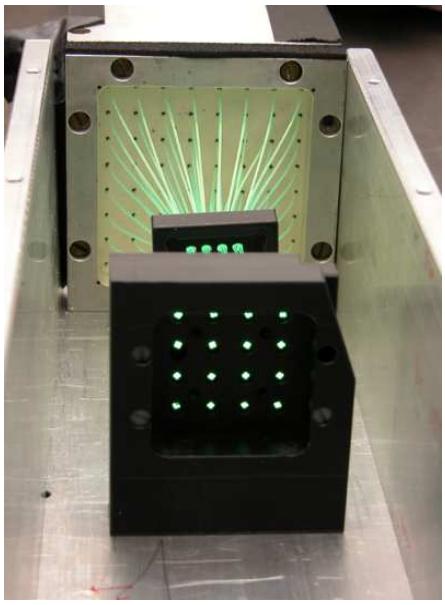

(c)

Figure 4.2: The calorimeter during the assembly phase: the fibers during the insertion inside the calorimeter tiles (a), grouped in bundles of four (b) and plugged into the SiPM plastic holder (c).

The SiPMs for the calorimeter readout have been manufactured by FBK-irst and have a sensitive area of $\sim$1 mm^2. These devices are the same ones used for

the scintillating bar tracker tests and consist of 688 40x40 μm^2 pixels arranged in a circular geometry and covered with an epoxy resin: their main characteristics are reported in Table 2.2.

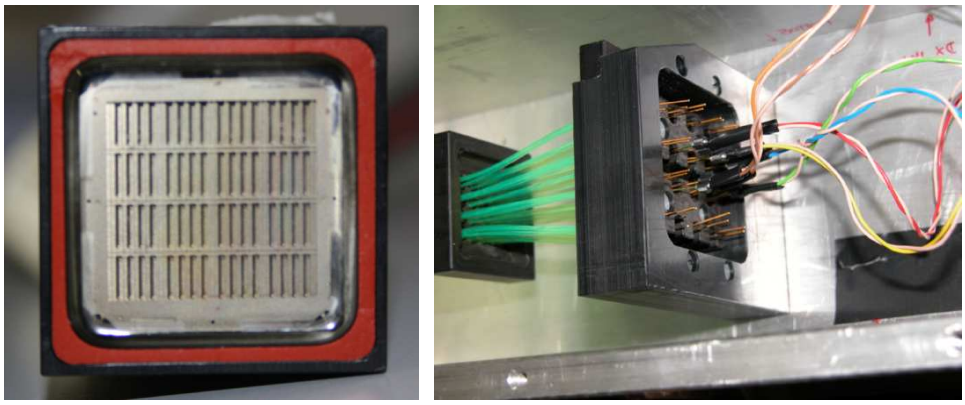

(a) (b)

Figure 4.3: Multianode PMT (a) and SiPMs array (b) used for the light readout.

The readout of the SiPMs has been performed using four custom boards (Fig. 4.4) (INFN Ts) each one managing four channels in parallel. The board also provides a single bias line for the four SiPMs. The power consumption of each SiPM has been estimated measuring its voltage drop on a 100 kΩ resistor.

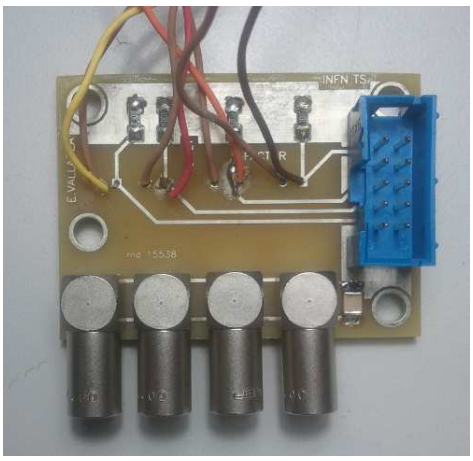

Figure 4.4: Custom SiPM board used for the bias and the readout of up to four SiPMs.

4.1.2 Experimental setups and DAQ

The shashlik calorimeter prototype 0 has been tested at CERN in two different experimental setups at high and low energies. In both the setups the output signal of the SiPMs is delayed by ∼140 ns and then sampled with a CAEN V792 12 bit QDC. The delay was necessary because some tens of ns are needed by the trigger board to generate the experiment trigger and send the gate signal to the V792 module (see Fig. 4.5). In both the tests the SiPMs have been divided into four groups according to their operating voltages and then biased using four different power supplies in order to equalize their gain as much as possible.

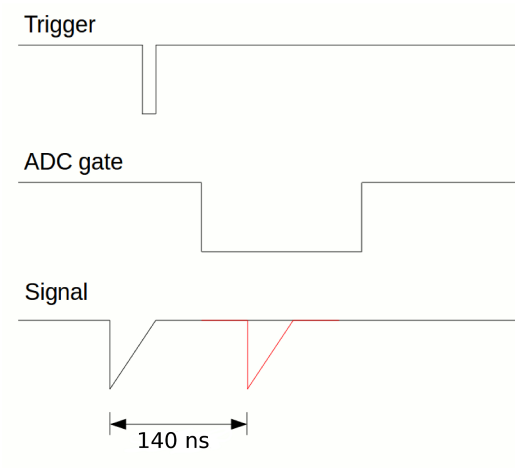

Figure 4.5: ADC timing: a signal delay of 140 ns is needed to be in time with the ADC gate.

4.1.2.1 Low Energy Setup

The low energy tests have been performed at the CERN PS T10 beamline in August 2009 with negative particles in a momentum range between 1.0 and 5.5 GeV/c. The T10 beamline shares part of the line and the primary target zone with the T9 beamline (described in section 3.1.1); thus the beam has similar features, but a lower maximum energy (7 GeV) and a lower intensity because of the larger bending of the beamline itself. The low energy setup consists of:

- a 10×10 cm^2 plastic scintillator for the trigger generation;
- a Cherenkov detector for the electron tagging;
- two silicon strip detectors for the track reconstruction (described in section 3.1.2.1);

- a remotely controlled movable platform, used to align the calorimeter with the particle beam.

A picture of the experimental setup and its DAQ scheme are shown in Fig. 4.6.

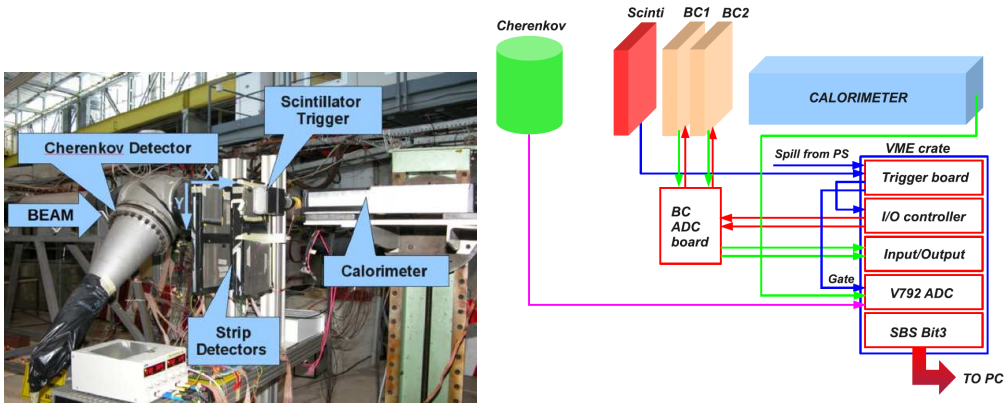

(a) (b)

Figure 4.6: The experimental setup (a) and the DAQ scheme (b) at the PS T10 beamline. The red arrows represent the configuration and control signals, while the blue and green arrows represent the detector outputs.

4.1.2.2 High Energy Setup - The H4 Beamline

The high energy tests have been performed at the CERN SPS H4 beamline in September 2009. The H4 beamline is located in the North Area experimental zone, that is the extraction point of the secondary beamlines of the SPS accelerator. The SPS primary beam (400 GeV protons) collides with a fixed target, producing secondary and tertiary beams which are then delivered to four extraction lines (H2-4-6-8). The typical beam structure features a single extraction spill with a duration of $\sim$6 s for each cycle: choosing the electron/positron operation mode an intensity of a few 10^4 particles per spill can be easily achieved; the maximum energy is 300 GeV while the momentum resolution $\Delta p/p$ is of the order of 1.4% [85]. A picture and a sketch of the North Area extraction beamlines are presented in Fig. 4.7.

The shashlik calorimeter prototype has been tested using a tagged photon beam obtained from the radiation emitted by 120 GeV positrons channeled in bent silicon crystals in the framework of the INSURAD experiment: more information on photon production by channeled positrons can be found in [87]. The experimental setup (Fig. 4.8) consists of:

- one plastic scintillator for the trigger (S1);

(a)

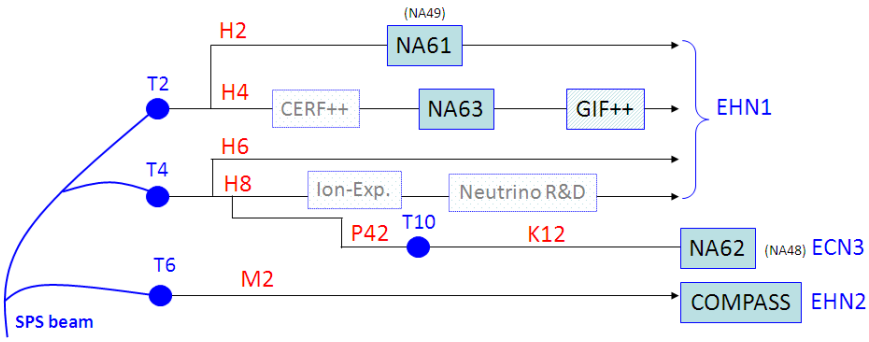

(b)

Figure 4.7: Picture (a) and sketch (b) of the North Area beamlines [86].

- three "high" resolution (6 μm) silicon strip detectors (SD1-3) [88] to identify the channeling effect by reconstructing the incoming particles deflection angle induced by the crystal;
- a 3.59 Tm magnet (BM) to separate the photon emitted in the crystal and the primary positron;
- a helium bag to reduce the multiple scattering (HB);
- two large area silicon strip detectors (BC1-2) to measure the deflection angle of the positron inside the magnet;
- two calorimeters: the first one is used to detect the photons (the calorimeter under test, indicated as WILLIE in the figure) and the second one (a scintillator-lead sampling calorimeter, indicated as DEVA) in the trigger to discriminate between positrons and minimum ionizing particles.

The photon is emitted in the silicon crystal and travels collinearly to the positron until the latter is deflected by the magnetic field; the positron energy is obtained

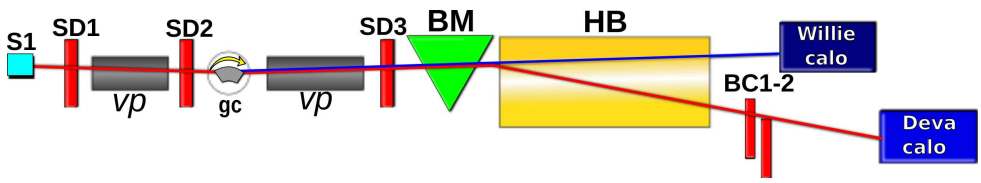

Figure 4.8: The experimental setup at the SPS H4 beamline: S1 is the scintillator used for the trigger, SD1-3 the three high resolution silicon strip detectors, *vp* the vacuum pipes, BM the bending magnet, HB the helium bag, BC1-2 the two silicon beam chambers and WILLIE and DEVA the two calorimeters.

with a spectrometer method by measuring its deflection angle. The energy of the photon is then computed by subtracting the deflected positron energy from its initial value (120 GeV). The DAQ system is a standard VME system controlled by a SBS Bit3 optically linked to a Linux PC-system: a sketch of the DAQ system is presented in Fig. 4.9.

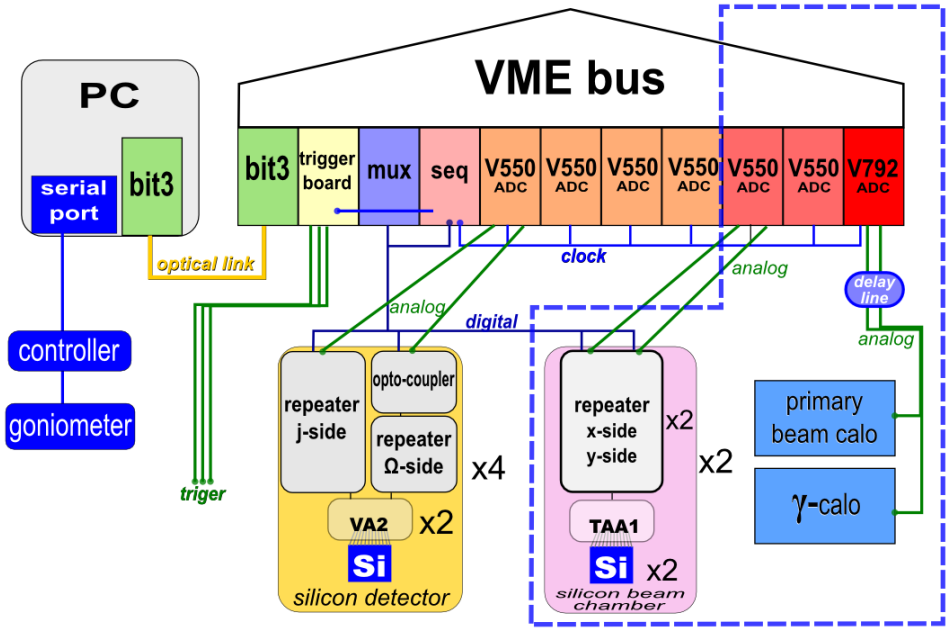

Figure 4.9: The DAQ chain for the high energy tests.

The trigger signals are generated by a combination of the scintillator and the primary beam calorimeter (DEVA) signals; they are discriminated by NIM discriminators and sent to the VME trigger board which is controlled by the DAQ program. This board allows to choose the trigger mode during the data taking. The resulting output trigger is sent to the sequencer (seq, INFN Ts) that starts the

DAQ sequence generating the ASIC control signals. Since the sequencer has a single output, a multiplexer (mux, INFN Ts) is used to cope with all the modules, that are readout in parallel. The interface between the frontend (the detector and the hybrid with the ASICs) and the readout (the VME board) is provided by the repeater boards that have to transform the RS422 differential signals to single ended ones as requested by the ASICs, to provide the bias, the power and the digital signals to the ASICs through 50 pin ERNI cables, to amplify the analog output of the hybrid. The multiplexed analog output of the repeaters is digitized by the flash ADC boards (CAEN V550), which work in zero suppression mode. The trigger board is also used to start the gate of the V792 module for the readout of both the calorimeters.

4.1.3 Calorimeter Performance Simulation with GEANT4

The high and low energy experimental setups have been simulated using the GEANT4 [89] simulation package in order to characterize the calorimeter in terms of linearity, energy resolution and energy leakage. The simulation takes into account the aluminum vessel which contains the scintillator and lead tiles, the holes drilled in the layers to insert the WLS fibers and the presence of the WLS fibers themselves (4.10). However, the simulation does not take into account the light production in the scintillator tiles and the WLS collection efficiency, so the results should be considered as a best estimate of the real calorimeter performance.

The physics list used to perform the simulation is the QGSP_BERT model[1], a composite model which uses the Quark Gluon String theory and the Precompound model for high energy hadron interactions (above 10 GeV), the Bertini cascade model for low energy (below 10 GeV) hadron interactions and the standard G4EmStandardPhysics list for the electromagnetic processes. The electromagnetic cuts on the secondary particles have been set to 10 μm: the GEANT4 kernel transforms the length cuts into different energy cuts according to the density of the different materials defined in the simulation. In order to define the energy linearity and resolution for the electrons, the histograms of the energy deposit at different energies in the scintillator tiles have been fitted with a Gaussian function in the [-1.5σ,3σ] range, as shown in Fig. 4.11: the resolution parameter is defined as the ratio of the sigma to mean value. Two types of beam have been generated: the first is a “point-like” beam impinging on the center of the tiles, while the second is “Gaussian-shaped” with σ=1.5 cm in both the horizontal and vertical directions.

As far as the low energy simulation is concerned, a monochromatic beam of 10000 electrons has been generated with an energy between 1 GeV and 6 GeV.

[1] GEANT4 physics lists *http://geant4.cern.ch/support/proc_mod_catalog/physics_lists/referencePL.shtml*

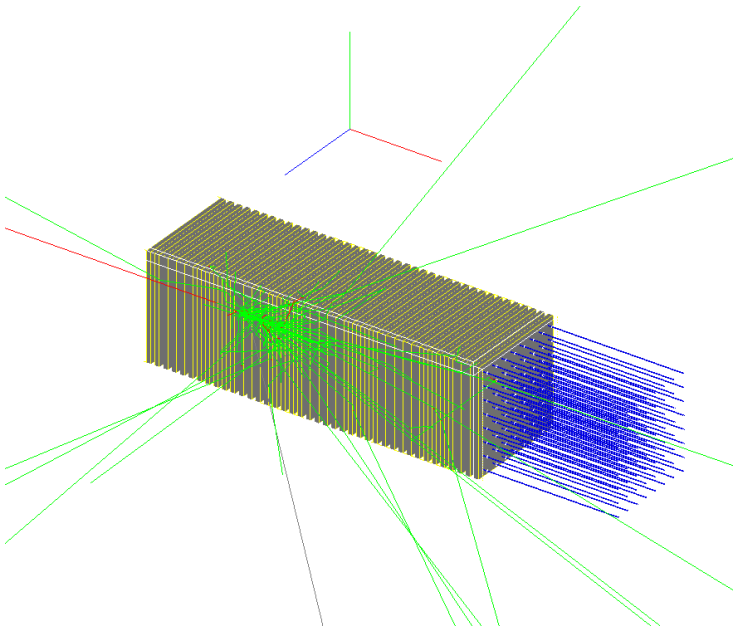

Figure 4.10: GEANT4 geometrical simulation of the prototype 0 shashlik calorimeter after an interaction with a 500 MeV electron: the electrons are depicted in red and the gammas in green.

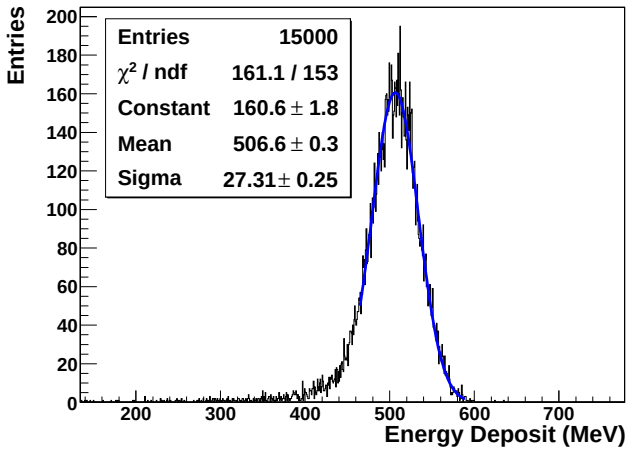

Figure 4.11: Gaussian fit in the [-1.5σ,3σ] range of the total energy deposit histogram for a 6 GeV simulated electron beam.

The resolution energy scan has been fitted using the function $\frac{\sigma_E}{E} = P_0 \oplus \frac{P_1}{\sqrt{E}}$, where the $\oplus$ indicates that the terms are added in quadrature. In this function P_0 represents the constant term, which parametrizes the detector non-uniformities and

imperfections and dominates at high energies, and P_1 represents the stochastic term which depends on the fluctuations related to the physical development of the shower. The results for electrons are presented in the plots in Fig. 4.12.

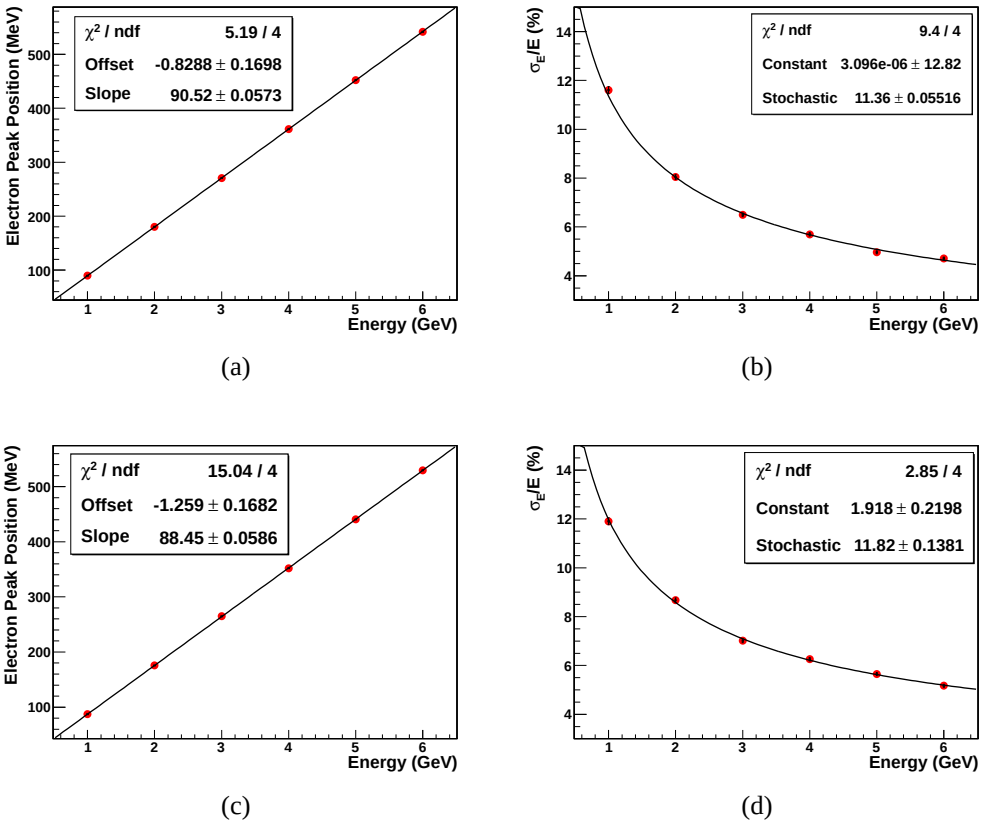

Figure 4.12: The linearity and the energy resolution plots in the low energy range using the "point-like" ((a) and (b)) and "Gaussian-shaped" ((c) and (d)) simulated beam.

Here and in the following, the uncertainty bars on the linearity plots are the fitted mean parameter errors of the Gaussian distribution. No significant deviations from linearity can be observed in the two beam-type configurations. As far as the energy resolution is concerned, in the "point-like" configuration a stochastic term of 11.36% with a very small (compatible with zero) constant term have been obtained, while in the "Gaussian-shaped" configuration a slightly larger stochastic term (11.8%) and a constant term of 1.9% have been measured. In particular, the increase of the constant term should be related to the increased leakage of the calorimeter in the "Gaussian-shaped" beam. The energy leakage of the calorimeter at low energies has been evaluated considering the energy deposit inside the

lead and scintillator tiles and subtracting it from the primary incident beam. In the low energy scan the leakage is practically independent from the energy and is equal to 8.0% and 9.0% of the incident particle energy in the "point-like" and "Gaussian-shaped" configuration respectively. These values seem consistent with the Molière radius of the calorimeter and explain the differences in the fitted stochastic and constant terms obtained in the two beam configurations.

The high energy setup has been simulated using a monochromatic beam of 10000 photons with an energy between 10 GeV and 120 GeV; also in this case two beam-types have been generated. The results of this simulation are shown in Figs. 4.13 and 4.14.

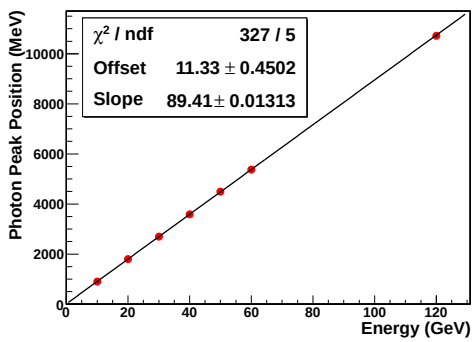

(a)

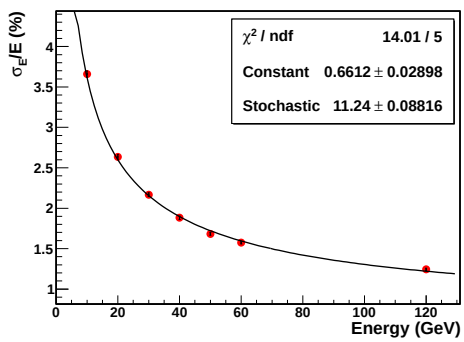

(b)

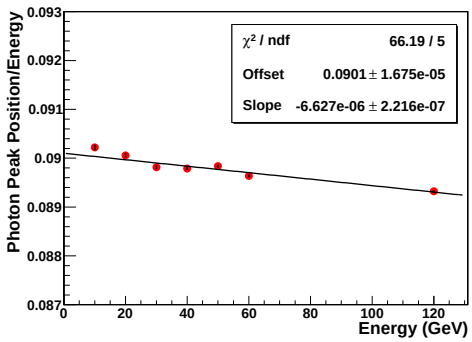

(c)

Figure 4.13: The linearity (a) and the energy resolution (a) plots in the high energy range using the "point-like" simulated beam. The plot in (c) is a "reduced" linearity plot to highlight the linearity deviations.

The linearity is good up to 120 GeV; however, due to the large energy range, these plots are weakly sensitive to the deviations induced by the increase of the energy leakage (as shown in Table 4.1). These deviations can be seen in the plots

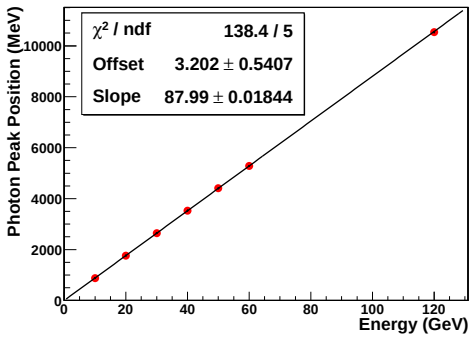

(a)

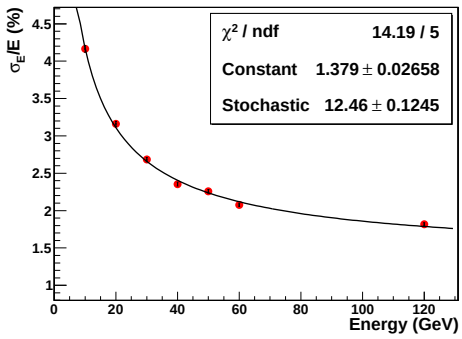

(b)

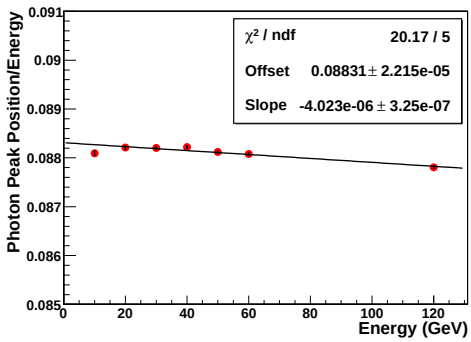

(c)

Figure 4.14: The linearity (a) and the energy resolution (a) plots in the high energy range using the "Gaussian-shaped" simulated beam. The plot in (c) is a "reduced" linearity plot to highlight the linearity deviations.

of Figs. 4.13(c) and 4.14(c), presenting the ratio between the deposited energy and the beam one; the large reduced χ^2 values of these plots can be due to an underestimation of the uncertainties, which are defined as the uncertainties of the linearity plots of Figs. 4.13(a) and 4.14(a) divided by the beam energy. However, it has to be noted that the slopes of the linear fits are of the order of 10^{-6}: this means that the deviations are of the order of $\sim$100 keV in an energy range which extends up to 100 GeV.

As far as the energy resolution is concerned, the stochastic term of the "point-like" beam (11.24%) is comparable within the uncertainties to the one obtained in the low energy scan. The constant term is indeed larger compared to the one of the low energy case (0.6% and 10^{-6}% respectively), due to the energy leakage from the rear of the calorimeter which becomes important at energies above 30 GeV (Fig. 4.15).

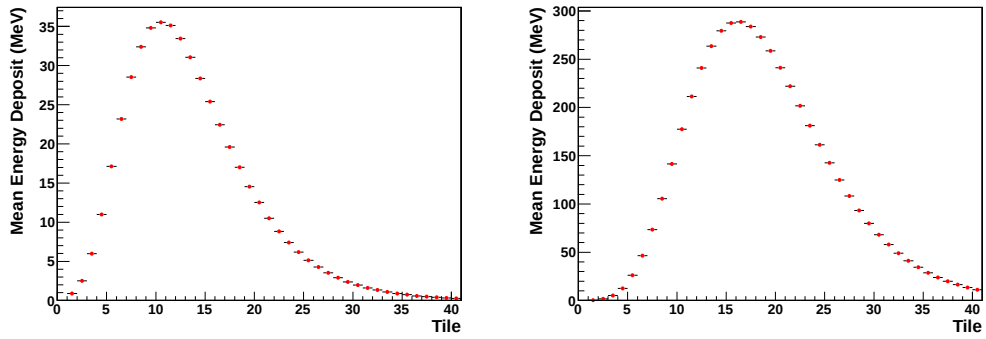

(a) (b)

Figure 4.15: Energy deposit profile as a function of the number of the scintillator tile at 6 GeV (a) and 60 GeV (b). At high energy the energy deposit in the last tiles becomes relevant, thus resulting in an increase of the energy leakage.

In the "Gaussian-type" configuration (Fig. 4.14(b)), the stochastic term is equal to 12.5% with a constant term of 1.4%, slightly different values with respect to the ones obtained in the low energy case (11.8% and 1.9% respectively). It is possible to improve the energy resolution fitting procedure merging the low and high energy datasets: the results for the "point-like" and "Gaussian-shaped" beam-types are shown in Fig. 4.16.

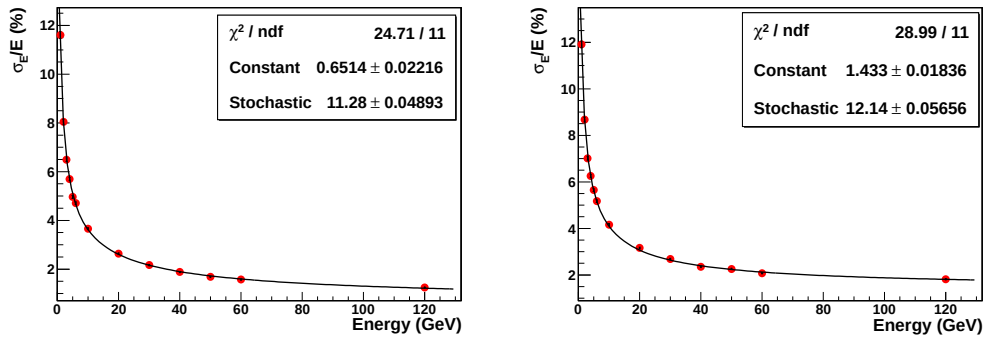

(a) (b)

Figure 4.16: Energy resolution with the complete dataset in the "point-like" (a) and "Gaussian-shaped" (b) configurations.

Using the complete dataset no big differences with respect to the previous fits can be seen in the "point-like" configuration, while in the "Gaussian-shaped" one the constant and stochastic terms level-off to the values of 12.1% and 1.4%, which will be considered as the reference value for the calorimeter performance.

The energy leakage at high energies has been evaluated with the same procedure used for the low energy case, subtracting the scintillator and lead energy deposit from the incident beam energy; the results are shown in Table 4.1.

Beam energy (GeV)	Point-like	Gaussian-shaped
10	8.18%	9.20%
20	8.31%	9.21%
30	8.39%	9.27%
40	8.51%	9.33%
50	8.54%	9.38%
60	8.63%	9.48%
120	8.86%	9.81%

Table 4.1: Energy leakage of the calorimeter at high energy as a function of the incident particle energy with the two beam configurations.

The fraction of energy leaking from the calorimeter can be considered substantially constant as a function of the incident particle energy, with an increase of 0.5% between 10 and 120 GeV.

4.1.4 Low Energy Results

4.1.4.1 Linearity and energy resolution

The calorimeter has been characterized in terms of linearity and energy resolution with low energy electrons. The first event selection is performed using the information provided by the silicon strip detectors, selecting only the single track events. The Cherenkov detector has been used to discriminate between the electrons and the other particles (typically muons and pions). In the first phase the 16 channels MAPMT has been used for the readout of the calorimeter. In both the MAPMT and SiPM readout, the total energy deposit information is obtained summing together the 16 channels of the calorimeter after applying an equalization procedure to the different channels. The pads of the MAPMT have been equalized using a dedicated minimum ionizing particle beam impinging on the front of the calorimeter. The signal of each pad has been fitted with a Landau function and the signal peak positions have been normalized according to a reference channel. As far as the SiPMs are concerned, two different equalizations have been performed:

- hardware equalization: it consists in the equalization of the SiPMs dark current biasing the devices at different voltages, using four different power supplies as reported in Table 4.2;

- software equalization: it has been performed using a dedicated minimum ionizing particle beam as in the MAPMT case.

Group	1 μA	1.5 μA	2 μA
1	34.88 V	35.30 V	35.90 V
2	35.32 V	35.83 V	36.80 V
3	35.10 V	35.64 V	36.60 V
4	35.0 V	35.40 V	36.00 V

Table 4.2: Bias values for the four SiPMs groups in the three current configurations.

An example of the software equalization performed on the pulse height of a pad of the MAPMT and of a SiPM is presented in Fig. 4.17.

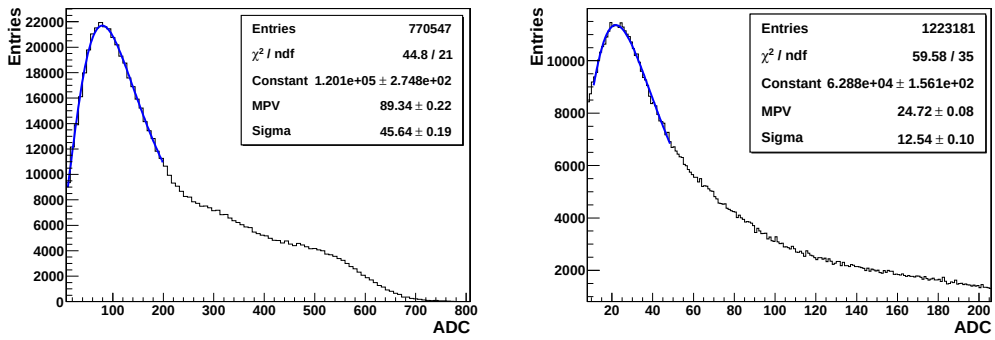

(a) (b)

Figure 4.17: MIP pulse height of a MAPMT pad (a) and of a SiPM (b) with the Landau fit superimposed.

Fig. 4.18(a) presents the total energy deposit inside the calorimeter for a 2 GeV beam. Three main regions can be observed: the first peak (at low ADC values) corresponds to the minimum ionizing particle energy deposit, while the last peak (at large ADC values) is due to the electron interactions. The intermediate energy deposit region between the two peaks is due to the hadronic showers (started by pions). The number of electron events, calculated as the integral of the electron peak (Fig. 4.18(b)), decreases with the beam energy, requiring longer runs to acquire enough statistics at energies above 4 GeV. All the calorimeter data have been collected using the T6 target, composed of a high Z material to enhance the electron percentage.

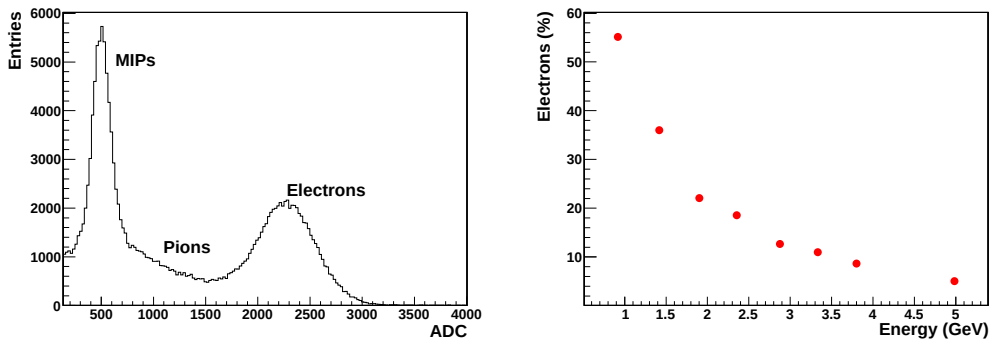

(a) (b)

Figure 4.18: Total energy deposit inside the calorimeter at 2 GeV (a) and electrons abundance (b) as a function of the beam energy with the T6 target.

Considering the dimensions of the calorimeter compared with its Molière radius, a second selection is performed on the electron events in order to select only the events impinging on a "fiducial area" of 3x3 cm^2 in the central part of the calorimeter. This selection is fundamental to reject the events with a high energy leakage which can artificially worsen the energy resolution measurement. The scatter plots showing the fiducial area selection as a function of the beam position and energy deposit are presented in Fig. 4.19.

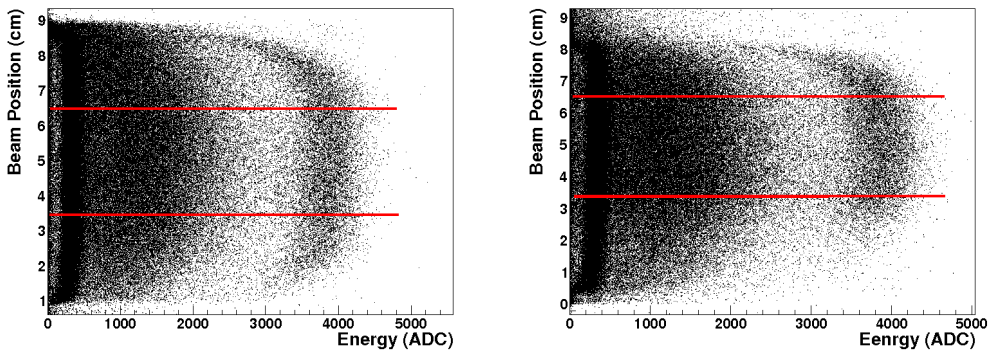

(a) (b)

Figure 4.19: Scatter plot of the fiducial area selection in the x (a) and y (b) beam directions.

After the selections, the electron peak has been fitted with a Gaussian function in the [-σ,3σ] range (Fig. 4.20) and the resolution value has been obtained dividing the sigma by the mean parameter. In order to estimate the systematic error

due to the beam momentum spread, given that a 1% Δp/p for each 5 mm collimators opening is expected [90] and that the beamline was operated with at least a 10 mm slit opening, a 2% uncertainty on the fitted mean value has been added in quadrature to the parameter fit error in the linearity plot.

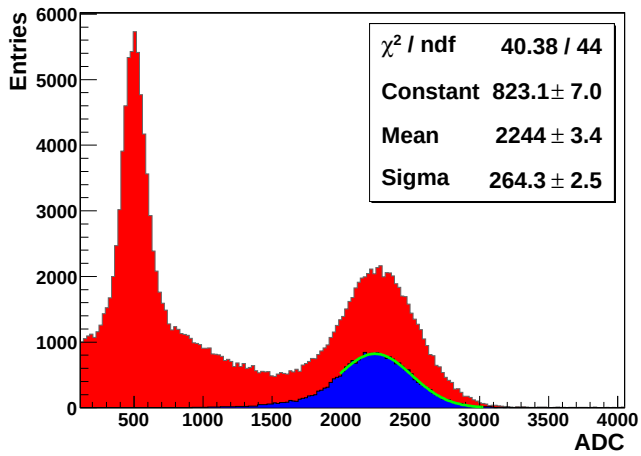

Figure 4.20: Total (red) and selected electron events (blue). The selected electron peak is fitted with a Gaussian function in the [-σ,3σ] range.

The preliminary low energy runs were performed using the multichannel PMT in order to setup the beamline and to have a comparison for the SiPM runs. The energy resolution scan has been fitted with the same function used to fit the GEANT4 simulated data: the linearity and energy resolution results are shown in Fig. 4.21.

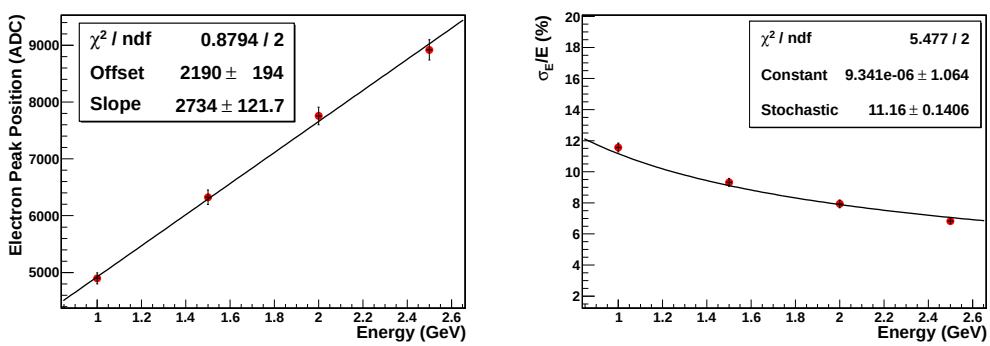

(a) (b)

Figure 4.21: Prototype 0 linearity (a) and energy resolution (b) with the MAPMT readout.

The linearity is good and the fit to the energy resolution gives a stochastic term of 11.2% and a very small constant term. The stochastic term is very similar to the one obtained in the "point-like" simulation: this is probably due to the fact that only a very limited number of energy points (and all below 2.5 GeV) have been used for the PMT scan.

As far as the SiPM runs are concerned, three different energy scans have been performed using three different bias currents (2, 1.5 and 1 μA). The bias values used for the hardware equalization of the four groups are shown in Table 4.2. The power consumption is monitored at the end of each run. According to [69], these bias values should correspond to gains of the order of 2–4$\times 10^6$. During the assembly phase, one of the SiPMs was damaged, thus only 15 channels were available: the missing SiPM corresponds to channel 1 in the sketch in Fig. 4.1(a).

The SiPMs have been operated at ambient temperature and thus they were sensitive to temperature variations during the run, which modified the gain of the devices. Considering the temperature coefficient of the FBK-irst SiPMs (65 mV/°C), the runs more affected by the gain variations are the ones with a low overvoltage. An example of the gain drifting as a function of the number of event in the run (*i.e.* the time) is presented in Fig. 4.22(a).

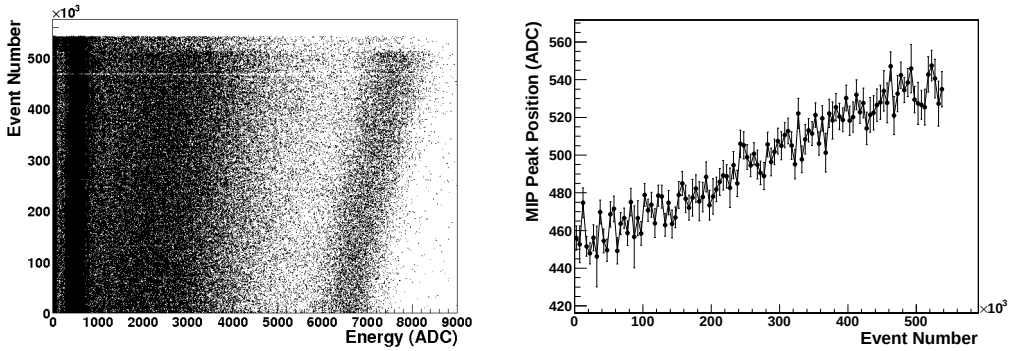

(a) (b)

Figure 4.22: Drifting of the electron and MIP peaks due to the SiPM gain variations during the run (a) and plot of the MIP peak position as a function of the event number (b) which has been used to correct the energy deposit.

In order to correct the gain drifting, the signal of the MIPs impinging on the fiducial area of the calorimeter has been used as a reference "candle", taking advantage from the fact that their signal is practically independent from the beam energy. The MIP peak position has been sampled as a function of the event number in steps of 5000 events, as shown in Fig. 4.22(b). The energy deposit has then

been corrected event by event using the following formula:

$$E_{line} = E \times \frac{A}{Peak_{(evNumber)}} \tag{4.1}$$

where E_{line} is the linearized energy deposit, E is the total deposited energy, A is a normalization constant (the MIP peak position in a reference run) and $Peak_{(evNumber)}$ is the position of the MIP peak as a function of the event number. A linear interpolation between the points of the MIP drift plot has been used for the intermediate event numbers. Fig. 4.23 presents the result of the linearization procedure on the same data of Fig. 4.22(a).

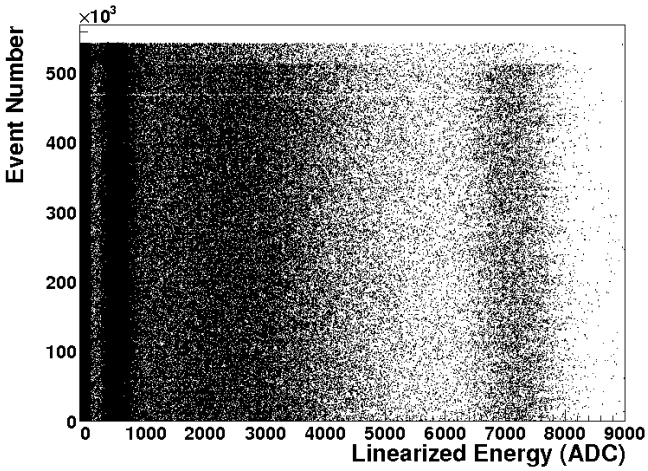

Figure 4.23: Linearization using the MIP correction procedure.

The results in terms of linearity and energy resolution with the three different SiPM bias currents are presented in Figs. 4.24 and 4.25.

The energy resolution scan has been fitted with the function $\frac{\sigma_E}{E} = P_0 \oplus \frac{P_1}{\sqrt{E}} \oplus \frac{P_2}{E}$, where the P_2 term takes into account the electronic noise contribution (see section A.5) and dominates the energy resolution at low energy. The value of the P_2 parameter has been fixed in the fit as the sigma value of the pedestal peak (Fig. 4.26) divided by the ADC value of the 1 GeV electron peak:

$$P_2 = \sigma_{noise}(ADC)/E_{1\ GeV}(ADC) \times 100 \tag{4.2}$$

In all the configurations the P2 parameter has been found to be equal to ∼1.25%.

Thanks to the energy linearization procedure, good results have been obtained with the 2 and 1.5 μA runs, with a slightly worse linearity (in terms of χ^2/ndf) in the 1 μA configuration. This effect is consistent with the fact that the temperature drift becomes more relevant in the low bias current configuration, thus the

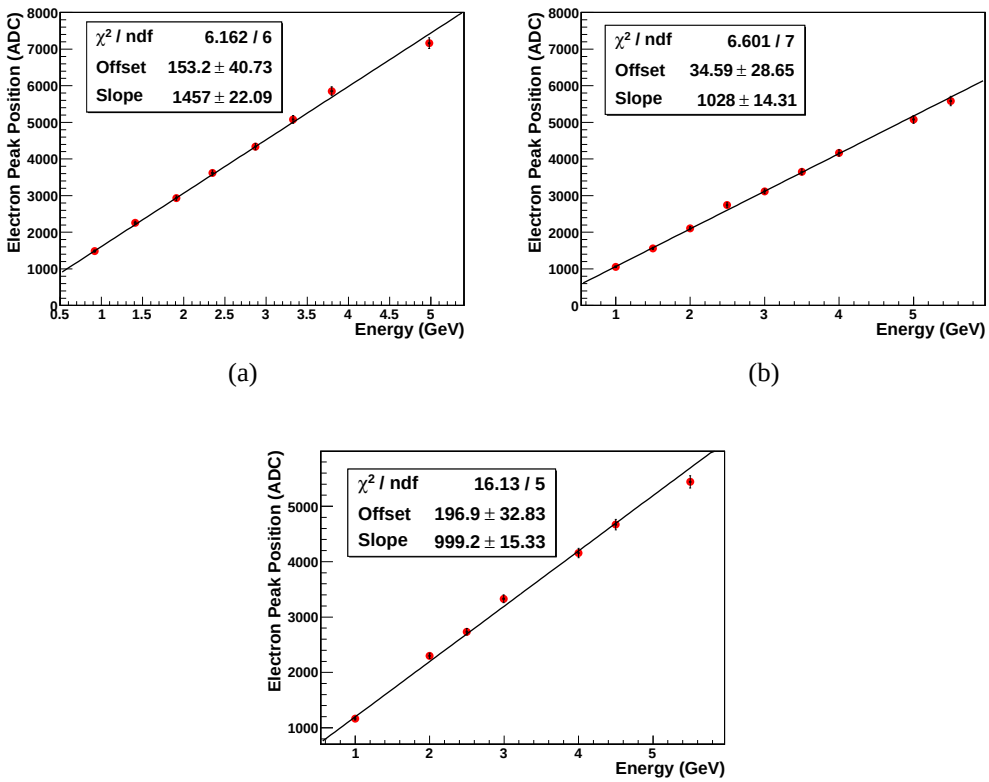

Figure 4.24: SiPMs energy linearity in the 2 (a), 1.5 (b) and 1 μA (c) bias current configurations.

MIPs correction algorithm can be less effective. As far as the energy resolution is concerned, stochastic terms between 13.3 and 14.2% have been obtained, with constant terms comparable with zero in all the configurations. This means that the SiPMs readout behaves slightly worse than expected considering the results of the GEANT4 simulation and the MAPMT tests. Several factors can be taken into account to explain this discrepancy:

- residual non-uniformities in the SiPMs gains even after the hardware and software equalization;
- non-optimal correction of the gain drifting due to temperature variations (this problem can be overcome using a LED system instead of the MIPs peak position, as performed in the prototype 1 calorimeter tests described in section 5.3);
- fluctuations in the light collection due to the fact that the area covered by the

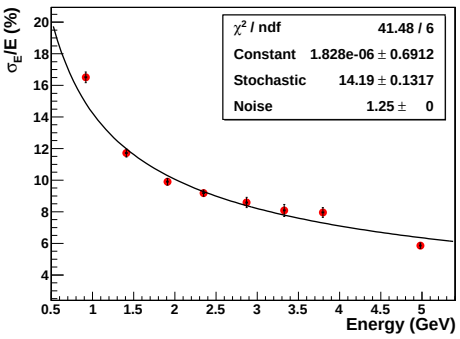

(a)

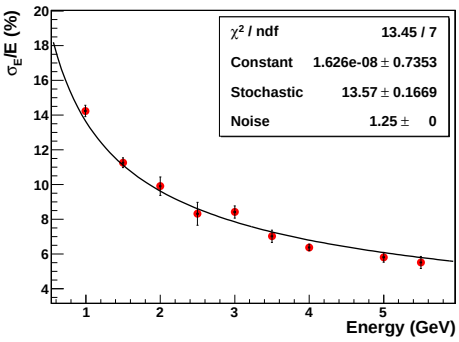

(b)

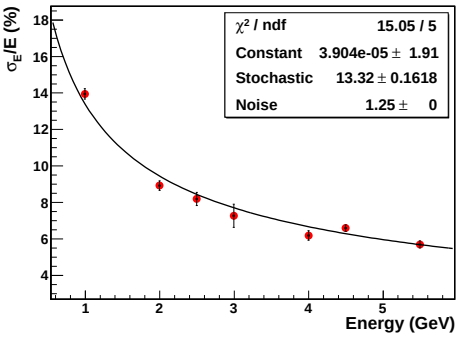

(c)

Figure 4.25: SiPM energy resolution in the 2 (a), 1.5 (b) and 1 μA (c) bias current configurations.

four WLS fibers is larger than the sensitive area of the SiPMs; this problem can be overcome using larger area SiPMs.

4.1.5 Spatial resolution

Exploiting the fact that the calorimeter has a segmented readout in the x-y direction, an analysis has been performed in order to understand the calorimeter capability to reconstruct the hit position. The analysis is based on the logarithmic barycenter algorithm described in [91], which takes into account the exponential radial falloff of the shower. The output channels have been divided into x and y

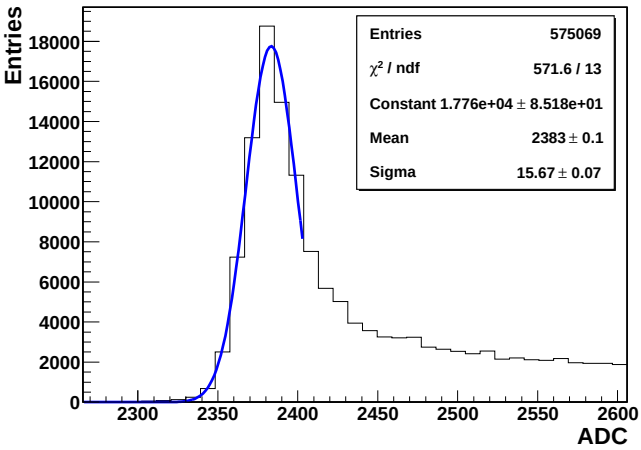

Figure 4.26: Pedestal distribution of the prototype 0 calorimeter fitted with a Gaussian function. The σ value is used to fix the noise parameter in the energy resolution fit. The tail on the right is due to low signal events mis-tagged as noise events.

planes according to the following relations:

$$Layer_{1X} = ([1]+[5]+[9]+[13]) \qquad Layer_{1Y} = ([1]+[2]+[3]+[4])$$
$$Layer_{2X} = ([2]+[6]+[10]+[14]) \qquad Layer_{2Y} = ([5]+[6]+[7]+[8])$$
$$Layer_{3X} = ([3]+[7]+[11]+[15]) \qquad Layer_{3Y} = ([9]+[10]+[11]+[12])$$
$$Layer_{4X} = ([4]+[8]+[12]+[16]) \qquad Layer_{4Y} = ([13]+[14]+[15]+[16])$$

The channel number is indicated in Fig. 4.27 together with the x-y directions. The missing SiPM channel ([1]) pulse height has been assigned using the mean of the three adjacent channels ([2],[5],[6]).

To estimate the coordinate of the incident particle, the center of gravity has been computed using the following equation:

$$X_{calc} = \frac{\sum_i w_i x_i}{\sum_i w_i} \tag{4.3}$$

where the x_i are the x or y coordinates of the center of the planes and the w_i are weight factors calculated using the relation:

$$w_i = Max\left\{0, \left[w_0 + \ln\frac{E_i}{E_{tot}}\right]\right\} \tag{4.4}$$

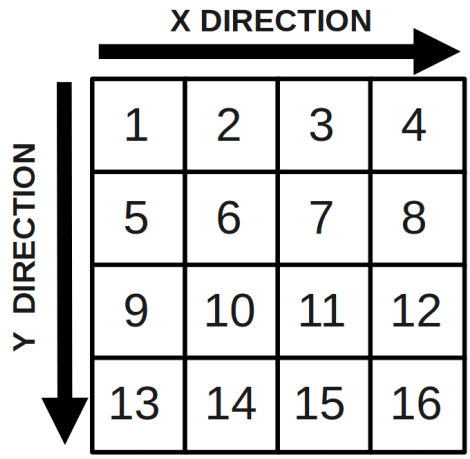

Figure 4.27: Calorimeter channel division.

where E_i is the energy deposited in each plane, E_{tot} is the total energy measured by the calorimeter and w_0 is a free and dimensionless parameter with a twofold function: to define a threshold for the inclusion of a plane in the coordinate calculation and to set the relative importance of the tails of the shower. The spatial resolution of the calorimeter has been computed using the residuals, that is the difference between the hit position obtained by the silicon chambers and the one reconstructed by the calorimeter itself. The results obtained using 1.5 GeV electrons are presented in Figs. 4.28 and 4.29 for the MAPMT and SiPM readout respectively. The w_0 parameter was chosen after a scan over the residual values, selecting the minimum residual and it has been set to 1.75 for the PMT run and to 1.9 for the SiPM run.

The resolution obtained for the PMT readout is very good, of the order of 0.45 cm both in the x and y directions; as far as the SiPM readout is concerned, the results are even better, probably due to the complete absence of optical crosstalk between the channels, with a resolution of the order of 0.4 cm in both the x and y directions. Fig. 4.30 summarizes the spatial resolution for different energies for both the MAPMT and SiPM readout. The spatial resolution improves with the beam energy, reaching an asymptote at $\sim$2 mm (visible only in the SiPM run) due to the finite readout pitch of the calorimeter.

4.1.6 High Energy Results

Also in the high energy tests the calorimeter has been characterized in terms of linearity and energy resolution. Unfortunately, due to time schedule problems, the tests have been performed using only the SiPM readout configuration with a bias

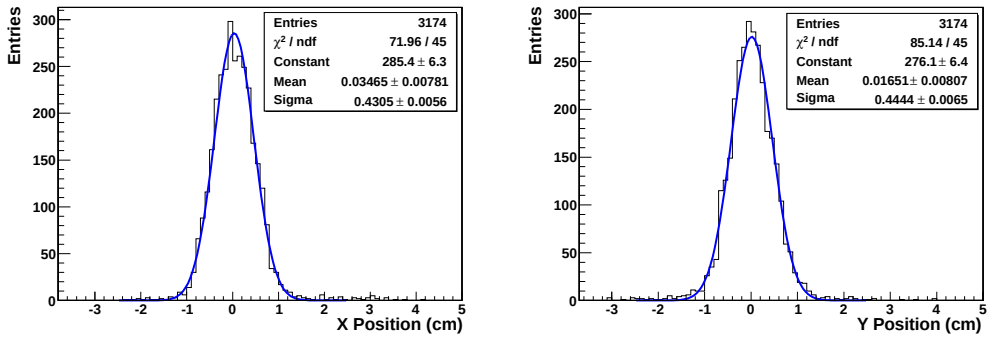

(a) (b)

Figure 4.28: Fit to the x (a) and y (b) spatial resolution plot obtained with the residuals method using a w_0 value of 1.75 and the MAPMT readout.

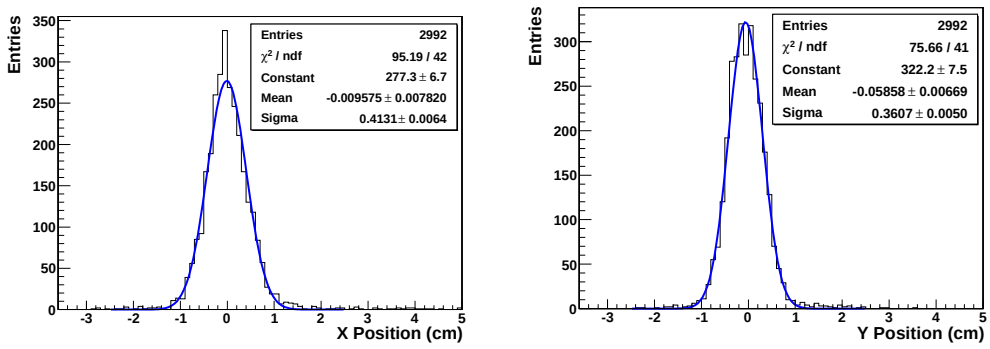

(a) (b)

Figure 4.29: Fit to the x (a) and y (b) spatial resolution plot obtained with the residuals method using a w_0 value of 1.9 and the SiPM readout.

current of the order of 1.5 μA. As in the low energy tests, the first event selection considers only the single track events using the information provided by the silicon strip detectors. The energy of the photon emitted inside the crystal is obtained by measuring the deflection angle of the positron after the 3.59 Tm magnet, knowing the energy of the incident beam. The energy spectrum of the positrons is shown in Fig. 4.31: the 120 GeV peak is fitted with a Gaussian function to obtain the energy resolution of the spectrometer, which is $\sim$390 MeV at this energy.

The output channels of the calorimeter are calibrated and summed together to obtain the total energy deposit; a scatter plot is then filled with the total energy deposit value and the tagged photon energy value. The plot is sliced along the calorimeter energy direction with a step of 1 GeV and each slice is fitted with

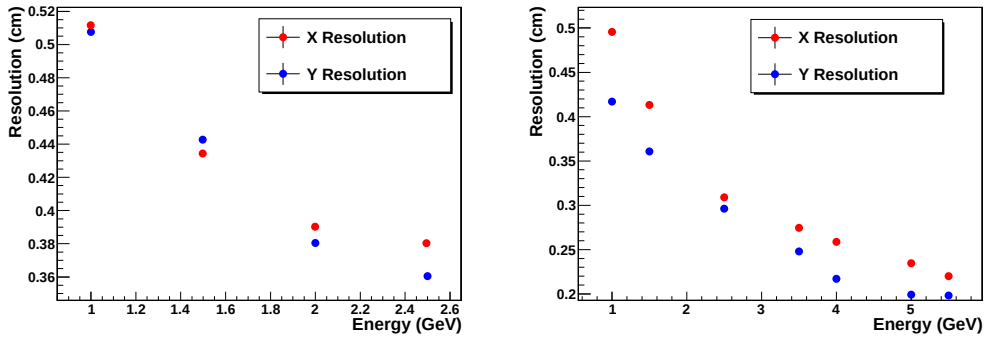

(a) (b)

Figure 4.30: Energy dependence of the calorimeter spatial resolution for the MAPMT (a) and SiPM (b) readout.

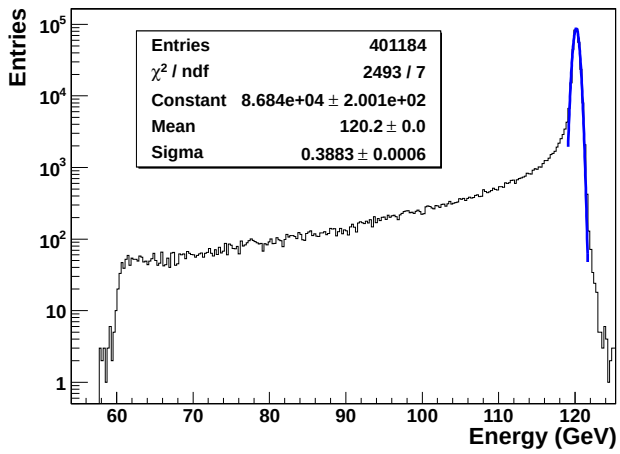

Figure 4.31: Energy spectrum measured with the magnetic spectrometer and Gaussian fit of the 120 GeV peak.

a Gaussian function in order to obtain the mean and resolution parameters. An example of the scatter plot and a slice (the 20 GeV one) fitted with the Gaussian function are shown in Fig. 4.32.

On the contrary of the low energy tests, the particular setup used for the high energy ones did not allow to correct the gain drifting of the SiPMs using MIPs. MIPs in fact were deflected by the magnetic spectrometer in the middle of the beamline and did not impinge on the calorimeter.

The results obtained in terms of linearity and energy resolution are shown in Fig. 4.33. The 120 GeV point has been measured in a dedicated run with the

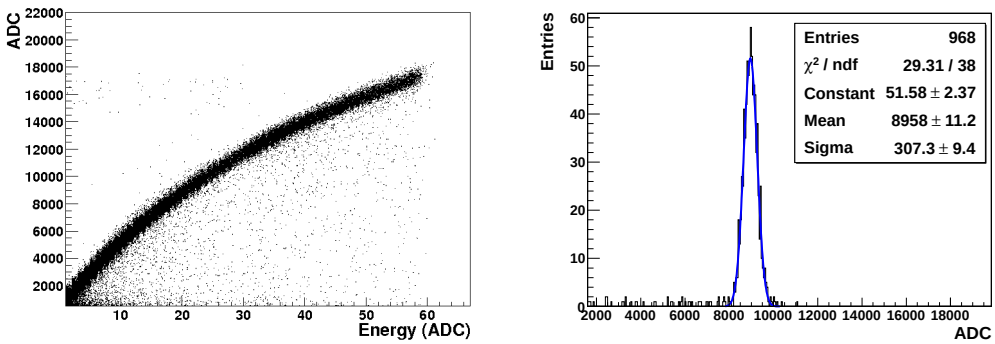

(a) (b)

Figure 4.32: Scatter plot of the photon energy measured with the calorimeter (vertical axis) and with the magnetic spectrometer (horizontal axis) (a) and 20 GeV slice of the photon energy scatter plot fitted with a Gaussian function (b).

magnet switched off and the positron beam impinging directly on the calorimeter.

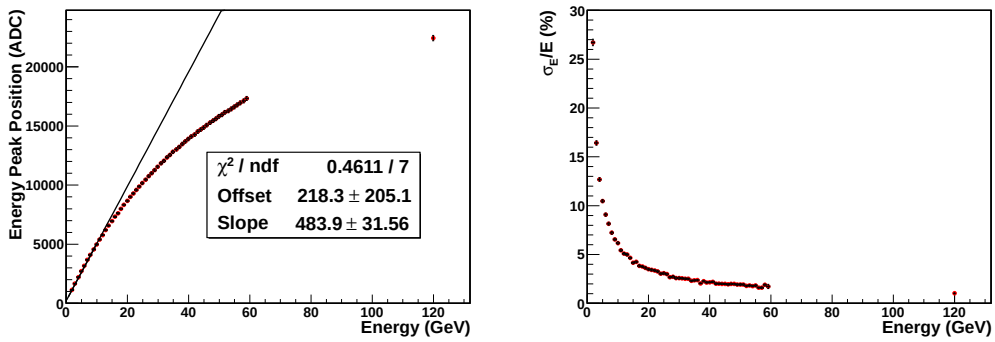

(a) (b)

Figure 4.33: Energy linearity (a) and resolution (b) obtained in the high energy test. In the (a) plot the linear fit in the 1–10 GeV range is depicted.

As can be seen looking at the dashed line in Fig 4.33(a), the linearity is good up to 10 GeV, but at higher energies a clear saturation effect is present. The saturation effect is due to the relatively small number of pixels in the 1 mm^2 SiPMs compared to the large photon flux at this energy. Better results can in principle be obtained using a larger area SiPM. No fit has been performed to the energy resolution scan in the saturated configuration. As in the low energy runs, the beam momentum uncertainty was taken into account by adding in quadrature to the parameter fit error the expected momentum resolution at the H4 beamline (1% of the fitted mean value). To correct for the non linearity of the SiPMs, a

calibration has been performed inverting the plot in Fig. 4.33(a) and fitting it with a 4th degree polynomial, as shown in Fig. 4.34(a). The parameters of the fit have then been used to convert the ADC counts into a linearized energy scale expressed in GeV, as shown in Fig. 4.34(b).

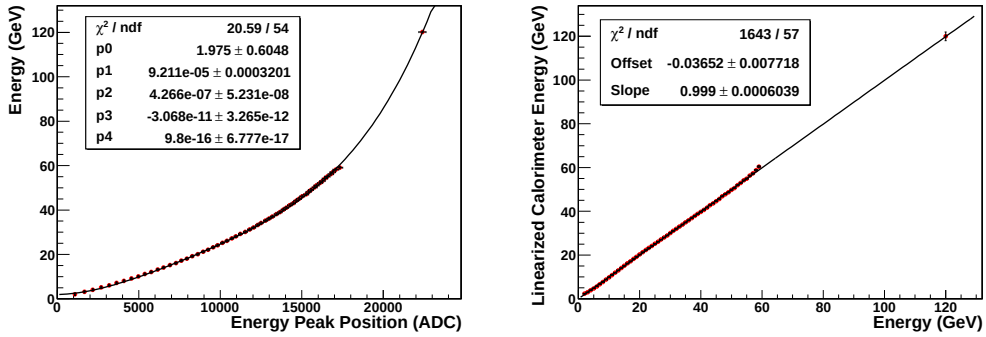

(a) (b)

Figure 4.34: Inverted energy linearity fitted with a 4th degree polynomial function (a) and linear fit (b) to the calibrated high energy linearity plot.

In order to compare the results obtained in the low energy region with electrons and photons, the same slicing procedure (with a 100 MeV step) has been applied to select only photons with an energy up to 10 GeV: the results in terms of linearity and energy resolution are presented in Fig. 4.35. On the contrary of the low energy tests, the noise term (P_2) has not been fixed in the fit in order to evaluate the contribution of the magnetic spectrometer to the calorimeter energy resolution.

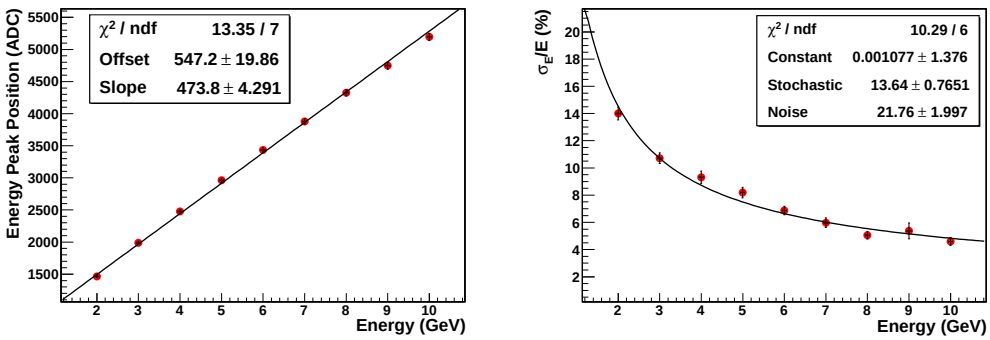

(a) (b)

Figure 4.35: Energy linearity (a) and resolution (b) using only tagged photons with an energy up to 10 GeV.

As anticipated, the linearity is verified up to 10 GeV, and the fit of the energy resolution converges to a stochastic term of 13.6% and a noise term of 22.0% which corresponds to a spectrometer resolution of 220 MeV at 1 GeV. These results are compatible with the stochastic terms obtained in the low energy scans and with the spectrometer energy resolution measured at 120 GeV ($\sim$390 MeV).

4.2 The 2010 CERN Beamtest

In winter 2010 the prototype 0 calorimeter has been tested in a new beamtest performed at CERN on the T9 beamline (section 3.1.1). The aim of the test was to evaluate the performance of the calorimeter with a first version of the MAROC3 readout system. The main advantages of this type of readout are the signal conditioning of the SiPM output (shaping and amplification) and the fact that no more delay lines are needed for the SiPM readout. The beamtest has been performed on the T9 beamline with electrons up to 6 GeV, using the same SiPMs of the 2009 tests.

4.2.1 Experimental Setup

The setup is very similar to the one used on the T10 line in 2009 (section 4.1.2.1) and consists of:

- two Cherenkov detectors for the electron tagging;
- two silicon strip chambers for the track reconstruction;
- a 10×10 cm^2 plastic scintillator for the trigger.

The readout and the bias of the SiPMs have been performed with the custom boards used for the 2009 tests (Fig. 4.4). The output signals were then sampled by the MAROC board (section 3.2.1.1) instead of using the V792 QDC. While for the V792 readout a gate signal is needed to integrate the total charge, with the MAROC readout only the peak of the signal is sampled. Setting the analog shaper to have the slowest possible peaking time (120 ns), there is time enough for the trigger board to generate the trigger signal. The sampling of the signal peak can then be tuned using different values of the hold parameter, which has been set to 20 ns during the prototype 0 test. The output signals of the SiPM board are then connected to the inputs of the MAROC one using custom LEMO cables (Fig. 4.36): the advantage of this approach is the easy implementation, while the drawback is the use of long cables which increase the electromagnetic noise which in turn increases the RMS value of the pedestal distribution (Fig. 4.37).

Figure 4.36: The custom LEMO cables used to connect the SiPM output signal to the MAROC input pins.

The overall result is an increased noise term in the energy resolution with respect to the 2009 test: the typical sigma value of the noise distribution was ∼15 ADC with the QDC readout (Fig. 4.26), while it is ∼115 ADC with the MAROC one (Fig. 4.37). As will be shown in the following, the enlarged noise component is only partially due to the use of the LEMO cables, and directly depends on the MAROC readout itself.

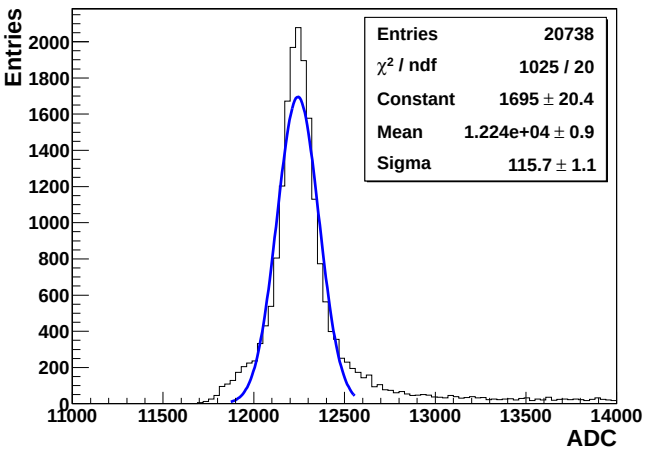

Figure 4.37: Pedestal distribution fitted with a Gaussian function. The σ value is used as a fixed parameter in the energy resolution fit.

4.2.2 Results

The performance of the prototype 0 calorimeter with the MAROC readout has been tested in terms of linearity, energy and spatial resolution. Three configurations of the MAROC pre-amplifier gain (15,10 and 5) and two values of the SiPMs bias currents (1.2 and 0.5 μA) have been used, for a total of four different energy scans. As in the 2009 beamtest, two types of equalization have been performed: the hardware one, using four different power supplies to bias the SiPMs (Table 4.3) and a software one, using a MIP beam impinging on the calorimeter to equalize the gain of the different devices. The devices were monitored in terms of current and voltage during the run using a digital multimeter (Keithley K2700), readout via a GPIB interface.

Group	1.2 μA	0.5 μA
1	35.0 V	34.2 V
2	35.52 V	34.5 V
3	36.0 V	33.7 V
4	34.0 V	32.7 V

Table 4.3: Bias values for the four SiPMs groups in the two current configurations.

The gain variations due to the temperature drift during the run have been corrected using the same approach of the 2009 beamtest, based on the MIPs signal. Since the MAROC unitary gain corresponds to a setting of 64 (section 3.2.1.1), the values of 5, 10 and 15 used for the tests correspond to an attenuation of the SiPM signal which is necessary to avoid the saturation of the conditioning stages (shaper and pre-buffer). As in the 2009 test, the event selection is performed choosing only the single track events impinging on a 3x3 cm^2 fiducial area (Fig. 4.38).

After the selection, the electron peak has been fitted with a Gaussian function in the [-σ,3σ] range and the resolution value has been obtained dividing the sigma by the mean parameter. The beam momentum spread contribution is included in the linearity plot adding in quadrature the 2% of the mean fitted value to the mean parameter error. The results obtained in terms of linearity and energy resolution are shown in Figs. 4.39 and 4.40.

As far as the linearity is concerned, a small saturation effect is present in the maximum gain scan as shown in Fig. 4.39(c). The saturation is due to a single SiPM channel (Fig. 4.41), positioned in the center of the calorimeter, characterized by a large gain which saturates the MAROC ASIC at 5 GeV (and also at 4 GeV).

Given that a potential ADC saturation should be located at $\sim$3300 ADC (considering the 12 bits dynamic range and the pedestal position at $\sim$750 ADC), the

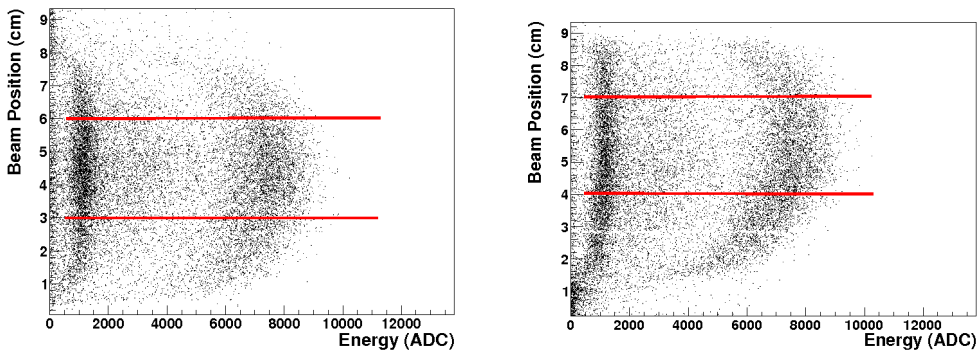

(a) (b)

Figure 4.38: Scatter plot of the fiducial area selection in the x (a) and y (b) beam directions.

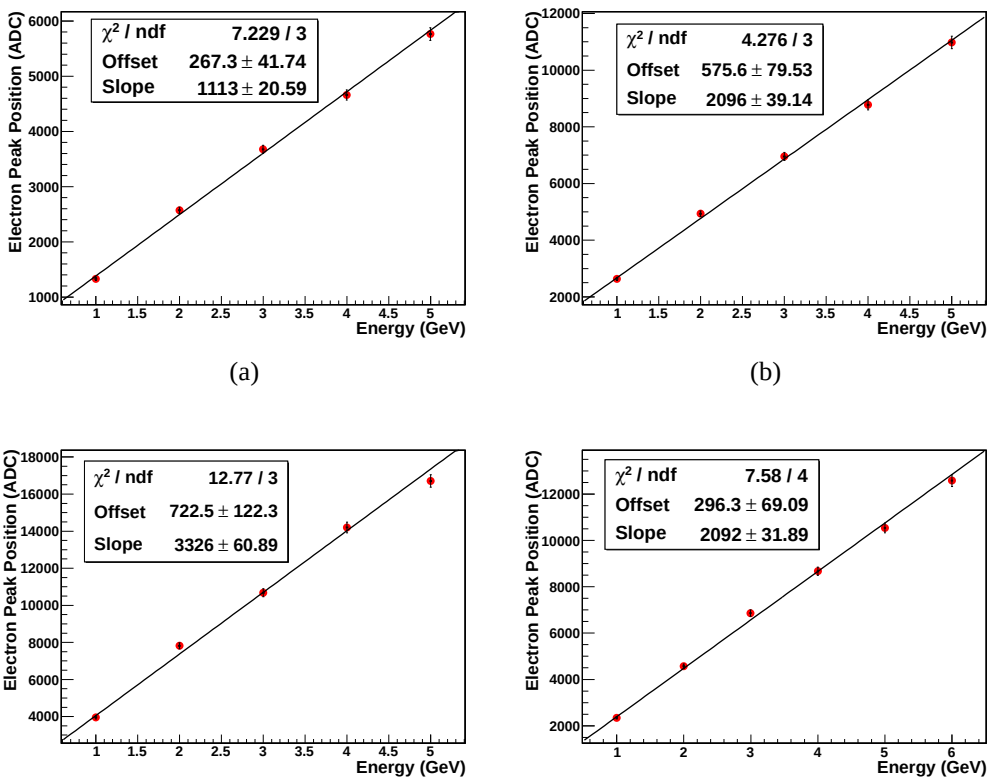

(a) (b)

(c) (d)

Figure 4.39: Energy response linearity in the 1.2 μA configuration with gain 5 (a), 10 (b), 15 (c) and in the 0.5 μA configuration with gain 15 (d).

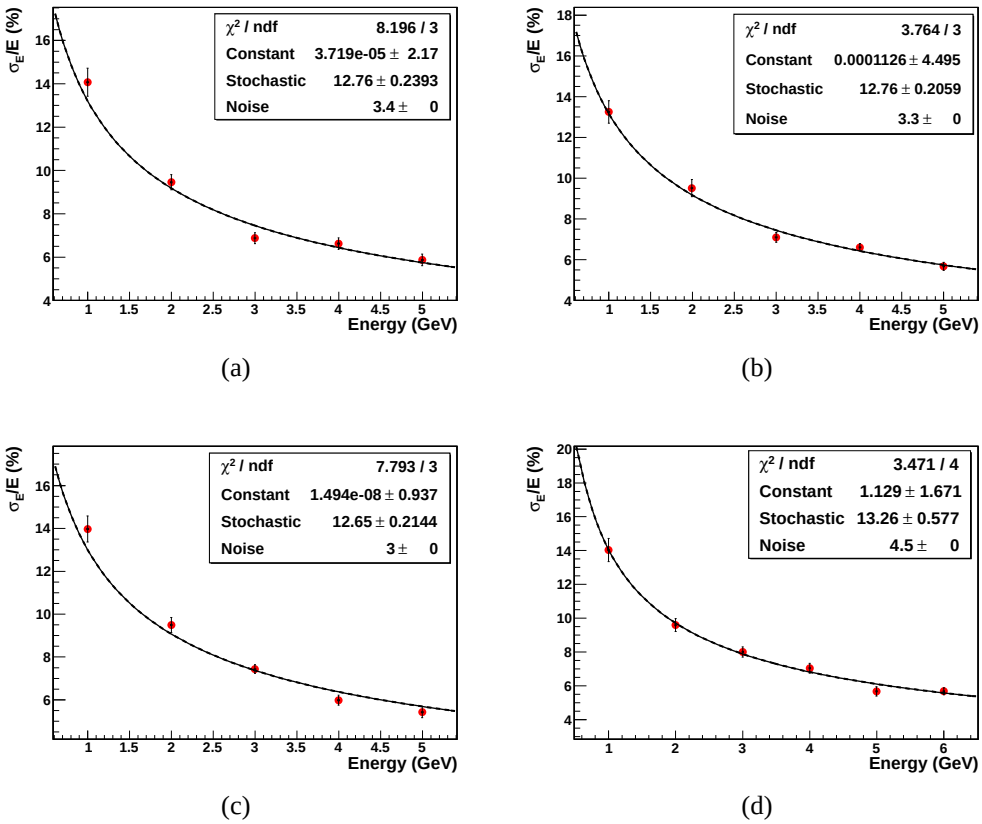

Figure 4.40: Energy resolution in the 1.2 μA configuration with gain 5 (a), 10 (b), 15 (c) and in the 0.5 μA configuration with gain 15 (d).

position of the saturation peak below 3000 ADC suggests that the saturation may occur in the shaper or in the pre-buffer stages, located between the amplifier and the ADC.

As far as the energy resolution is concerned, very similar values of the stochastic (12.8%) and constant ($\sim$0%) terms have been obtained in all the three runs with a bias current of 1.2 μA. Slightly worse results characterize the 0.5 μA configuration, with a stochastic term of 13.3% and a constant term of $\sim$1%, but still compatible with zero considering the errors. In all the configurations the noise term has been fixed in the fit to the RMS value of the pedestal distribution divided by the peak position of 1 GeV electrons: this term is of the order of 3% in the 1.2 μA configuration and of 4.5% in the 0.5 μA configuration. This is consistent with the assumption that the primary source of electronic noise is the coupling between the SiPM readout board and the MAROC board inputs. In fact if this is the case, the amount of noise should be constant during the runs, while its relative importance

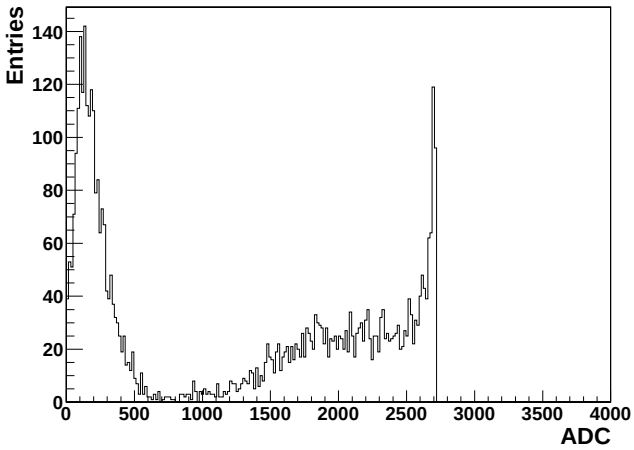

Figure 4.41: Saturation of a SiPM channel with the MAROC readout.

(the noise term in the energy resolution) should depend on the gain of the devices (which depends on the bias of the SiPMs and on the pre-amplifier gain), thus resulting in a larger noise term at small gain values. In general, the results obtained with the MAROC readout are slightly better than the ones obtained in the 2009 tests with the same calorimeter readout by SiPMs, except for the larger noise term. These preliminary tests have also highlighted the problem of the MAROC saturation, which will become more important in the tests performed with the second prototype of the shashlik calorimeter, described in the next chapter.

Chapter 5

Shashlik Calorimeters and SiPMs - Prototype 1

This chapter is dedicated to the description of the tests performed on a second prototype of a shashlik calorimeter, defined as “Prototype 1” or with its nickname “Jack”. This new calorimeter has been built by the mechanical workshop of INFN-Trieste to improve the performance of the previous prototype. It is characterized by a larger active volume of plastic scintillator and it is readout using a larger area SiPM with 3600 pixels.

The results obtained during the tests of 2009 and 2010 led to the development of more accurate simulations, including a complete description of the optical photon propagation, that have been used to explain the discrepancies between the standard GEANT4 simulation and the real data. The results of this simulation have been used as a hint to modify the calorimeter structure both in terms of number of readout channels and inter-tile material. The modified version of the calorimeter has been tested at CERN in summer 2011, with a new type of SiPM with 6400 pixels and a readout based on the MAROC3 ASIC, directly coupled to the array of SiPMs using a custom interface board in order to improve the compactness and the integration of the readout system. This chapter describes both the results and the problems met during the tests, focusing in particular on the large electronic noise that has yet to be addressed.

5.1 The 2009-2010 Beamtests

The prototype 1 calorimeter has been tested at CERN in two different beamtests at the end of 2009 and in summer 2010. The tests have been performed on the T9 and H4 beamlines using electrons up to 6 GeV and tagged photons up to 120 GeV. The main goal of these tests was the evaluation of the performance of this new

calorimeter in terms of linearity, energy and spatial resolution, using a larger area and dynamic range SiPM. In order to compare the prototype 0 and 1 calorimeters, the readout electronics was the same (the V792 QDC). The results described in the following are a refined version of the analysis published in [92].

5.1.1 The Prototype 1 Shashlik Calorimeter

This shashlik calorimeter consists of 70 4 mm thick tiles of plastic scintillator and 69 1.5 mm thick tiles of zinc-coated lead, for a total of $\sim$19 radiation lengths and a Molière radius of $\sim$6 cm. Each tile has an area of 11.5$\times$11.5 cm^2; the readout is performed using 144 1.2 mm WLS fibers (Saint-Gobain BCF-92 [93]). The calorimeter design is very similar to a prototype of an electromagnetic shashlik calorimeter developed in Russia at the beginning of the '90s [94]. The sensitive part of the calorimeter is contained in a 1 cm thick aluminum vessel which covers the top and bottom part of the tiles; in the first version of the calorimeter tested in 2009-2010 no reflective material was used at the interface between the scintillator and lead tiles to improve the light collection. A sketch of the calorimeter is presented in Fig. 5.1.

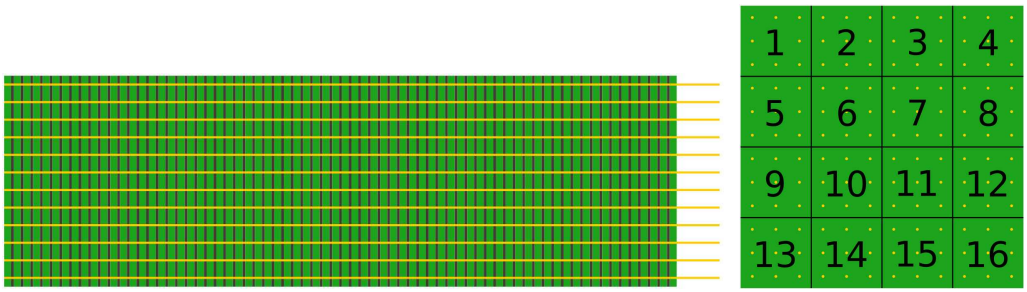

(a) (b)

Figure 5.1: Lateral (a) and frontal sketch (b) of the calorimeter with the lead and the scintillator tiles and the WLS fibers. The number of the readout channels is also indicated.

The WLS fibers cross the whole calorimeter, so that each fiber collects the light of all the scintillator tiles. According to Fig. 5.1, the fibers are placed in a 12x12 matrix of 1 cm spaced holes in the scintillator and lead tiles; they are then grouped and glued in bundles of nine fibers each using 16 plastic holders, and plugged into a support designed to hold an array of SiPMs. A few pictures of the calorimeter during the assembly phases are presented in Fig. 5.2.

The calorimeter is readout using 16 SiPMs manufactured by FBK-irst with a sensitive area of 9 mm^2 with 3600 50x50 μm^2 pixels. The SiPMs have a squared geometry and are glued to a FR-4 PCB that has a twofold purpose: an electric one,

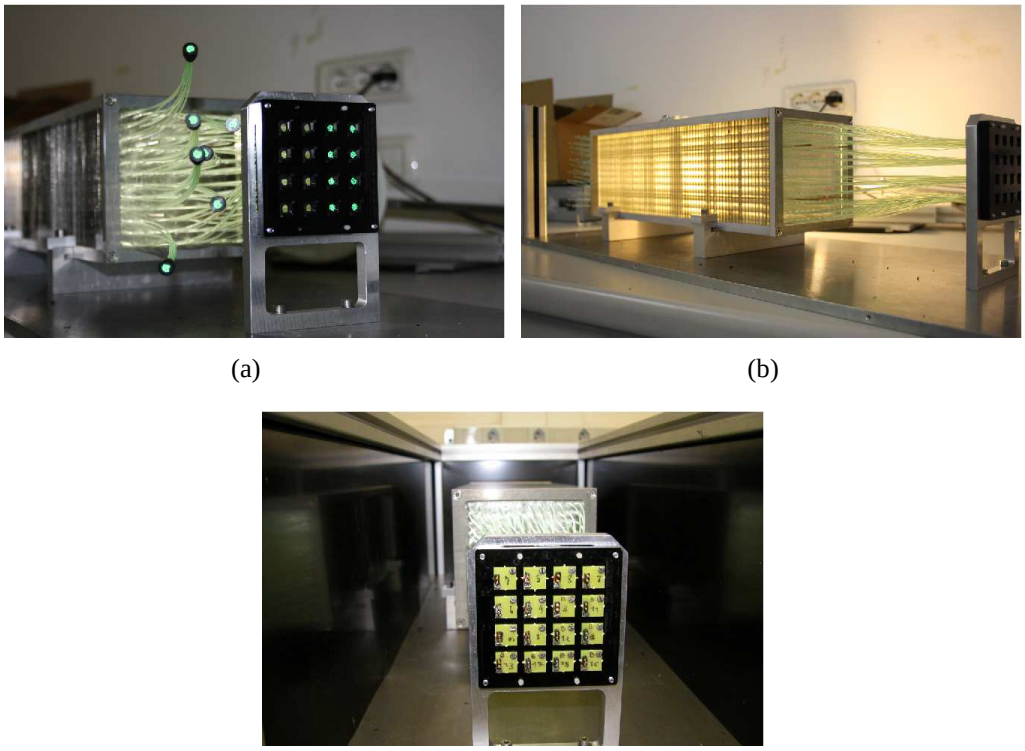

(a) (b)

(c)

Figure 5.2: The calorimeter during the assembly phase: (a) the fibers insertion; (b) the fibers plugged into the SiPM plastic holder; (c) the SiPMs placed into the holder.

providing the bias and the readout connectors, and a mechanical one, providing the coupling to the calorimeter fiber holder; a picture of the device is presented in Fig. 5.3, while its main features are reported in Table 2.2.

The readout is performed with the same readout boards used for the prototype 0 calorimeter (Fig. 4.4).

5.1.2 Experimental Setups

As in the prototype 0 case, the prototype 1 calorimeter has been tested at CERN in two different experimental setups at high and low energy. The goal of the tests was twofold:

- to evaluate the linearity and the energy resolution of the new calorimeter with respect to the old one;
- to see if the use of large area SiPMs can reduce the saturation effects seen

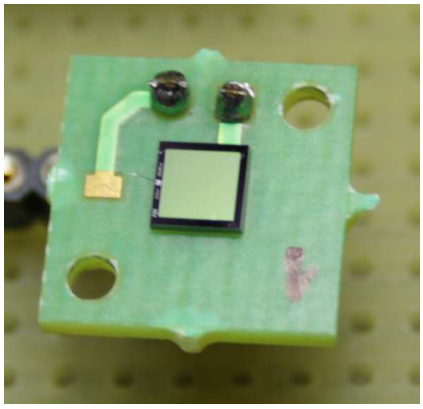

Figure 5.3: Picture of the 9 mm^2 SiPM bonded on the FR-4 PCB.

at high energies with the prototype 0 calorimeter (Fig. 4.33(a)).

For both these reasons it has been decided not to amplify the output signal of the SiPMs and to keep the setup as similar as possible to the 2009 one.

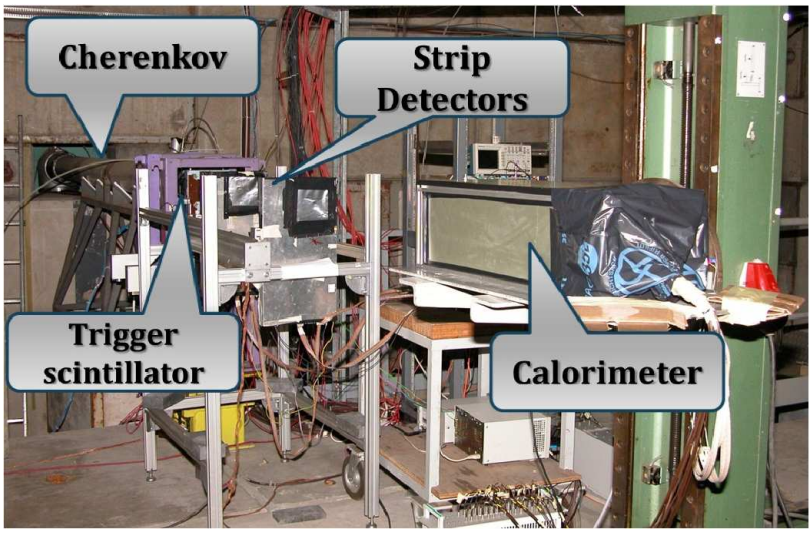

Figure 5.4: Picture of the low energy setup on the T9 beamline.

The low energy tests have been performed at the PS T9 beamline (Fig. 5.4) with negative particles in an energy range between 1 and 7 GeV. The setup, which is very similar to the ones described in sections 4.1.2.1 and 4.2.1 consists of:

- two Cherenkov detectors for the electron tagging;
- two silicon strip chambers for the track reconstruction;

- a 10×10 cm^2 plastic scintillator for the trigger.

The high energy tests have been performed in the framework of the PHOTAG experiment on the H4 beamline, using the same setup described in section 4.1.2.2. The high energy photons have been obtained using channeled positrons with an energy up to 120 GeV inside bent silicon crystals. The only difference with respect to the prototype 0 high energy setup is the use of two scintillator detectors for the trigger generation. The new scintillator (S2 in the sketch of Fig 5.5) has a hole of $\sim$0.3x2 cm^2 to be used as an anti-coincidence; once combined with S1 the number of acquired events corresponding to particles impinging on the crystal increases.

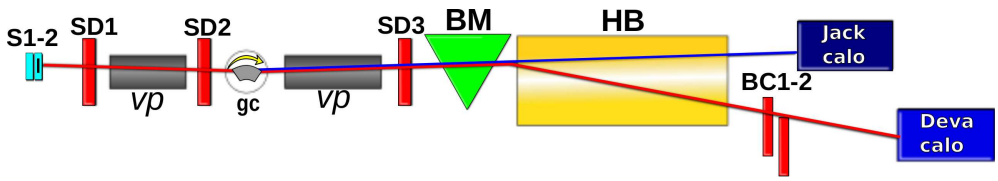

Figure 5.5: Sketch of the high energy setup on the H4 beamline.

As in the prototype 0 tests, the output signal of the SiPMs is delayed by $\sim$140 ns and then sampled with a CAEN V792 12 bit QDC. In both the tests the SiPMs have been divided into two groups according to their operating voltages and then biased using two different power supplies to equalize their gain as much as possible.

5.1.3 Calorimeter Performance Simulation with GEANT4

Following the same procedure described in section 4.1.3, the GEANT4 package has been used to evaluate the performance of the prototype 1 calorimeter in terms of linearity, energy resolution and leakage. Considering the much larger volume of active scintillator material, the expected stochastic term of the energy resolution should be better than the one obtained with prototype 0. On the contrary, considering the smaller number of radiation lengths ($\sim$19 with respect to $\sim$22.4), a worse constant term is expected at high energy due to leakage effects. The simulation takes into account the mechanical frame, the holes in the scintillator and lead tiles and the plastic material of the WLS fibers (Fig. 5.6). The optical processes have not been implemented, so the results obtained with this simulation can be considered as a best estimate of the calorimeter behavior (a complete optical simulation of the calorimeter, performed after the beamtest results described in this section, will be presented in section 5.2).

As in the prototype 0 simulation, the physics list is the QGSP_BERT model with the electromagnetic cuts on the secondary particles set at 100 μm. Two types

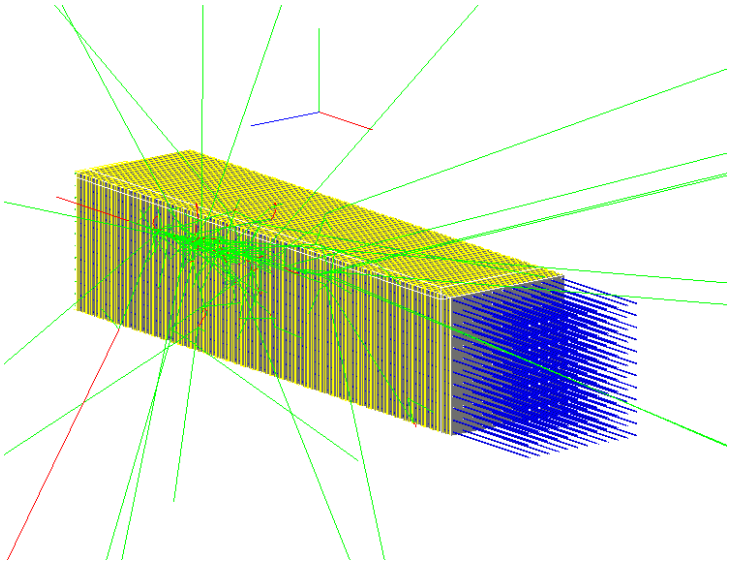

Figure 5.6: GEANT4 geometrical simulation of the prototype 1 shashlik calorimeter after an interaction with a 500 MeV electron: the electrons are depicted in red and the gammas in green.

of beam have been simulated: a "point-like" one and a "Gaussian-shaped" one with σ=1.5 cm in both the horizontal and vertical directions. As far as the low energy simulation is concerned, a monochromatic beam of 10000 electrons has been generated with an energy between 1 GeV and 6 GeV. The energy resolution scan has been fitted using the function $\frac{\sigma_E}{E} = P_0 \oplus \frac{P_1}{\sqrt{E}}$. The results for the "Gaussian-shaped" configuration are presented in the plots in Fig. 5.7.

The simulation shows no deviation from the linearity in the low energy range (Fig. 5.7(a)), while minor deviations that can only be seen in the "reduced" linearity plot are present in the high energy scan (Fig. 5.7(c)). As far as the energy resolution is concerned, a stochastic term of the order of ∼7% and a constant term of roughly ∼0.5% have been obtained in the low energy range (Fig. 5.7(b)). As previously stated, these results were expected considering the larger fraction of active material and the smaller number of radiation lengths compared to the prototype 0 calorimeter. Moreover, the beamtest results in [94] with a very similar shashlik calorimeter confirm the simulation expected values. As in the prototype 0 simulation, it is possible to merge the low and high energy datasets together (Fig. 5.7(d)) obtaining a stochastic term of 7.0% and a constant term of 1.1%. Table 5.1 summarizes the energy resolution results obtained with the "point-like" and "Gaussian-shaped" beam configurations.

The energy leakage has been computed summing the energy deposit in the scintillator and lead tiles and subtracting this value from the beam energy. The

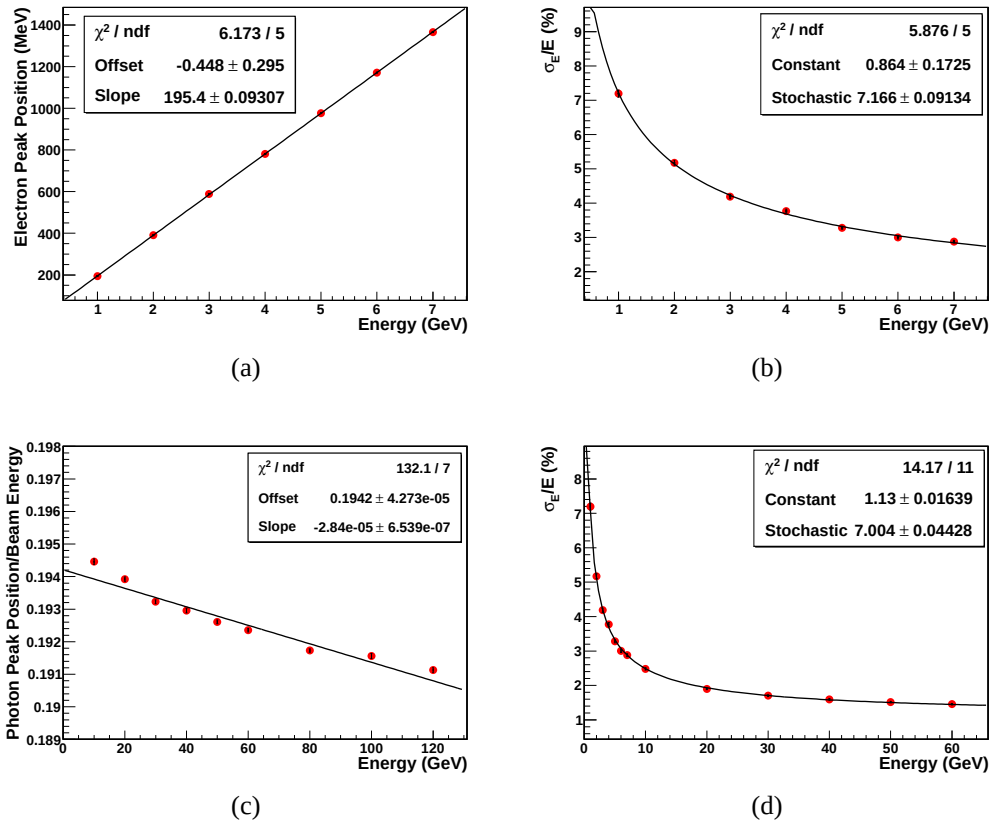

Figure 5.7: Linearity (a) and energy resolution (b) in the low energy case; "reduced" linearity (c) in the high energy range; energy resolution with the complete dataset (d). All the plots refer to the "Gaussian-shaped" simulated beam configuration.

Energy range	Point like Constant	Point like Stochastic	Gaussian shaped Constant	Gaussian shaped Stochastic
Low energy	0.22%	7.08%	0.86%	7.17%
High energy	0.94%	6.57%	1.18%	6.76%
Complete dataset	0.87%	6.86%	1.13%	7.00%

Table 5.1: Prototype 1 energy resolution results with low and high energy simulated data.

results are summarized in Table 5.2.

The leakage can be considered substantially constant in the low energy range,

Beam energy (GeV)	Point like	Gaussian shaped	Beam energy (GeV)	Point like	Gaussian shaped
1	8.86%	9.68%	20	9.99%	10.79%
2	8.93%	9.72%	30	10.28%	11.19%
3	9.08%	9.80%	40	10.46%	11.27%
4	9.12%	9.85%	50	10.76%	11.55%
5	9.18%	9.92%	60	10.88%	11.68%
6	9.21%	9.95%	80	11.21%	12.00%
7	9.28%	10.00%	100	11.48%	12.35%
10	9.58%	10.27%	120	11.75%	12.54%

Table 5.2: Energy leakage of the calorimeter with two beam configurations as a function of the incident particle energy.

with an increase of $\sim$2% in the high energy range which is responsible for the increase in the fitted constant terms and for the deviations from linearity observed in the high energy reduced linearity plot (Fig. 5.7(c)).

5.1.4 Low Energy Results

5.1.4.1 Linearity and energy resolution

The calorimeter has been characterized in terms of linearity and energy resolution with low energy electrons using the same event selection and equalization procedure described in section 4.1.4.1. The bias values for the hardware equalization are presented in Table 5.3.

Group	40 μA	30 μA	20 μA	10 μA
1	37.5 V	36.0 V	34.4 V	32.5 V
2	38.2 V	36.9 V	35.1 V	33.0 V

Table 5.3: Bias values for the two SiPM groups in the four current configurations.

The SiPMs have been operated at ambient temperature, thus the gain drifting of the device had to be corrected in the off-line analysis. The same algorithm developed for the prototype 0 analysis, based on the signal of MIPs impinging on the calorimeter, has been used. It has to be noted that, considering the large overvoltage values used for the SiPMs bias and the small ambient temperature changes during the beamtest, the gain variations are smaller with respect to the prototype 0 tests (as can be seen in the linearity plots of Fig. 5.9). As in the

previous analysis, a fiducial area of 4x4 cm^2 has been chosen to reject the events with a large lateral leakage. An example of the electron peak distribution obtained with the prototype 1 calorimeter is presented in Fig. 5.8.

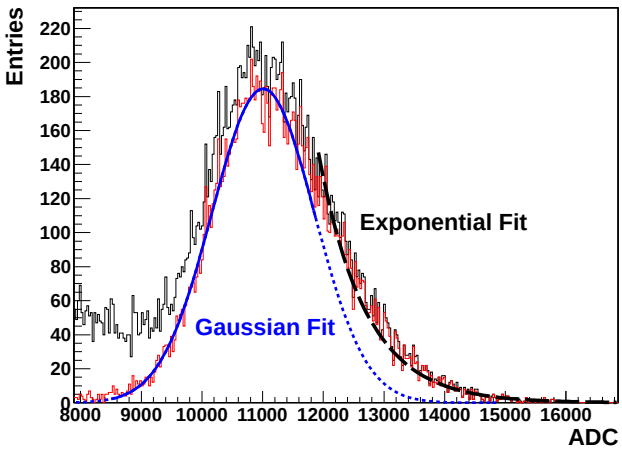

Figure 5.8: Fit of the 4 GeV electron events distribution of the prototype 1 calorimeter. The Gaussian fit is drawn in blue, while the exponential fit is drawn in dashed black. The red histogram is obtained tagging the electron events with the Cherenkov detectors.

On the contrary of the prototype 0 results, the electron events distribution is characterized by a long exponential tail on the large values side. As will be explained in section 5.2 using the full GEANT4 optical simulation, this tail may depend on the attenuation of the photons in the scintillator tiles, due to the absence of reflective material between the lead and scintillator layers. To avoid the exponential tail, the energy resolution has been obtained fitting the electron events distribution with a Gaussian function in the $[-3\sigma, \sigma]$ interval, dividing the sigma by the mean parameter. The momentum spread of the beamline has been taken into account adding in quadrature to the mean parameter error the 2% of the mean parameter itself. For the energy scan, four different runs with four different bias currents (40, 30, 20 and 10 μA) have been performed: the linearity and energy resolution results (for two values of the bias current) are presented in Figs. 5.9 and 5.10.

The linearity is very good in each current configuration, with maximum deviations of the order of 1%. Larger deviations from linearity (with a maximum of $\sim$6% at 4 GeV) are only present in the 10 μA plot due to the fact that the temperature deviations are proportionally more relevant in the low bias configuration. On the other hand the energy resolution results are much more puzzling. As in the

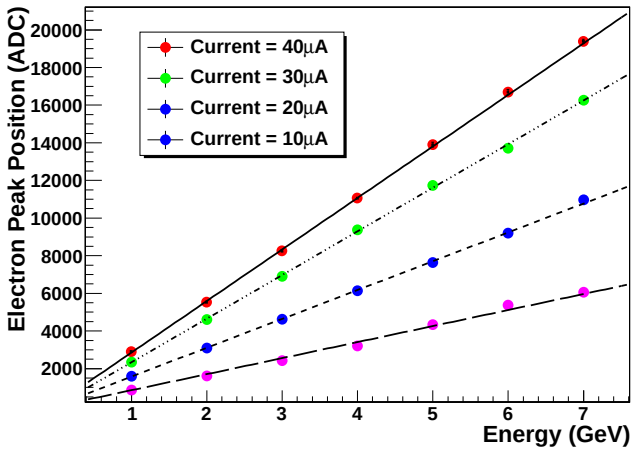

Figure 5.9: Linearity using the SiPMs biased with 40 μA, 30 μA, 20 μA and 10 μA.

prototype 0 tests, the noise parameter of the energy resolution has been fixed in the fit considering the sigma of the noise (pedestal) distribution (Fig. 5.11).

However, the fitted stochastic terms are deeply different from the values expected from the GEANT4 simulation. In particular, the expected energy resolution is of the order of 7%, while the experimental results are of the order of 16%. Moreover, the large χ^2 values and the mismatch between the fitted function and the experimental points at low energy (1-2 GeV), are a clear indication that the noise term is underestimated. This hypothesis can be confirmed performing the energy resolution fit considering the noise term as a free parameter. In this case the χ^2/ndf value is approximately equal to 1, and the energy resolution parameters converge to $\sim$4–5%, $\sim$11–12% and $\sim$12–14% for the constant, stochastic and noise terms respectively. Moreover, the energy resolution does not seem to be correlated with the bias current (*i.e.* the gain) of the devices. Table 5.4 summarizes the results obtained in the different bias configurations with a fixed or floating noise parameter.

Considering the much better results expected from the GEANT4 simulation, it is clear that some kind of noise contribution worsens the energy resolution. Two possibilities have to be taken into account:

- problems introduced by the SiPM readout; given that the electronics chain used for the prototype 1 tests is the same of the prototype 0 one which gave good results, the problems must be due to the SiPMs themselves;
- mechanical or construction problems in the calorimeter.

The full GEANT4 optical simulation presented in section 5.2 will show that

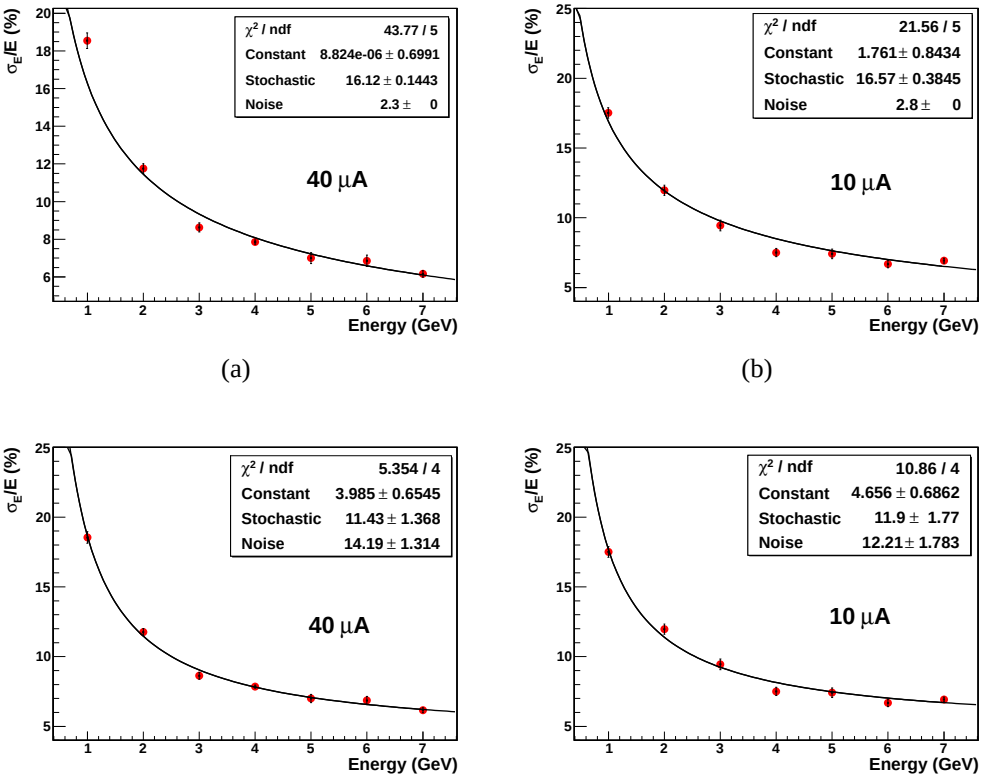

Figure 5.10: Energy resolution using the SiPMs biased with 40 μA ((a) and (c)) and 10 μA ((b) and (d)) with a fixed and floating noise term.

Bias	Constant	Stochastic	Noise
40 μA	$\sim$0%	16.12%	2.30% ($FIXED$)
	3.99%	11.43%	14.19%
30 μA	1.14%	16.24%	2.45% ($FIXED$)
	5.00%	10.46%	13.50%
20 μA	$\sim$0%	16.43%	2.56% ($FIXED$)
	4.99%	9.69%	14.92%
10 μA	1.76%	16.57%	2.8% ($FIXED$)
	4.66%	11.90%	12.21%

Table 5.4: Prototype 1 low energy resolution results.

the energy resolution together with the exponential tail in the electron peak may be ascribed to the absence of a reflective interface between the scintillator and lead

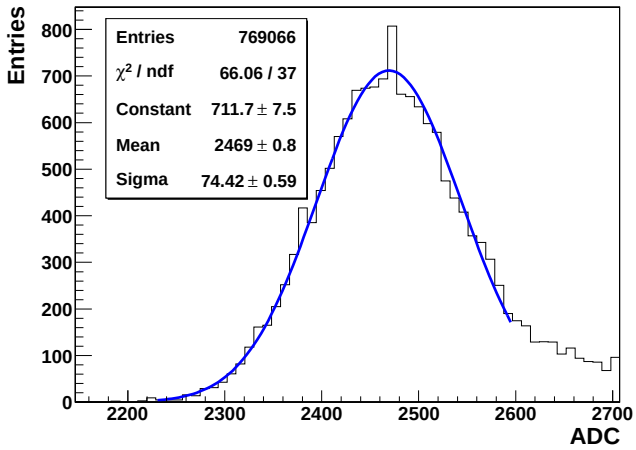

Figure 5.11: Pedestal distribution of the prototype 1 calorimeter fitted with a Gaussian function. The σ value is used to fix the noise parameter in the energy resolution fit.

tiles which introduces large fluctuations in the collected optical photon statistics.

5.1.4.2 Spatial resolution

The spatial resolution of the calorimeter has been evaluated with the algorithm developed by [91] and described in section 4.1.5 using the residuals. As in the prototype 0 tests (Fig. 4.27), the output channels have been divided into x and y planes according to the following relations:

$$Layer_{1X} = ([1]+[5]+[9]+[13]) \qquad Layer_{1Y} = ([1]+[2]+[3]+[4])$$
$$Layer_{2X} = ([2]+[6]+[10]+[14]) \qquad Layer_{2Y} = ([5]+[6]+[7]+[8])$$
$$Layer_{3X} = ([3]+[7]+[11]+[15]) \qquad Layer_{3Y} = ([9]+[10]+[11]+[12])$$
$$Layer_{4X} = ([4]+[8]+[12]+[16]) \qquad Layer_{4Y} = ([13]+[14]+[15]+[16])$$

Two examples of residuals obtained with the SiPMs biased with a 40 μA current, using an electron beam of 4 GeV, are shown in Fig. 5.12. The w_0 parameter has been chosen minimizing the residual value, and it is equal to 2.9 for the x direction and to 2.2 for the y one.

Table 5.5 summarizes the spatial resolution values for the different energies in the 40 μA configuration.

As previously found in the prototype 0 tests, the spatial resolution improves with the energy, reaching an asymptote of ∼0.2 cm at 7 GeV.

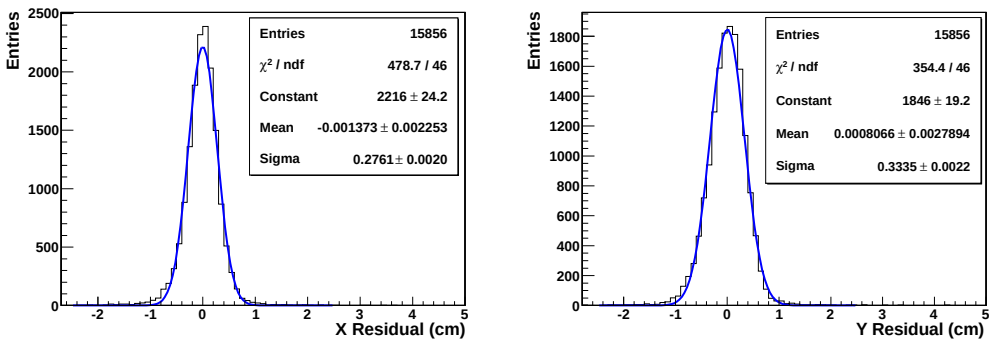

(a) (b)

Figure 5.12: The calorimeter x (a) (w_0=2.9) and y (b) (w_0=2.2) resolution with a 4 GeV beam.

Energy	Resolution X	Resolution Y
1 GeV	0.66 cm	0.70 cm
2 GeV	0.40 cm	0.48 cm
3 GeV	0.32 cm	0.37 cm
4 GeV	0.28 cm	0.33 cm
5 GeV	0.25 cm	0.30 cm
6 GeV	0.23 cm	0.29 cm
7 GeV	0.21 cm	0.28 cm

Table 5.5: Spatial resolution for different beam energies using the SiPMs biased at 40 μA.

5.1.5 High Energy Results

Differently from the low energy tests, the high energy ones have been performed using a single bias current (3 μA). This small value (compared to the bias used in the low energy tests) has been chosen in order to reduce the SiPM gain and to avoid the QDC saturation. To equalize the gain of the devices, the SiPMs have been divided into four groups according to their power consumption (Table 5.6).

The energy of the photon emitted inside the crystal is obtained as the difference between the beam energy and the outgoing positron energy, measured with a spectrometer. The energy resolution of the spectrometer has been computed fitting the 120 GeV peak (as in Fig. 4.31) and is equal to $\sim$540 MeV[1] at this energy.

[1]The value of $\sim$540 MeV is slightly different from the one of $\sim$390 MeV found in 2009 during the high energy tests of the prototype 0 calorimeter. This difference is due to the different position of the silicon chambers on the beamline.

Bias Group 1	Bias Group 2	Bias Group 3	Bias Group 4
32.0 V	31.7 V	31.3 V	31.2 V

Table 5.6: Bias values for the four SiPMs groups corresponding to a 3 μA current consumption.

The analysis procedure is the same described in section 4.1.6 for the prototype 0 test.

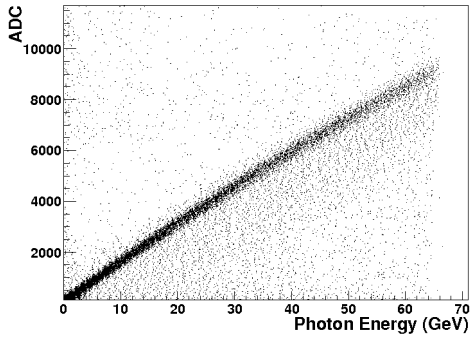

(a)

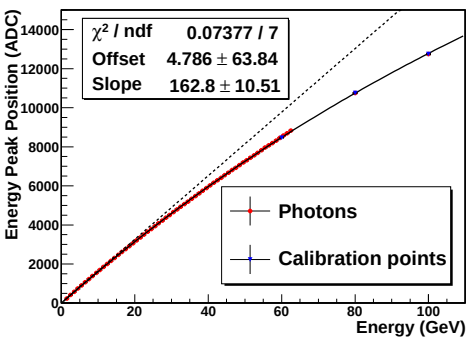

(b)

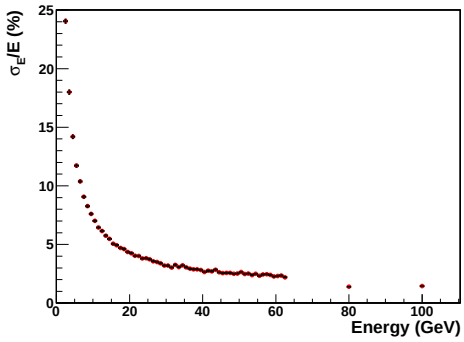

(c)

Figure 5.13: Energy scatter plot (a), linearity (b) and energy resolution (c) obtained in the high energy tests. The dashed line in (b) represents the linear fit up to 20 GeV; the solid line is a fit with a 4th degree polynomial.

Fig. 5.13(a) presents the scatter plot which is sliced in the photon energy direction to obtain the linearity and energy resolution plots of Figs. 5.13(b) and 5.13(c). The 60, 80 and 100 GeV points of Fig. 5.13(b) have been measured in three dedi-

cated runs with the magnet switched off and the positron beam impinging directly on the calorimeter to check the tagging accuracy of the spectrometer. As it can be seen looking at the dashed line in Fig 5.13(b), the linearity is good up to ∼20 GeV, but at higher energies a clear saturation effect is present, as in the prototype 0 calorimeter tests. In the new test, the larger dynamic range of the 9 mm^2 SiPMs is overwhelmed by the huge amount of photons generated in the larger volume of active material (3703 cm^3 compared to 858 cm^3 in the prototype 0 calorimeter). No fit has been performed on the energy resolution scan in Fig. 5.13(c) in the saturated configuration.

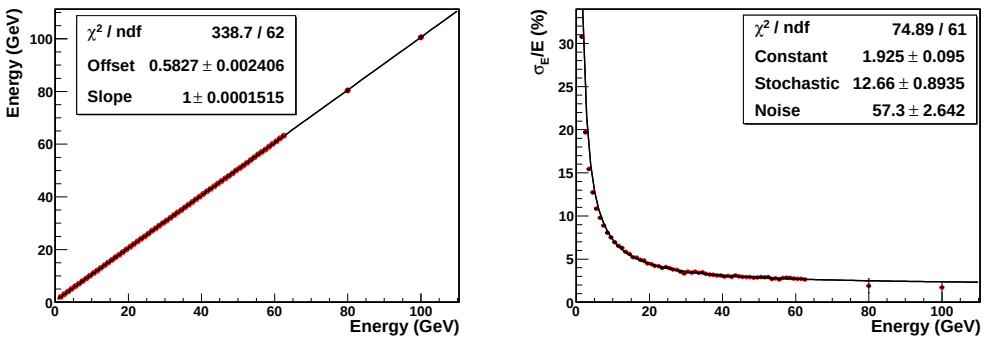

(a) (b)

Figure 5.14: Linearized plot (a) and corrected energy resolution scan (b) in the high energy tests.

After the linearization procedure (using a 4th degree polynomial fit) the linearity is restored and the resolution has a stochastic term of 12.66% (Fig. 5.14), comparable with the results obtained in the low energy runs (10–12%). The noise term cannot be directly compared with the low energy results because it includes also the energy resolution of the magnetic spectrometer. However the value of 57%, corresponding to 570 MeV at 1 GeV, is compatible with the resolution of ∼540 MeV computed from the fit to the positron energy spectrum. For a better comparison between the high energy results (in the linear region) and the low energy ones, the same slicing procedure (with a 100 MeV step) has been applied to select only photons with an energy up to 10 GeV. As in the low energy tests, the fitting range is $[-3\sigma, \sigma]$ to avoid the exponential tail: the results in terms of linearity and energy resolution are shown in Fig. 5.15.

As in the low energy tests, the linearity is good, and the fit of the energy resolution converges to a stochastic term of 11.6% and to a constant term of ∼4% (considering the error). These values are in good agreement with the stochastic term of 10–12% and with the constant term of 4–5% obtained in the low energy runs. As far as the noise term is concerned, a value of 47.0% has been obtained

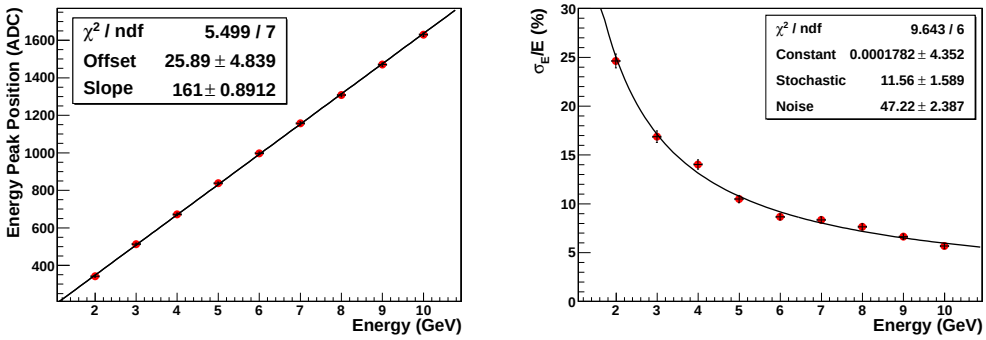

(a) (b)

Figure 5.15: Linearity (a) and energy resolution (b) obtained in the high energy tests selecting only the low energy photons.

which corresponds to a spectrometer resolution of 470 MeV at 1 GeV, very similar to the previously computed values (540 and 570 MeV).

5.2 The Optical GEANT4 Simulation

As shown in the previous section, the experimental results obtained in the 2009–2010 low and high energy tests were very different from the expected performances of the prototype 1 calorimeter inferred using the preliminary GEANT4 simulation. In fact, the preliminary simulation can be considered only as a best estimate of the calorimeter capabilities: inefficiencies due to the optical propagation of light inside the calorimeter or to the noise introduced by the readout chain can worsen the energy resolution. For these reasons a new GEANT4 simulation has been developed with the goal to study the inefficiencies that can be induced by the optical processes. The *OpticalPhysics* physics list which handles a great number of optical processes has been activated; among the processes one can list:

- the generation processes through scintillation for both the slow and fast components;
- the Cherenkov light emission;
- the exponential light attenuation processes;
- the wavelength-shifting processes;
- the reflection and refraction processes between materials with different refractive indices.

The drawback of this type of simulation is that each optical photon is tracked as a single particle: considering the large number of photons involved in the scintillation processes, the simulation requires a lot of CPU time (∼9 minutes for each event with a 1 GeV electron beam): for this reason only the low energy setup has been simulated with this procedure.

The first step is the assignment of the optical properties to the materials which compose the calorimeter as the refractive index or the scintillation yield factor. The values have been extracted from the datasheets of the BC-400 plastic scintillator and of the BCF-92 WLS fibers (Fig. 5.16) as shown in Table 5.7.

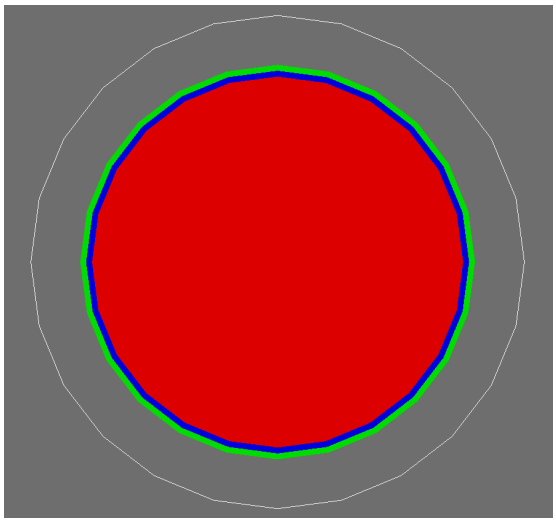

Figure 5.16: Sketch of the WLS fiber simulated in the complete GEANT4 optical simulation. The core of the fiber is depicted in red, while the first and the second cladding are blue and green colored.

	Material	Refractive index	Emission peak	Light yield (per keV)	Attenuation length
BC-400	Polyvinyltoluene	1.58	423 nm	∼10 photons	160 cm
BCF-92 (core)	Polystyrene	1.60	492 nm	N/A	>3.5 m
BCF-92 (clad 1)	Acrylic	1.49	N/A	N/A	N/A
BCF-92 (clad 2)	Fluor-acrylic	1.42	N/A	N/A	N/A

Table 5.7: Optical properties of the scintillator tiles and the WLS fibers.

While the propagation of the light from the plastic scintillator to the WLS fibers is handled by the GEANT4 program using the rules of the geometrical op-

tics (reflection and refraction, see Fig. 5.17), particular attention must be paid for the definition of the scintillator-lead interface.

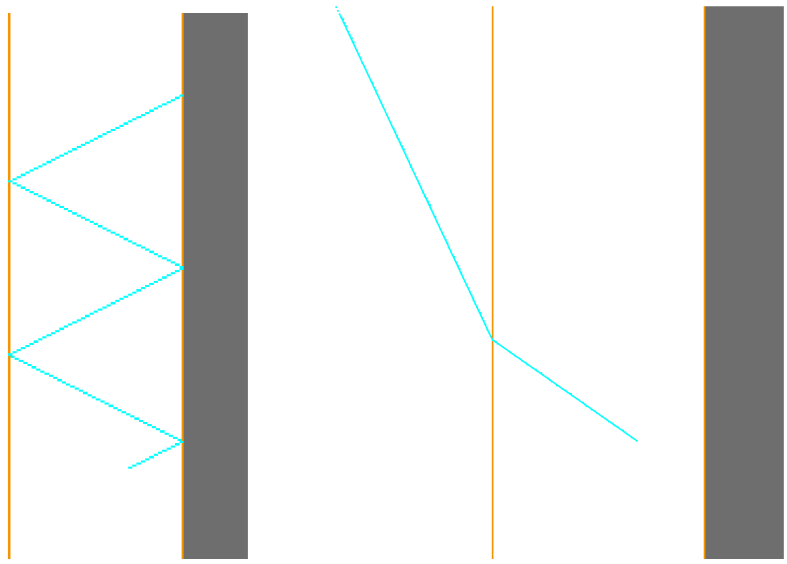

(a) (b)

Figure 5.17: Reflection (a) and refraction (b) processes of an optical photon (cyan) simulated by GEANT4 inside the scintillator tile.

As stated in section 5.1.1, no reflective material has been inserted between the scintillator and lead tiles. However, the reflectivity of the interface cannot be set to zero for the following reasons:

- the presence of a tiny air gap between the tiles (due to mechanical imperfections) which makes total internal reflection phenomena possible at certain angles;
- the presence of a partially reflective zinc-coating on the surface of the lead tiles.

For these reasons the internal borders of the scintillator tiles have been defined as a “LogicalSkinSurface”, whose reflection coefficient is defined as a photon reflection probability between 0 and 1. To reproduce the SiPM behavior, the number of photons collected by each fiber is counted by a couple of sensitive detectors, placed at both the ends of the fiber. The sensitive detectors are geometrical entities able to increase an internal counter each time an optical photon hits them. In the off-line analysis the fibers are grouped in bundles of nine as in the experimental case. No gap is present between the fibers and the sensitive detectors, so the detected number of photons does not take into account geometrical effects due to the numerical aperture and to the distance of the surface of the SiPMs from the fibers.

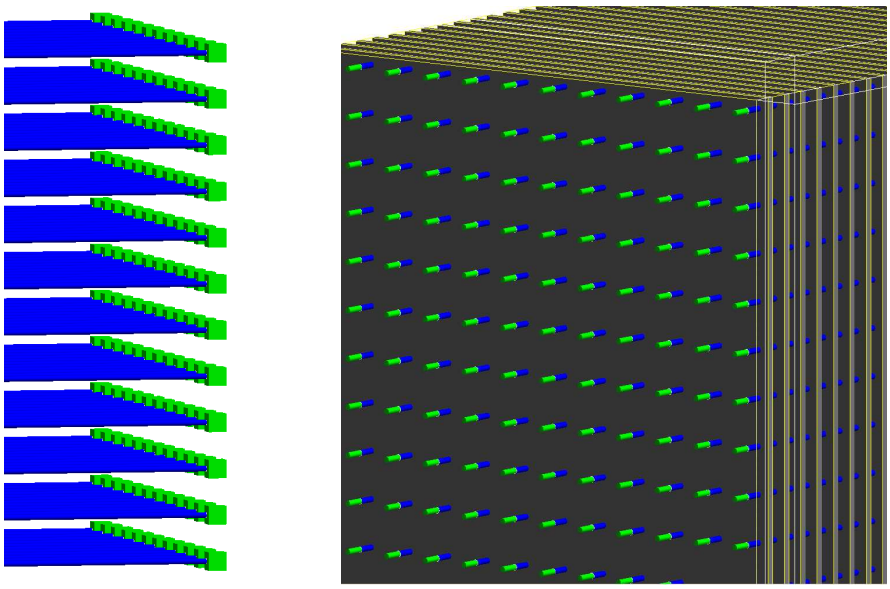

(a) (b)

Figure 5.18: Back (a) and front (b) sensitive detectors (depicted in green) used to count the number of photons collected by each WLS fiber.

The first set of sensitive detectors (designed with a cubic shape, Fig. 5.18(a)) is used to simulate the light collected by the SiPMs. The second group (designed with a cylindrical shape and placed inside the front aluminum cover, Fig. 5.18(b)) is used to test the benefits of the fiber mirroring to enhance the light collection. Four energy scans with reflection coefficients of 0.2, 0.4, 0.6 and 0.9 have been simulated. Considering the long CPU time needed to complete the simulation, only the "Gaussian-shaped" beam configuration has been used (centered in the central part of the calorimeter), with a total of 2400 electron events for each energy. An example of a complete simulation event with one single 1 GeV electron impinging on the calorimeter is depicted in Fig. 5.19.

A histogram is filled with the total number of photons collected in each event by all the fibers and fitted with a Gaussian function to extract the resolution parameter and the linearity (Fig. 5.20(a)). The mean number of photons collected by each SiPM (*i.e.* by a bundle of nine fibers) is obtained by means of a 2D profile histogram (Fig. 5.20(b)).

As can be seen in Fig. 5.20(a), the distribution of the total number of photons is not completely Gaussian and it is characterized by a long tail which can be described with an exponential function, as found in the 2009 tests. The origin of the tail can be understood looking at Fig. 5.20(c) which presents the simulated beam profile considering only the tail events. The pattern shows that these events

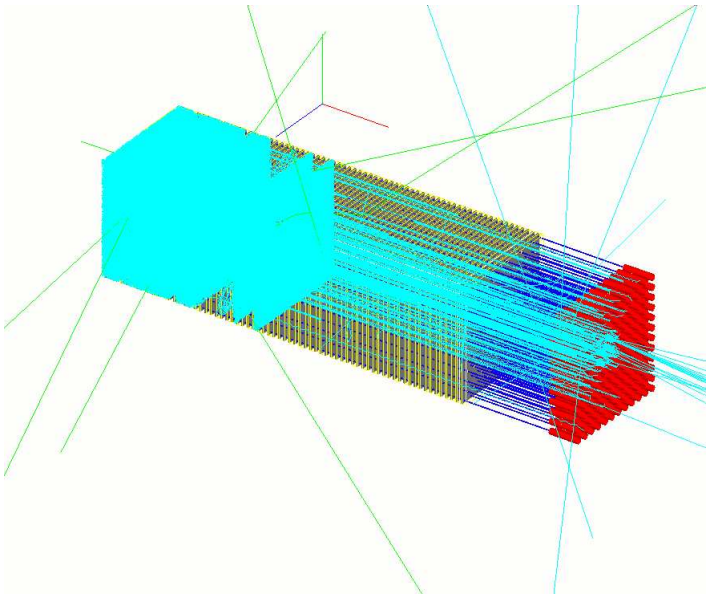

Figure 5.19: Optical simulation event of one single 1 GeV electron impinging on the calorimeter. The optical photons are created into the scintillator tiles and are transported by the WLS fibers to the sensitive detectors.

correspond to the events that impinge on the calorimeter near the WLS fibers. This is due to the fact that, considering the small reflective coefficient used for the scintillator-lead interface, the number of collected photons is maximum for the particles that emit scintillation light near the fibers. For these reasons, to extract the resolution parameter, the histogram has been fitted with a Gaussian function in the $[-3\sigma, \sigma]$ interval, as in the prototype 1 data analysis.

5.2.1 Energy Resolution and Linearity

The first result of the optical simulation is the evidence that the energy resolution of the calorimeter depends strongly on the reflection coefficient used for the LogicalSkinSurface. An example of the energy resolution obtained with several values of the reflection coefficient (0.2, 0.4, 0.6 and 0.9) is shown in Fig. 5.21.

The energy resolution improves with the reflection coefficient (*i.e.* the light collection efficiency): this behavior is somehow expected, and it is the reason why the scintillator tiles of the sampling calorimeters are usually wrapped by a reflective coating material. The energy resolution is deeply different from the values obtained in the preliminary simulation, with stochastic terms of 18.4, 14.5 and 10.7% for reflection coefficients of 0.2, 0.4 and 0.6 respectively. Also the constant term depends on the reflection coefficient, varying from 6.2% with a 0.2

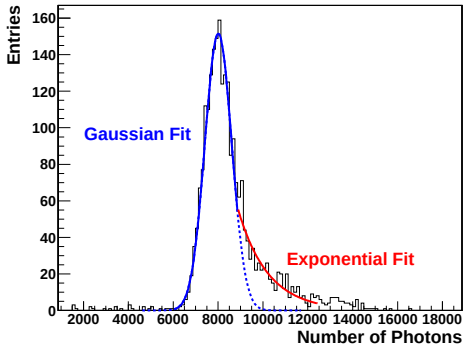

(a)

51.6529	203.448	208.562	63.0533
206.597	1589.59	1663.46	227.778
218.882	1691.29	1641.72	240.506
65.6904	218.382	226.656	61.5196

(b)

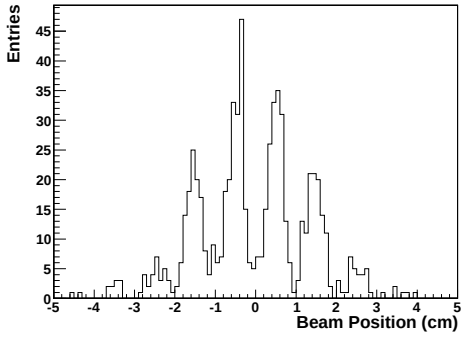

(c)

Figure 5.20: Total number of photons (a) fitted with a Gaussian and an exponential function; mean number of photons (b) for each of the 16 SiPMs; position of the exponential tail events, corresponding to the WLS fibers pattern (c). The plots refer to a 7 GeV beam with the reflective coefficient of the LogicalSkinSurface set to 0.4.

value to 4.1% in the 0.6 case. Only in the 0.9 case, characterized by an almost perfect reflection coefficient, the results expected from the preliminary simulation ($\sim$7% stochastic and $\sim$1% constant) can be reached. In particular, considering the results obtained in the 2009 tests, the reflection coefficient of 0.6 seems to be the most adequate to describe the real data. To take into account also the noise contribution, a noise term is introduced in the off-line analysis adding for each readout channel a constant number of photons multiplied by a random value uniformly distributed between -1 and 1. The results in terms of energy resolution for different values of noise using a reflection coefficient of 0.6 are presented in Fig. 5.22.

The introduction of the noise term modifies the energy resolution behavior

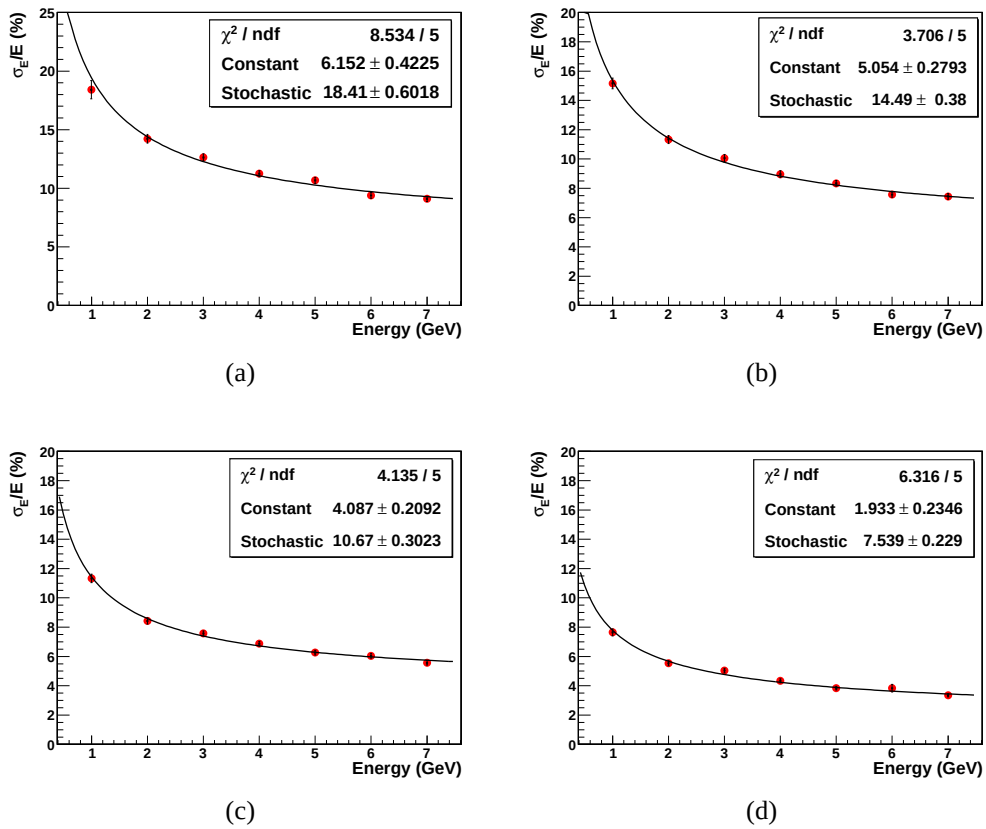

Figure 5.21: Energy resolution obtained with a reflection coefficient of 0.2 (a), 0.4 (b), 0.6 (c) and 0.9 (d).

at low energies, with a fitted noise term which depends on the amount of photons added in the analysis. The best agreement between experimental data and simulation has been obtained using a noise value between 120 and 150, which corresponds to the signal produced by ∼1-2 MIPs in the central channels of the calorimeter. As far as the linearity is concerned, the results are good in all the configurations, with or without noise: an example of a linearity scan with a reflection coefficient of 0.6, with and without noise, is presented in Fig. 5.23.

Considering the fact that the comparison between the real data and the optical simulation suggests that the equivalent reflection coefficient of the calorimeter is equal to 0.6, a value of 0.9 could be reasonably achieved using a reflective material between the tiles. Moreover, the light collection can be increased mirroring one side of the WLS fibers (the effect of mirroring can be included in the simulation using the second set of sensitive detectors). Fig. 5.24 presents the performance that can be achieved by the calorimeter considering a reflection coefficient of 0.9

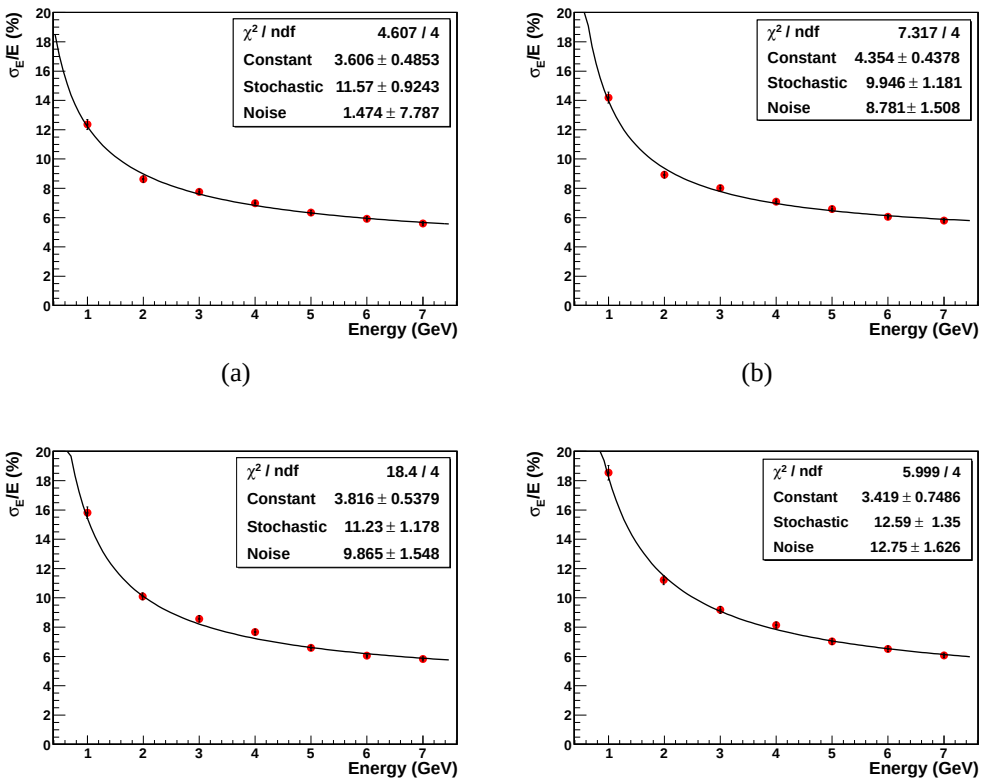

Figure 5.22: Energy resolution obtained with a reflection coefficient of 0.6 and noise values of 40 (a), 80 (b), 120 (c) and 150 (d).

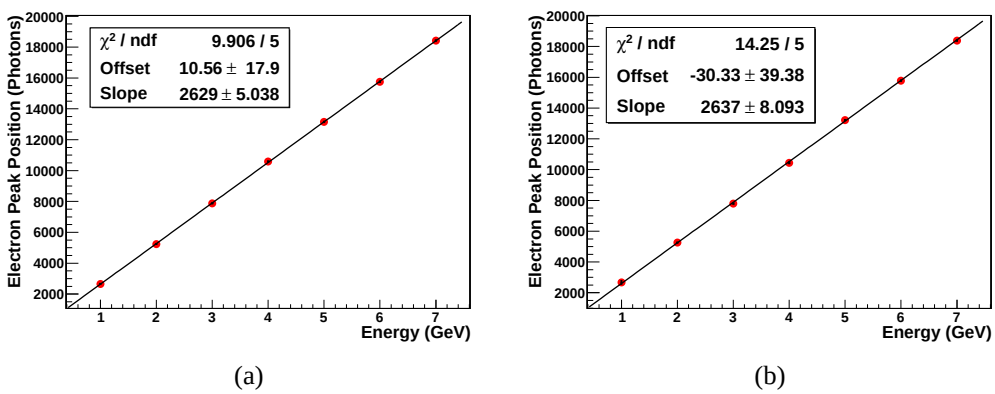

Figure 5.23: Linearity using a reflection coefficient of 0.6 with (a) and without (b) noise.

and a mirroring efficiency of 0.8.

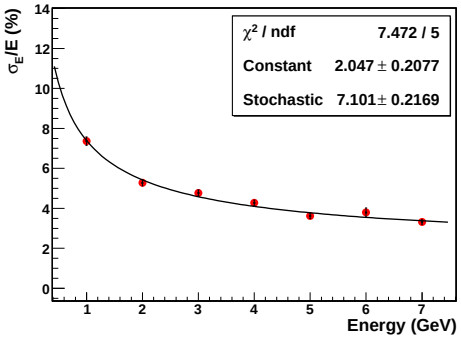

(a)

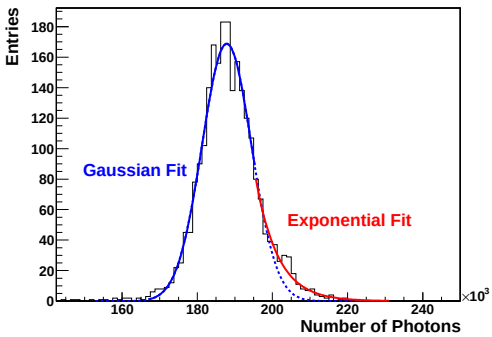

(b)

3680.2	5796.58	5779.54	3609.61
5815.1	10363.9	10344	5675.39
5855.36	10559.4	10341	5852.89
3736.57	5876.33	5760.24	3668.68

(c)

Figure 5.24: Energy resolution (a), photon peak fit without the noise tail (b) and mean number of photons per SiPM (c) using a reflection coefficient of 0.9 and a mirroring efficiency of 0.8.

In this way, the final calorimeter performances are quite similar to the ones predicted by the preliminary GEANT4 simulation, with a stochastic term of ∼7% and a constant term slightly larger than 2%. Moreover, the good reflective interface reduces the inhomogeneities in the light collection, almost erasing the exponential contribution to the photons distribution (Fig. 5.24(b) compared to Fig. 5.20(a)). However, the improved light collection has a drawback: as can be seen in Fig. 5.24(c), the expected number of photons per SiPM is very large, much larger than the number of cells available in the SiPMs of the 2009 tests. Two methods can be used to avoid the saturation of the devices:

- the use of new SiPMs with a larger dynamic range (*i.e.* more cells);
- the increase of the number of readout channels, thus reducing the number

of fibers bundled together and the light provided to each SiPM.

After the results of the optical simulation, it has been decided to modify the prototype 1 calorimeter, inserting white Tyvek sheets as the inter-tile material and increasing the number of readout channels from 16 to 36, using larger area (4x4 mm^2) SiPMs. The results of the tests with the modified calorimeter will be described in section 5.3.

5.2.2 Spatial Resolution

One of the advantages of the optical simulation with respect to the preliminary one is the fact that, knowing the number of photons collected by each fiber, it is possible to reconstruct the hit position evaluating the calorimeter spatial resolution. The residuals method approach described in sections 5.1.4.2 and 4.1.5 has been used. The output channels have been divided in x and y planes and the coordinate of the incident particle has been computed using the algorithm developed in [91]. The results obtained for two values of the reflection coefficient (0.6 and 0.9) without the inclusion of the noise contribution are presented in Fig. 5.25.

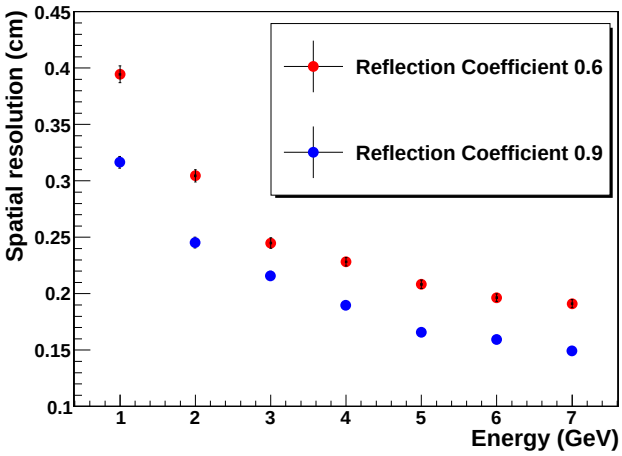

Figure 5.25: Spatial resolution with the optical simulation using a reflection coefficient of 0.6 (red dots) and 0.9 (blue dots) without the noise term in the 16 channels configuration.

Comparing the two reflection coefficients, slightly better results have been obtained in the 0.9 configuration, with a resolution of 3.2 mm at 1 GeV and of 1.6 mm at 7 GeV. As in the energy resolution scan, real and simulated data can be directly compared introducing a noise term: Table 5.8 presents the comparison

between the 2009 data with a bias current of $\sim$40 μA and the simulated ones with a reflection coefficient of 0.6 and a noise term of 150 photons.

Energy	Resolution X (data)	Resolution Y (data)	Resolution X (simulation)	Resolution Y (simulation)
1 GeV	0.66 cm	0.70 cm	0.59 cm	0.60 cm
2 GeV	0.40 cm	0.48 cm	0.34 cm	0.35 cm
3 GeV	0.32 cm	0.37 cm	0.28 cm	0.27 cm
4 GeV	0.28 cm	0.33 cm	0.24 cm	0.23 cm
5 GeV	0.25 cm	0.30 cm	0.22 cm	0.22 cm
6 GeV	0.23 cm	0.29 cm	0.21 cm	0.21 cm
7 GeV	0.21 cm	0.28 cm	0.20 cm	0.20 cm

Table 5.8: Spatial resolution for different beam energies using the SiPMs biased at 40 μA, compared with the optical simulation results with a reflection coefficient of 0.6 and a noise term of 150.

The optical simulation gives overall results which are consistent with the experimental data. However, in the low energy range (1–3 GeV) there is not a perfect agreement, in particular for the y direction. The differences between data and simulation may originate from small non-uniformities in the SiPMs gain and in the WLS readout efficiency, which are not included in the optical GEANT4 simulation. The optical simulation can be also used to check if the spatial resolution depends on the number of readout channels, which modifies the readout pitch. In particular, the simulation has been used to test the spatial resolution capability of the 36 readout channels configuration described in the following part of the chapter (section 5.3). The comparison between the 0.6 and 0.9 reflection coefficient configurations with 36 readout channels is presented in Fig. 5.26.

As expected, due to the smaller pitch of the 36 channels configuration, the spatial resolution performances are better than the ones obtained in the 16 channels case, with a resolution of 2.5 and 2.0 mm at 1 GeV and of 1.5 and 1.3 mm at 7 GeV using the reflection coefficients of 0.6 and 0.9.

5.3 The 2011 Beamtests

During 2011 the modified version of the prototype 1 calorimeter has been tested at CERN in three different beamtests on the T9 and H2 beamlines with energies up to 8 GeV and 150 GeV respectively. The calorimeter has been modified according to the results of the GEANT4 optical simulation, increasing the number of readout channels, inserting white Tyvek sheets as inter-tile material to enhance the light

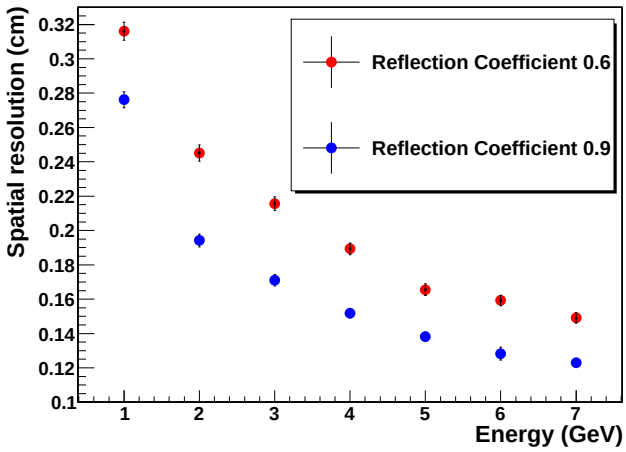

Figure 5.26: Spatial resolution with the optical simulation using a reflection coefficient of 0.6 (red dots) and 0.9 (blue dots) without the noise term in the 36 channels configuration.

output and using a wide area and large dynamic range SiPM for the light readout. Moreover, a readout system based on the MAROC3 ASIC has been developed for the SiPMs readout. A custom board, directly plugged on the SiPMs, has been used as an interface between the SiPMs array and the MAROC3 input pins; the board provides also nine independent lines for the SiPM bias.

5.3.1 Calorimeter Modifications

The prototype 1 calorimeter has been disassembled and modified at the University of Insubria. The edges of each scintillator tile have been wrapped with thin strips of Tyvek, held in place near the corners with small pieces of tape. Tyvek sheets have been positioned between the lead and scintillator tiles: considering the number of layers and the thickness of the Tyvek sheets (130 μm), some tiles have been removed in order to fit the dimensions of the aluminum vessel. The new version of the calorimeter is composed of 65 tiles of scintillator and 65 tiles of lead (70 and 69 in the previous configuration), for a total of $\sim$18 radiation lengths ($\sim$19 in the previous version). Some pictures of the calorimeter during the Tyvek wrapping are shown in Fig. 5.27.

The number of readout channels has been increased from 16 to 36, using bundles of four fibers for each channel (Fig. 5.28(a)). The back side of the fibers (Fig. 5.28(b)) has been polished and mirrored using disks of Tyvek, glued with optical glue on the fiber surface.

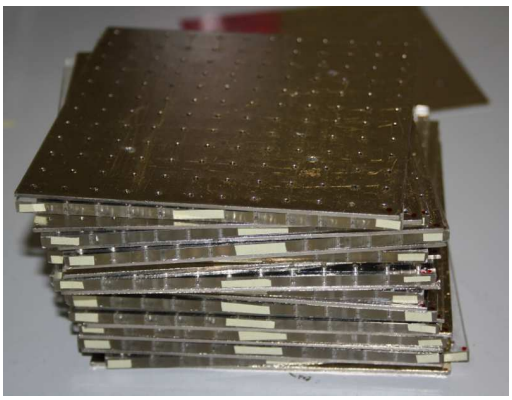

(a)

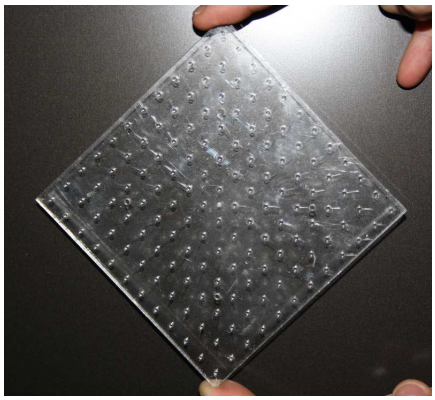

(b)

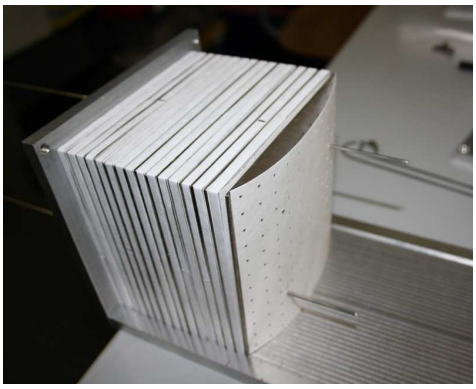

(c)

Figure 5.27: Lead and scintillator tiles (a): the small pieces of tape on the scintillator tiles are clearly visible; wrapping of a scintillator tile (b); assembly phase of the calorimeter with the Tyvek sheets used as the inter-tile material (c).

The bundles of fibers have been fixed to a fiber/SiPMs holder by means of three plastic “combs”. Two types of holder have been used:

- a plastic holder (Fig. 5.29(a)) for the May 2011 tests, characterized by 36 fibers holes and 36 SiPMs seats (one SiPM for each fiber hole);
- an aluminum holder (Fig. 5.29(b)) for the August and September 2011 tests, characterized by 36 fibers holes and 40 SiPMs seats. The four extra SiPMs were used for the common mode evaluation and subtraction and were not interfaced to any fiber. This holder has been used to perform preliminary tests on the use of a Peltier system to cool and stabilize the temperature of the SiPMs during the run.

The modified prototype 1 calorimeter has been equipped with a LED monitor

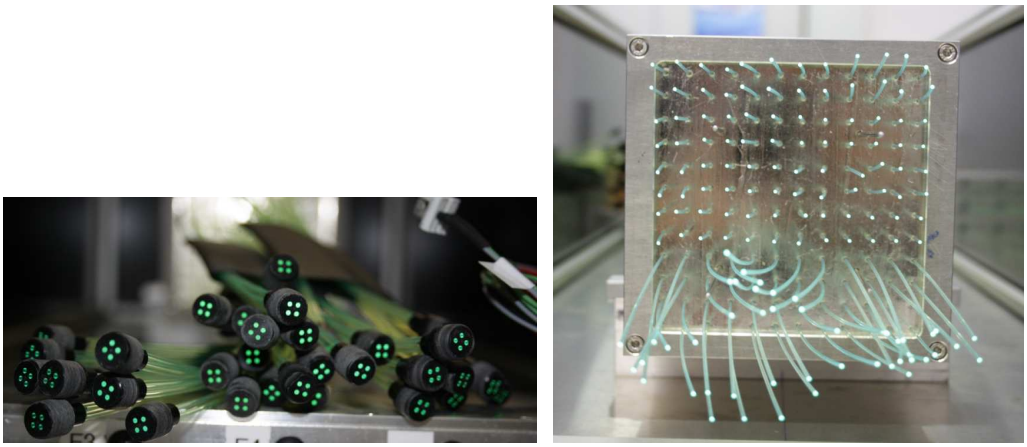

(a) (b)

Figure 5.28: New plastic holders with four fibers (a) and back side of the fibers (b) before the mirroring procedure.

system, which was used during the run to correct the gain variations of the SiPMs, due essentially to the temperature variations. In the May tests the LED system consisted in a single LED placed in the middle of the fibers bundles. In the August and September tests the system has been improved and integrated into the fibers holder: three custom PCBs have been developed, each one able to host six LEDs. The PCBs have then been plugged directly on the "combs" used to hold the fibers in position (Fig. 5.30) to illuminate all the fibers.

In the August and September tests the calorimeter has also been equipped with a preliminary temperature control system, based on four Peltier thermal devices. The Peltier cells have been placed beneath the aluminum holder in order to cool it, while the hot side was positioned on a large aluminum block, used also as a base for the holder (Fig. 5.31(a)). In this way the heat generated by the thermal devices was absorbed by the large aluminum block and dissipated through the metallic base of the calorimeter box. Thermal conducting grease has been used as an interface between the Peltier cells and all the aluminum components to enhance the thermal propagation, while the fibers/SiPMs holder has been covered with neoprene rubber to thermally insulate it (Fig. 5.31(b)). The temperature of the fiber/SiPMs holder has been monitored using two temperature gauges placed inside two holes drilled on the side of the holder itself.

The calorimeter was readout by 36 SiPMs manufactured by FBK-irst with a sensitive area of 16 mm^2 and 6400 50x50 μm^2 pixels. The larger dynamic range with respect to the previous 9 mm^2 SiPMs and the increased number of readout channels (*i.e.* less fibers per channel) should reduce the saturation effects at high energy of the 2010 tests, even considering the light collection enhancement due

(a)

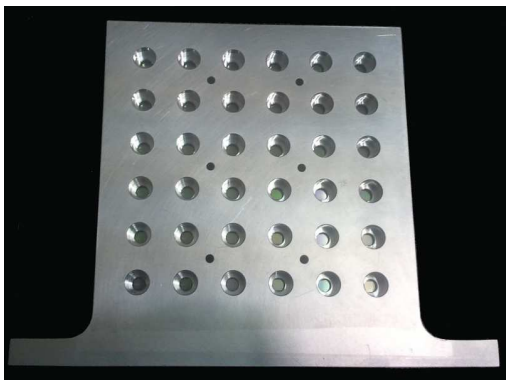

(b)

(c)

Figure 5.29: Plastic (a) and aluminum (b) fibers holders. The aluminum holder has 4 extra SiPMs seats (c) used for the common mode evaluation.

to the Tyvek sheets. The features of the SiPMs are the same of the 9 mm^2 ones and are reported in Table 2.2. A custom interface board (Fig. 5.32(a)) has been developed to couple the SiPMs to the MAROC3 board. The board is directly plugged on the SiPMs pins in order to avoid the use of LEMO cables (as in the prototype 0 tests described in section 4.2). The custom board provides also nine independent lines for the bias of the SiPMs.

The final assembly of the MAROC3 and custom board is quite compact and light, thus no extra supports are needed to hold the boards in position more than the SiPM pins themselves. In Fig. 5.33 the assembly used in the May 2011 tests is presented, with the plastic fibers/SiPMs holder and no Peltier system.

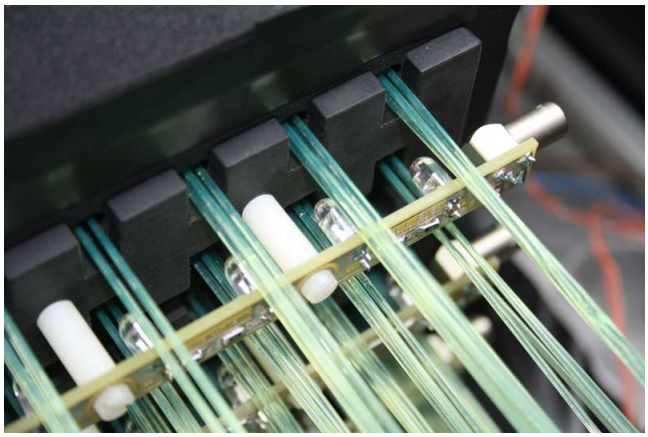

Figure 5.30: Complete LED system used in the August and September test. The LEDs are soldered on three custom PCBs (six LEDs per PCB) and screwed on the plastic "comb" used to hold the fibers in position.

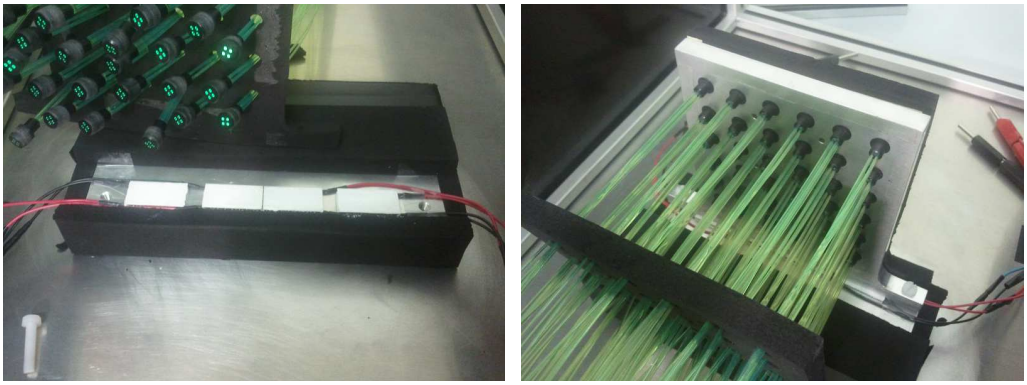

(a) (b)

Figure 5.31: Peltier cells positioned on the large aluminum block used to dissipate the produced heat (a) and aluminum fiber/SiPMs holder (b) in position.

5.3.2 Experimental Setups

The experimental setups of the 2011 tests are quite similar to the ones previously described in sections 4.1.2.1, 4.2.1 and 5.1.2. Fig. 5.34(a) presents the setup on the H2 beamline. During these tests, a remotely controlled multichannel power supply (Fig. 5.34(b)) manufactured by CAEN has been used for the SiPM biasing; it consists of:

- a rack system (SY2527) which provides the bias and the ethernet interface for the remote controlling;

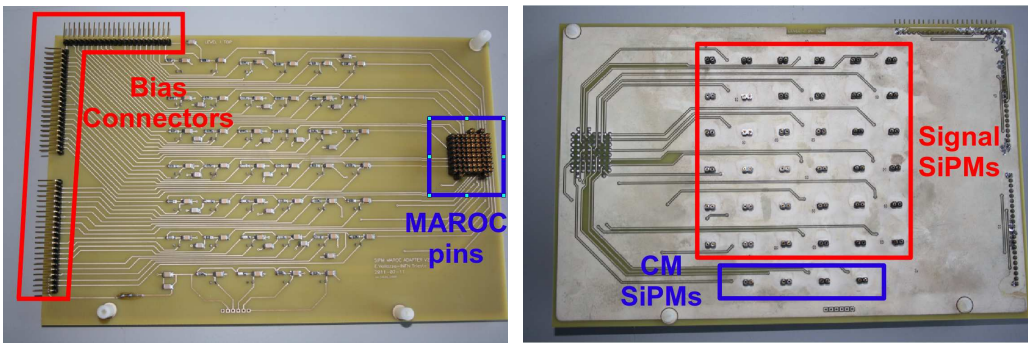

(a) (b)

Figure 5.32: Custom board used to bias the SiPMs and to couple them to the MAROC3 board. In (a) the bias connectors (top left) and the connection pins to the MAROC3 board can be seen, while in (b) the 40 SiPM connectors are visible.

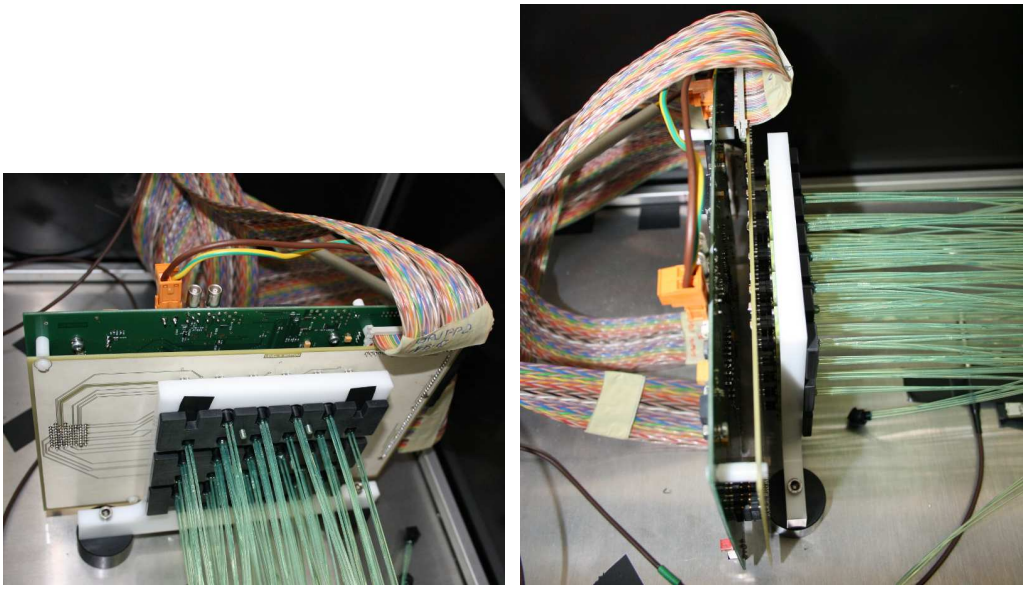

(a) (b)

Figure 5.33: Frontal (a) and lateral (b) view of the final assembly of the MAROC3 board and the custom SiPMs readout board, directly plugged on the SiPMs pins.

- a multichannel board (A1520P) with 12 output lines with a maximum of 500 V–15 mA each. The voltages can be set in steps of 1 mV, while the resolution of the current monitoring is 25 nA.

Considering the number of SiPMs and the number of bias lines provided by the MAROC/SiPM interface board, only nine of the available twelve channels have

(a)

(b)

Figure 5.34: Experimental setup on the H2 beamline (a) and the CAEN power supply front panel (b).

been used, dividing the 36 SiPMs into nine groups of four SiPMs each. During the data taking, the bias voltages and the power consumptions of the nine groups have been logged by the DAQ. Table 5.9 summarizes the different bias values used in the 2011 tests for the nine SiPMs groups.

The LED system was driven by a Agilent 33220A pulse generator, set to provide fast pulses with a width of 200 ns and a rise time of 30 ns. The pulses were triggered by the DAQ trigger board after each extraction spill and tagged in the data to be used for the gain correction in the off-line analysis.

Group	15 μA	10 μA	5 μA	2 μA
1	36.1 V	34.9 V	33.5 V	32.3 V
2	35.8 V	34.7 V	33.3 V	32.2 V
3	35.5 V	34.4 V	32.6 V	31.7 V
4	36.2 V	35.0 V	33.6 V	32.5 V
5	36.4 V	35.2 V	33.8 V	32.6 V
6	35.3 V	34.2 V	32.8 V	31.7 V
7	34.7 V	33.3 V	32.2 V	31.2 V
8	34.5 V	33.3 V	32.0 V	31.0 V
9	36.2 V	34.8 V	33.6 V	32.5 V

Table 5.9: Bias values for the nine SiPMs groups in the four current configurations.

5.3.3 Low energy Results - May 2011

The first tests of the improved version of the calorimeter have been performed in May 2011 on the T9 beamline with an energy up to 8 GeV, using the same analysis procedure described in the previous sections. Three energy scans have been performed with bias values of 5, 10 and 15 μA and a MAROC gain of 10, 8 and 5.

The information provided by the LED has been used to correct the gain drift of the SiPMs with the temperature using the same algorithm developed for the MIPs correction. The LED ADC information has been sampled as a function of the event number with a granularity of 5000 events (Fig. 5.35(c)) and the energy deposit has been corrected using the following formula:

$$E_{line} = E \times \frac{A}{Peak_{(evNumber)}} \tag{5.1}$$

where E_{line} is the linearized energy deposit, E is the total deposited energy, A is a normalization constant (the LED peak position in a reference run) and $Peak_{(evNumber)}$ is the position of the LED peak as a function of the event number. A linear interpolation between the points of the LED drift plot has been used for the intermediate event numbers. Figs. 5.35(a) and 5.35(b) present the drift of the electrons and MIPs peaks before and after the linearization procedure. The LED correction system is much more reliable with respect to the MIP one and is able to correct pretty large deviations. This is due to the fact that the accuracy of the correction with the MIP system depends on the number of particles available in the MIP peak, which is a function of the beam energy. This problem is overcome by the use of the LED system, in which a fixed number of LED events is collected after each

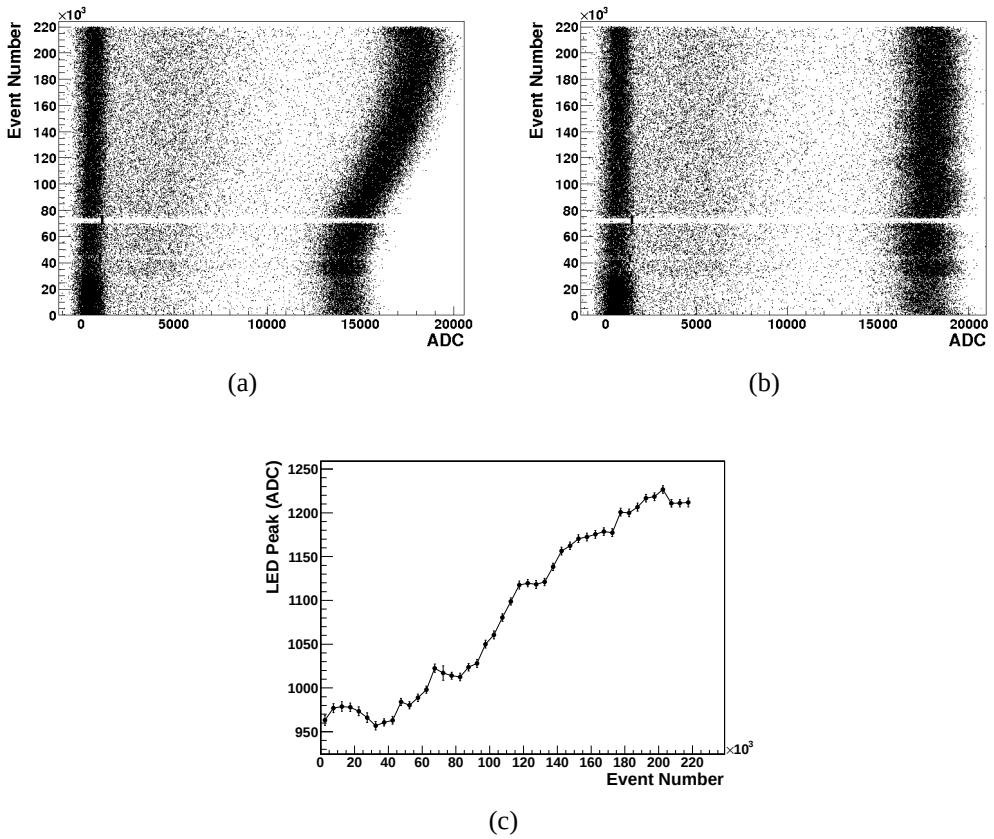

Figure 5.35: Drift of the electron and MIP peaks before (a) and after (b) the linearization procedure performed with the LED system (c).

spill independently from the energy.

In the modified prototype 1, the exponential tail in the electron peak is absent (Fig. 5.36), confirming the results of the optical GEANT4 simulation. The electron peaks have thus been fitted with a Gaussian function in the [-σ,3σ] range to define the energy resolution value.

The results in terms of linearity and energy resolution are presented in Fig. 5.37. The linearity is quite good, thanks to the improvements in the linearity correction performed with the LED system. Only a small saturation effect is present at 8 GeV in the 10 μA bias and gain 8 configuration.

As far as the energy resolution is concerned, the best result is the one of the 15 μA configuration, with a stochastic term of 8.6%, very similar to the reference performance of the calorimeter (in both the standard and optical GEANT4 simulations). However, the energy resolution scans are characterized by large noise terms, much larger than the ones obtained in the 2010 preliminary test using the

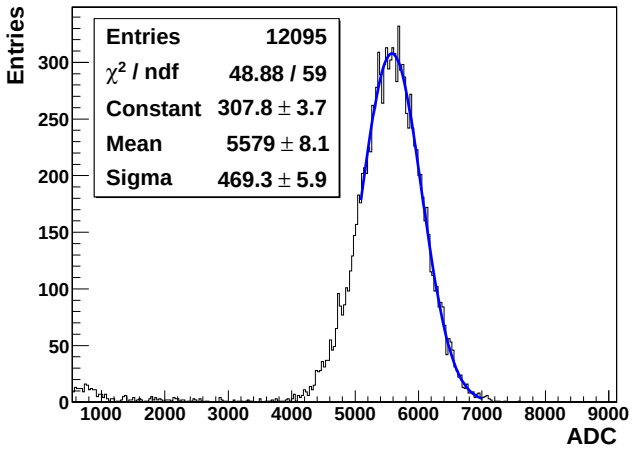

Figure 5.36: 2 GeV electron peak fitted with a Gaussian function in the [-σ,3σ] interval. The improved light collection efficiency has removed the exponential tail on the right found in the 2009 and 2010 tests.

prototype 0 calorimeter and the MAROC readout. The noise term is even larger than the one expected by the fit of the pedestal distribution, as if a second effect in addition to the electronics noise enters the game. For this reason the noise term has been left as a free parameter in the fit. In fact, the expected noise terms from the pedestal fit are 5.85, 8.15 and 14.11% compared to the values of 11.78, 12.07 and 16.96% extracted from the fit. The energy resolution results are summarized in Table 5.11 (see next section).

In agreement with the optical simulation, the larger number of readout channels has improved also the spatial resolution capability of the calorimeter, as shown in Fig. 5.38 for a 8 GeV beam (current 15 μA, gain 5). Table 5.10 presents the results between 1 and 6 GeV, compared to the ones obtained in the 2009 tests; even better results can in principle be achieved reducing the electronic noise.

To conclude, the results of the May tests can be summarized as follows:

- the use of the Tyvek sheets has removed the exponential tails in the energy distribution confirming the predictions of the optical GEANT4 simulation;
- the stochastic terms of the energy resolution are of the order of 9–10%, with a major improvement with respect to the 2009 and 2010 tests;
- considering the small saturation effect in the 10 μA scan at 8 GeV, a careful selection of the SiPMs bias and MAROC gain should be performed to avoid the saturation with the MAROC readout system. Given the high gain of the SiPMs even at small bias values, the use of the MAROC minimum possible

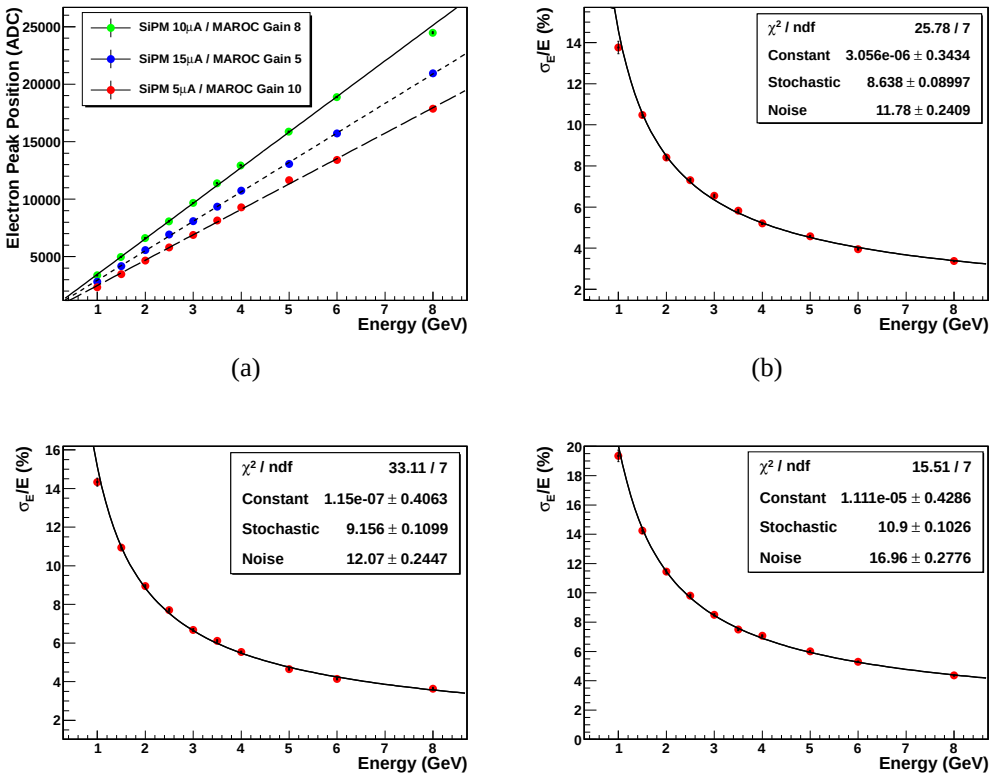

Figure 5.37: Linearity (a) and energy resolution in the 15 μA (gain 5) (b), 10 μA (gain 8) (c) and 5 μA (gain 10) (d) configurations.

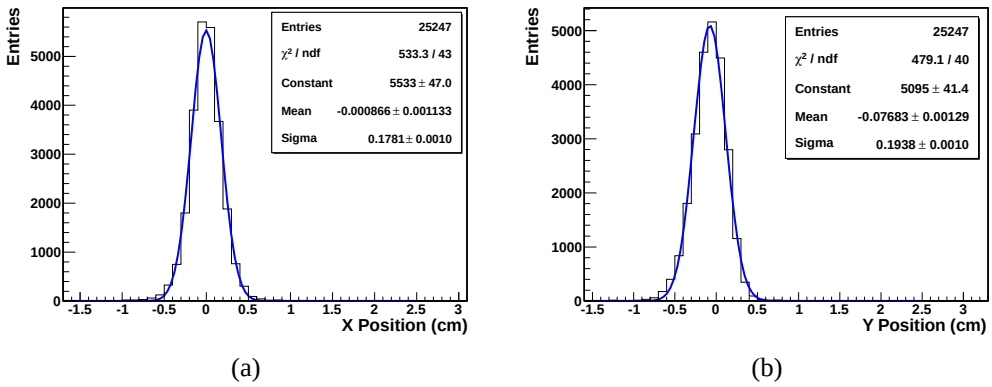

Figure 5.38: Spatial resolution at 8 GeV in the x (a) and y (b) direction using the 15 μA and gain 5 configuration.

Energy	Resolution X (2009 data)	Resolution Y (2009 data)	Resolution X (2011 data)	Resolution Y (2011 data)
1 GeV	0.66 cm	0.70 cm	0.55 cm	0.64 cm
2 GeV	0.40 cm	0.48 cm	0.39 cm	0.46 cm
3 GeV	0.32 cm	0.37 cm	0.33 cm	0.35 cm
4 GeV	0.28 cm	0.33 cm	0.28 cm	0.28 cm
5 GeV	0.25 cm	0.30 cm	0.25 cm	0.25 cm
6 GeV	0.23 cm	0.29 cm	0.22 cm	0.22 cm

Table 5.10: Comparison between the spatial resolutions for different beam energies obtained with the 2009 40 μA and the 2011 15 μA data.

gain (*i.e.* 1, which actually corresponds to an attenuation of a factor 64 of the signal) seems mandatory for energies above 10 GeV.

The main problem is still represented by the large electronics noise introduced by the MAROC/SiPM interface, even if a custom board directly plugged between the MAROC inputs and the SiPM output pins has been used. One of the possible explanations is the presence of a common mode[2] component, induced by a non-optimal impedance matching between the input stages of the MAROC ASIC and the circuitry of the interface board. For this reason in the August tests four more SiPMs, not connected to any WLS fiber, have been used to evaluate the common mode contribution.

5.3.4 Low energy Results - August 2011

The goal of the August test was to re-check the performance of the calorimeter at low energies using the minimum MAROC gain value. Moreover, some modifications had been introduced with respect to the May setup:

- an improved LED system, with 18 LEDs positioned near the WLS fibers and the SiPMs using custom PCBs (Fig. 5.30);
- four more SiPMs (CM-SiPMs), not connected to any WLS fiber, to evaluate and correct event by event the common mode of the MAROC ASIC;
- a preliminary temperature control system, based on four Peltier cells, placed beneath the fiber/SiPMs holder.

[2]The common mode can be considered as a fluctuation common to all the ASIC channels, usually induced by noise on the bias lines.

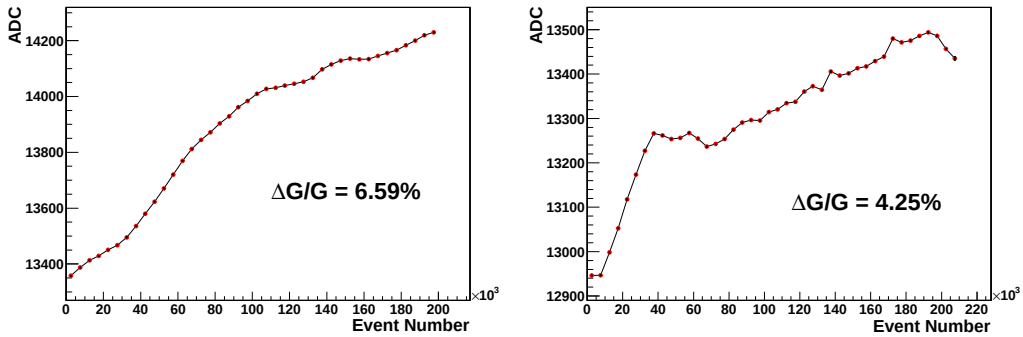

(a) (b)

Figure 5.39: LED peak drift without (a) and with (b) the Peltier system. Using the Peltier system the gain variations are still present, but reduced with respect to the run without the control system.

The Peltier system worked as follows: the temperature of the fiber/SiPMs holder was monitored by two temperature gauges inserted in the upper and lower part of the holder itself. The temperature values were readout by a Keithley K2700 multimeter, while the Peltier cells were biased with a TTI TXS1820P power supply. Both the multimeter and the power supply were remotely controlled via a GPIB interface. A Tcl/Tk routine modified the Peltier bias in order to keep the temperature as stable as possible. However, due to the non perfect thermal insulation of the fiber/SiPMs holder (despite the neoprene rubber covering) and to the limited sampling frequency of the temperature feedback (approximately 1 s was needed for the readout of the temperature value and the change of the bias value), the Peltier system has not been able to completely correct the temperature variations during the runs. The limited effect of the Peltier system can be observed in the LED peaks drift of Fig. 5.39, a drift which is only reduced and not eliminated.

As far as the common mode is concerned, its value is evaluated for each event calculating the mean value of the CM-SiPMs. The common mode value is then subtracted from each channel event by event. The common mode distribution and the effect of its subtraction on the total energy deposit are presented in Fig. 5.40 for a MAROC gain of 10.

The common mode subtraction does not introduce particular benefits, improving only slightly the energy resolution, becoming almost ineffective in the energy scan results. Similar results have been obtained with the MAROC gain set to 1.

As far as the linearity is concerned, the new low energy measurements with the minimum value of the gain are quite good, with no saturation effect at all (Figs. 5.41(a) and 5.41(b)). Moreover, the improved LED system helps to correct the SiPMs gain variations even better. On the other hand, the efficacy of the

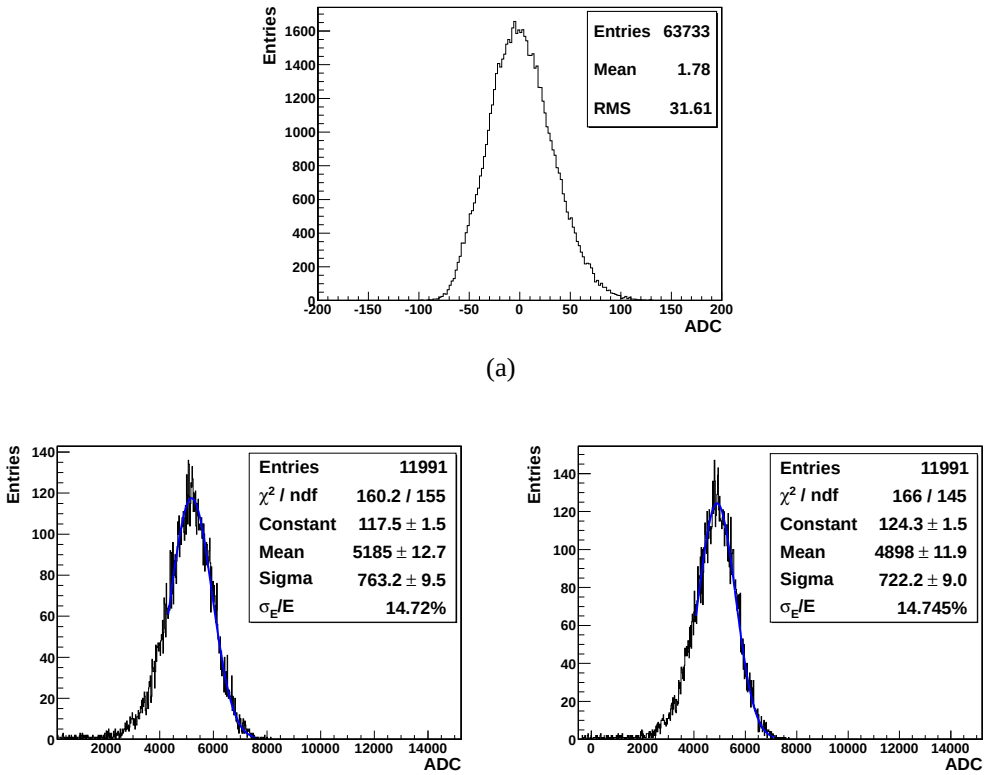

Figure 5.40: Common mode distribution (a) and total energy distribution at 1 GeV with (b) and without (c) the common mode subtraction with a MAROC gain of 10.

Peltier system is very small. As far as the the energy resolution is concerned, a stochastic term of the order of 10% and a constant term compatible with zero have been obtained in all the configurations, while the noise parameter has been fixed to the sigma value of the pedestal distribution (Figs. 5.41(c) and 5.41(d)). However, the resulting fit underestimates the low energy points (as in the May tests), as can be seen looking at the large χ^2 values of the fit. In conclusion, the common mode subtraction does not improve the energy resolution measurements, with results very similar to the ones obtained in May. Table 5.11 summarizes the energy resolution results of the May and August beamtests. A more detailed analysis of the noise problem introduced by the MAROC readout and a possible solution is presented in appendix B.

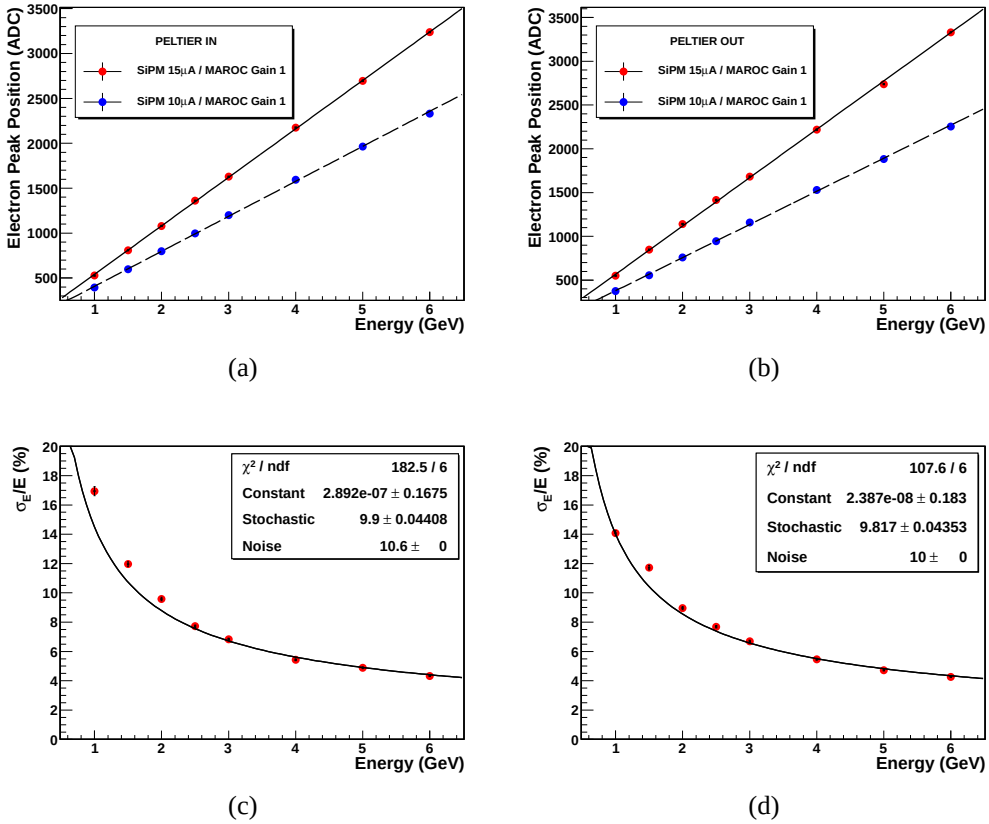

Figure 5.41: Linearity in the 10 μA and 15 μA configurations with (a) and without (b) the Peltier system; energy resolution in the 15 μA configuration with (c) and without (d) the Peltier system.

5.3.5 High Energy Results - September 2011

The main goal of the high energy tests was to check if the new configuration with the larger number of channels and the use of the large area SiPMs was able to avoid the saturation effects above 20 GeV as seen in all the previous tests with the two calorimeter prototypes. Differently from the tests on the H4 beamline, where tagged photons have been used, on the H2 beamline the approach was more similar to the T9 tests. In particular, four energy scans have been performed with energies between 15 and 150 GeV with different values of the SiPMs bias and MAROC gain configurations. Considering the small impact on the calorimeter performance of the Peltier system, it has been decided not to use it in this test. The linearity results in the different configurations are presented in Fig. 5.42.

A clear saturation effect due to the MAROC ASIC has been found at energies above 30 GeV using the 10 μA bias value. The saturation effect has been avoided

Configuration	Beamtest period	Constant term (%)	Stochastic term (%)	Noise term (%)
Bias 15 μA Gain 5	May	$\sim$0 $\pm$0.34	8.64 $\pm$0.09	11.78 $\pm$0.24
Bias 10 μA Gain 8	May	$\sim$0 $\pm$0.41	9.16 $\pm$0.11	12.07 $\pm$0.24
Bias 5 μA Gain 10	May	$\sim$0 $\pm$0.43	10.90 $\pm$0.10	16.96 $\pm$0.28
Bias 15 μA Gain 1 Peltier OFF	August	$\sim$0 $\pm$0.18	9.82 $\pm$0.04	10.0 $FIXED$
Bias 15 μA Gain 1 Peltier ON	August	$\sim$0 $\pm$0.17	9.90 $\pm$0.04	10.6 $FIXED$
Bias 10 μA Gain 1 Peltier OFF	August	$\sim$0 $\pm$0.31	10.21 $\pm$0.06	11.2 $FIXED$
Bias 10 μA Gain 1 Peltier ON	August	$\sim$0 $\pm$0.37	10.36 $\pm$0.06	10.7 $FIXED$

Table 5.11: Energy resolution comparison between the May and August 2011 beamtests.

decreasing the gain of the SiPMs (*i.e.* the bias). Starting from the 5 μA configuration an acceptable linearity was achieved, with the best results obtained in the two 2 μA configurations. As far as the energy resolution is concerned, a large deviation from the standard $\frac{1}{\sqrt{E}}$ behavior has been observed at energies above 30 GeV, as shown in Fig. 5.43. This deviation can be understood looking at the common mode distributions obtained with the four CM-SiPMs, which are characterized by the presence of a second peak (Fig. 5.44). This peak is probably due to particles leaking from the back of the calorimeter that interact with the SiPMs, firing some pixels. This hypothesis is confirmed by the fact that the position of the second peak increases with the beam energy, where more particles leak from the back. The signals and the fluctuations induced by these particles deteriorate the energy resolution measurements, resulting in the observed deviation from the $1/\sqrt{E}$ behavior.

The only way to improve this situation is to increase the number of radiation lengths of the calorimeter ($> 24\,X_0$), thus reducing the particles leaking from the back, with positive effects also on the constant term of the energy resolution. Another solution could be to move the fiber/SiPMs away from the back of the calorimeter (for example on a side), using longer WLS fibers. Both these approaches are now under study for the next beamtest campaign in 2012.

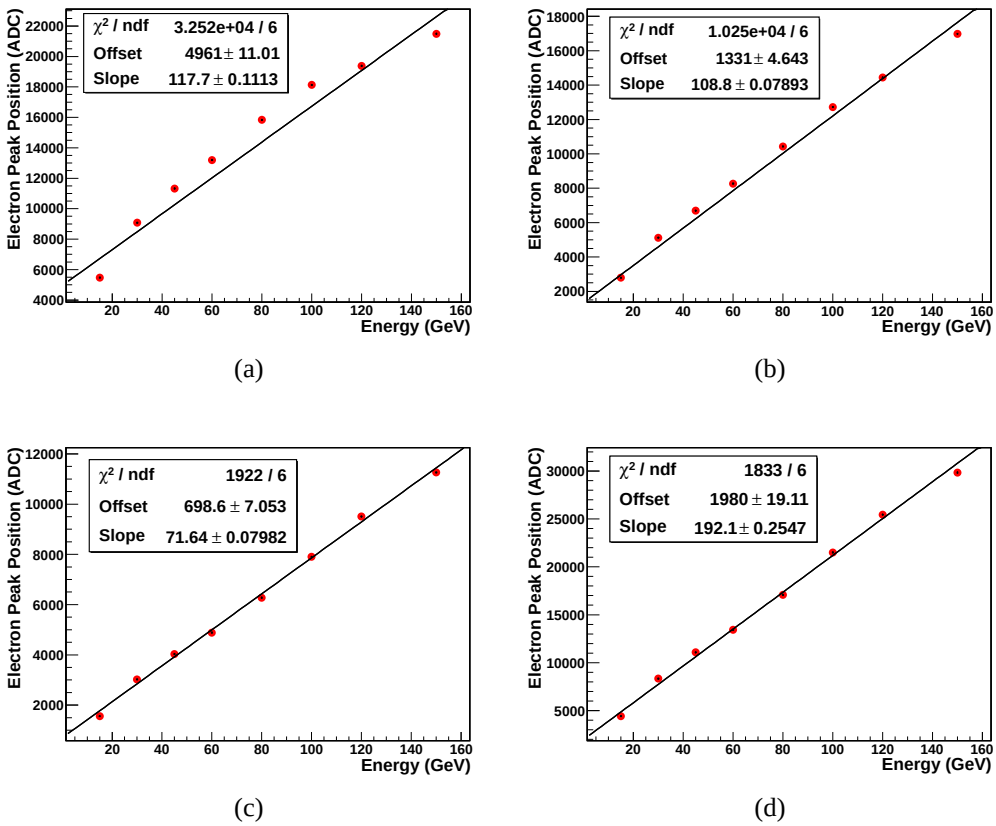

Figure 5.42: Linearity in the 10 μA (a), 5 μA (b) and 2 μA (c) bias configurations with the MAROC gain 1 and in the 2 μA bias configuration (d) with the MAROC gain 3.

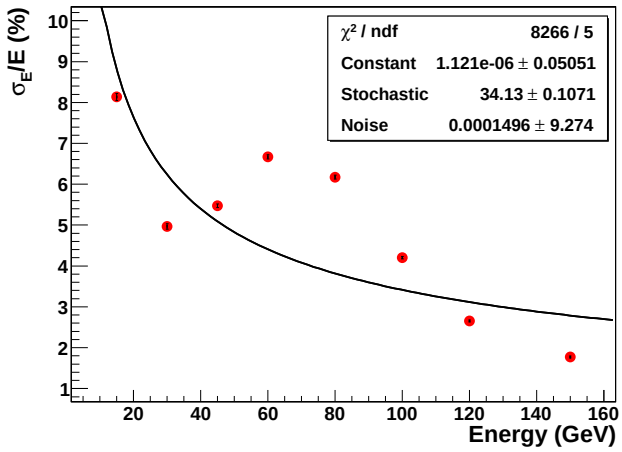

Figure 5.43: Energy resolution deviation from the $1/\sqrt{E}$ behavior in the H2 high energy tests.

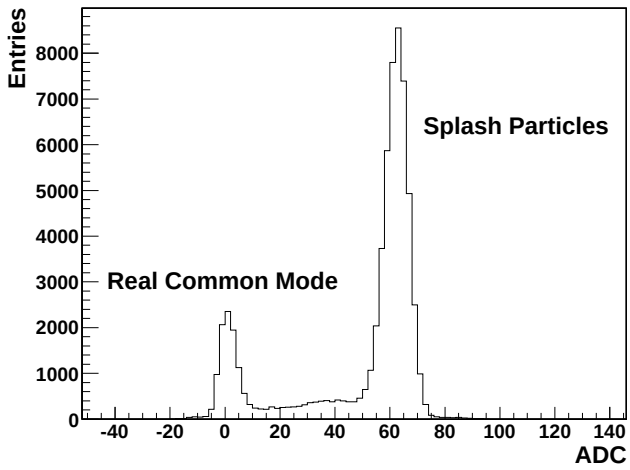

(a)

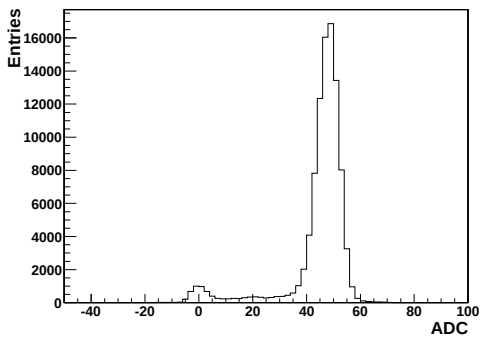

(b)

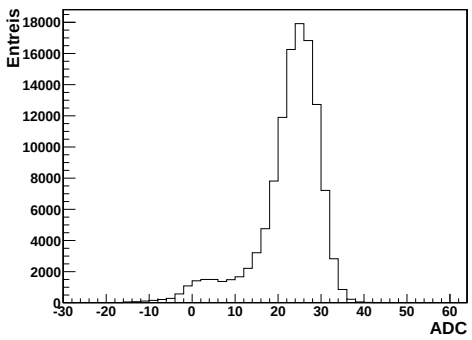

(c)

Figure 5.44: Common mode distributions at 150 (a), 100 (b) and 30 (c) GeV. The second peak in the distribution is due to particles leaking from the back of the calorimeter which fire some of the pixels.

Chapter 6

From Sampling to Homogeneous Calorimeters: the Lead Tungstate Crystals

Lead tungstate is an inorganic scintillating crystal with features which make it a perfect candidate for high energy physics applications. Studied since 1940, lead tungstate crystals have recently been used by the CMS experiment at the LHC to build a very compact electromagnetic calorimeter which is operated inside a strong magnetic field, thus being readout by silicon based detectors (APDs and VPTs). This chapter is devoted to a brief description of the tests of lead tungstate crystals coupled to a new type of SiPM manufactured by FBK-irst. These tests are very preliminary and can be considered as a first evaluation of the new SiPMs performance in a real high energy physics context.

6.1 The $PbWO_4$ Crystals

Lead tungstate, or $PbW0_4$ according to its chemical formula, is a non-hygroscopic scintillating crystal developed for high energy physics experiments, and in particular for the CMS electromagnetic calorimeter [95] at the LHC. More details on the lead tungstate crystals can be found in [96]. $PbWO_4$ crystals are characterized by an exceptional high density (8.28 g/cm^3), a small radiation length (0.89 cm^{-1}) and a very fast scintillation constant ($\sim$6 ns). These qualities have been exploited by the CMS experiment to build a very compact calorimeter (26 X_0 using 23 cm long crystals), able to work in the harsh LHC environment, where bunches spaced of 25 ns are used, thus needing a fast scintillation component in order to avoid dramatic pile-up effects. The main drawbacks of $PbWO_4$ are a relatively small light yield (200 γ/MeV, of the order of one hundred times less than CsI), and a

temperature dependent light emission (-2.1% °C^{-1} at 18° C [97]) which forces the use of these crystals in a temperature controlled environment. As can be seen in Fig. 6.1, the emission peak of $PbWO_4$ is located around 420 nm, while the optical transparency is good over the whole visible spectrum.

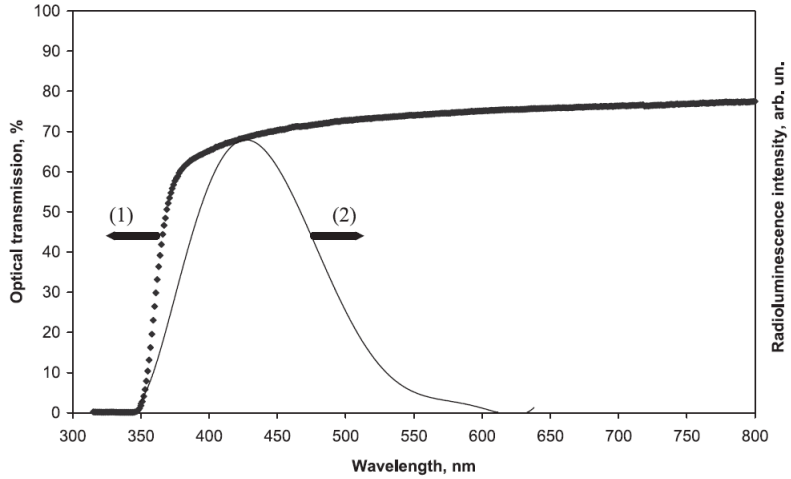

Figure 6.1: Optical transmission (percentage, left Y axis) and emission spectra (arbitrary units, right Y axis) of $PbWO_4$ crystals [96].

The scintillation mechanism of lead tungstate is not modified by irradiation. However, the exposure to large doses of ionizing radiation produces absorption bands due to oxygen vacancies and impurities in the lattice. The practical consequence is a wavelength-dependent loss of light transmission without changes to the scintillation mechanism [97]. The radiation damage effects can be corrected monitoring the optical transparency of the crystals: in the CMS experiment this task is performed through the injection and detection of a laser light inside the crystal. As previously stated, the scintillation light of the crystals is readout using silicon photodetectors, in particular APDs in the barrel and VPTs in the endcaps. More details on the APDs can be found in section 2.2.3.

6.2 Experimental Setup

The lead tungstate crystals have been tested at CERN on the T9 beamline, during a beamtest dedicated to the study of a scintillating bar tracker. The setup is the typical one described in sections 4.1.2.1 and 5.1.2 and it is composed of:

- two Cherenkov detectors for the electron tagging;
- two silicon strip chambers for the track reconstruction;

- two 10×3 cm^2 plastic scintillators for the trigger.

The $PbWO_4$ crystal (provided by INFN-Trieste) used for the test is an early-prototype version of the crystals developed for the electromagnetic calorimeter of the CMS experiment. It consists of a 23 cm long trapezoid bar (corresponding to $\sim$26 X_0) with a front face of 20.5x20.5 mm^2 and a back face of 24.4x24.4 mm^2, forming a quasi-projective geometry. The crystal is wrapped with a Tyvek sheet to enhance the light output (Fig. 6.2).

Figure 6.2: Picture of the $PbWO_4$ crystal wrapped in the Tyvek sheet.

The scintillation light has been readout using a new type of SiPM manufactured by FBK-irst, called *quad*, which consists in a monolithic array of four SiPMs with an area of 4x4 mm^2 and 5625 pixels each (Fig. 6.3). Even if the four SiPMs are all grown on the same silicon substrate, their bias and output is independent. For this reason a custom board (Fig. 4.4), consisting of a single bias line and four outputs, has been used for each quad SiPM. The signal of the quad has been delayed of 120 ns and then sampled using the V792 QDC, thus no signal amplification is present.

The quad SiPMs have been coupled to the $PbWO_4$ crystal using a plastic C-clamp, held in place on a side of the crystal with a nylon screw. The clamp is used as a base for one or two quads on the crystal face, which are then held in position using a plastic plate. Optical grease has been used between the face of the crystal and the quad to enhance the light collection. A picture of the crystal assembled with the quad SiPMs positioned on the plastic clamp is presented in Fig. 6.4.

The quad SiPMs have been preliminary tested in the laboratory in order to study the I-V curves of each element. During these tests, it has been found that the I-V characteristics of each SiPM can be very different even inside the same quad (Fig. 6.5(a)). For this reason, only the SiPMs with the more similar I-V curves have been selected for the beamtest (Fig. 6.5(b)).

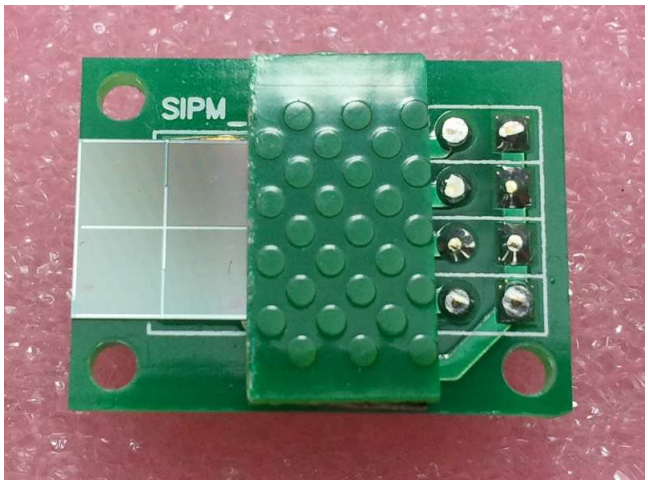

Figure 6.3: Picture of the FBK-irst quad SiPM assembled on its PCB.

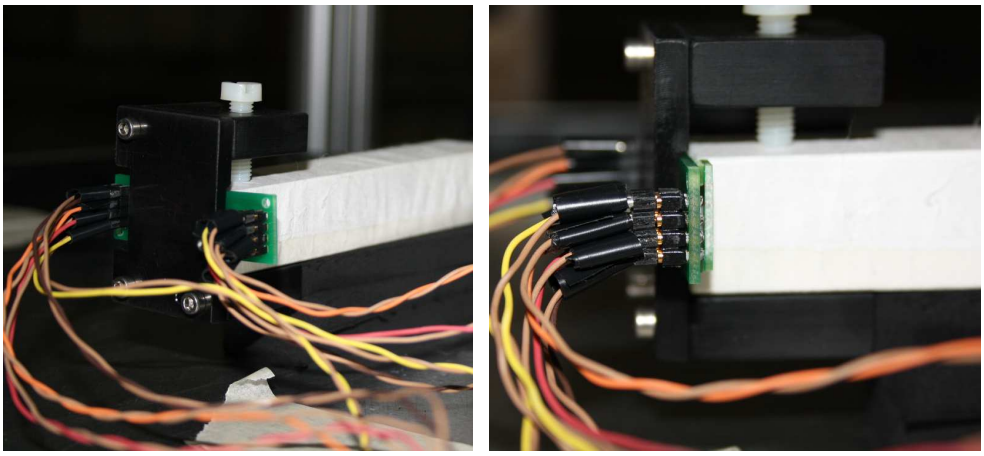

(a) (b)

Figure 6.4: Pictures of the plastic clamp used to hold the quad SiPMs in position on the crystal. The clamp is fixed on the crystal using a nylon screw, and the SiPMs are positioned over the clamp, held in place by a plastic plate.

During the beamtest, the bias voltage of the quad has been set to 46.5 V, which corresponds to bias currents between 25 and 35 μA depending on the SiPM. As will be presented in the following, an equalization procedure based on the MIP signal has been applied during the beamtest in order to equalize the gain and the response of each SiPM. Two types of tests have been performed:

- the comparison between the single and dual quad readout in terms of efficiency and energy resolution, using a single beam energy of 1 GeV;

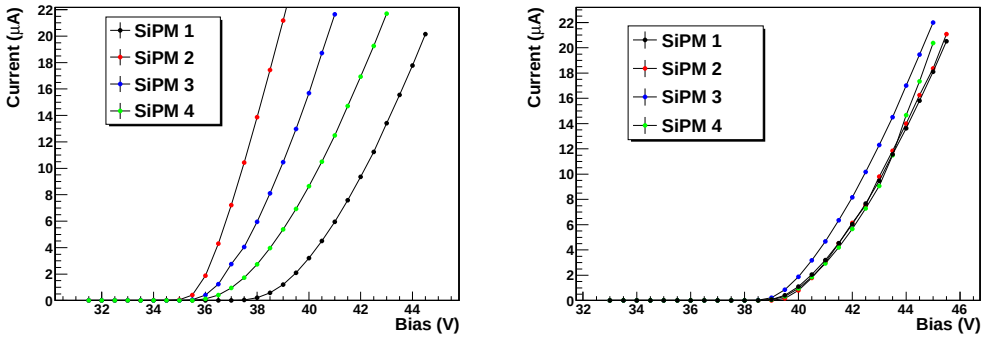

(a) (b)

Figure 6.5: Example of I-V curves obtained for two quads characterized by very different (a) and very similar (b) pads characteristics.

- a partial energy scan between 1 and 3 GeV to evaluate the linearity and the energy resolution of the system.

6.3 Results

The crystal used on the T9 beamline has been selected after a laboratory test performed at the University of Insubria using cosmic rays. The available crystals have been coupled to a P30CW5 (Electron Tubes[1]) photomultiplier and the best crystal in terms of light output has been selected. The pulse heights of the different crystals are presented in Fig. 6.6.

The crystal chosen for the beamtest is labeled as "T02"; at a visual inspection this crystal is the least yellowish of the batch. As far as the T9 beamtest is concerned, the first event selection is performed using the silicon beam chambers, selecting only the single track events, as described in the tests presented in the previous chapters. The electron events are then tagged using the information provided by the two Cherenkov detectors. Considering the small dimensions of the crystal, only the events impinging on a fiducial area of 1x1 cm^2 centered in the central part of the crystal itself have been selected. Each output of the quad SiPMs has been corrected for the temperature using the same algorithm based on the position of the MIP peak developed for the shashlik calorimeters analysis. The first step of the analysis is the comparison of the detection efficiency of the single and dual SiPMs readout.

As can be seen in Fig. 6.7 the detection efficiency is larger than ∼95% for both the single and dual SiPM readout.

[1]Now Sens-Tech Ltd.; www.senstech.com

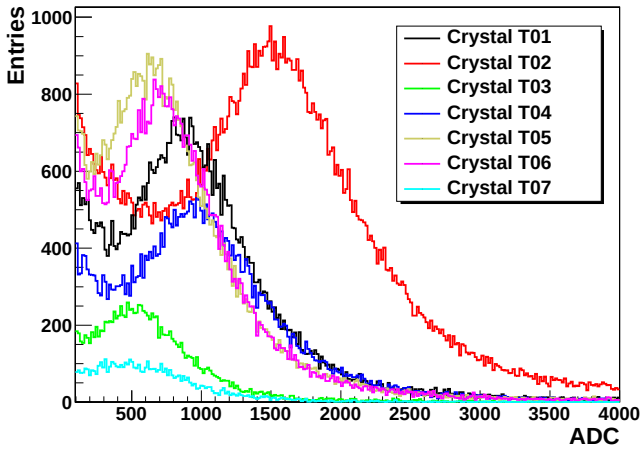

Figure 6.6: Pulse height of the different crystals in the cosmic rays test. The crystal labeled as "T02" is the one that has been chosen for the beamtest.

As far as the energy resolution at 1 GeV is concerned (Fig. 6.8), the dual readout method proved to be more effective, with an energy resolution of 13.7% compared to the 14.6% of the single readout. For this reason it has been decided to perform the linearity and the energy resolution scan with this readout configuration.

As can be seen in Fig. 6.9(a), the linearity is quite good, thanks also to the MIP drift correction algorithm. As far as the energy resolution is concerned (Fig. 6.9(b)), the scan is dominated by a stochastic term of 11.9%, a very small constant term (but compatible with 2% considering the errors), and a noise term which has been fixed to the energy equivalent of the pedestal noise. The energy resolution results are very different from the beamtest results quoted by the CMS collaboration [4], that are of the order of 2.8% for the stochastic term and of 0.26% for the constant term. It must be said that the test performed with the SiPM readout cannot be directly compared with the CMS official tests because of a large number of factors:

- a large energy leakage due to the use of a single crystal, instead of using clusters of 3x3 or 5x5 crystals as in the final CMS calorimeter;
- the used $PbWO_4$ crystal is an early prototype, probably characterized by a small light yield and with performances affected by aging;
- a non optimized electronic chain;
- the absence of a temperature control to keep the light output of the lead tungstate stable.

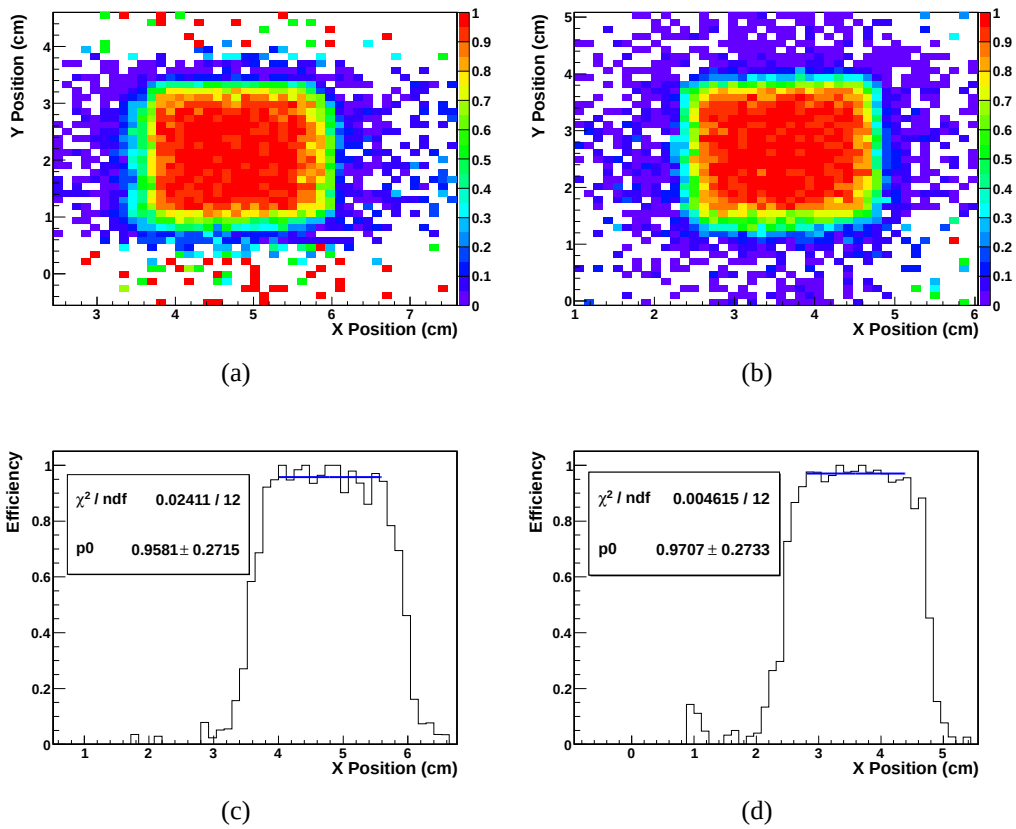

Figure 6.7: Crystal detection efficiency with the single (a) (c) and dual (b) (d) quad SiPM readout.

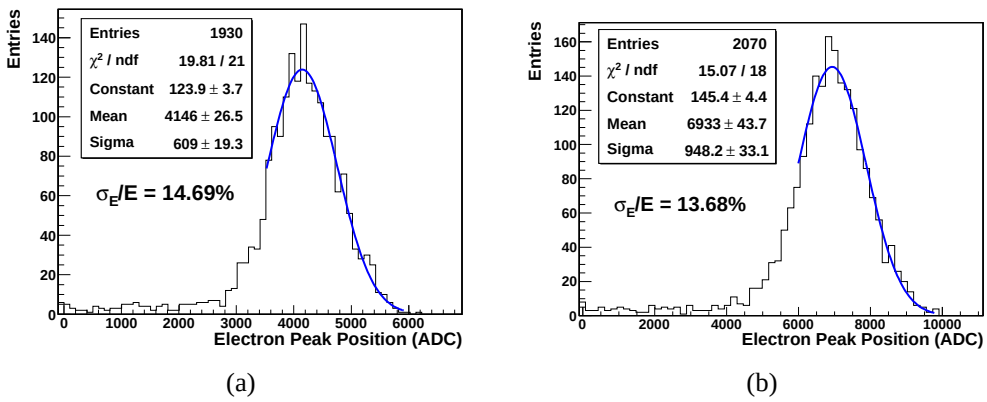

Figure 6.8: Energy resolution at 1 GeV with the single (a) and dual (b) SiPM readout.

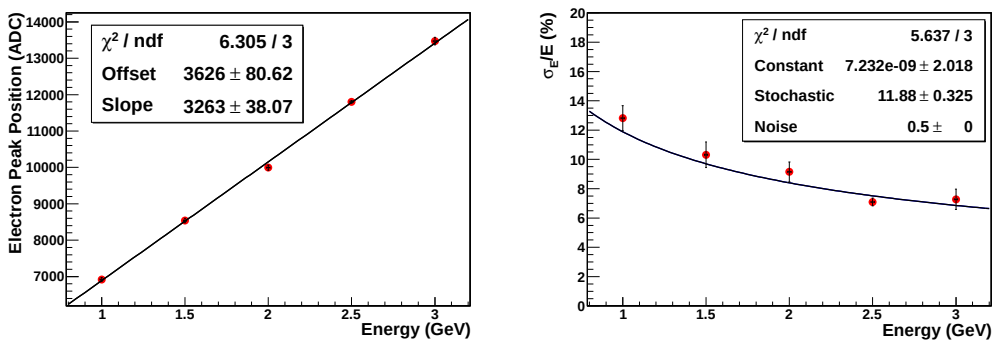

(a) (b)

Figure 6.9: Energy linearity (a) and energy resolution (b) with the dual SiPM readout.

Conclusions and outlooks

Nowadays silicon photomultipliers represent one of the most important alternatives to the widespread PMTs especially in high energy and space physics applications, where very stringent requirements in terms of magnetic insensitivity, power consumption, dimensions and costs have to be fulfilled. As explained in the first chapter of this thesis work, the key requirement of the next generation colliders will be to efficiently separate the $W^{\pm}$ and Z^0 bosons through their hadronic decays. On the other hand, the next generation space experiments will require large area calorimeters with fine segmentation and large dynamic range. In both these fields, scintillator based detectors have been chosen by several R&D projects for their advantages in terms of cost per channel, mechanical durability and weight. However, the light readout system is still an open field with several options depending on the application, a field where silicon photomultipliers represent a real breakthrough.

This thesis has dealt with the study of different types of silicon photomultipliers (with different dimensions, dynamic range and technology) and the development of a complete readout system for scintillating detectors. Both these tasks have been fulfilled by means of three ”reference detectors” (a scintillating bar tracker and two prototypes of shashlik calorimeters) used as benchmarks for the study of the SiPMs and the readout systems performance. Taking into account the scintillation mechanism and the fiber readout, these detectors are conceptually similar to the ones recently proposed to improve the hadronic resolution of the next generation colliders.

As far as the SiPM characterization is concerned, four types of devices with progressively larger dynamic range have been tested:

- the $\sim$1 mm diameter ones with 688 cells;
- the 3x3 mm^2 ones with 3600 cells;
- the 4x4 mm^2 ones with 6400 cells;
- a matrix of four SiPMs (called *quad*), each one with an area of 4x4 mm^2, embedded on the same silicon substrate for a total of 22500 cells (5625 per

SiPM).

The 1 mm diameter SiPMs have been first coupled to a scintillating bar tracker, obtaining comparable results with respect to the multi-anode photomultiplier tubes in terms of detection efficiency and spatial resolution, and with an even better performance in terms of timing resolution. On the other hand, the tests showed that SiPMs are characterized by a smaller signal to noise ratio (due to their large intrinsic noise) and their performance can be affected by radiation damage, especially by the neutron induced one. These SiPMs have also been used for the readout of the first prototype of shashlik calorimeter (prototype 0), with the following problems:

- the saturation of the calorimeter response in the high energy range, due to the limited number of cells of the SiPMs;
- a slightly worse energy resolution (compared to the Monte-Carlo simulation and to the MAPMT readout), due to the larger noise of the SiPMs;
- the SiPM gain dependence on the operating temperature.

In particular, the SiPM gain variation was identified as a primary issue since it affects both the linearity and the energy resolution. During the beamtest, the gain of the SiPMs has been monitored and corrected off-line using the MIPs signal; however, the effectiveness of this correction procedure was limited by the amount of collected MIPs (which varied with the beam energy) and could not be applied in the high energy tests due to the different type of beam.

The 3x3 mm^2 and 4x4 mm^2 SiPMs have been used with the second prototype of the shashlik calorimeter. Characterized by a larger number of pixels, these devices have been chosen to improve the calorimeter linearity with respect to the 1 mm diameter ones. The prototype 1 calorimeter was tested using the 3x3 mm^2 SiPMs with results mainly affected by the non optimal features of the calorimeter, and corresponding to a large stochastic term and the presence of long tails in the electron peak. The results have been reproduced with a dedicated GEANT4 simulation which takes into account all the optical processes, like the scintillation, the wavelength shifting and the light transport inside the fibers. The simulation showed that the long exponential tails and the poor energy resolution could be ascribed to the absence of inter-tile reflective material. Thus, an improved version of the calorimeter was assembled inserting Tyvek sheets as inter-tile material to enhance the light output, increasing the number of readout channels (in order to avoid saturation effects) and introducing a LED system in order to monitor and correct the SiPM gain variations with the temperature.

The improved version of the calorimeter has been tested using the 4x4 mm^2 SiPMs, obtaining a good linearity for energies up to 150 GeV. Moreover, the introduction of the Tyvek sheets improved the light output and the stochastic term of the energy resolution, while the LED system proved to be able to correct the SiPMs gain variations more effectively than the MIP procedure.

From the readout point of view, two types of systems have been developed:

- a standard one, based on a multichannel charge integrating 12 bit ADC;
- a new one, based on the MAROC3 frontend ASIC, a 64 channel readout chip with both analog and digital outputs, originally designed for MAPMTs.

The standard system based on the 12 bit QDC can be considered a valuable alternative in the case of a small number of channels. Among the advantages, the large dynamic range and the versatility should be listed. However, this type of readout is not suitable for a large number of channels, given that delay lines are needed to align in time the SiPMs signal with the ADC gate generated by the DAQ.

The new readout system is based on the MAROC ASIC and has been specifically developed to improve the overall system integration when a large number of readout channels is needed. This system can be adapted both to MAPMTs and SiPMs (maintaining the versatility of the standard QDC system), but it is characterized by a limited dynamic range. This is obviously a limit, especially for high energy calorimetric applications, but the results obtained with the second calorimeter prototype showed that an acceptable linearity could be maintained up to 150 GeV using the minimum pre-amplifier gain value and a small SiPM overvoltage.

On the other hand, the MAROC readout introduces a large noise term which worsened the signal to noise ratio of the SiPMs (in the tracker test) and the noise parameter of the energy resolution (in the calorimeter test). The source of the noise was at the beginning ascribed to a non optimal integration of the SiPMs with the MAROC board (*i.e.* the use of custom LEMO cables to connect the SiPMs board with the MAROC one). For this reason, the modified version of the prototype 1 calorimeter has been equipped with a custom interface board for the SiPM-MAROC coupling in order to reduce the noise contribution of this readout system as much as possible. The non satisfactory results obtained also in this configuration led to an accurate analysis of the MAROC readout noise described in Appendix B. This study allowed to identify the noise sources in the “very long” shaping time of the MAROC pre-amplifier ($\sim$500 ns) and in the SiPM current monitoring cables. The tests performed with a low intensity LED showed that it is possible to reduce the MAROC noise by (at least) a factor two implementing a new monitoring cable and reducing the shaping time of the MAROC output.

Recently, a new type of ASIC specifically developed for the SiPM readout (EASIROC, Extended Analogue SI-pm ReadOut Chip) has been produced. This frontend chip features 32 parallel inputs with 2 variable gain pre-amplifiers, a maximum input charge of 320 pC (compared to $\sim$5 pC of the MAROC) and a 4.5 V range, 8-bit DAC per channel used for the tuning of the overvoltage/gain of the SiPM. A new readout system based on the EASIROC ASIC will be developed for the second part of 2012 and will be used for the readout of the calorimeters and the scintillating tracker.

The last part of the thesis describes the tests performed with a new type of SiPM, a matrix of four 4x4 mm^2 SiPMs called *quad*, coupled to an inorganic scintillating crystal of lead tungstate. The $PbWO_4$ crystal has been preliminary tested using low energy electrons, evaluating the linearity, energy resolution and detection efficiency of the complete system. The MIPs signal has been used to equalize all the pads of the *quad* and to correct the gain drifting with temperature variations, obtaining a good linearity and a detection efficiency larger than 97%. New tests are foreseen with a 3x3 module that will be readout using both the *quads* or an array of 16 independent SiPMs (the 4x4 mm^2 version with 6400 cells) integrated on a single tile (Fig. 7.1), for a total of 102400 cells.

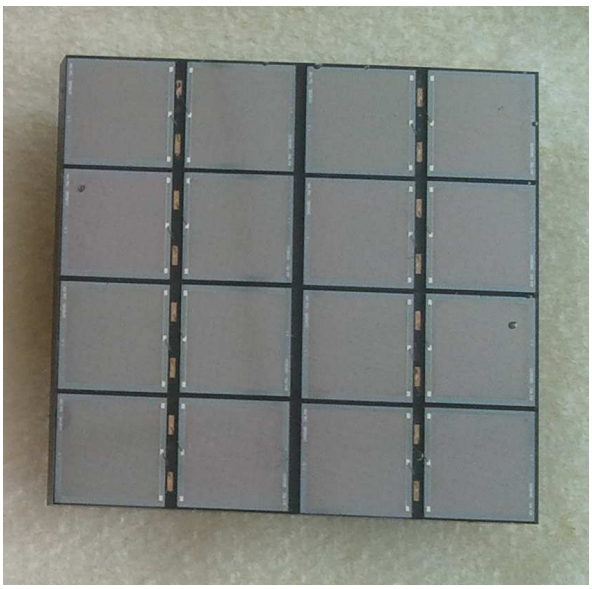

Figure 7.1: SiPM tile with 16 4x4 mm^2 SiPMs.

Considering the extremely large dynamic range of this device, crystals characterized by a larger light output with respect to $PbWO_4$, as BGO or LYSO, could be in principle used without any saturation problem.

At the time of writing, many research groups are testing or using SiPMs in

a large number of fields. Besides the calorimetry topic, SiPMs can be used for TOF systems, RICH detectors, muon and tail catcher detectors for the Super-LHC experiments or the new generation colliders. Moreover, extensive tests are being performed in the medical physics field, aiming at the introduction of combined PET-NMR scanners or real time and portable dosimeters based on plastic scintillators. In other words, if the introduction of the photomultiplier tubes can be considered as a milestone in the scintillating detectors development, the silicon photomultipliers represent without any doubt the future of light readout.

Appendix A

Electromagnetic Calorimeters

High energy photons or electrons create showers of particles during their passage inside a medium: electromagnetic calorimeters are detectors designed to degrade and completely absorb the shower in order to give an accurate measurement of its energy. This appendix is devoted to a brief description of the processes characterizing the longitudinal and lateral development of an electromagnetic shower and the energy resolution capability of the calorimeter itself. A complete and comprehensive treatment of this topic can be found in [1, 98].

A.1 Homogeneous or Sampling

Considering their construction, electromagnetic calorimeters can be divided in *homogeneous* and *sampling*. Homogeneous calorimeters are made of a single type of material which is used both to degrade the incoming particle and to measure its energy. On the contrary, sampling calorimeters are composed of alternating layers of two (or more) types of material: the first ones, usually formed by high density material, are used to degrade the incoming particle energy while the second ones consist of a sensitive material which measures the energy deposit. Homogeneous calorimeters are characterized by a smaller number of fluctuations in the energy deposit, thus their energy resolution is usually better than the one of sampling calorimeters (see section A.5). On the contrary, for their intrinsic construction sampling calorimeters can be easily segmented in both the lateral and longitudinal dimensions, thus providing better information on the impact point of the particles. Moreover, sampling calorimeters are usually less expensive than the homogeneous ones. The shashlik calorimeter used for most of this thesis work belongs to the sampling category.

A particular type of homogeneous calorimeters are the ones built for the study of cosmic ray particles [98]. These types of calorimeters use the sea water, the air

in the atmosphere and even the ice of the polar ice-cap as the active medium to measure the energy deposit of the extremely high energy cosmic rays, which are characterized by a very low flux and are spread over a large area.

A.2 Electron/Positron Energy Loss

Like heavy charged particles, electrons and positrons lose energy through collisions with the atoms of the medium. However, because of their small mass, an additional mechanism comes on the scene: the electromagnetic emission of radiation arising from the scattering of the electrons with the electric field of the atomic nucleus. This phenomenon is called irradiation or *bremsstrahlung* (Fig. A.1).

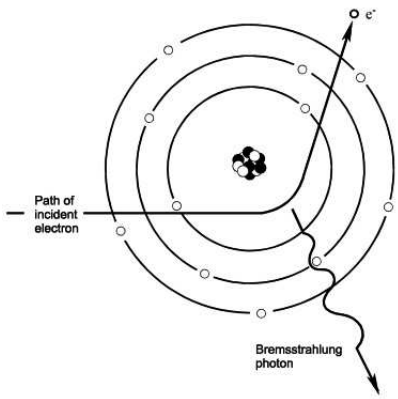

Figure A.1: Schematic representation of the bremsstrahlung process.

Bremsstrahlung can be considered as the quantum mechanical equivalent of the classical emission of electromagnetic waves by accelerated charged particles. The total electron/positron fractional energy loss is presented in Fig. A.2.

Other interactions, like the Møller and Bhabha scattering, take place at very low energy but the ionization and bremsstrahlung processes are the dominant ones. The electron ionization cross section is computed starting from a modified version of the Bethe-Bloch formula, which takes into account the fact that the incident particle can be deflected by the interaction and the collisions are between identical particles [35]. Omitting the less important contributions, the ionization cross section can be expressed as:

$$\left(\frac{dE}{dx}\right)_{ion} \simeq Z \ln(E) \tag{A.1}$$

On the contrary, the bremsstrahlung cross section depends on the energy and

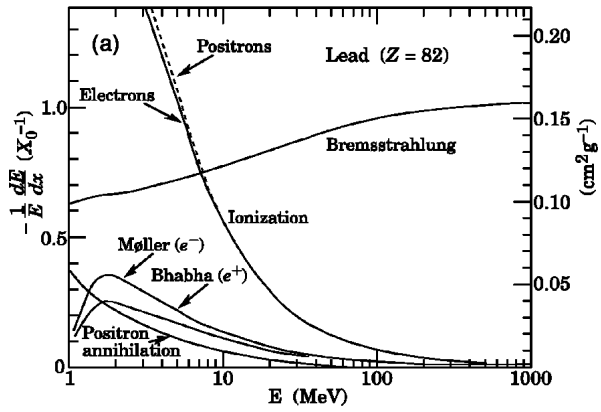

Figure A.2: Electron/positron fractional energy loss per radiation length in lead as a function of energy [6].

atomic number according to [35]:

$$\left(\frac{dE}{dx}\right)_{brem} \simeq r_e^2 \, Z^2 \, E \tag{A.2}$$

where $r_e \simeq e^2/mc^2$ is the electron classical radius. Considering the energy dependence of equations A.1 and A.2, the bremsstrahlung process should dominate the electron energy loss at high energy thanks to the linear energy dependence. Moreover, the dependence from the inverse of the squared mass of the particle explains why the bremsstrahlung process is important only for electrons. For example the muon, the next lightest particle, has a mass 200 times larger than the one of the electron, resulting in a bremsstrahlung cross section reduced by a factor 40000.

The energy at which the energy loss via bremsstrahlung equals the ionization one is called *critical energy* or ε_c. Considering the Z dependence of the ionization and bremsstrahlung cross sections, the critical energy is a material dependent quantity and its numerical approximation can be expressed as [35]:

$$\left(\frac{dE}{dx}\right)_{ion} = \left(\frac{dE}{dx}\right)_{brem} \Leftrightarrow \quad \varepsilon_c = \frac{800 \text{ MeV}}{Z + 1.2} \tag{A.3}$$

A slightly different definition of the critical energy is given in [6], where it is defined as the energy at which the ionization loss per radiation length (X_0[1]) equals the electron energy. Using this definition, the critical energy value can be

[1]The radiation length is the scale parameter of the electromagnetic showers and will be defined in section A.4.

expressed as:

$$\left(\frac{dE}{dx}\right)_{ion} X_0 = E \Leftrightarrow \varepsilon_c = \frac{610\ \text{MeV}}{Z+1.24}(\text{solid/liquid}), \frac{710\ \text{MeV}}{Z+0.92}(\text{gas}) \qquad \text{(A.4)}$$

As will be shown in the following, this second definition describes better the transversal profile of an electromagnetic shower. The difference between the two definitions is presented in Fig. A.3.

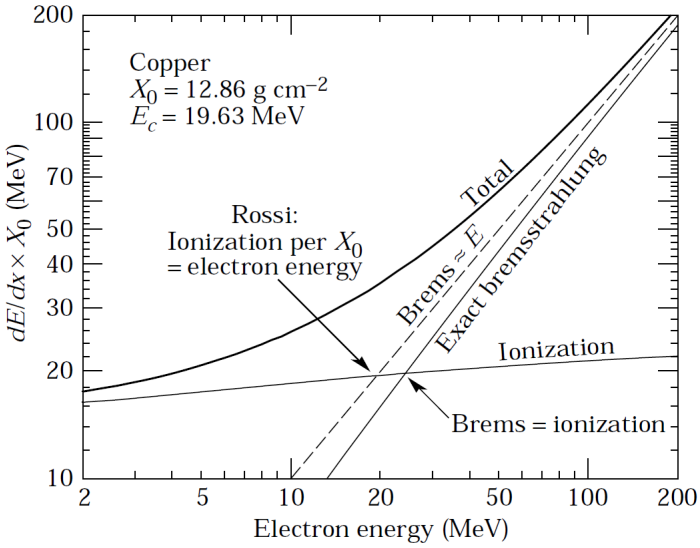

Figure A.3: The two definitions of the critical energy in copper [6].

A.3 Photon Energy Loss

The photon interaction with matter is mainly ruled by three different phenomena [6]:

- the photoelectric effect, in which the photon is absorbed by an atom with the emission of an electron;
- the Compton effect, in which the photon interacts with one of the electrons of the atomic shell giving it part of its energy but without being absorbed;
- the pair production, in which the photon, after the interaction with an atom, disappears creating an electron-positron pair.

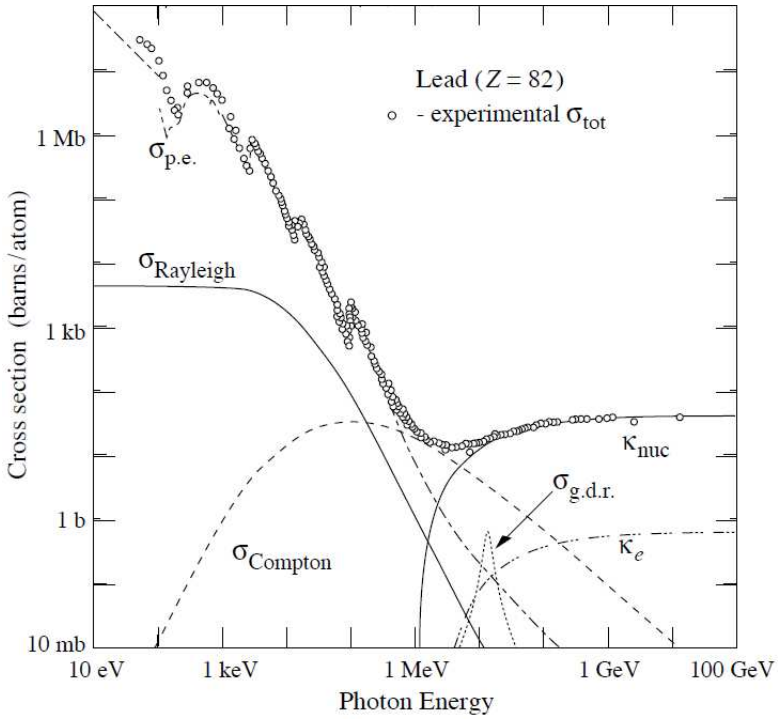

Figure A.4: Photon interaction cross section in lead as a function of the energy [6]: $\sigma_{p.e.}$ is the photoelectric cross section; σ_C is the Compton cross section; $\sigma_{Rayleigh}$ is the Rayleigh coherent scattering cross section; κ_{nuc} and κ_e are the pair production cross sections on the nuclear and electron fields; $\sigma_{g.d.r.}$ is the Giant Dipole Resonance cross section.

The total cross section of the three different phenomena in lead is presented in Fig. A.4.

These processes are deeply different with respect to the ones of charged particles. The photon is a massless and neutral particle: this means that the elastic collisions with the atomic electrons are no longer possible. The second and most important difference is that the energy of a beam of photons is not degraded in its passage through matter, but it is only attenuated in intensity. The attenuation of a photon beam crossing a material can be expressed as:

$$I(x) = I_0 \exp(-\mu x) \tag{A.5}$$

where I_0 is the incident beam intensity, x the thickness of the absorber and μ the absorption coefficient. The absorption coefficient is a medium dependent quantity, directly related to the total interaction cross section in a particular material. The details of the three different interactions will be described in the following paragraphs.

A.3.1 Photoelectric Effect

As shown in Fig. A.4, the photoelectric effect is the dominant phenomenon at low energy. In this process an atom absorbs the photon and emits an electron. After the electron emission the atom is left in an excited state and a X-ray emission can occur during the de-excitation process (Fig. A.5).

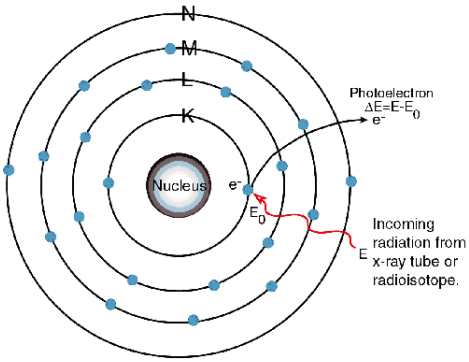

Figure A.5: Graphic representation of the photoelectric effect.

For kinematic constraints due to the momentum conservation, this effect cannot occur with a free electron. For this reason the photoelectric effect involves atomic electrons (the deep shell electrons are the ones expelled with a higher probability), and the nucleus absorbs a small part of the recoil momentum. The energy of the outgoing electron can be calculated using the energy conservation principle:

$$E = h\nu + \phi \tag{A.6}$$

where $h\nu$ is the energy of the incoming photon and ϕ is the binding energy of the shell electron. As far as the photoelectric cross section is concerned, a rigorous treatment is difficult because of the complexity of the Dirac wavefunctions of the atomic electrons. However, an approximated formula can be computed as [35]:

$$\sigma_{ph} \simeq Z^n \, E^{-\frac{7}{2}} \tag{A.7}$$

where n varies between 4 and 5 according to the energy scale. The $E^{-\frac{7}{2}}$ energy dependence explains the plot in Fig. A.4, where the cross section scales very rapidly, becoming a negligible effect beyond $\sim$500 keV.

A.3.2 Compton Effect

The Compton effect consists in the scattering of a photon on a free electron; an atomic electron can be considered free if the energy of the incoming photon is

large enough. During the interaction, the photon gives part of its energy to the electron and is then re-emitted at a lower energy. A sketch of the Compton scattering is presented in Fig. A.6.

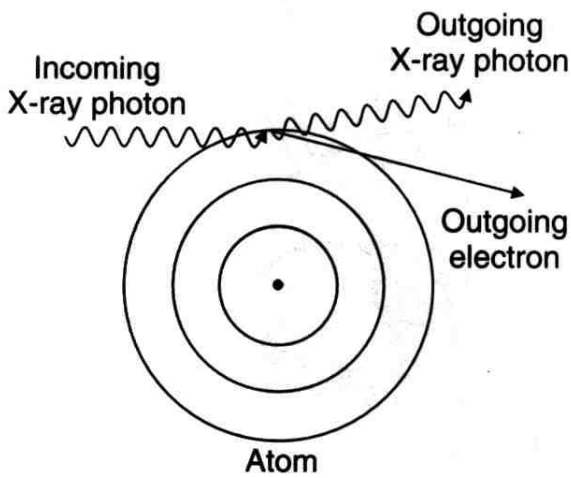

Figure A.6: Graphic representation of the Compton effect.

The Compton effect cross section was one of the first processes to be calculated using QED and it is known as the *Klein-Nishina* formula; the integration of this formula over the solid angle results in [35]:

$$\sigma_c = 2\pi r_e^2 \left\{ \frac{1+\gamma}{\gamma^2} \left[\frac{2(1+\gamma)}{1+2\gamma} - \frac{1}{\gamma}\ln(1+2\gamma) \right] + \frac{1}{2\gamma}\ln(1+2\gamma) - \frac{1+3\gamma}{(1+2\gamma)^2} \right\} \quad \text{(A.8)}$$

where γ is equal to $\frac{h\nu}{m_e c^2}$. As can be seen in the previous equation and in Fig. A.4, the Compton cross section decreases with the energy, and this effect is the dominant one in the 100 keV–10 MeV energy range.

A.3.3 Pair Production

The pair production process consists in the creation of an electron-positron pair by a photon. In order to conserve the momentum, this phenomenon can occur only in presence of a third body, usually an atomic nucleus. Moreover, the energy of the photon should be larger than 1.022 MeV, that is the sum of the rest masses of electron and positron. A representation of the pair production process is sketched in Fig. A.7.

Theoretically, pair production is very similar to the bremsstrahlung process [35]. This means that the energy and medium dependence of the cross section are the

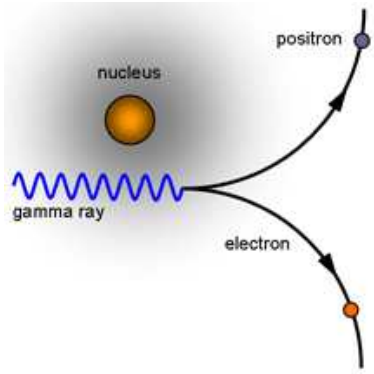

Figure A.7: Graphic representation of the pair production process.

same of the one obtained with the bremsstrahlung cross section:

$$\sigma_{pp} \simeq r_e^2 \, Z^2 \, E \tag{A.9}$$

The linear energy dependence confirms the results shown in Fig. A.4, where pair production is the dominant interaction at energies above 10 MeV. As will be shown in the following, pair production (along with the bremsstrahlung process for electrons) plays a key role in the development of electromagnetic showers.

A.4 Electromagnetic Showers

At high energies, electrons and photons lose energy via bremsstrahlung and pair production. Suppose now that a high energy electron interacts with matter: the electron may radiate photons via the bremsstrahlung process, and if the emitted photons have enough energy, they can convert in an electron-positron pair through the pair production effect. These secondary electrons and positrons will emit other photons, starting an avalanche process that is called *electromagnetic shower*. However, as the shower develops, the average energy of the secondary particles decreases and at some point no further multiplication takes place. The depth at which the shower multiplication stops is called shower maximum; it occurs when the electrons energy is below the critical energy ε_c and when the cross section for the Compton and photoelectric effect starts to dominate the photons absorption. The shower energy is deposited in the absorber material by the electrons and positrons generated by the photon interactions. In particular, it can be shown that the majority of the shower particles through which the energy is deposited are very soft, with energies below 20 MeV (Fig. A.8).

This means that, while the shower development is driven by the high energy pair production and bremsstrahlung processes, the energy deposit is completely

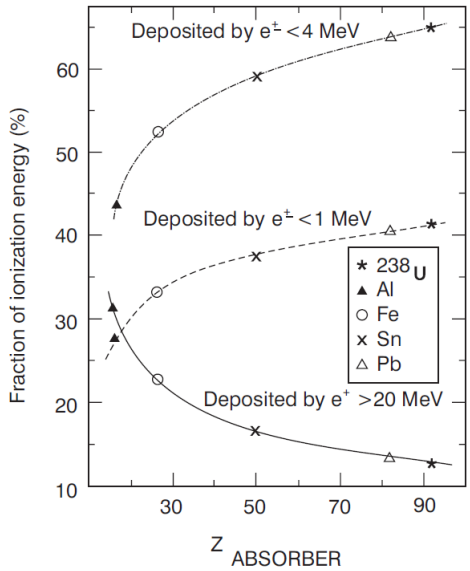

Figure A.8: Monte-Carlo calculation of the shower energy fractions as a function of the atomic number of the absorber. The majority of the shower energy is deposited by low energy electrons and positrons [1].

driven by the low energy processes. In other words, the performances of calorimeters designed to measure the particle energies in the multi-GeV range are determined by processes that take place in the keV range.

The development of an electromagnetic shower can be parametrized in terms of a single parameter, called *radiation length*, X_0, which depends on the characteristics of the material. An approximated formula with an accuracy within 3% is given in [6]:

$$X_0 = \frac{716.4\,A}{Z(Z+1)\,\ln(287/\sqrt{Z})}\ \mathrm{g\ cm^{-2}} \tag{A.10}$$

where Z is the atomic number and A is the atomic weight. The X_0 parameter is defined as the distance over which a high energy electron (or positron) loses on average 1-e^{-1} ($\sim$63%) of its energy through bremsstrahlung. It can be shown that the X_0 parameter is related also to the photon interaction cross section:

$$\sigma(E \to \infty) = \frac{7}{9}\frac{A}{N_A\,X_0} \tag{A.11}$$

where X_0 is expressed in g/cm^2 and the ratio of the Avogadro's number (N_A) and the atomic weight (A) represents the number of atoms per gram of material. This formula implies that the mean free path of a high energy photon is $\frac{9}{7}X_0$. A representation of the shower development as a function of the number of radiation lengths is presented in Fig. A.9.

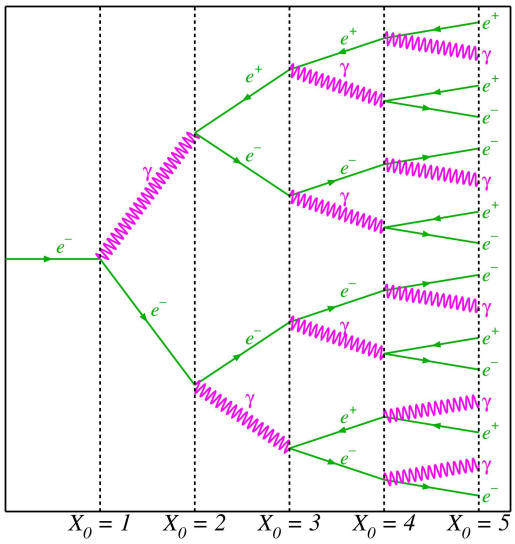

Figure A.9: Representation of the development of an electromagnetic shower as a function of the number of radiation lengths.

The radiation length of a mixture of different materials can be computed using the following relation:

$$\frac{1}{X_0} = \sum_i \frac{V_i}{X_i} \tag{A.12}$$

where V_i represents the volume fraction and X_i the radiation length of the i-th component of the mixture. The radiation length of a compound can be calculated in a similar way:

$$\frac{1}{X_0} = \sum_i \frac{m_i}{X_i} \tag{A.13}$$

where m_i and X_i are the mass fraction and the radiation length expressed in g/cm^{-2} of the i-th component of the compound.

A.4.1 Longitudinal Profile

The mean longitudinal profile of the shower can be computed using the following approximation [6]:

$$\frac{dE}{dt} = E_0 b \frac{(bt)^{a-1} e^{-bt}}{\Gamma(a)} \tag{A.14}$$

where the parameter $t = x/X_0$ is the depth inside the material in terms of radiation lengths and a and b are parameters related to the nature of the incident particles.

The depth at which the largest number of secondary particles is produced can be approximated as [98]:

$$t_{max} \simeq \ln\frac{E_0}{\varepsilon_c} + t_0 \tag{A.15}$$

where t_{max} is the maximum depth expressed in radiation lengths, E_0 is the incident particle energy and t_0 is equal to 0.5 or -0.5 for photons or electrons. It is possible to calculate the required thickness to contain 95% of the electromagnetic shower, using the following approximated formula [98]:

$$t_{95\%} \simeq t_{max} + 0.08Z + 9.6 \tag{A.16}$$

As can be seen in equation A.16, the longitudinal containment of the shower depends weakly on the material properties. A Monte-Carlo calculation confirming the Z dependence of the longitudinal containment is presented in Fig. A.10.

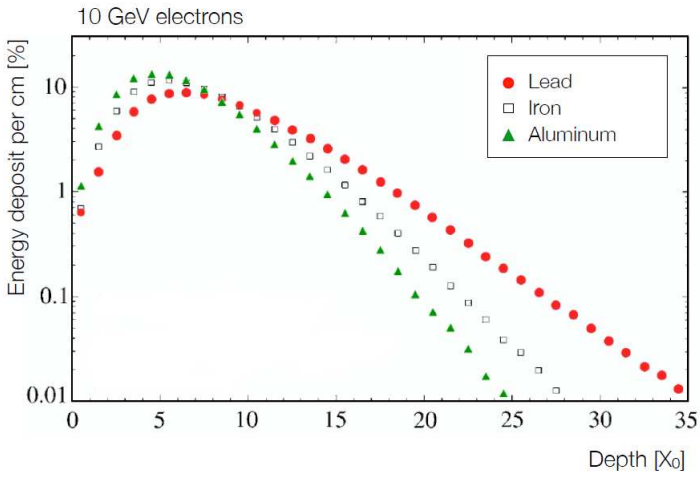

Figure A.10: Monte-Carlo calculation of the energy deposit as a function of depth for a 10 GeV electron shower developing in lead, iron and aluminum [1].

Two main differences can be observed in the energy deposit profile:

- as Z increases, the shower maximum slightly shifts to a larger depth;
- as Z increases, the shower profile is completely absorbed at larger radiation lengths.

Both these effects are due to the fact that in high-Z materials the shower multiplication continues down to much lower energies with respect to low-Z materials because of the Z dependence of the pair production and bremsstrahlung cross sections. Just to give an example, the critical energy in lead is only 7 MeV, while in

iron it is 22 MeV, rising to 43 MeV in aluminum. This means that below 43 MeV, particles in aluminum stop their multiplication and start to be absorbed through ionization and Compton scattering, while in lead their multiplication continues down to ∼7 MeV. As a result of these effects, it takes a larger number of radiation lengths to contain a given electromagnetic shower in lead with respect to iron or aluminum.

The energy dependence of the longitudinal containment is taken into account in the t_{max} parameter definition (equation A.15). The top plot of Fig. A.11 shows a Monte-Carlo calculation of an electromagnetic shower in copper with different initial energies.

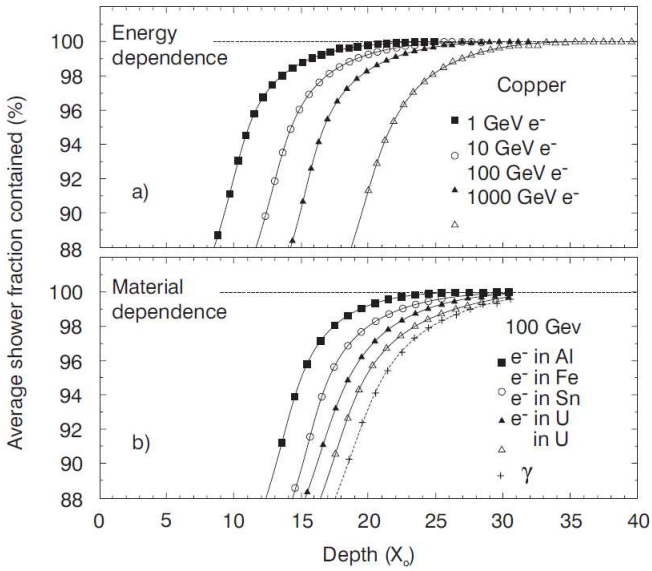

Figure A.11: Monte-Carlo calculation of the energy deposit as a function of depth and energy in copper [1].

The absorber thickness needed to contain 95% of the shower ranges from ∼11 X_0 at 1 GeV to ∼22 X_0 at 1 TeV; for a 99% containment, at least 16 X_0 and 27 X_0 are necessary. In the bottom plot of Fig. A.11 a comparison between different absorbers is presented. Once again, the Z dependence in the shower containment is clearly visible. The same figure shows that γ-induced showers require approximately one radiation length more to be contained with respect to electrons with the same energy. This is due to the fact that the mean free path of a photon is $\frac{9}{7}X_0$, so approximately one X_0 is needed to create an electron-positron pair and start the shower development.

A.4.2 Lateral Profile

The lateral spread of the electromagnetic shower is caused by two primary effects:

- the electrons and positrons created in the shower move away from the central axis because of multiple scattering;
- bremsstrahlung, the photoelectric effect and the Compton scattering are isotropic processes and the photons and electrons generated in these phenomena move away from the shower axis.

The first effect dominates in the early stages of the shower development, while the second becomes important after the shower maximum, where the low energy Compton scattering and photoelectric effect start to contribute to the shower, especially in the high-Z materials.

The lateral profile of an electromagnetic shower is described by the *Molière radius*, a material and energy independent parameter:

$$\rho_M = E_s \frac{X_0}{\varepsilon_c} \tag{A.17}$$

where E_s is the *scale energy* defined as:

$$E_s = m_e c^2 \sqrt{4\pi/\alpha} = 21.2 \text{ MeV} \tag{A.18}$$

The Molière radius represents the average lateral deflection of electrons at the critical energy after crossing one radiation length. On average, only $\sim$1 ρ_M is needed to contain 90% of the shower. The typical ρ_M values are of the order of a few centimeters, thus reflecting the compactness of the electromagnetic shower lateral profile. The independence of the Molière radius from the Z of the material can be explained as follows. Considering equation A.10, the radiation length scales approximately as A/Z^2: assuming that A is proportional to Z, X_0 scales as $1/Z$. The same is true for the critical energy, which according to equation A.4 scales as $1/Z$. As a result, the ratio of X_0 and ε_c is roughly Z-independent. The Molière radius of mixtures/compounds of different elements can be computed using the same formulas defined for the radiation length parameter, replacing the X_i parameter with ρ_i. Fig. A.12(a) presents the Monte-Carlo calculation of the average fraction of the shower contained in an infinitely long cylinder centered on the shower axis as a function of the Molière radius.

As can be seen, 90% of the shower is contained in $\sim$1.5 ρ_M, with very little differences between different materials (aluminum and copper). Fig. A.12(b) presents the simulated radial shower profile in $PbWO_4$ crystals for 1 GeV and 1 TeV electrons, showing no substantial differences in the lateral profile, confirming the energy independence of the ρ_M parameter.

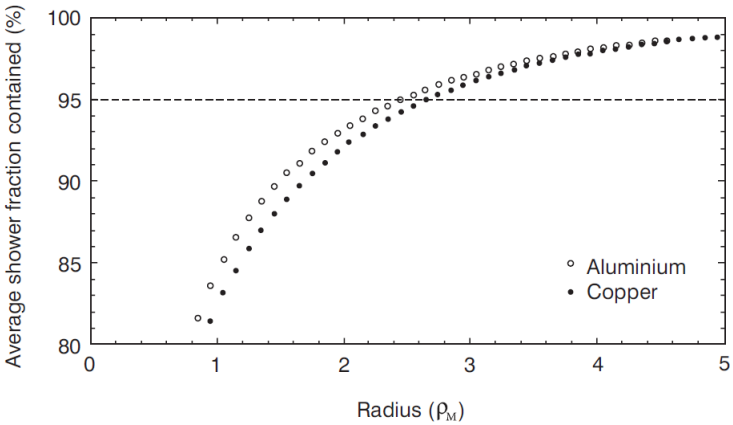

(a)

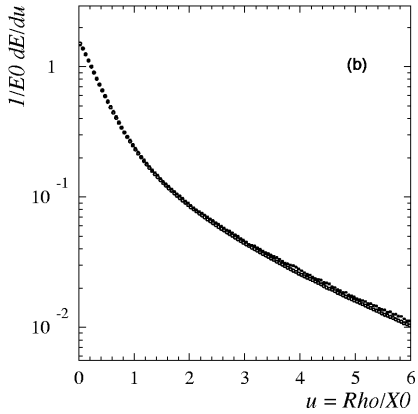

(b)

Figure A.12: (a) Monte-Carlo calculation of the average shower fraction contained in a cylinder of absorber material as a function of the Molière radius [1]; (b) simulated radial shower profile in $PbWO_4$ crystals for 1 GeV (closed circles) and 1 TeV (open circles) electrons [98].

A.5 Energy Resolution

The energy resolution of a calorimeter determines the precision with which the energy of a given particle can be measured. The precision in the energy measurement is limited by the *fluctuations* which characterize the calorimeter response; the most important fluctuation sources are the following:

- the fluctuations in the processes through which the energy of the particle is absorbed;
- the fluctuations induced by the experimental technique used to measure the

deposited energy inside the calorimeter.

The fluctuations in the shower development are unavoidable and represent the ultimate limit on the energy resolution. On the contrary, the fluctuations induced by the chosen experimental technique can be reduced, for example using very low noise charge amplifiers (in the case of calorimeters based on charge collection) or improving the number of photoelectrons collected by a photomultiplier tube (in the case of scintillation calorimeters). In general, the energy resolution σ_E/E of a calorimeter can be expressed as the sum of three parameters, each one with a different energy dependence:

$$\frac{\sigma_E}{E} = \frac{a}{\sqrt{E}} \oplus \frac{b}{E} \oplus c \tag{A.19}$$

The three terms are called respectively *stochastic* $\left(\frac{a}{\sqrt{E}}\right)$, *noise* $\left(\frac{a}{E}\right)$ and *constant* (a) terms, and their quadratic sum describes the energy resolution of a real calorimeter (Fig. A.13).

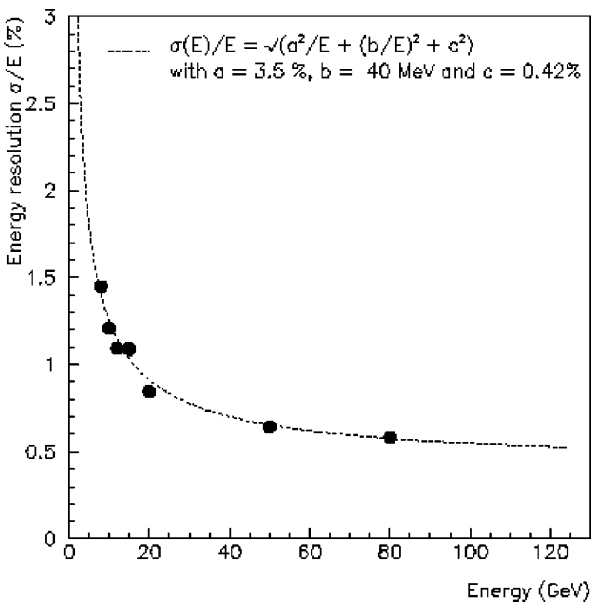

Figure A.13: Fit to the energy resolution obtained with a prototype of liquid-krypton calorimeter [98].

Two main features can be inferred from the energy resolution behavior:

- on the contrary of other particle detection techniques (like the magnetic spectrometers), the energy resolution of a calorimeter *improves* increasing the energy;

- considering the different energy dependence of the various terms, the optimal calorimeter technique depends on the energy range.

The details of the different contributions will be described in the following sections.

A.5.1 Stochastic Term

The stochastic term includes the unavoidable statistical fluctuations which characterize the development of the shower inside the calorimeter and represents its intrinsic energy resolution. The energy measurement is based on the fact that the energy released inside the calorimeter by the charged particles is proportional to the energy of the incident particle. Since the number of charged particles inside the calorimeter can be expressed as:

$$N_p \simeq \frac{E_0}{\varepsilon_c} \tag{A.20}$$

the total track length is equal to:

$$T_0 \simeq X_0 \frac{E_0}{\varepsilon_c} \tag{A.21}$$

The total track length is a sum of a large number of independent tracks, whose length fluctuates event by event according to the Poisson statistics. If the deposited energy inside the calorimeter can be considered proportional to the total track length, the energy resolution can be expressed as:

$$\sigma_E \simeq \sqrt{T_0} \tag{A.22}$$

Thus, the intrinsic energy resolution $\frac{\sigma_E}{E}$ is given by:

$$\frac{\sigma_E}{E} \simeq \frac{\sqrt{T_0}}{T_0} \simeq \frac{\sqrt{E_0}}{E_0} = \frac{1}{\sqrt{E_0}} \tag{A.23}$$

These calculations are valid in the case of a homogeneous and infinitely large calorimeter and can be referred to as *shower fluctuations*. In the case of sampling calorimeters, one more process is involved in the definition of the stochastic term: the *sampling fluctuations*. These fluctuations are due to the variations in the number of charged particles that cross the active layers event by event. This number can be approximated as:

$$N_{cr} = \frac{E_0}{t} \tag{A.24}$$

where t is the thickness of the absorber layers in units of radiation lengths. Using the former arguments, the number of particles crossing the active layers fluctuates event by event according to the Poisson statistics, thus resulting in the following expression:

$$\frac{\sigma_E}{E} \simeq \frac{1}{\sqrt{N_{cr}}} \simeq \sqrt{\frac{t}{E_0}} \tag{A.25}$$

As can be seen in equation A.25, the energy resolution improves reducing the thickness of the absorbing layer, thus enlarging the *sampling frequency*. In the limit of $t \to 0$, the sampling calorimeter becomes a homogeneous calorimeter, thus reducing the sampling fluctuations to zero. These fluctuations represent the most important limit of sampling calorimeters and are the reason of their worse energy resolution compared to the homogeneous ones.

A.5.2 Noise Term

In real calorimeters the energy deposit is converted in some kind of signal by an active medium. Two main processes can occur:

- the generation of free charges;
- the generation of scintillation (or Cherenkov) light.

The noise contribution is a term associated to the electronic noise characterizing the two different readout types. In charge collecting detectors, the typical signals amount to a few pC per GeV of deposited energy. This means that the first stage of the readout chain is usually a charge amplifier. Even if low noise signal filtering and shaping techniques are usually used, the intrinsic capacitance of the detector and the thermally generated charges in the active medium will introduce a certain noise contribution. The standard deviation of these fluctuations (σ_{noise}) is usually given in terms of equivalent charge (or ENC, Equivalent Noise Charge): since the calorimeter measures the energy of the particle in the same way, the noise term is equivalent to a certain amount of energy. Considering the fact that this quantity is a constant number (depending on the properties of the charge amplification electronics), its contribution to the energy resolution σ_E/E scales as E^{-1}. Considering its energy dependence, the noise term represents a limit to the energy resolution in the low energy range.

In the case of scintillating calorimeters the ENC is usually smaller with respect to charge collecting ones because of the presence of a high gain and low noise device (usually a photomultiplier tube) which converts the scintillation photons in electrical signals. Nevertheless, fluctuations induced in the pedestal of the detector (*e.g.* improper impedance matching, ground loops or temperature variations) may contribute to the electronic noise.

A.5.3 Constant Term

The constant term is an energy independent parameter which limits the calorimeter performance in the high energy range. Considering the high energies reached in modern collider experiments, the constant term is becoming the most important contribution to the desired energy resolution. Many phenomena are responsible for the increase of the constant term:

- longitudinal leakage: if the calorimeter thickness in terms of radiation lengths is not enough to contain the whole electromagnetic shower, some of the particles escape from its rear end. The fraction of escaping particles fluctuates event by event, deteriorating the energy resolution. The fluctuations in the longitudinal development are mainly due to the different point of conversion of the high energy photons;

- lateral leakage: it occurs when a part of the electromagnetic shower escapes from the side of the calorimeter. In high energy experiments small clusters of calorimeter cells are usually used to reduce the noise and the pile-up probability. If the cluster is too small, or if the calorimeter itself is built with an insufficient lateral extension (*e.g.*$<1.5\ \rho_M$), the number of escaping particles fluctuates event by event, worsening the energy resolution as in the case of the longitudinal leakage. However, the lateral leakage is usually less important with respect to the longitudinal one, because the fluctuations in the lateral development of the shower are dominated by low energy particles, thus poorly affecting the total energy deposit. A comparison between the effects of the lateral and the longitudinal leakage on the energy resolution is presented in Fig. A.14;

- detector cracks and non hermetic coverage: a certain amount of mechanical supports, power and signal cables are needed to operate the calorimeters in the high energy physics experiments. The quality of the energy measurement is degraded by the development of the shower in this non-active areas, resulting in fluctuations which affect the energy resolution. It has also to be noted that in collider experiments other detectors (like the particle tracking systems) can be placed in front of the calorimeter: particular attention has to be payed to reduce as much as possible the (non-active) material budget in front of the calorimeter itself;

- Detector non uniformities: they are given by mechanical imperfections or asymmetries due to the geometry or to the readout of the calorimeter. They can be divided in:

1. mechanical imperfections: the irregular shapes of the absorber or active layers introduce fluctuations in the sampling of the shower, resulting in a degraded energy resolution;
2. variation in the sampling fractions: in order to reduce the cost or the dimension of a calorimeter, the sampling frequency at large depths may be reduced, for example increasing the thickness of the absorber layers. This means that the shower is sampled with an accuracy which depends on the position inside the calorimeter. This approach dramatically increases the signal fluctuations, thus degrading the energy resolution;
3. light attenuation: this problem is present only in the calorimeters based on light collection. Light attenuation can be caused by a variety of factors like self-absorption and reflection losses inside the scintillator or the wavelength shifter fibers. Light attenuation causes the signal to be dependent on the distance that the light has to travel between the generation and readout points, thus creating position dependences and fluctuations in the calorimeter response.

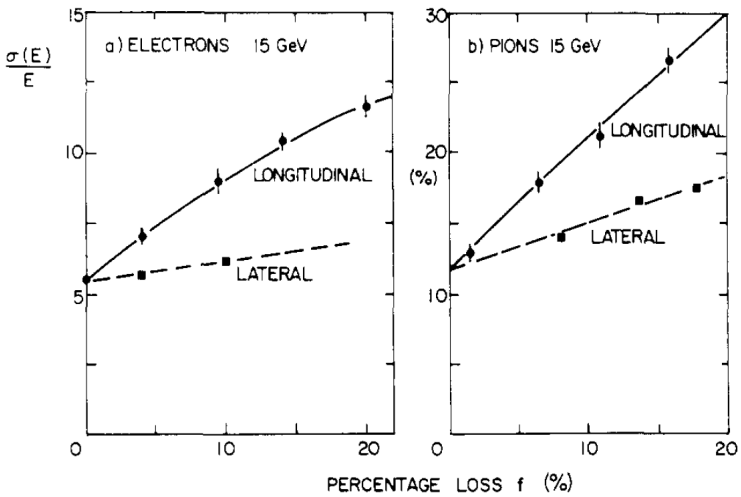

Figure A.14: Effects of longitudinal and lateral shower leakage on the energy resolution for 15 GeV electrons [1].

A.6 Shashlik Calorimeters

Shashlik calorimeters are particular types of sampling calorimeters composed of layers of absorber and scintillating material, readout by WLS fibers. The concep-

tual design of this type of calorimeter has been proposed in the middle ’80s by Fessler in [99]: a sketch of the original design is presented in Fig. A.15.

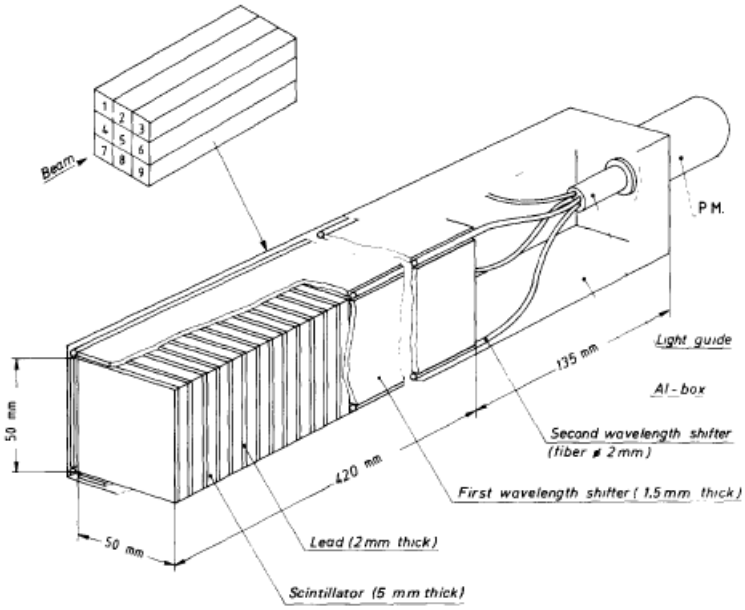

Figure A.15: Schematic representation of the fiber calorimeter originally proposed in [99].

The fundamental tower of Fessler’s calorimeter (formed by nine modules) was composed of 60 2 mm thick lead tiles sandwiched with 60 5 mm thick tiles of plastic scintillator (polystyrene-based); thin reflective white sheets were placed between the scintillator and lead tiles in order to enhance the light reflection. The surface of the tiles was 5x5 cm^2 and the overall module was 420 cm long, corresponding to 22 X_0. The four sides of each module were covered by a WLS 1.5 mm thick sheet which was used to collect the light from the scintillator tiles and to diffuse it on four WLS fibers with a diameter of 2 mm placed on the corners of the module. A photomultiplier tube has been used for the light readout. The main advantages of the WLS fiber readout are:

- a compact and simple construction;
- an efficient light collection without the use of expensive and complicated light guides; this approach is very useful in presence of a magnetic field, since the WLS fibers can transport the scintillation light to a photomultiplier tube placed outside the high field zone.
- minimal dead spaces at the boundaries of a module, thus resulting in a suitable technique for the creation of a cluster;

- its being relatively inexpensive, given that plastic scintillator is used as the active medium.

The energy resolution of Fessler's calorimeter was measured during a beamtest at CERN with electrons up to 5 GeV. The obtained energy resolution, presented in Fig. A.16, was:

$$\frac{\sigma_E}{E} = \frac{10\%}{\sqrt{E}} + 1\% \tag{A.26}$$

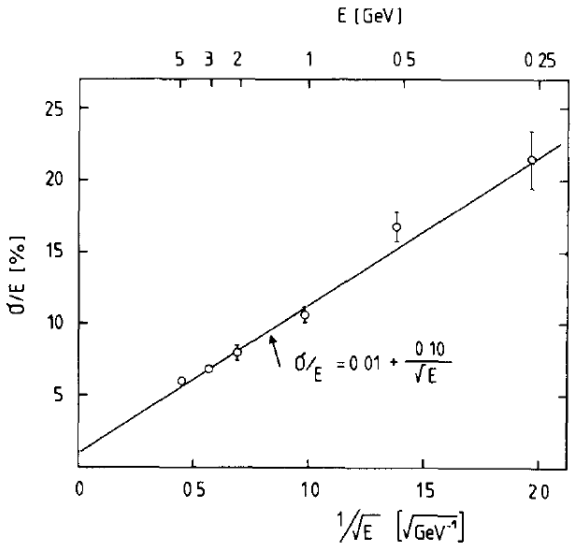

Figure A.16: Energy resolution of Fessler's calorimeter [99].

Shashlik calorimeters are a modification of the original Fessler's device, where many WLS fibers cross the whole calorimeter throughout its length, replacing the original WLS sheets as the readout system for the scintillator light; the name *shashlik* (the Russian translation of skewer) given to this type of calorimeter is due to the particular layout of the WLS fibers. Developed at first in Russia by Atoyan [94], the construction of these types of calorimeter was made possible by the improvements of the molding technique for the production of scintillator tiles with built-in holes.

The base module described in [94] was composed of 60 1.4 mm thick tiles of lead and 60 4 mm thick tiles of scintillator for a total of $\sim$15 X_0; white reflecting sheets placed between the scintillator and lead tiles were used to enhance the light reflection. The overall module dimension was 11.4x14.4x33 cm^3. The scintillator light was carried out using 72 end-looping WLS fibers of 1.2 mm of diameter, inserted in 144 holes arranged in a 12x12 matrix in the scintillator and lead tiles:

the holes spacing was 9.6 mm. The light was finally collected by a photomultiplier tube. A sketch of the base module of Atoyan's calorimeter is presented in Fig. A.17.

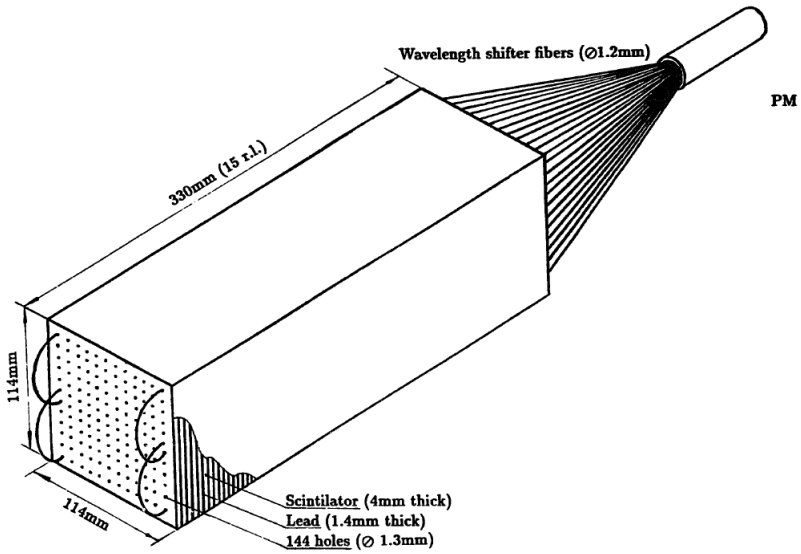

Figure A.17: Schematic representation of the first shashlik calorimeter originally proposed in [94].

The linearity and energy resolution of a super-module composed of four Atoyan's towers have been measured with electrons up to 5 GeV, obtaining an energy resolution of:

$$\frac{\sigma_E}{E} = \frac{6.7\%}{\sqrt{E}} \oplus 3\% \tag{A.27}$$

The experimental results are shown in Fig. A.18. Since the first Atoyan's prototype, the shashlik technique has been used to build many electromagnetic calorimeters for high energy physics experiments. Among them, the LHCb electromagnetic calorimeter [100] and the DELPHI STIC luminometer [82] can be listed as the most important and successful ones. In particular, two prototypes of shashlik calorimeters, one of which very similar to the one developed by Atoyan, have been used as a test bench to develop the silicon photomultiplier readout system, the main topic of this thesis work.

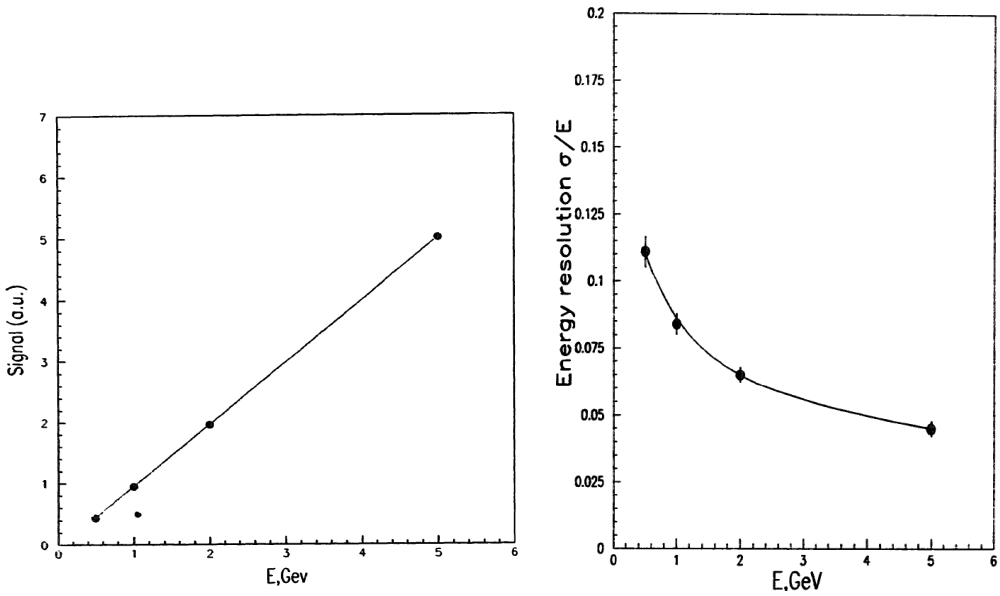

(a) (b)

Figure A.18: Linearity and energy resolution for electrons obtained with Atoyan's calorimeter [94].

Appendix B

Noise Characterization of the MAROC Readout System

This appendix is devoted to a characterization of the electronic noise of the MAROC board based SiPM readout. The noise has been studied by means of pedestal runs, measuring the RMS of the channels connected to the ASIC and the equivalent energy resolution simulated using a pulsed LED as a light source.

B.1 Alternative Readout Circuit

Considering the fact that the MAROC ASIC is designed for the readout of MAPMTs, the first test consisted in a different implementation of the SiPM readout circuit. The layout of the standard circuit used for the SiPM readout is depicted in Fig. B.1(a). In order to check if the electronic noise could be induced by an impedance mismatch between the output capacitor of the circuit and the input one of the MAROC ASIC, a modified circuit (Fig. B.1(b)) has been tested.

This second circuit is not AC coupled, and the (negative) SiPM bias is provided on the opposite electrode. The new circuit has been implemented in a new readout board very similar to the one presented in Fig. 4.4. The board has been connected to the MAROC input pins by means of custom LEMO cables. The SiPMs have been biased at 34 V, while the gain of the MAROC amplifier has been set to 1 in order to avoid any saturation effect.

The first test of the new board consisted in the evaluation of the pedestal RMS: the comparison between the old AC coupled circuit and the new one, in the same conditions, using the same SiPM (connected to a different channel) is presented in Fig. B.2.

The channel connected to the SiPM can be clearly seen and it corresponds to the MAROC channels #10 and #55, which are characterized by a larger RMS

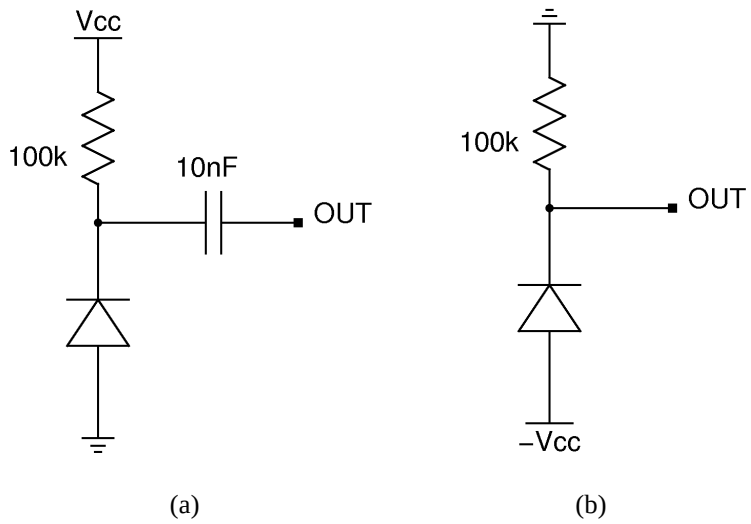

Figure B.1: Layout of the old (a) and new (b) circuits used for the electronic noise tests.

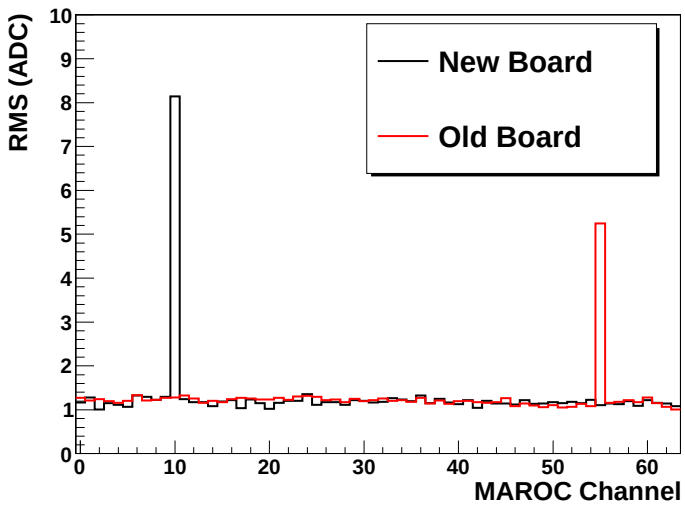

Figure B.2: RMS of the pedestal distribution obtained with the new and old SiPM readout circuit.

value. The results obtained with the new board are worse (RMS value of ∼8) than the ones obtained with the old circuit (RMS value of ∼5). Moreover, the layout of the board introduced further problems: the new circuit is connected to ground through the 100 kΩ resistor, which is used also to monitor the SiPM power consumption. When the circuit is connected to a MAROC input, the current flows

directly into the first stage of the pre-amplifier (due to its low input impedance). The following considerations hold:

- after the connection to the MAROC inputs, the 100 kΩ resistor cannot be used anymore to measure the current consumption of the SiPM;
- the SiPM bias is slightly different with respect to the one set with the power supply ($\Delta V \simeq 0.79$ V);
- the current which flows directly in the pre-amplifier creates some saturation effects at high gain values (starting from gain 64) that are absent using the old AC coupled circuit.

After the pedestal runs, the new board has been also tested with a pulsed LED light source (3 V, 100 ns long pulses with a frequency of 1 kHz) to simulate the scintillation mechanism. The results obtained with the old and new circuits are presented in Fig. B.3.

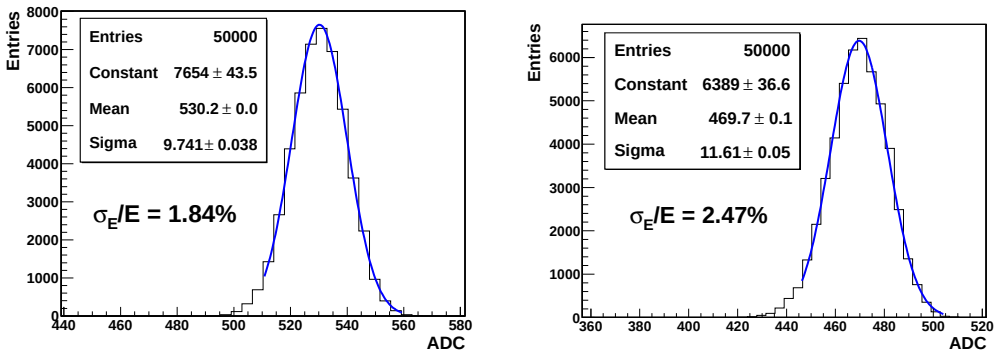

(a) (b)

Figure B.3: Peak resolution obtained with a pulsed LED with the old (a) and new (b) readout circuit.

The LED results are consistent with the ones obtained with the pedestal runs, confirming that the old AC coupled circuit is characterized by a better peak resolution (1.87%) compared to the one obtained with the new circuit (2.47%).

B.2 Low Frequency Jitters and Dual-Hold Readout

The second hypothesis for the large noise was the possible presence of some sort of low frequency “jitters” induced on the MAROC input which could change the ASIC baseline, artificially moving up or down the SiPM signal on an event by

event basis. If this is the case, it should be possible to remove this contribution sampling twice the shaper output (that is at two different hold values) and subtracting the obtained values. This approach can be performed with the MAROC3 ASIC thanks to the fact that two different hold values can be implemented. Fig. B.4 presents a sketch of the low frequency "jitters" and the sampling with the two hold parameters.

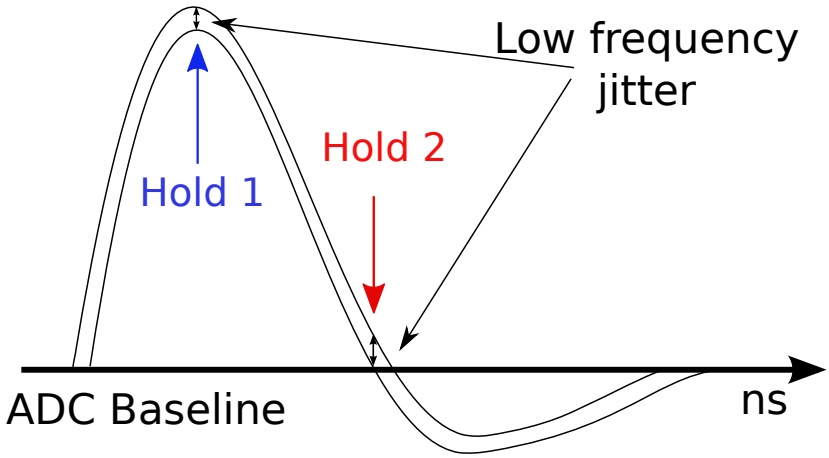

Figure B.4: Sketch of the MAROC shaper output with the dual hold system. The low frequency jitters, if present, should be removed subtracting the second sampled signal from the first one.

The efficacy of this procedure can be tested directly on the pedestal runs, looking at the RMS of the difference between the two sampled values. This test has been performed using the same readout board (Fig. 5.32) and SiPMs installed on the prototype 1 calorimeter. The gain control LED system has been used as a light source to simulate the real scintillation light, while only a single group of SiPMs (4 SiPMs out of 36) has been biased at 33 V (corresponding to the 10 μA configuration tested in the prototype 1 calorimeter beamtests). Many trials have been performed with different values of the MAROC gain: the results obtained with a gain of 10 are presented in Fig. B.5.

The RMS of the difference is in general larger than the one of each hold value, indicating that no common fluctuations are present, thus the two RMS values are uncorrelated and the RMS of the difference can be calculated as:

$$\sigma_{Diff} = \sqrt{\sigma_1^2 + \sigma_2^2} \tag{B.1}$$

If σ_1 and σ_2 are equal:

$$\sigma_{Diff} = \sqrt{2\sigma^2} = \sigma\sqrt{2} \tag{B.2}$$

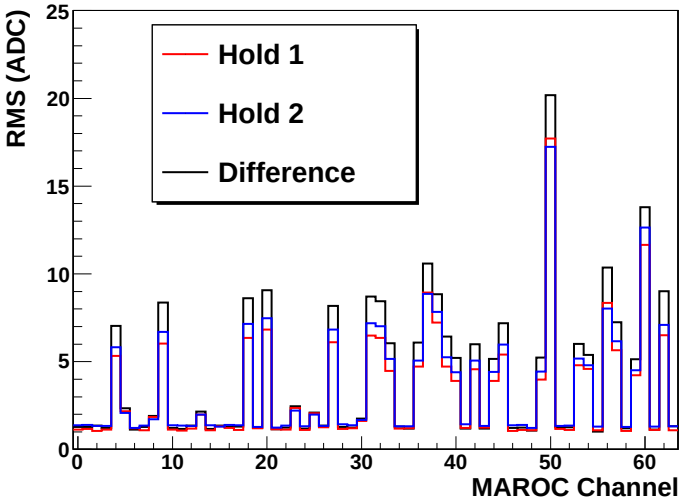

Figure B.5: Comparison between the pedestal RMS with the dual hold correction system. The RMS values corresponding to the two holds are depicted in red and blue, while the RMS of the difference is depicted in black.

which seems consistent with the RMS values of Fig. B.5.

Similar results have been obtained using the pulsed LEDs (Fig. B.6), with a peak resolution of 7.42% with the single hold readout, and of 8.04% for the dual hold readout; in this case, the MAROC gain has been set to 1.

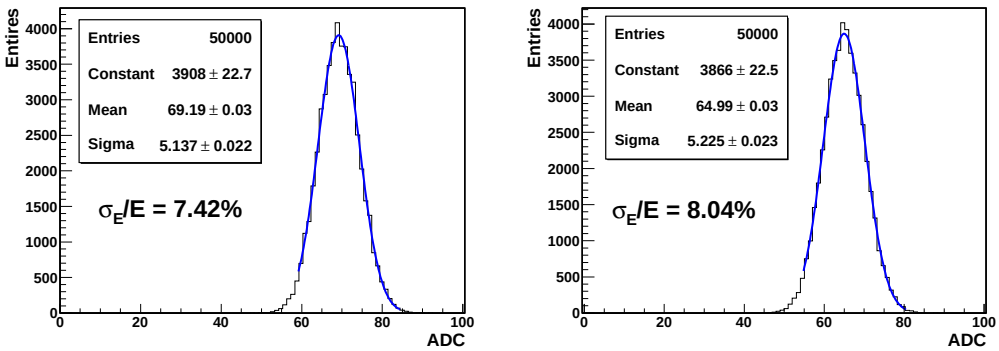

(a) (b)

Figure B.6: Peak resolution obtained with a pulsed LED with the single (a) and dual (b) hold readout method.

B.3 New Bias Cable

During the tests with the dual hold procedure, it has been noted that the cables used for the readout of the power consumption of each SiPM could be responsible of a slight increase of the noise; these cables measure the voltage drop across the 100 kΩ resistor of each SiPM channel, and are always connected to one end of the resistor. The cables are embedded in the flat cable used also for the SiPMs bias, and are 2 m long. Thus, they can work as antennas, introducing some kind of electromagnetic noise that, considering the position of the cable in the circuit, is directly picked up by the MAROC input.

To evaluate the noise induced by the cable used in the beamtests, a modified version without the current consumption pins has been produced. Fig. B.7 presents a comparison of the pedestal RMS between the old and the new cable with the MAROC gain set to 10.

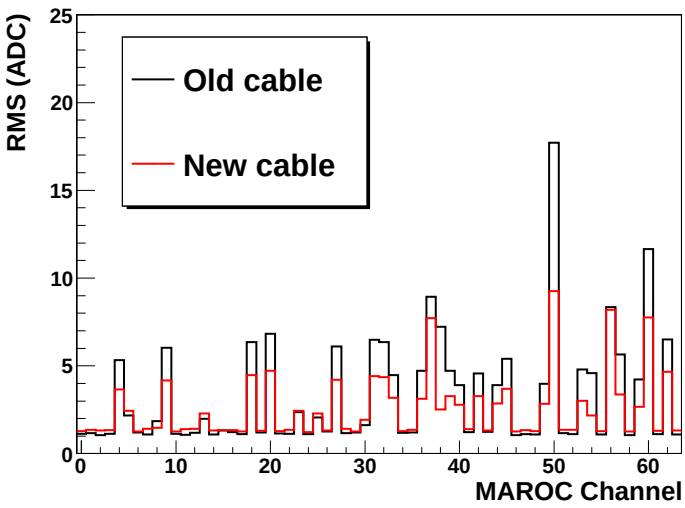

Figure B.7: Comparison of the pedestal RMS with the new (red one) and old (black one) cables.

The RMS is clearly reduced using the new cable with respect to the old configuration (in some cases, even of 50%). The new cable has been also tested using the LED system: the result (using a MAROC gain of 1 and the single hold readout) is presented in Fig. B.8. The 7.35% resolution is only slightly better with respect to the 7.42% of the old configuration (Fig. B.6(a)). However, it has to be noted that the light pulse injected by the LED (∼70 ADC) corresponds to the light collected by a central SiPM of the prototype 1 calorimeter at 4 GeV. By comparison, the ADC signal in the same SiPM at 1 GeV was only ∼12 ADC. This means

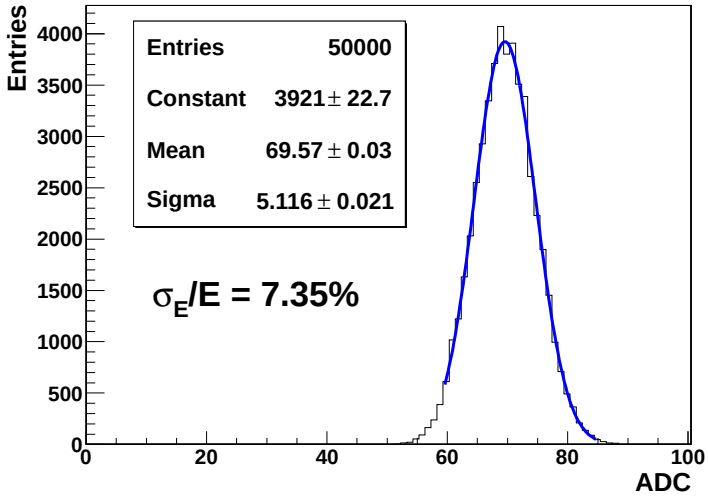

Figure B.8: Peak resolution obtained with a pulsed LED in the new cable configuration.

that the noise introduced by the cables should be more relevant in the low energy points, as it has been found in the low energy scans performed with the prototype 1 calorimeter. For this reason, a second test has been performed using a smaller bias value of the LED system (2.65 V with respect to 4.3 V), in order to have a signal on the SiPM of ∼10 ADC. The peak resolution results for both the old and new cables are presented in Fig. B.9.

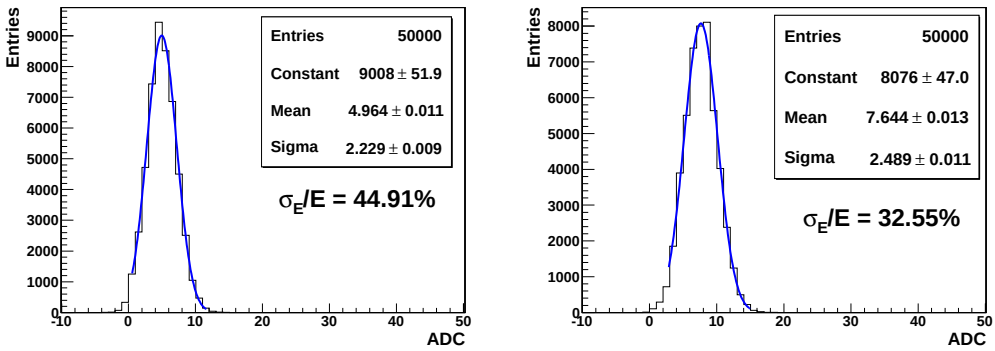

(a) (b)

Figure B.9: Peak resolution obtained with a low intensity pulsed LED with the old (a) and new (b) connection cables.

The new cable improves considerably the peak resolution in the low light con-

figuration (32.55% with respect to 44.91%). Thus, the noise problem observed during the beamtests could be partially ascribed to a non-optimal configuration of the bias/monitoring cable. If this is the case, a new system for the power consumption readout can be implemented in order to remove the direct connection to the input pins of the MAROC and to avoid the noise pickup.

B.4 Slow Shaper Parameters

As previously explained, the MAROC3 ASIC has been developed for the readout of MAPMTs. From the MAROC point of view, the main differences between SiPMs and MAPMTs are the following:

- a dark noise of the order of $\sim$MHz for the SiPMs, compared to $\sim$10 kHz in the MAPMT case;
- a single photoelectron gain of $\sim 10^6$ for the SiPMs, compared to $\sim 10^5$ (at maximum) in the MAPMT case.

These two differences play a fundamental role on how the signals are shaped by the analog slow shaper. In particular, the shaping time and amplitude of the shaper can be set opening or closing three switches, connected to 300, 600 and 1200 fC capacitors, as presented in Fig B.10.

During the beamtests, the C0, C1 and C2 switches have been always set to $\{1,1,1\}$ in order to have the longest possible shaping time, so that the hold generated by the readout logic (which is based on the DAQ trigger) samples the signal on the peak. According to the hold scan performed with the different capacitor configurations (Fig. B.10(b)), the complete shaping (including the undershoot) lasts about 500 ns. Considering a SiPM dark noise of 1 MHz, a dark pulse each 1 μs is expected. It is clear that, if the dark noise rate is slightly larger than 1 MHz (for example, due to a larger SiPM overvoltage), a second dark pulse can occur during the 500 ns shaping window. The input stage of the MAROC pre-amplifier is always open, thus it continuously shapes the dark pulses, and if the dark noise is above 1 MHz the shaped signal is a superposition of different shaped pulses. The overall effect is equivalent to a noisy baseline, which is the sum of the different shaped dark pulses and explains the large RMS values in the pedestal runs with respect to the MAPMT ones. Moreover, this effect is amplified by the large gain of the SiPMs, which results in a larger ADC value for the single photoelectron with respect to the MAPMT one.

The effect of the shaped signal superposition can be partially avoided modifying the shaping parameters and reducing the shaping time. Fig. B.11 presents a comparison between three pedestal runs performed with the slower (C0, C1 and

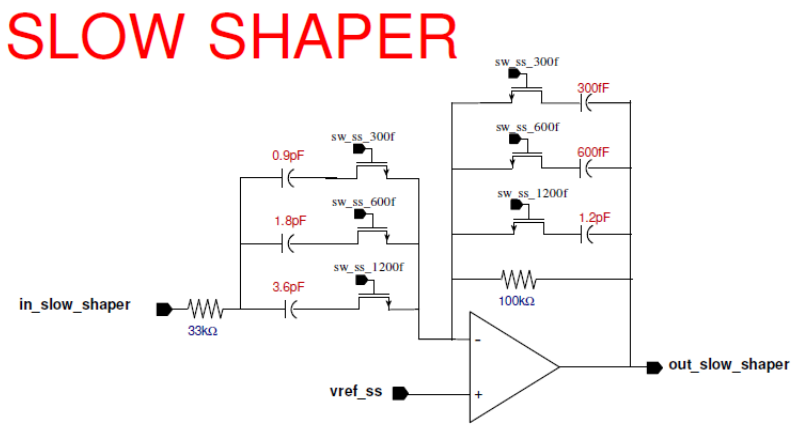

(a)

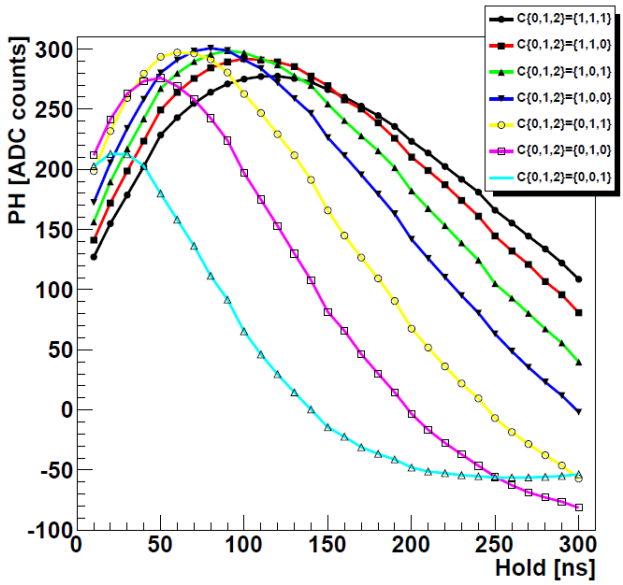

(b)

Figure B.10: (a) The slow shaper circuit: C0, C1 and C2 are the switches associated to the feedback capacitors of 1200, 600 and 300 fC [101]; (b) the hold scan with different shaper settings.

C2 set to 1) and faster (C0 set to 1 and C1 and C2 set to 0) shaper configurations. As can be noted in Fig. B.10(b), the faster configuration is also characterized by a smaller signal amplitude (due to the different capacitor configuration the peak is located at ∼2/3 of the one of the slower shaper configuration). Thus, the gain of the MAROC pre-amplifier has been set to 64 (the unitary gain) for the slower shaper configuration and to 96 for the faster one in order to have an equal signal

amplitude. A third run with a gain of 64 and the faster shaper configuration has been acquired for comparison. These large gain values have been used in order to underline the RMS fluctuations. As previously stated, the slower shaper configuration corresponds to ∼500 ns, while the faster one to ∼180 ns. For all the tests described in the following, the new cable configuration introduced in the previous section has been used.

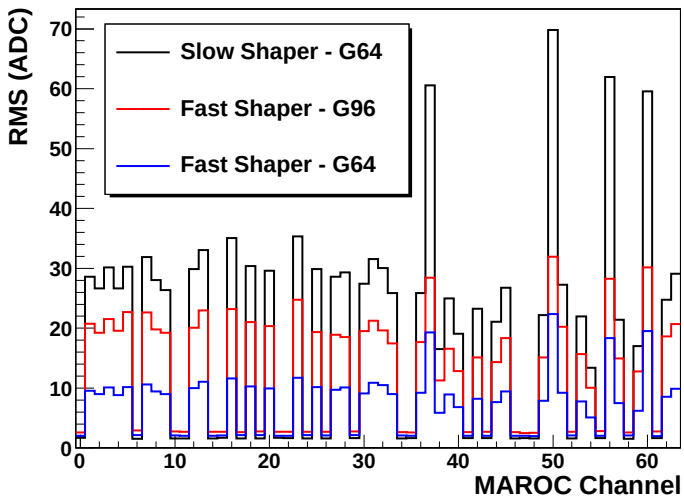

Figure B.11: Pedestal RMS with the slower and faster shaper configuration.

As expected, the RMS of the faster configuration is substantially reduced with respect to the slower one, even if a larger gain has been used. The effect is more evident in the four biased channels (#37, #50, #56 and #60), where a reduction of a factor ∼2 is observed. The pulsed LED has then been used in order to evaluate the impact on the LED peak resolution. The LED has been biased at 2.65 V (to simulate the low energy case), while the gain of the pre-amplifier has been set to 2 for the slower shaper configuration and to 3 for the faster one. In this way, both the configurations have a signal of ∼10 ADC. The peak resolution results are presented in Fig. B.12.

The peak resolution of the faster shaper is slightly better (24.74%) with respect to the slow shaper one (29.55%), confirming the pedestal results.

In conclusion, the large dark count rate combined with the high gain of the SiPMs represents a problem for the slow shaper readout, especially using large values of the pre-amplifier gain. It has been shown that the faster shaper configuration improves this situation, with smaller pedestal RMS values and with a slightly better peak resolution at low light values. However, a faster trigger logic should be implemented in the readout sequence to allow the use of the fast shaper:

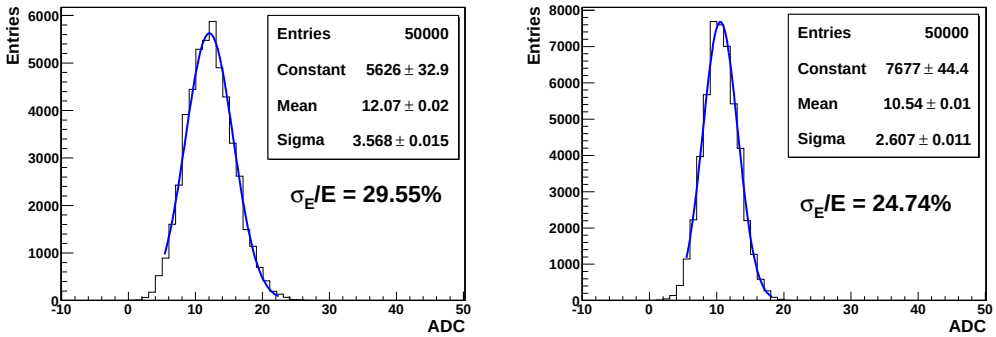

(a) (b)

Figure B.12: Peak resolution obtained with a low intensity pulsed LED with the slow (a) and fast (b) shaper configuration.

this can be done implementing the trigger logic directly on the MAROC board or on a dedicated board near the MAROC one. Both these approaches are being studied at the moment and will be implemented in the beamtests foreseen in 2012.

List of acronyms

ADC	Analog to Digital Converter
AGILE	Astro rivelatore Gamma a Immagini LEggero
ALEPH	Apparatus for LEp PHysics
AMS-02	Alpha Magnetic Spectrometer - 02
APD	Avalanche Photo-Diode
ASCII	American Standard Code for Information Interchange
ASI	Agenzia Spaziale Italiana
ASIC	Application-Specific Integrated Circuit
ATLAS	A Toroidal LHC ApparatuS
BGO	Bismuth Germanate
CALICE	CAlorimeter for LInear Collider Experiment
CERN	European Organization for Nuclear Research (Conseil Europeen pour la Recherche Nucleaire)
CMOS	Complementary Metal-Oxide Semiconductor
CMS	Compact Muon Solenoid
CPU	Central Processing Unit
DAQ	Data AcQuisition
DELPHI	DEtector with Lepton, Photon and Hadron Identification
DESY	Deutsches Elektronen-SYnchrotron
DREAM	Dual REAdout Method
DST	Data Summary Tape
EASIROC	Extended Analogue SI-pm Read Out Chip
ECAL	Electromagnetic CALorimeter
EGRET	Energetic Gamma-Ray Experiment Telescope
EM	ElectroMagnetic
EMR	Electron Muon Ranger

ENC Equivalent Noise Charge
ENF Equivalent Noise Factor

FACTOR Fiber Apparatus for Calorimetry and Tracking with Optoelectronic Read-out
FBK Fondazione Bruno Kessler
FNAL Fermi National Accelerator Laboratory
FPGA Field Programmable Gate Array
FWHM Full Width Half Maximum

GEANT GEometry ANd Tracking
GM-APD Geiger-Mode Avalanche Photo-Diode
GUI Graphical User Interface

HCAL Hadronic CALorimeter
HEP High Energy Physics
HPD Hybrid Phodo-Diode

ILC International Linear Collider
INFN Istituto Nazionale di Fisica Nucleare

LED Light Emitting Diode
LEP Large Electron Positron (collider)
LHC Large Hadron Collider
LHCb Large Hadron Collider beauty (experiment)
LINAC LINear ACcelerator
LYSO Lutetium-Yttrium OxyorthoSilicate

MAPMT Multi Anode Photo-Multiplier Tube
MAROC Multi Anode Read Out Chip
MICE Muon Ionization Cooling Experiment
MIP Minimum Ionizing Particle
MRS Metal Resistor Semiconductor

NIM Nuclear Instrumentation Module
NMR Nuclear Magnetic Resonance

PAMELA Payload for Antimatter Matter Exploration and Light-nuclei Astrophysics
PAW Physics Analysis Workstation
$PbWO_4$ Lead Tungstate
PC Personal Computer
PCB Printed Circuit Board

PDE	Photo-Detection Efficiency
PEBS	Positron Electron Balloon Spectrometer
PET	Positron Emission Tomography
PFlow	Particle Flow
PID	Particle IDentification
PIN	P-type Intrinsic N-type
PMT	Photo-Multiplier Tube
PN	P-type N-type
PS	Proton Synchrotron
QCD	Quantum Chromo-Dynamics
QDC	Charge (Q) to Digital Converter
QE	Quantum Efficiency
QED	Quantum Electro-Dynamics
R&D	Research & Development
RAL	Rutherford Appleton Laboratory
RCA	Radio Corporation of America
RICH	Ring Imaging CHerenkov detector
RMS	Root Mean Square
SiPM	Silicon Photo-Multiplier
S/N	Signal-to-Noise (ratio)
SMT	Surface-Mount Technology
SPACAL	SPAghetti CALorimeter
SPAD	Single Photon Avalanche Diode
SPS	Super Proton Synchrotron
STIC	Small angle TIle Calorimeter
Tcl/Tk	Tool Command Language/Toolkit
TDC	Time to Digital Converter
TOF	Time-Of-Flight
TRD	Transition Radiation Detector
TTL	Transistor Transistor Logic
UV	Ultra Violet
USA	United States of America
USSR	Union of Soviet Socialist Republics
VME	Versa Module Eurocard
VPT	Vacuum PhotoTriode

WLS Wave Length Shifter

List of Figures

1.1 Jet energy resolution effect on the $W^{\pm}$ and Z^0 bosons reconstruction. 7
1.2 Fraction of the EM component in a hadronic shower as a function of the energy. 8
1.3 Average energy fraction contained in a block of material as a function of λ_{int}. 9
1.4 The SPACAL calorimeter. 10
1.5 Energy resolution of the SPACAL calorimeter. 11
1.6 Calorimeter signal as a function of the impact point and the tilt angle. 12
1.7 Light attenuation in the scintillating fibers of the SPACAL calorimeter and energy resolution for pions. 13
1.8 Sketch of the CALICE ECAL structure. 15
1.9 Sketch of the CALICE ECAL scintillator tiles. 16
1.10 Picture of the CALICE ECAL. 16
1.11 Linearity and energy resolution of the first prototype of the CALICE ECAL. 17
1.12 Linearity and energy resolution of the second prototype of the CALICE ECAL. 18
1.13 Layout of the active layer and tiles of the prototype of the CALICE HCAL. 19
1.14 Schematic representation of a cassette of the CALICE HCAL. . . 19
1.15 Linearity and energy resolution for electrons of the prototype of the CALICE HCAL. 20
1.16 Energy response to pions and π/e value at different energies of the prototype of the CALICE HCAL. 21
1.17 Energy resolution of the HCAL using different analysis approaches. 22
1.18 Basic module of the DREAM calorimeter. 23
1.19 DREAM calorimeter readout structure and fiber bundles. 24
1.20 Pion signals and energy resolution of the uncorrected DREAM calorimeter. 25

1.21 Value of the Q/S ratio and linear fit to the scintillator versus f_{em} value. 26
1.22 Energy resolution and linearity before and after the Q/S correction. 27
1.23 Energy resolution and linearity before and after the $(Q+S)/E$ correction. 27
1.24 Layout of the PAMELA and AMS-02 experiments. 30
1.25 Picture of the PAMELA calorimeter module. 31
1.26 Energy resolution and electron/pion discrimination of the PAMELA calorimeter. 31
1.27 Particle identification performed with the PAMELA calorimeter with in flight data. 32
1.28 Sketch and picture of the AMS-02 calorimeter. 33
1.29 Linearity, energy and angular resolution of the AMS-02 calorimeter. 34
1.30 Map of the sky obtained with gamma rays above 100 MeV. 35
1.31 Layout of a gamma telescope. 36
1.32 Layout of the Gamma-400 observatory. 37

2.1 A *p-n* junction. 40
2.2 The *p-n* junction with different bias configurations. 41
2.3 I-V characteristic curve for a *p-n* junction. 42
2.4 Rate of ionization energy loss as a function of the energy. 44
2.5 Detection of light inside a reverse biased *p-n* junction. 45
2.6 Absorption length in silicon as a function of the photon wavelength. 45
2.7 Qualitative explanation of the avalanche multiplication. 47
2.8 Comparison of the typical QE of PMTs and PIN diodes. 48
2.9 Picture and schematic representation of a PIN diode. 50
2.10 Sketch and energy resolution of a module of the BaBar calorimeter. 51
2.11 Sketch and picture of a HPD. 52
2.12 Sketch of the LHCb HPD detector and light cone of a 120 GeV/c pion. 52
2.13 Device structures and electric field profiles of different APDs. . . 53
2.14 Sketch and pictures of the CMS APDs. 54
2.15 Structure and electric field of a Sadygov Geiger-mode APD. . . . 56
2.16 Pulse height and gain linear dependence of a SiPM. 57
2.17 SiPM non-linear response to a 40 ps laser light signal. 58
2.18 Thermal and field-assisted generation of free carriers. 59
2.19 Dark count rate as a function of bias and temperature. 59
2.20 Dark count rate as a function of the electronics threshold. 60
2.21 PDE as a function of the wavelength and bias voltage. 61
2.22 Sketch of the optical crosstalk phenomenon. 61
2.23 Optical grooves and their effect on the SiPM pulse height. 62

2.24 Breakdown voltage as a function of temperature of a FBK-irst SiPM. 63
2.25 Gain as a function of the bias voltage for different temperatures. . 64
2.26 Single photoelectron timing resolution. 65
2.27 Single photoelectron timing resolution with diffusion tail events. . 65
2.28 Time resolution as a function of the overvoltage. 66
2.29 Gamma irradiation effects. 67
2.30 Neutron irradiation effects on the SiPM pulse height. 68
2.31 Neutron irradiation effects on the SiPM dark counts and V_{BD}. . . . 68
2.32 Proton irradiation effects on the SiPMs dark counts. 69
2.33 Proton irradiation effects on the SiPMs pulse height. 70
2.34 Sketch of the typical FBK-irst micro-cell composing the SiPM. . . 71
2.35 Signal shape and pulse height distribution of FBK-irst SiPMs. . . 72
2.36 Gain and dark counts as a function of the temperature and the bias voltage. 72
2.37 PDE comparison between different FBK-irst SiPMs. 73
2.38 Timing resolution as a function of the overvoltage. 74

3.1 The East Hall of the PS complex. 77
3.2 Beam profile and divergence of the T9 beamline. 78
3.3 The experimental setup on the PS T9 beamline. 79
3.4 Pictures of the silicon beam chambers. 79
3.5 The EMR prototype. 80
3.6 SiPMs plastic mask. 81
3.7 DAQ chain and GUI. 82
3.8 The Hamamatsu S10362-050U and FBK-irst devices. 84
3.9 Multi-peak distribution and linearity of the FBK-irst device. . . . 85
3.10 Noise and signal event distribution of the FBK-irst SiPM. 86
3.11 Signal to noise ratio of the FBK-irst SiPM. 86
3.12 Bar overall efficiency for the PMT and FBK-irst SiPM. 87
3.13 Signal to noise ratio of the Hamamatsu SiPMs 88
3.14 Bar overall efficiency with the Hamamatsu SiPMs 89
3.15 Timing resolution of the Hamamatsu SiPMs 90
3.16 Picture of the experimental setup of the 2011 cosmic ray test. . . . 92
3.17 Sketch of the DAQ scheme of the 2011 cosmic ray test. 93
3.18 Scheme of one of the MAROC3 channels. 94
3.19 Picture of the MAROC3 board. 95
3.20 Cosmic ray distribution in the x and y direction. 96
3.21 SiPM and PMT pulse height and S/N ratio. 97
3.22 2D detector efficiency for the SiPMs and MAPMT readout. 98
3.23 1D detector efficiency for the SiPMs and MAPMT readout. 98
3.24 Cross talk effect for the SiPMs and MAPMT readout. 99

3.25 Spatial resolution for the SiPMs and MAPMT readout. 100
3.26 Example of TDC spectrum for the SiPMs and MAPMT readout. . 100
3.27 Sketch of the event selection at the two bar ends. 101
3.28 Comparison between the SiPM TDC spectrum obtained for the two ends of the bar. 101

4.1 Lateral and frontal sketch of the prototype 0 calorimeter. 104
4.2 The prototype 0 calorimeter during the assembly phase. 105
4.3 Multianode PMT and SiPMs array used for the light readout. . . . 106
4.4 Custom SiPM readout board. 106
4.5 ADC timing and signal delay. 107
4.6 Experimental setup and DAQ scheme at the PS T10 beamline. . . 108
4.7 Picture and sketch of the North Area beamlines. 109
4.8 The experimental setup at the SPS H4 beamline. 110
4.9 The DAQ chain for the high energy tests. 110
4.10 GEANT4 simulation of the prototype 0 calorimeter. 112
4.11 Gaussian fit to the energy deposit histogram. 112
4.12 Low energy linearity and energy resolution with the simulated prototype 0 data. 113
4.13 Linearity and energy resolution of the prototype 0: simulated “point-like” beam. 114
4.14 Linearity and energy resolution of the prototype 0: simulated “Gaussian-shaped” beam. 115
4.15 Energy deposit profile as a function of the scintillator tile number. 116
4.16 Energy resolution with the complete prototype 0 simulated dataset. 116
4.17 Software equalization of the readout channels. 118
4.18 Total energy deposit and electron abundance. 119
4.19 Fiducial area selection. 119
4.20 Total and electron events. 120
4.21 Prototype 0 linearity and resolution with the MAPMT readout. . . 120
4.22 SiPM gain drifting. 121
4.23 SiPM drifting linearization. 122
4.24 Prototype 0 low energy linearity. 123
4.25 Prototype 0 low energy resolution. 124
4.26 Pedestal distribution of the prototype 0 calorimeter. 125
4.27 Calorimeter channel division. 126
4.28 MAPMT readout spatial resolution. 127
4.29 SiPM readout spatial resolution. 127
4.30 Resolution scan at different energies. 128
4.31 Magnetic spectrometer high energy spectrum. 128
4.32 Photon energy scatter plot and fit of the 20 GeV slice. 129

4.33 Linearity and energy resolution in the prototype 0 high energy tests. 129
4.34 Inverted and linearized linearity in the prototype 0 high energy tests. 130
4.35 Low energy photons linearity and energy resolution with the prototype 0 calorimeter. 130
4.36 Custom LEMO cables for the SiPM/MAROC connection. 132
4.37 Total pedestal distribution fitted with a Gaussian function. 132
4.38 Fiducial area selection. 134
4.39 Linearity of the prototype 0 with the MAROC readout. 134
4.40 Energy resolution of the prototype 0 with the MAROC readout. . . 135
4.41 Saturation of a SiPM channel with the MAROC readout. 136

5.1 Lateral and frontal sketch of the prototype 1 calorimeter. 138
5.2 The prototype 1 calorimeter during the assembly phase. 139
5.3 The 9 mm^2 FBK-irst SiPM. 140
5.4 Low energy setup for the prototype 1 calorimeter tests. 140
5.5 High energy setup for the prototype 1 calorimeter tests. 141
5.6 GEANT4 simulation of the prototype 1 shashlik calorimeter. . . . 142
5.7 Linearity and energy resolution with the simulated prototype 1 data. 143
5.8 Prototype 1 electron peak fit. 145
5.9 Prototype 1 low energy linearity. 146
5.10 Prototype 1 low energy resolution with a fixed and floating noise term. 147
5.11 Pedestal distribution of the prototype 1 calorimeter. 148
5.12 Calorimeter spatial resolution at 4 GeV. 149
5.13 Linearity and energy resolution in the prototype 1 high energy tests. 150
5.14 Linearized linearity and corrected energy resolution in the prototype 1 high energy tests. 151
5.15 Low energy photons linearity and energy resolution with the prototype 1 calorimeter. 152
5.16 Sketch of a WLS fiber in the GEANT4 optical simulation. 153
5.17 Reflection and refraction processes simulated by GEANT4. 154
5.18 Sensitive detectors used to count the collected photons. 155
5.19 Optical simulation of a 1 GeV electron event. 156
5.20 Total and mean number of photons per SiPM and fiber pattern of the exponential tail events. 157
5.21 Energy resolution obtained with different values of the reflection coefficient. 158
5.22 Energy resolution obtained with different values of the noise term. 159
5.23 Linearity with and without the noise term. 159
5.24 Final performance of the calorimeter according to the optical simulation. 160

5.25 Optical simulation spatial resolution with reflection coefficients of 0.6 and 0.9 and 16 readout channels. 161
5.26 Optical simulation spatial resolution with reflection coefficients of 0.6 and 0.9 and 36 readout channels. 163
5.27 Prototype 1 calorimeter modifications. 164
5.28 Prototype 1 calorimeter new fibers. 165
5.29 Prototype 1 calorimeter fiber holders. 166
5.30 Complete LED system. 167
5.31 Prototype 1 calorimeter Peltier system. 167
5.32 Prototype 1 calorimeter SiPMs custom board. 168
5.33 Prototype 1 calorimeter final electronic assembly. 168
5.34 H2 beamline setup and CAEN power supply. 169
5.35 LED system linearization procedure. 171
5.36 Electron peak without the exponential tail. 172
5.37 Linearity and energy resolution results in the May 2011 tests. . . . 173
5.38 Spatial resolution results in the May 2011 tests. 173
5.39 LED drift with or without the Peltier system. 175
5.40 Common mode distribution and subtraction. 176
5.41 Linearity and energy resolution in the August 2011 tests. 177
5.42 Linearity in the H2 tests. 179
5.43 Energy resolution deviation from the $1/\sqrt{E}$ behavior. 180
5.44 Common mode distribution at high energy. 181

6.1 Emission and absorption spectra of $PbWO_4$ crystals. 184
6.2 Picture of the $PbWO_4$ crystal. 185
6.3 FBK-irst quad SiPM. 186
6.4 $PbWO_4$ crystal plastic clamp. 186
6.5 Example of I-V curves obtained for two quads characterized by very different (a) and very similar (b) pads characteristics. 187
6.6 $PbWO_4$ crystal pulse height. 188
6.7 $PbWO_4$ crystal efficiency. 189
6.8 Energy resolution at 1 GeV with a single and dual SiPM readout. . 189
6.9 Linearity and energy resolution scan of a $PbWO_4$ crystal. 190
7.1 SiPM tile with 16 4x4 mm^2 embedded. 194

A.1 Schematic representation of the bremsstrahlung process. 198
A.2 Electron/Positron fractional energy loss per radiation length in lead. 199
A.3 Critical energy definition in copper. 200
A.4 Photon interaction cross section in lead. 201
A.5 Graphic representation of the photoelectric effect. 202
A.6 Graphic representation of the Compton effect. 203

A.7 Graphic representation of the pair production process. 204
A.8 Monte-Carlo calculation of the composition of the EM shower. . . 205
A.9 EM shower development as a function of the radiation lengths. . . 206
A.10 Monte-Carlo calculation of the energy deposit as a function of depth in different materials. 207
A.11 Monte-Carlo calculation of the energy deposit as a function of depth and energy in copper. 208
A.12 Molière radius dependence on Z and energy. 210
A.13 Energy resolution of a liquid-krypton calorimeter. 211
A.14 Effects of longitudinal and lateral shower leakage on the energy resolution. 215
A.15 Schematic representation of the first fiber calorimeter. 216
A.16 Energy resolution of the Fessler calorimeter. 217
A.17 Schematic representation of the first shashlik calorimeter. 218
A.18 Linearity and energy resolution with the Atoyan calorimeter. . . . 219

B.1 Layout of the two circuits used for the SiPMs readout. 222
B.2 RMS of the pedestal distribution obtained with the new and old SiPM readout circuit. 222
B.3 Peak resolution obtained with a pulsed LED with the old and new readout circuit. 223
B.4 Sketch of the MAROC shaper output with the dual hold method. . 224
B.5 Comparison between the pedestal RMS with the dual hold method. 225
B.6 Peak resolution obtained with a pulsed LED with the single and dual hold readout method. 225
B.7 Comparison of the pedestal RMS with the new and old cables. . . 226
B.8 Peak resolution obtained with a pulsed LED in the new cable configuration. 227
B.9 Peak resolution obtained with a low intensity pulsed LED with the old and new connection cables. 227
B.10 The MAROC slow shaper circuit. 229
B.11 Pedestal RMS with the slower and faster shaper configuration. . . 230
B.12 Peak resolution obtained with a low intensity pulsed LED with the slow and fast shaper configuration. 231

List of Tables

2.1 Different photodetectors available on the market listed according to their gain factor. 49
2.2 FBK-irst SiPM specifications. 74

3.1 Tracker SiPMs specifications. 84
3.2 Performance of the Hamamatsu SiPMs in the 2008 tests. 91

4.1 Prototype 0 simulated energy leakage. 117
4.2 Bias values for the four SiPMs groups in the three current configurations - 2009 tests. 118
4.3 Bias values for the four SiPMs groups in the two current configurations - 2010 tests. 133

5.1 Prototype 1 energy resolution results with low and high energy simulated data. 143
5.2 Prototype 1 simulated energy leakage. 144
5.3 Bias values for the two SiPM groups in the four current configurations - 2009 tests. 144
5.4 Prototype 1 low energy resolution results. 147
5.5 Spatial resolution for different beam energies using the SiPMs biased at 40 μA. 149
5.6 Bias values for the four SiPMs groups corresponding to a 3 μA current consumption - 2010 tests. 150
5.7 Optical properties of the scintillator tiles and the WLS fibers. . . . 153
5.8 Simulated and experimental spatial resolution. 162
5.9 Bias values for the nine SiPMs groups in the four current configurations - 2011 tests. 170
5.10 2009 and 2011 spatial resolution comparison. 174
5.11 Energy resolution comparison between the May and August 2011 beamtests. 178

Bibliography

[1] R. Wigmans: *Calorimetry: energy measurements in particle physics*. Oxford Science Publications, Oxford, 2000.

[2] N. Akchurin, R. Wigmans: "Hadron Calorimetry". *Nucl. Instr. and Meth. in Phys. Res. A*, 666:80–97, 2012.

[3] M. Aleksa *et al.*: "Measurement of the response of the ATLAS liquid argon barrel calorimeter to electrons at the 2004 combined test-beam". *Nucl. Instr. and Meth. in Phys. Res. A*, 614:400–432, 2010.

[4] P. Adzic *et al.*: "Energy resolution of the barrel of the CMS Electromagnetic Calorimeter". *Journal of Instrumentation*, 2:P04004, 2007.

[5] J. Brau *et al.*: "ILC Reference Design Report: Physics at the ILC". *ILC-REPORT-2007-001*, 2, 2007.

[6] K. Nakamura *et al.*: "The Review of Particle Physics". *J. of Phys. G*, 37:075021, 2010.

[7] J. Repond *et al.*: "Calorimetry at the International Linear Collider". *Nucl. Instr. and Meth. in Phys. Res. A*, 572:211–214, 2007.

[8] E. Bernardi *et al.*: "Perfomance of a compensating lead-scintillator hadronic calorimeter". *Nucl. Instr. and Meth. in Phys. Res. A*, 262:229–242, 1987.

[9] D. Acosta *et al.*: "Electron, pion and multiparticle detection with a lead/scintillating-fiber calorimeter". *Nucl. Instr. and Meth. in Phys. Res. A*, 308:481–508, 1991.

[10] M. A. Thomson: "Particle flow calorimetry and the PandoraPFA algorithm". *Nucl. Instr. and Meth. in Phys. Res. A*, 611:25–40, 2009.

[11] D. Buskulic *et al.*: "Performance of the ALEPH detector at LEP". *Nucl. Instr. and Meth. in Phys. Res. A*, 360:481–506, 1995.

[12] The CALICE collaboration: “CALICE Report to the Calorimeter R&D Review Panel”. *arXiv:1003.1394v2 [physics.ins-det]*, 2007.

[13] The CALICE collaboration: “The SCintillator-ECAL Beam Test at DESY: First Results”. *CALICE analysis note*, 005, 2007.

[14] K. Kotera *et al.*: “Study of the granular electromagnetic calorimeter with PPDs and scintillator strips for ILC”. *Nucl. Instr. and Meth. in Phys. Res. A*, 628:347–350, 2011.

[15] G. Eigen on behalf of the CALICE collaboration: “Construction and commissioning of the CALICE analog hadron calorimeter prototype”. *Journal of Instrumentation*, 5:P05004, 2010.

[16] The CALICE collaboration: “Analysis of low-energetic electron and pion data collected with the AHCAL prototype at Fermilab”. *CALICE analysis note*, 34, 2011.

[17] The CALICE collaboration: “Initial Study of Hadronic Energy Resolution in the Analog HCAL and the complete CALICE Setup”. *CALICE analysis note*, 15, 2011.

[18] N. Akchurin *et al.*: “Hadron and jet detection with a dual-readout calorimeter”. *Nucl. Instr. and Meth. in Phys. Res. A*, 537:537–561, 2005.

[19] N. Akchurin *et al.*: “Dual-Readout calorimetry with crystal calorimeters”. *Nucl. Instr. and Meth. in Phys. Res. A*, 598:710–721, 2009.

[20] V. F. Hess: “Unsolved Problems in Physics: Tasks for the Immediate Future in Cosmic Ray Studies”. *Nobel Lecture*, 1936.

[21] V. Berezinsky: “Ultra high energy cosmic rays”. *Nuclear Physics B - Proceedings Supplements*, 70:419–430, 1999.

[22] V. Bonvicini *et al.*: “Performance of the PAMELA Si-W imaging calorimeter in space”. *J. Phys.: Conf. Ser.*, 160:012039, 2009.

[23] K. Lübelsmeyer *et al.*: “Upgrade of the Alpha Magnetic Spectrometer (AMS-02) for long term operation on the International Space Station (ISS)”. *Nucl. Instr. and Meth. in Phys. Res. A*, 654:639–648, 2011.

[24] AMS-02 experiment official internet page: *http://www.ams02.org/what-is-ams/tecnology/*.

[25] M. Pearce: "The status of the PAMELA experiment". *Nucl. Phys. B*, 113:314–321, 2002.

[26] S. Di Falco *et al.*: "Results of 2007 test beam of AMS-02 Electromagnetic Calorimeter". *Advances in Space Research*, 45:112–122, 2010.

[27] NASA Web Site: "Gamma-ray Astronomy Satellites and Missions". *http://imagine.gsfc.nasa.gov/docs/sats_n_data/gamma_missions.html*.

[28] D. J. Thompson *et al.*: "Calibration of Energetic Gamma-Ray Experiment Telescope (EGRET) for the Compton Gamma-Ray Observatory". *Astrophysical Journal Supplement Series*, 86:629, 1993.

[29] M. Tavani *et al.*: "The AGILE space mission". *Nucl. Instr. and Meth. in Phys. Res. A*, 588:52–62, 2008.

[30] A. A. Moiseev: "Gamma-ray Large Area Space Telescope: Mission overview". *Nucl. Instr. and Meth. in Phys. Res. A*, 588:41–47, 2008.

[31] C. Labanti *et al.*: "Design and construction of the Mini-Calorimeter of the AGILE satellite". *Nucl. Instr. and Meth. in Phys. Res. A*, 598:470–479, 2009.

[32] A. M. Galper *et al.*: "The possibilities of simultaneous detection of gamma rays, cosmic-ray electrons and positrons on the GAMMA-400 space observatory". *Astrophys. Space Sci. Trans.*, 7:75–78, 2011.

[33] S. M. Sze: *Semiconductor devices*. Wiley, New York, 1985.

[34] G. Lutz: *Semiconductor radiation detectors*. Springer, Berlin, 1999.

[35] W. R. Leo: *Techniques for Nuclear and Particle Physics Experiments*. Springer-Verlag, Berlin, 1993.

[36] S. Korpar: "Status and perspectives of solid state photon detectors". *Nucl. Instr. and Meth. in Phys. Res. A*, 639:88–93, 2011.

[37] D. Renker: "New developments on photosensors for particle physics". *Nucl. Instr. and Meth. in Phys. Res. A*, 598:207–212, 2009.

[38] D. Renker, E. Lorenz: "Advances in solid state photon detectors". *Journal of Instrumentation*, 4:P04004, 2009.

[39] M. Danilov: "Novel photo-detectors and photo-detector systems". *Nucl. Instr. and Meth. in Phys. Res. A*, 604:83–189, 2009.

[40] R. J. Barlow: “Results from the BaBar electromagnetic calorimeter beam test”. *Nucl. Instr. and Meth. in Phys. Res. A*, 420:162–180, 1999.

[41] B. Aubert: “The BaBar detector”. *Nucl. Instr. and Meth. in Phys. Res. A*, 479:1–116, 2002.

[42] P. Weilhammer: “Silicon-based HPD development: sensors and front ends”. *Nucl. Instr. and Meth. in Phys. Res. A*, 446:289–298, 2000.

[43] G. Anzivino *et al.*: “Review of the hybrid photo diode tube (HPD) an advanced light detector for physics”. *Nucl. Instr. and Meth. in Phys. Res. A*, 365:76–82, 1995.

[44] S. Easo: “Development of the RICH detectors in LHCb”. *Nucl. Instr. and Meth. in Phys. Res. A*, 502:46–51, 2003.

[45] J. Grahl *et al.*: “Radiation hard avalanche photodiodes for CMS ECAL”. *Nucl. Instr. and Meth. in Phys. Res. A*, 504:44–47, 2003.

[46] E. Pilicer *et al.*: “Excess noise factor of neutron-irradiated silicon avalanche photodiodes”. *Nucl. Instr. and Meth. in Phys. Res. A*, 552:146–151, 2005.

[47] R. J. McIntyre: “Theory of Microplasma Instability in Silicon”. *Journal of Applied Physics*, 32:983–995, 1961.

[48] R. H. Haitz: “Model for the Electrical Behavior of a Microplasma”. *Journal of Applied Physics*, 35:1370–1376, 1964.

[49] V. Saveliev, V. Golovin: “Silicon avalanche photodiodes on the base of metal-resistor-semiconductor (MRS) structures”. *Nucl. Instr. and Meth. in Phys. Res. A*, 442:223–229, 2000.

[50] D. Bisello *et al.*: “Metal-Resistive layer-Silicon (MRS) avalanche detectors with negative feedback”. *Nucl. Instr. and Meth. in Phys. Res. A*, 360:83–86, 1995.

[51] P. Buzhan *et al.*: “ICFA Instrumentation Bulletin”. 23:28–41, 2001.

[52] B. Dolgoshein *et al.*: “Status report on silicon photomultiplier development and its application”. *Nucl. Instr. and Meth. in Phys. Res. A*, 563:368–376, 2006.

[53] D. Renker: “Geiger-mode avalanche photodiodes, history, properties and problems”. *Nucl. Instr. and Meth. in Phys. Res. A*, 567:48–56, 2006.

[54] A. Piazza *et al.*: "Characterization and simulation of different SiPM structures produced at FBK". *Nucl. Instr. and Meth. in Phys. Res. A*, 617:417–419, 2010.

[55] V. C. Spanoudaki *et al.*: "Use of single photon counting detector arrays in combined PET/MR: Characterization of LYSO-SiPM detector modules and comparison with LSO-APD detector". *Journal of Instrumentation*, 2:P12002, 2007.

[56] F. Retière *et al.*: "Characterization of Multi Pixel Photon Counters for T2K Near Detector". *Nucl. Instr. and Meth. in Phys. Res. A*, 610:378–380, 2009.

[57] S. Wang *et al.*: "Analysis of breakdown probabilities in avalanche photodiodes using a history-dependent analytical model". *Applied Physics Letters*, 82:1971–1973, 2003.

[58] P. Eckert *et al.*: "Characterization studies of silicon photomultipliers". *Nucl. Instr. and Meth. in Phys. Res. A*, 620:217–226, 2010.

[59] C. Piemonte: "A new Silicon Photomultiplier structure for blue light detection". *Nucl. Instr. and Meth. in Phys. Res. A*, 568:224–232, 2006.

[60] B. Dolgoshein *et al.*: "Large area silicon photomultipliers: performance and applications". *Nucl. Instr. and Meth. in Phys. Res. A*, 567:78–82, 2006.

[61] G. Collazuol *et al.*: "Studies of silicon photomultipliers at cryogenic temperatures". *Nucl. Instr. and Meth. in Phys. Res. A*, 628:389–392, 2011.

[62] S. Uozumi *et al.*: "Development and study of the multi pixel photon counter". *Nucl. Instr. and Meth. in Phys. Res. A*, 581:427–432, 2007.

[63] B. Dolgoshein *et al.*: "Silicon photomultiplier and its possibile applications". *Nucl. Instr. and Meth. in Phys. Res. A*, 504:48–52, 2003.

[64] G. Collazuol *et al.*: "Single photon timing resolution and detection efficiency of the IRST silicon photo-multipliers". *Nucl. Instr. and Meth. in Phys. Res. A*, 581:461–464, 2007.

[65] T. Matsubara *et al.*: "Radiation damage of MPPC by γ-ray irradiation with ^{60}Co". *Proceedings of the International Workshop on New Photon-Detectors PD07*, 032:1–6, 2007.

[66] I. Nakamura: "Radiation damage of pixelated photon detector by neutron irradiation". *Nucl. Instr. and Meth. in Phys. Res. A*, 610:110–113, 2009.

[67] Y. Musienko *et al.*: “Study of radiation damage induced by 82 MeV protons on multi-pixel Geiger-mode avalanche photodiodes”. *Nucl. Instr. and Meth. in Phys. Res. A*, 610:87–92, 2009.

[68] C. Piemonte *et al.*: “Recent developments on Silicon Photomultipliers produced at FBK-irst”. *IEEE Nuclear Science Symposium Conference Record*, N41-2:2089–2092, 2007.

[69] C. Piemonte: “Characterization of the first prototypes of Silicon Photomultiplier fabricated at ITC-irst”. *IEEE Transactions on Nuclear Science*, 54:236–244, 2007.

[70] A. Tarolli *et al.*: “Characterization of FBK SiPMs under illumination with very fast light pulses”. *Nucl. Instr. and Meth. in Phys. Res. A*, 617:430–431, 2010.

[71] Y. Kudenko for the T2K collaboration: “The near neutrino detector for the T2K experiment”. *Nucl. Instr. and Meth. in Phys. Res. A*, 598:289–295, 2009.

[72] H. Gast *et al.*: “PEBS - Positron Electron Balloon Spectrometer”. *Nucl. Instr. and Meth. in Phys. Res. A*, 581:151–155, 2007.

[73] D. Bolognini *et al.*: “Tests of the MICE Electron Muon Ranger frontend electronics with a small scale prototype”. *Nucl. Instr. and Meth. in Phys. Res. A*, 646:108–117, 2011.

[74] A. Pla-Dalmau *et al.*: “Extruded plastic scintillator for MINERνA”. *IEEE Nuclear Science Symposium Conference Record*, N35-25, 2005.

[75] A. Berra *et al.*: “Silicon Photomultipliers characterization for the EMR prototype of the MICE experiment”. *Nucl. Instr. and Meth. in Phys. Res. A*, 609:129–135, 2009.

[76] L. Durieu *et al.*: “Optics studies for the T9 beam line in the CERN PS East Area secondary beam facility”. *Proceedings of the 19th IEEE PAC 2001*, CERN-PS-2001-037-AE, 2001.

[77] M. Prest *et al.*: “The AGILE silicon tracker: an innovative γ-ray instrument for space”. *Nucl. Instr. and Meth. in Phys. Res. A*, 501:280–287, 2003.

[78] D. Lietti *et al.*: “The prototype of the MICE Electron Muon Ranger: design, construction and test”. *Nucl. Instr. and Meth. in Phys. Res. A*, 604:314–318, 2009.

[79] Hamamatsu catalog: *MPPC: Multi-Pixel Photon Counter datasheet*, 2011.

[80] S. Franz, P. Barillon: "ATLAS ALFA-measuring absolute luminosity with scintillating fibres". *Nucl. Instr. and Meth. in Phys. Res. A*, 610:35–40, 2009.

[81] G. Llosà *et al.*: "Characterization of a PET detector head based on continuous LYSO crystals and monolithic, 64-pixel silicon photomultiplier matrices". *Physics in Medicine and Biology*, 55:7299–7315, 2010.

[82] S. J. Alvsvaag *et al.*: "The Small Angle Tile calorimeter in the DELPHI experiment". *Nucl. Instr. and Meth. in Phys. Res. A*, 425:106–139, 1999.

[83] A. Berra *et al.*: "Silicon Photomultipliers as a Readout System for a Scintillator-Lead Shashlik Calorimeter". *IEEE Transactions on Nuclear Science*, 58:1297–1307, 2011.

[84] B. C. Choudhary, L. Mualem: "Technical Specifications for the procurement of wavelength shifting fibre". *MINOS Internal Note*, NuMI-L-589, 2000.

[85] SPS user's page: *http://sl.web.cern.ch/sl/eagroup/beams.html#h4*.

[86] AIDA official page: *http://aida.web.cern.ch/ aida/activities/access/CERN/*.

[87] W. Scandale *et al.*: "Experimental study of the radiation emitted by 180-GeV/c electrons and positrons volume-reflected in a bent crystal". *Phys. Rev. A*, 012903, 2009.

[88] L. Celano *et al.*: "A high resolution beam telescope built with double sided silicon strip detectors". *Nucl. Instr. and Meth. in Phys. Res. A*, 381:49–56, 1996.

[89] J. Allison *et al.*: "Geant4 developments and applications". *IEEE Transactions on Nuclear Science*, 53:270–278, 2006.

[90] PS user's page: *http://gatignon.web.cern.ch/gatignon/EastArea/*.

[91] T. C. Awes *et al.*: "A simple method of shower localization and identification in laterally segmented calorimeters". *Nucl. Instr. and Meth. in Phys. Res. A*, 311:130–138, 1992.

[92] A. Berra *et al.*: "A shashlik calorimeter readout with silicon photomultipliers with no amplification of the output signal". *Journal of Instrumentation*, 6:P10004, 2011.

[93] Saint-Gobain: "Scintillating optical fibers". *http://www.detectors.saint-gobain.com/uploadedFiles/SGdetectors/Documents/Brochures/Scintillating-Optical-Fibers-Brochure.pdf*.

[94] G. S. Atoyan *et al.*: "Lead-scintillator electromagnetic calorimeter with wavelength shifting fiber readout". *Nucl. Instr. and Meth. in Phys. Res. A*, 320:144–154, 1992.

[95] Y. Musienko for the CMS ECAL Collaboration: "The CMS Electromagnetic Calorimeter". *Nucl. Instr. and Meth. in Phys. Res. A*, 490:30–50, 2002.

[96] A. A. Annenkov *et al.*: "Lead tungstate scintillation material". *Nucl. Instr. and Meth. in Phys. Res. A*, 494:308–312, 2002.

[97] S. Chatrchyan *et al.*: "The CMS experiment at the CERN LHC". *Journal of Instrumentation*, 8:S08004, 2008.

[98] C. W. Fabjan, F. Gianotti: "Calorimetry for particle physics". *Review of Modern Physics*, 75:1243–1286, 2003.

[99] H. Fessler: "A tower structured scintillator-lead photon calorimeter using a novel fiber optics readout system". *Nucl. Instr. and Meth. in Phys. Res. A*, 228:303–308, 1985.

[100] R. Dzhelyadin: "The LHCb calorimeter detectors". *Nucl. Instr. and Meth. in Phys. Res. A*, 581:384–388, 2007.

[101] Omega Group: "MAROC Datasheet". *Private Communication*, 2009.